Lower Airway Exposure to Particulate Emissions from Cooking Oil by a CT-Imaging Based 3D-Printed Human Airway Model

Kirstine Meyer Frandsen and Malthe Haahr Hvelplund

Master Thesis
June 2018
Indoor Environmental and Energy Engineering
Aalborg University

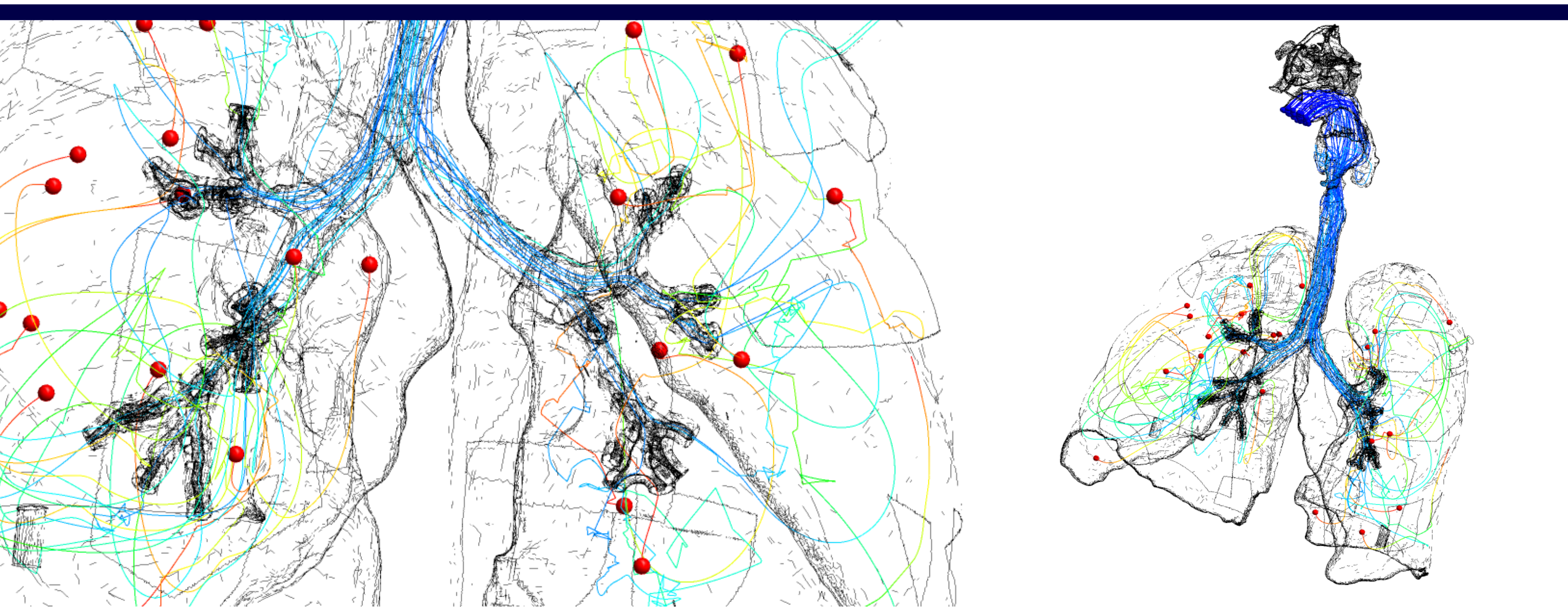

AALBORG UNIVERSITY
STUDENT REPORT

School of Engineering and Science
Department of Civil Engineering
Indoor Environmental and Energy Engineering
Thomas Manns Vej 23
9220 Aalborg East
http://www.civil.aau.dk/

Titel:

Lower Airway Exposure to Particulate Emissions from Cooking Oil by a CT-imaging Based 3D-Printed Human Airway Model

Project:

Master Thesis

Project Period:

01-09-2017 - 08-06-2018

Group Members:

Kirstine Meyer Frandsen
Malthe Haahr Hvelplund

Supervisors:

Li Liu, Associate Professor
Chen Zhang, Assistant Professor
Peter V. Nielsen, Professor Emeritus

Copies: 2
Pages: 109
Appendices: 54

Synopsis:

This Master Thesis investigates the lower airway exposure to indoor airborne particles by a CT-imagining based 3D printed human airway model, where the indoor airborne particles are limited to cooking generated particles by oil heating.
The report is divided intro three parts: "Experimental Investigation of Lower Airway Exposure by Cooking Oil", "Numerical Investigation of Particle Exposure in the Lower Airways" and "Final Assessment of the Investigations".

In the first part the spatiotemporal and size-resolved dynamics of particle concentration generated by cooking oil is examined by experimental investigation. A 3D printed human airway model is applied to examine particle exposure within the occupant's lower airways under controlled experimental conditions.

In the second part the size-resolved regional particle deposition within the airways is investigated by CFD simulations conducted on the same 3D airways model. The results are compared to existing studies to determine any variations and interpreted the use of this new technology.

In the third part an overall assessment of the investigations is conducted, including a discussion of methodology.

Abstract in English

The purpose of this project is to gain a deeper understanding of particle exposure in an anatomically correct model of the lower airways. The model has been developed from the CT-scanning of a human male. This is a new approach to investigating the effect of indoor airborne particles on the human occupants. The CT-scanning is applied to develop a 3D printed model for experimental use and the same geometry was used to conduct CFD simulations in a numerical investigation.

The experimental investigation focused on four different types of cooking oil, which generate real polydispersed particles. The 3D printed airway model was placed in close proximity to the emission source and particle concentration was measured in several locations in the displacement ventilated clean room. The duration of the measurement extended from the start of the source-active period until initial conditions were reached.

The investigation concluded that the mass concentration varies with a factor of five between peak concentrations of the different oil types. Olive oil generated the most particles and sunflower oil generated the least. The size-resolved distribution of the cooking emitted particles were based on number concentration and showed to be very similar for the different oil types, as well as during the different times of the measurement. Thereby the difference in mass concentration was not due to the sizes of the particles but more likely the smoke points of the various oils. Peak concentration was almost reached simultaneously for the different measurement locations.

The effect of the thermal plume on mass concentration in the breathing zone was also investigated by a thermal manikin. This showed no differences in mass concentration due to an overpowering thermal plume generated by the emission source.

The numerical investigation was used to analyse the regional particle deposition of monodispersed particles. Steady state CFD simulations were carried out due to time constraints set by the computational power. Results showed that the majority of the particles were deposited in the bronchi. Accumulation particles (0.1 - 2.0 μm) have the smallest deposition fraction in the lower airways. An increase in the aerodynamic diameter (>2.0 μm) of the particles elevated the deposition fraction.

A comparison of the deposition fractions from the experimental and numerical investigations showed a big deviation. This is attributed to the different parameters set and assumptions applied in the process.

Overall this study advances knowledge on the characteristics of both exposure and intake of particles by the implementation of state-of-the-art technology. This knowledge contributes to future investigations into control methods that minimise the negative health impact of indoor emissions.

Abstract in Danish

Formålet ved dette afgangsprojekt er at opnå en dybere forståelse af partikeleksponeringen i de menneskelige luftveje. Dette udføres ved brug af en anatomisk korrekt model af de nedre luftveje udviklet på baggrund af CT-scanningen af en mand. Dette er en innovativ tilgang til at undersøge partikeleksponering fra forskellige forureningskilder, som ikke før er blevet anvendt i takt med den teknologiske udvikling.

CT-scanningen har ført til en 3D printet luftvejsmodel, der muliggør en eksperimentel undersøgelse. Luftvejsmodellens geometri bliver ligeledes brugt til en numerisk undersøgelse.

De eksperimentelle undersøgelser af partikeleksponeringen i de nedre luftveje tager udgangspunkt i stegning af fire forskellige typer madlavningsolier. I forsøgsopstillingen er luftvejsmodellen placeret tæt på forureningskilden, og partikelkoncentrationen bliver målt i flere lokationer i et *clean room* med fortrængningsventilation.

Den eksperimentelle undersøgelse viste en faktor fem til forskel på den maksimalt opnåede massekoncentrationen imellem de forskellige olietyper. Olivenolie genererede den største massekoncentration, og solsikkeolie den mindste. Størrelsesdistributionen på de inhalerede partikler var baseret på talkoncentrationen og viste sig næsten at være ens for de forskellige olietyper, såvel som i løbet af forsøget. Forskellen på massekoncentrationen var altså ikke forårsaget af størrelsesfordelingen på partiklerne, men skyldes nærmere oliernes forskellige røgpunkter.

Påvirkningen af den termiske søjle på massekoncentrationen i åndingszonen blev undersøgt ved brug af en termisk mannequin. Denne viste, at der ingen forskelle var i massekoncentrationen grundet den overdøvende varmestrøm fra forureningskilden.

Den numeriske undersøgelse omhandler en analyse af partiklers bevægelse samt disses deponering i luftvejene, som ikke er muligt at opnå igennem det eksperimentelle arbejde. Deponeringen blev undersøgt ift. luftvejenes opdeling og ud fra ens-spredte partikler. En stationær CFD simulering blev udført grundet tidsbegrænsningen for projektet. Resultaterne viste, at størstedelen af partiklerne blev deponeret i bronkierne, og at partikler med en aerodynamisk diameter over $<2.0\,\mu$m forårsagede en højere deponeringsfaktor grundet større risiko for impaktion og sedimentation.

En sammenligning imellem den eksperimentelle og numeriske undersøgelse viste en stor forskel i den undersøgte deponeringsfaktor. Forskellen skyldes de forskellige antagelser og undersøgelsesmetoder anvendt i forløbet.

Samlet set fremmer denne undersøgelse viden om eksponeringen og indtaget af partikler ved implementeringen af ny state-of-the-art teknologi. Denne viden bidrager til fremtidige undersøgelser af kontrolmetoder, der skal minimere de sundhedsmæssige konsekvenser ved husholdningens forureningskilder.

Preface

This project is a Master Thesis in Indoor Environmental and Energy Engineering at Aalborg University. The project period is from the 1st of September 2017 to 8th of June 2018 and covers 50 ECTS points.

Acknowledgments

First we would like to thank our supervisors Li Liu, Chen Zhang and Peter V. Nielsen from Aalborg University for constructive guidance and supervision.

A special thanks to Professor Wang Yi, the staff and students at Xi'an University of Architecture and Technology in Xi'an, China for giving us the opportunity to visit their University. We truly appreciate the time and effort they put into our stay, and their suggestions, advisement and valuable help with everyday life in China.

We are also grateful to Oticon Fonden, S. C. Van Fonden, Knud Højgaards Fonden and Aalborg University for the scholarships that covered the expenses for our stay in China.

Finally a big thank you to the internationals students at Xi'an University of Architecture and Technology, students of Indoor Environmental and Energy Engineering at Aalborg University, family and friends for bringing love, joy and support during the hard times in this process.

Reading Guide

This report uses the Harvard method for literature references. Information about the literature is listed in a bibliography in the end of the main report, where the literature is in alphabetical order according to author. A literature reference located before a full stop refers to the previous sentence, while a literature reference located after a full stop refers to the previous paragraph.

An edited figure or table is labelled with *,Ed.* behind the source in the caption.

References to figures, tables and equations are numbered according to the chapter and section they appear in.

The appendices are located in two places; the end of the report and in a Digital Appendix. A list of the documents in the Digital Appendix can be found in Appendix L.

Kirstine Meyer Frandsen

Malthe Haahr Hvelplund

Contents

1 | Introduction

The World Health Organisation (WHO) has estimated that 4.3 million people die annually from illnesses caused by household air pollution [World Health Organization, 2012]. There is a clear correlation between increased exposure to indoor airborne particles and the deteriorating health of those who reside in them. Particles may consist of or act as a transporter of harmful substances. They can damage the lung tissue or be absorbed directly in the bloodstream, which potentially leads to cardiovascular disease, cancer and asthma. [Palmgren, 2009]

The high numbers of deaths largely occur in low- and middle income countries due to the use of solid fuels burned in highly polluting stoves for heating and cooking [Palmgren, 2009]. However household air pollution is also considered a negative contributor to people's well-being and health in high-income countries.

As people spend approximately 90% of their life indoors, personal exposure is highly impacted by indoor concentration levels [Stabile et al., 2014]. In an indoor environment the particle concentration is a function of emission sources, outdoor concentration, ventilation and filtration. While there is a clear correlation with outdoor concentration levels, studies show that indoor emission sources and human activity cause peak indoor concentration levels [Hussein et al., 2006][Matson, 2005]. This can be seen in Figure 1.1.

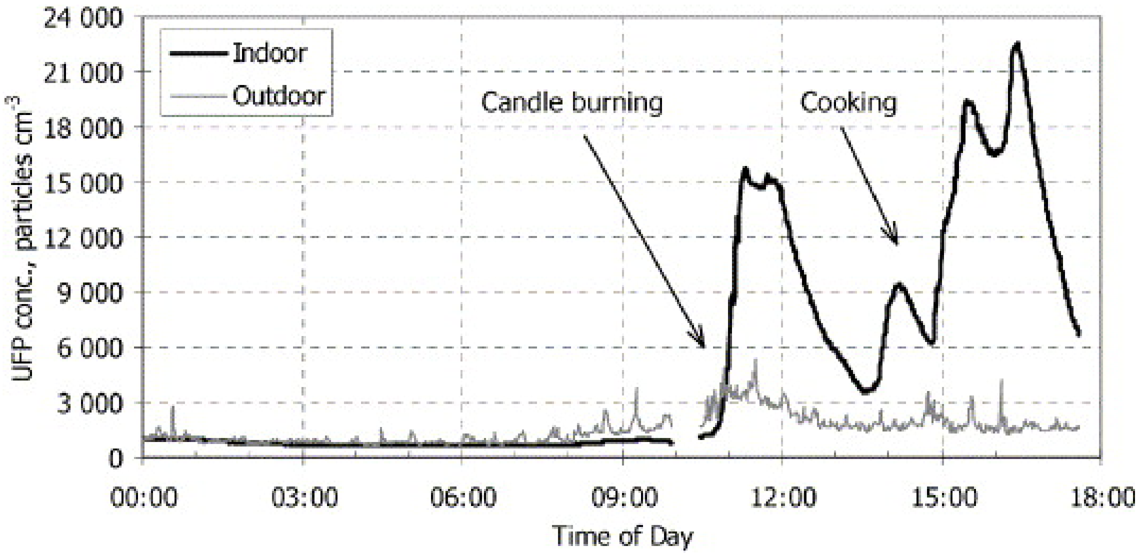

Figure 1.1. The effect of indoor emission sources on indoor particle concentration [Matson, 2005].

Investigations show that particles generated by cooking are considered to be the main contributor to indoor concentration levels, if smoking is disregarded [Lim et al., 2012][Kamens et al., 1991][He et al., 2004]. Cooking is conducted on an average daily basis and results in high peaks of indoor concentration levels compared to other indoor emission sources. However there is a big variation of the exposure from cooking, as the emission rates varies with different cooking styles and food. The highest emission rates occur from grilling and frying of food. [He et al., 2004]

Due to the large amount of time that a human occupant is exposed to cooking emitted particles, this study investigates the inhaled dose within the airways as well as the particles generated by the cooking process. Determining these will serve as a guideline to future studies investigating control methods to limit particle exposure and thereby reduce the health impact caused by indoor emission sources.

As cooking oil is commonly used in many types of cooking on a global scale, this study focuses on the heating of cooking oil to limit the scope of the project.

1.1 Aim of the Project

While extensive studies have investigated particle concentration in various indoor climates, investigations into the actual human body are more limited. Previous studies have been conducted on the airways but the majority have applied simplified geometries. This project serves to combine new technology involving the realistic airway geometry with pre-existing knowledge on particle transport in the indoor environment. The lower airways of a human male are modelled by a CT-scanning and therefore provide a more accurate representation of the anatomical structure of the human respiratory system.

Based on this the main focus of this study is to investigate the occupant's lower airway exposure to indoor airborne particles generated by cooking oil. The ability to control and reduce the occupant's exposure to indoor airborne particles requires an understanding of particle exposure metrics.

This project therefore entails a quantitative determination of particle exposure under controlled experimental conditions. The experimental investigation assesses the spatiotemporal and size-resolved dynamics of particle concentration generated by cooking, including the exposure in the indoor microenvironment and within the occupant's lower airways. It is supplemented by a numerical investigation to determine the size-resolved regional particle deposition within the airways.

2 | Literature review

Over the years there has been an increase in awareness of the effect of particle exposure on health [Nazaroff, 2008][Russo and Khalifa, 2010][Licina et al., 2017]. This has led to a large number of investigations on the subject that link exposure to particle air pollution to increases in morbidity [Deng et al., 2018]. Key studies on aerosols have been performed, through both empirical, numerical and experimental investigations. With this spread of topics, a review of the key studies relevant to this research topic is conducted.

2.1 Source-Receptor Relationship

Extensive studies have been carried out on particle movements in the indoor environment in terms of the occupant and thereby receptor in the room. These are largely dependent upon the indoor emission sources and thereby the source-receptor relationship. Often a metric known as the intake fraction is used an evaluating measure of this relationship. The intake fraction, iF, is defined as follows:

"*For the inhalation pathway, the intake fraction is defined as the attributable mass of a pollutant inhaled per unit mass released.*" [Nazaroff, 2008]

Otherwise expressed by:

$$iF = \frac{\sum\limits_{\text{People,time}} \text{Intake of pollutant by an individual (mass)}}{\text{Mass released into the environment (mass)}} \tag{2.1}$$

Intake fraction is considered a method to quantify emission exposure, which has been used in several studies conducted by Nazaroff. These include investigations into both the effect episodic indoor emissions [Nazaroff, 2008] and their localization [Licina et al., 2017]. Nazaroff [2008] investigates the understanding of intake fraction within building-related, occupant-related and pollutant behaviour related factors. In this investigation he recognizes the factors influencing health.

"*For each pollutant of concern, the partial health risk would be estimated as the product of four terms: usage factor, emission factor, intake fraction and toxicity.*" [Nazaroff, 2008]

The usage factor is dependent on occupant behaviour and the toxicity is dependent on the emission source. The focus of this study is limited to the emission factor and the intake fraction.

In Nazaroff [2008], mathematical models and analysis are used to investigate how episodic emissions affect particle exposure. His investigation applies the mass-balance approach, as described in Appendix A, in understanding intake fraction, in which mixing is a key parameter.

"*Incomplete mixing can be important in several circumstances, including these: (a) in buildings in which displacement or personalized ventilation systems are employed, (b) in large buildings with multiple air-handling units, and (c) in assessing exposures of building occupants associated with their own activities, owing to close proximity to pollutant emissions.*" [Nazaroff, 2008]

Incomplete mixing often occurs in reality, in particular rooms containing emission sources. The emission sources can thereby be said to be highly influential on the degree of mixing in the given room and therefore the exposure to the occupant [Nazaroff, 2008].

A study by Nazaroff highlights the uncertainty in applying the approximation of perfectly mixed indoor air when investigating the spatial distribution of indoor pollution. [Licina et al., 2017]

"*Further efforts are needed to deepen our understanding of inhalation intake fractions in relation to different types of localized particle-phase indoor pollutant emissions, their spatiotemporal variability, and the influential transport mechanisms*" [Licina et al., 2017]

The study consists of experiments carried out on both episodic emission sources released at various locations in a room and those emissions released by the envelope of a real human occupant. Each study was carried out with three different phases across the full monitoring period; the source-active period, the unmixed period and the well-mixed period. [Licina et al., 2017]

While the two studies do emphasize the effect of incomplete mixing, they are limited in the sole use of the intake fraction. The intake fraction does not consider the actual exposure but uses the environmental average by the mouth. The present study serves to examine the non-uniform particle concentration within the occupant's airways to directly evaluate real site exposure.

Licina et al. [2017] furthermore evidently shows the influence of the thermal plume from the human envelope on the intake fraction. The study on the emissions released in close vicinity to the manikin was conducted with the manikin both on and off. The results clearly show a large deference in intake fraction when the thermal plume is active. [Licina et al., 2017]

"*The findings of substantially higher contributions to the inhalation intakes for releases proximate to the body is likely a combined effect of the proximity of the source to the manikin and the influence of manikin's thermal plume transporting particles efficiently to the breathing zone.*" [Licina et al., 2017]

The study concludes:

"*The present study advances the understanding of how inhalation intake fraction varies in relation to spatially dependent episodic indoor emissions and influential transport mechanisms, but has not considered variation in other building- and occupancy-related parameters and pollutant attributes.*" [Licina et al., 2017]

One study has considered occupancy-related parameters in terms of short-range airborne transmission between two people [Liu et al., 2016]. The study consists of both experiments and CFD simulations. The distance between the sources has been considered, as well as different scenarios such as source breathing method, susceptible breathing droplet size, ventilation mode and rate, relative humidity. The study uses the susceptible exposure index as the metric instead of the intake fraction. A definition of the susceptible exposure can be found in Appendix B.

The study concludes that airborne exposure increases substantially when the subjects are placed within 1.5 m in proximity of each other. Furthermore relative humidity has a large impact on particle trajectories as the higher relative humidity increases the gravitational force of the particles. [Liu et al., 2016]

Based on studies on the source-receptor relationship, it is possible to define the parameters that are highly influential on particle exposure in occupants, such as breathing rate, location of the source, thermal plume of the occupant, etc. These are considered in the parameters set up for this study. However, as previously mentioned the studies are limited in their general expression of exposure by the occupants' nasal and oral openings. Real site exposure is the focus of this study.

2.2 Indoor Emission Sources

The sources that affect the health of humans and that are particularly susceptible in everyday life have been a matter of interest for a long time. These include those of high usage factor and emission factor. [Nazaroff, 2008]

"*Significant sources that can generate episodic emissions include smoking, cleaning and cooking.*" [Nazaroff, 2008]

The emission factor is a quantity for the mass a pollutant emits into the indoor air, and the usage factor is a quantity for how often the emission source is in use. Both factors have a big influence on health risk. The episodic emissions can be measured from an emission rate, where the emission changes over time. [Nazaroff, 2008]

As mentioned in Chapter 1, cooking has been determined to be the biggest contributor to particle concentration in indoor air excluding smoking.

Studies have concluded that there is a big variation in emission rates related to different cooking methods and different types of food. High particle concentration after cooking is dominated by the ultra-fine particles. [Wei See and Balasubramanian, 2006] The main problem with ultra-fine particles is that they remain airborne long after the cooking activity had ceased [Stabile et al., 2014].

Buonanno et al. [2009] investigates the influence of temperature on the emission factor. They conclude that particle emission rate varies by temperature and time. Furthermore they find that the cooking of fatty foods generates a bigger emission. [Buonanno et al., 2009]

The variation makes it difficult to make an assessment of particle exposure from cooking. The particle concentration is also highly dependent on the air distribution under different ventilation conditions. [Gao et al., 2013b]

The test results from heated sunflower oil from Gao et al. [2013b] is visualized in Figure 2.1.

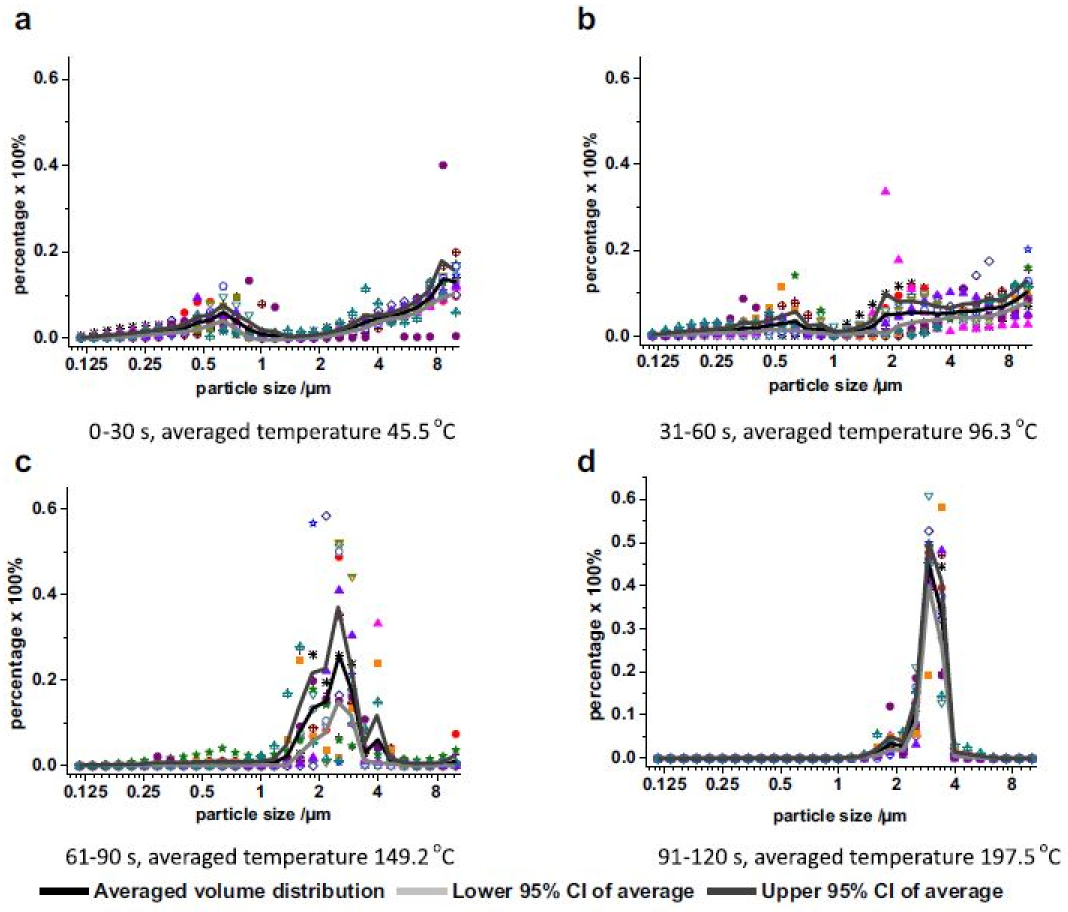

Figure 2.1. Measured volume-based size distribution of fume particles from heated sunflower oil at different time intervals [Gao et al., 2013b].

Figure 2.1 shows a clear variation in the size distribution dependent on time and temperature.

Researchers are trying to understand which chemical components are most unhealthy for the human body [Stabile et al., 2012]. However this is still a topic which requires additional of research. In general the health impact on human occupants can be assessed from the dose, the intake fraction and the toxicity [Marshall and Nazaroff, 2009].

2.3 Particle Deposition in the Lower Airways

Particle deposition in the human airways has been a matter of interest in the medical world, making it useful for deposition of pharmaceutical drugs, understanding infection, etc. A key study from 1986 used experimental data to determine the deposition of mono-dispersed particles in the human respiratory tract system when inhaled through the mouth or nose respectively. The experiments are carried out using a tracer on three human test subjects. This includes both the total and regional deposition in a wide range of particle sizes (0.005-15 μm). Through the experiment empirical equations were derived. The study is theoretical in its approach, as it does not account for the particle trajectory from the source to the receptor, as well as only investigating mono-dispersed particles. However, it does consider different breathing rates and periods of breathing cycles. [Heyder et al., 1986]

The study concludes on the deposition of particles based on the different regions of the respiratory tract and particle size. The can be seen in the Table 2.1.

Table 2.1. Particle deposition patterns dependent on breathing type [Heyder et al., 1986][Ed.].

Oral breathing	**Nasal breathing**
- Particles: $<2\,\mu$m In: Alveolar region By: Gravitational sedimentation	- Particles: 0.3-9.0 μm In: Nasal cavity and pharynx By: Inertial impaction In: Larynx, bronchi and bronchioli By: Gravitational sedimentation
- Particles: 2-15 μm In: Mouth and pharynx By; Inertial impaction In: Larynx, bronchi and bronchioli By: Gravitational sedimentation	- Particles: $>10\,\mu$m In: Nasal cavity and pharynx By; inertial impaction
- Particles: $>15\,\mu$m In: Mouth and pharynx during inspiration By: Inertial impaction	

Figure 2.2 shows the deposition fraction by aerodynamic diameter based on the both the total and regional parts of the respiratory tract. The study was conducted for both nasal and oral breathing.

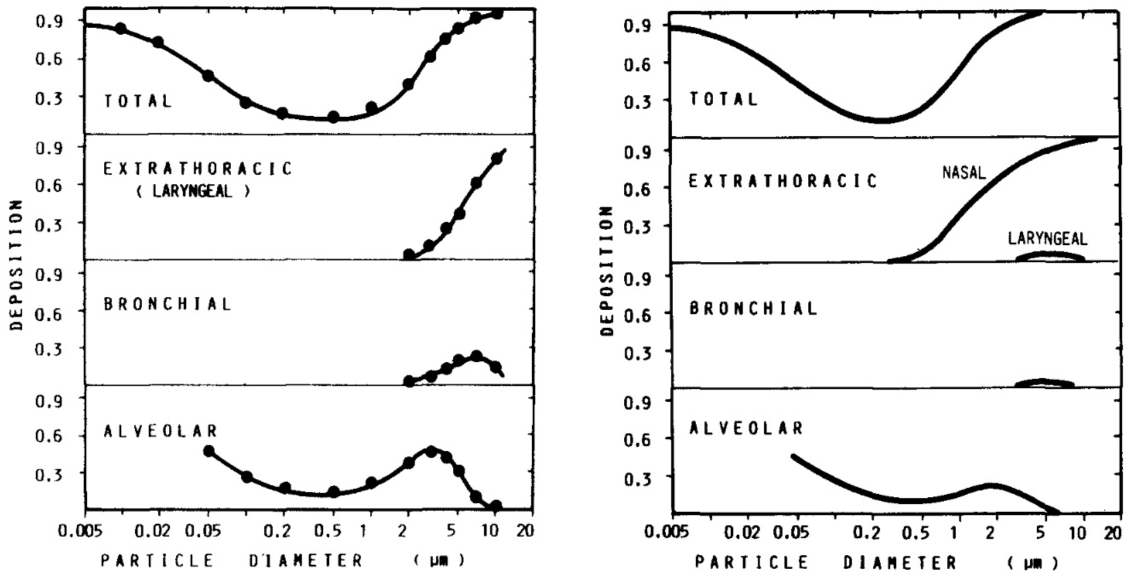

Figure 2.2. Deposition fractions of particles in the anatomical regions of the respiratory tract with a breathing cycle of 4 s. The left graph is for oral breathing with a flow rate of 750 cm^3/s and the right graph for nasal breathing with a flow rate of 250 cm^3/s [Heyder et al., 1986].

It can be seen from the study that coarse particles and to some extent ultrafine particles are more likely to be deposited in the respiratory tract. The accumulation particles (0.1 - 2.0 μm) are less likely to be deposited. The study also concludes that there is a slightly higher level of deposition with nasal breathing compared to oral breathing, due to nasal deposition. [Heyder et al., 1986]

Another empirical study has been carried out as a development of Heyder et al. [1986]. This study has developed a general equation for the deposition of particles in the total respiratory tract. [Martin and Finlay, 2007]

The studies carried out on deposition of particles in the airways range from empirical to experimental to computational. While Heyder et al. [1986] is notoriously referred to in particle deposition studies, it is based on mono-dispersed experimental data with a theoretical approach. Through the present study, particle exposure is considered from real emission sources, namely cooking oil, that are used in everyday life. Furthermore it investigates the deposition by both experimental and numerical methods. It also allows for investigations into the regional deposition as well as extensive studies, where the experimental data may be insufficient in terms of the human airways.

2.4 Numerical Investigations of the Lower Airways

A large number of studies have examined the respiratory tract deposition of aerosol particles using modern technology with CT or MRI scanning of the airway system [Tu et al., 2013]. The majority of these serve for medical purposes to examine the trajectory path of inhaled medicine such as in cases with asthma and therefore relates to a different situation than in the given natural room. However, the extensive knowledge on the subject serves to strengthen the basis of this study.

One study investigates inhalation injury from fire through a realistic human upper airway scanning by MRI scanning in CFD simulations. The study investigates flow rate, inhalation temperature and particle diameter. However, the study does not consider particle trajectories towards the receptor and furthermore does not have experimental data for validation or comparison. [Xu et al., 2017]

Many studies [Deng et al., 2018][Kolanjiyil and Kleinstreuer, 2017][Zhang et al., 2005] have also been conducted using the simplified universal model of the inner airways, in which the airways are modelled as cylinders and symmetrically. Such a symmetric model can be seen in Figure 2.3 used in Kolanjiyil and Kleinstreuer [2017]. Opinions on this model differ and are often dependent on its use.

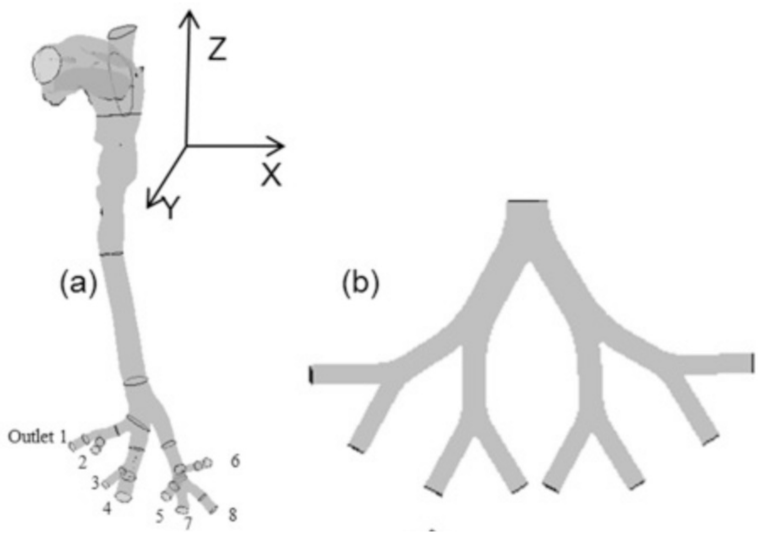

Figure 2.3. Symmetric airway used for a computational analysis [Kolanjiyil and Kleinstreuer, 2017].

The advantage of the present study lies in the use of the model of an actual human respiratory system as opposed to the universal reflected model. The study considers emission sources and combines the source-receptor relationship with the actual conditions within the occupant. The use of an anatomically correct model allows for more accurate results when compared to reality, more specifically as they include irregularities and bent deflections [Rahimi-Gorji et al., 2016]. It should be noted that the study of one random human respiratory system does not make it a representative standard for all human respiratory systems, as these may vary in size and shape, and thereby particle exposure may also vary. However, in the future studies such as this one may be more quick and common to conduct. [Tu et al., 2013]

3 Characteristics of Particle Metrics

Particles consist of small collections of solids and droplets. A lot of particles are created through natural sources such as sea salts and soil dust, but particles are also formed from all types of combustion and other types of human activities related to the release of volatile organic compounds (VOC). [Palmgren, 2009]

The evolution of particle exposure is shown in Figure 3.1.

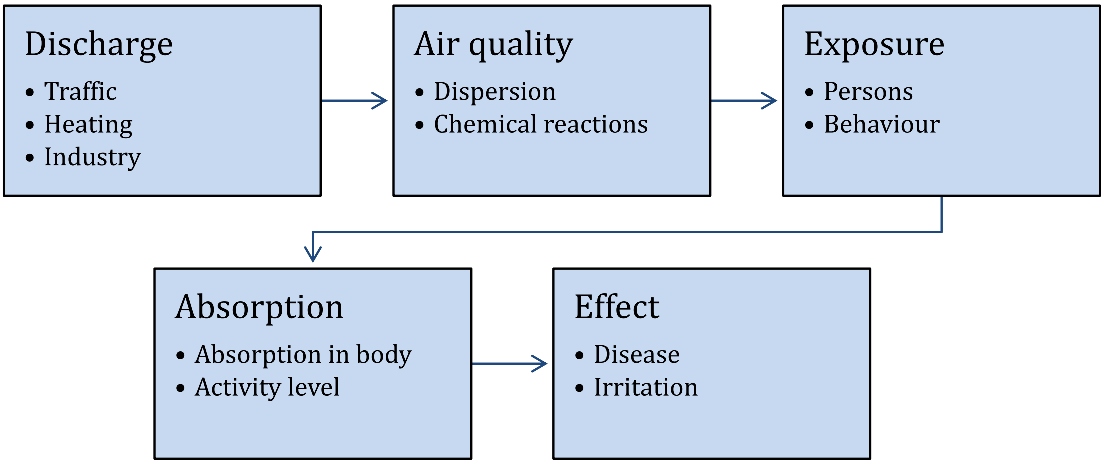

Figure 3.1. The evolution of particle exposure [Palmgren, 2009][Ed.].

3.1 Particle Magnitudes

The magnitude of a particle is categorized by the "aerodynamic diameter". The aerodynamic diameter is the diameter of an idealised spherical particle with a density of 1.0 g/cm^3, where the diameter is determined by the terminal settling velocity. The terminal settling velocity is the maximum velocity reached of a particle falling through a fluid when subjected to drag and gravity [Collins English Dictionary, 2018]. The terminal settling velocity is correlated with the size of the particle, and the trajectory of larger particles is mainly determined by the gravity. The size, weight and shape of the particles may differ, but they are categorically expressed in terms of their aerodynamic behaviour. The aerodynamic diameter often differs from the actual diameter of the particle. [Institut for Miljøvidenskab, 2016]

Particles are divided into three categories depending on their sizes: [Nazaroff, 2004]

- Ultrafine: $\leq 0.1\,\mu$m

- Accumulation: 0.1 - 2.0 μm
- Coarse: > 2.0 μm

The particle properties, along with air flow properties, greatly influence the forces acting on the particles and therefore their trajectories. The large range in particle sizes causes a significant difference in particle properties; evidently a particle with an aerodynamic diameter of 0.1 μm is 8000 times smaller than a particle with an aerodynamic diameter of 2.0 μm.

A diagram illustrating the size distribution of different particles in micrometres is shown in Figure 3.2.

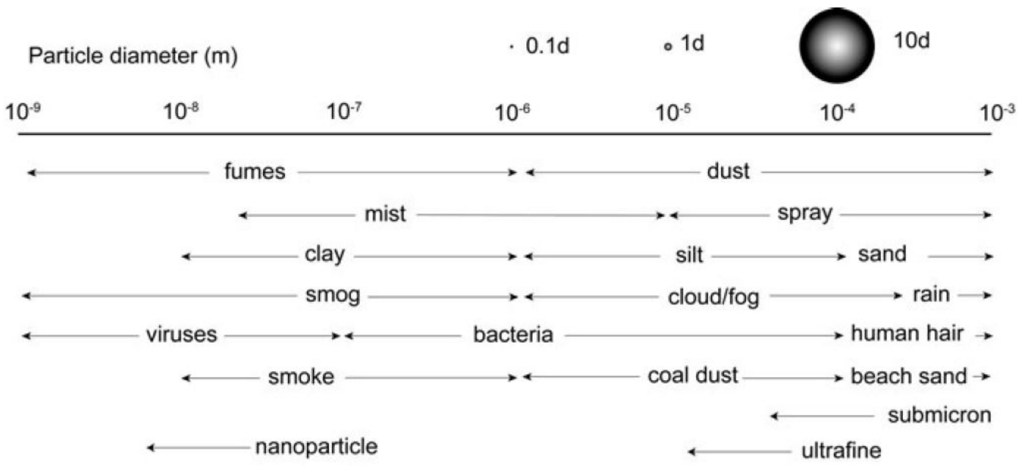

Figure 3.2. The size distribution of different types of particles [Tu et al., 2013].

Particles smaller than 0.5 μm are mainly driven by forces other than gravitational force. These forces are described in Chapter 10. [Palmgren, 2009]

Fine particles are the most dangerous type of particles for the human respiratory system. Coarse particles larger than 4 μm - 5 μm are captured by the body's defence mechanisms in the nose and throat while the smaller particles penetrate further into the airways. Some of these particles will pass through the airways and be deposited on the alveoli.

The impact of particles with the same magnitude are weighted equally in the discussion of health, due to a lack of knowledge on the impact of different particle matter in terms of the toxicities. [Palmgren, 2009]

3.2 Particle Exposure Metrics

The measure of quantity of particles can be expressed as the mass of particles or the numbers of particles. The allowable limits are often given as a concentration of mass [μg/cm^3] for larger particles and number of particles [numbers of particles/cm^3] for ultrafine particles due to their low mass. [Palmgren, 2009]

Particles mass concentration is expressed in terms of PM, used to define the limits of particles contamination. PM is the abbreviation of particulate matter. $PM_{2.5}$ and PM_{10}

describe the particulate matter of all solid and liquid particles up to 2.5 μg/cm^3 and 10 μg/cm^3 respectively. [Park and Allaby, 2016]

There is no legislative standard regarding the limit of $PM_{2.5}$ and PM_{10} for indoor air quality. However, WHO has published guidelines regarding particle matter for the outdoor environment, which are applicable to the indoor environment. The guidelines are based on statistics for the health effect on urban populations. The guidelines for the permissible limits for $PM_{2.5}$ and PM_{10} can be found in Table 3.1. [World Health Organization, 2005] The limit of the concentration of $PM_{2.5}$ and PM_{10} for outdoor environments are lower for WHO guidelines than the regulations from the European emission standards. [Palmgren, 2009]

Table 3.1. Guideline values for $PM_{2.5}$ and PM_{10} concentration [World Health Organization, 2005].

$PM_{2.5}$	Annual mean	10 μg/cm^3
	24-hour mean	25 μg/cm^3
PM_{10}	Annual mean	20 μg/cm^3
	24-hour mean	50 μg/cm^3

3.3 Mechanisms of Particle Deposition

Particles are deposited in the atmosphere in different ways. The deposition occurs by mainly by following the principal mechanisms of impaction, diffusion and sedimentation. [Palmgren, 2009]

Deposition from impaction is due to a high inertia, where the particles will continue its direction after a sudden change in the flow field. This mechanism is highly dependent on the size of the particles, since the inertia is larger for larger particles. The inertial impact on the particle trajectory is illustrated in Figure 3.3. [Sutherland, 2002]

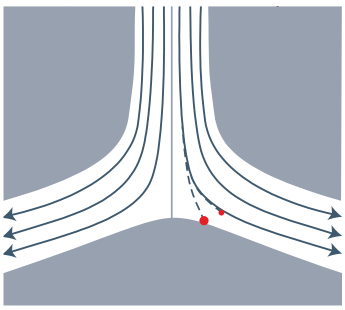

Figure 3.3. Illustration of particle deposition principle with impaction [Palmgren, 2009].

Deposition from diffusion is due to a random movement of the particles. The random movement is a reaction due to the Brownian force, which is described in Chapter 10. For particles less than 0.5 μm, diffusion is the primary mechanism for deposition. [Sutherland, 2002]

Deposition from sedimentation is due to the terminal settling velocity, where the particle will move in the direction of the gravity force. [Sutherland, 2002]

Other reasons for deposition can be due to a thermophoretic force, electrostatic force or turbulent transport. [Guha, 2008]

3.3.1 Particle Deposition in the Respiratory System

The deposition of inhaled particles varies for the individual and depends on many factors such as: breathing type, breathing rate, lung volume, health of the individual and changed flow field due to change of different properties in the body. [Sutherland, 2002] A detailed description of the anatomy of the human respiratory system can be found in Appendix C.

The deposition rate increases in the lower part of the airways as the airways become increasingly narrow. Particle size may also increase as they pass through humid and warm passages, where the particle potentially absorbs moisture. [Sutherland, 2002]

This phenomenon is referred to as hygroscopy. It has been proved that models of particle deposition within the human respiratory tract are improved when aerosol hygroscopy is accounted for [Youn et al., 2016]. It should therefore be included in studies revolving particle deposition in the respiratory airways.

In the lungs the particles may additionally be deposited by interception, where particles with a long shape may collide into the airway wall. This mechanic mostly occurs for fibres as they have small aerodynamic diameters compared to their form. [Sutherland, 2002]

4 CT-Imaging Based Human Airway Model

This study makes use of a CT-scanning performed on the human airways of a male, ensuring a more realistic model of the airways than used in previous studies. The model is to be used in both the experimental and numerical investigation, thereby also allowing for a more realistic assessment of particle exposure.

The scanning of the airways was conducted prior to the beginning of this project and was converted into an STL file. A modified version was later developed to enable 3D printing based on the original scanned model. The STL files of the original airway model and the modified 3D printed model are illustrated in Figures 4.1 and 4.2.

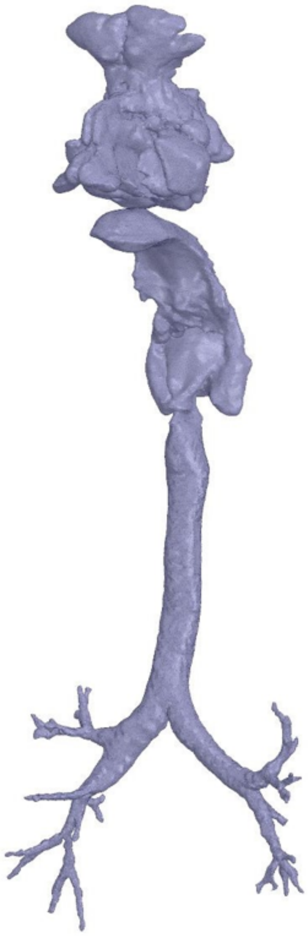

Figure 4.1. STL file of the original airway model.

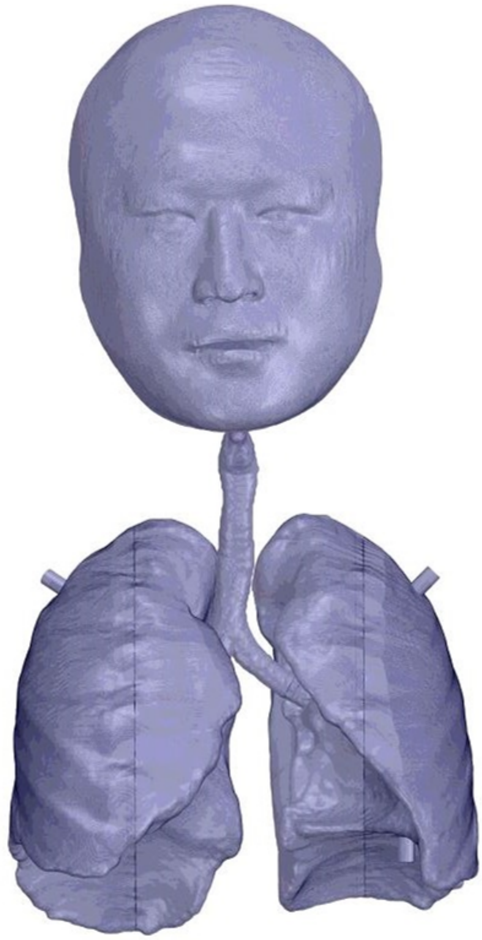

Figure 4.2. Modified STL file for the modified 3D printed model.

To highlight the difference between the original airway model and the modified 3D printed airway model, both models are visualized in Figure 4.3. The modified 3D printed model consists of the same tracheobronchial tree as the original scanned airway model. The similarities in the tracheobronchial tree are visualized in Figure 4.4.

Figure 4.3. Visualization of the original airway model (yellow) and the modified 3D printed model (transparent).
.

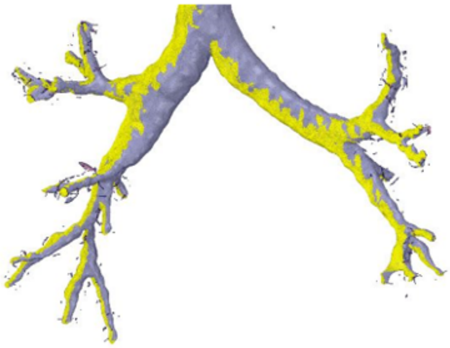

Figure 4.4. The tracheobronchial tree of the original airway model (yellow) and the modified 3D printed model (blue).

The modified 3D printed model consists of 27 outlets from the bronchioles to the lung volume; it has bronchioles down to seventh generation. This indicates that the airway model only embodies the upper part of the lower airways, as the respiratory zones begins in the 17th generation [Tu et al., 2013]. A table of the morphometry of the tracheobronchial tree cast is shown in Appendix D.

An experimental investigation is conducted using the 3D printed airway model to determine the quantitative particle exposure. This is described in Part I. A numerical investigation is then carried out using the same modified 3D printed model. This is an extension of the experimental investigation to further asses the particle trajectories and the locations of particle deposition. This investigation is described in Part II.

Part I

Experimental Investigation of Lower Airway Exposure by Cooking Oil

An experimental investigation is carried out on a realistic 3D printed model of the airways to investigate exposure in the lower airways to an emission source.

The emission source for this study has been determined to be cooking oil. In the measurements a variety of cooking oils are used to compare its effect on lower airway exposure.

In general experiments have the benefit of measuring actual situations under controlled circumstances. Through these controlled circumstances it is possible to determine the influence of one or more parameters, such as the ventilation flow rate or room temperature. Experiments are also able to be repeated and replicated, enabling results to be verified and the systematic uncertainty to be calculated.

However, they are limited by what variables are measurable by sensor availability and precision. This is where numerical investigations may act as an extension to the investigation.

5 Basis of the Experimental Investigation

Many studies on indoor emission sources have been performed under real operating conditions. While these show the actual particle concentration, they cannot determine the exact origin of the particle concentrations.

For this study, state-of-the-art experiments will be carried out due to the following parameters:

- Use of a 3D printed model of the lower airways
- Controlled conditions with no background concentration
- Use of real emission sources

The combination of the above parameters ensures innovative measurements using new technology.

The purpose of the measurements is to determine quantitative particle exposure to the human airways under controlled experimental conditions. The quantification is assessed through the spatiotemporal and size-resolved dynamics of the particle concentration. The investigation is determined by and limited to the conditions of the experimental set-up.

5.1 3D Printed Airway Model

The CT-imaging based 3D printed model of the airways provides a new method for testing the geometry of actual human airways through a realistic representation of the human anatomy. Previous studies are based on simplified geometries or are limited to particle exposure in the upper airways or the breathing zones of the occupant as mentioned in Chapter 2.

The 3D printed model has been described in Chapter 4. The model is divided into five main parts that can be assembled to form the airways. The assembled model, consisting of a face, the airways and lungs, can be seen in Figure 5.1. The STL files for the five individual parts can be seen in Appendix J.1.

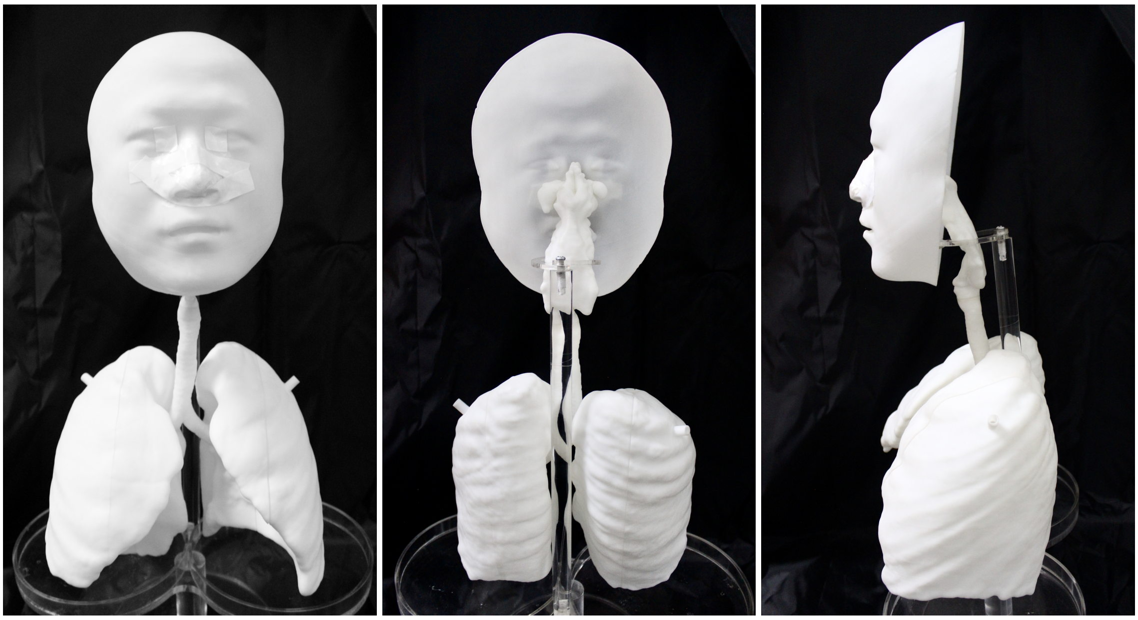

Figure 5.1. The assembled 3D printed model used for the measurements seen from the front, back and side respectively.

The surface of the 3D printed model has a roughness of approximately 0.1 mm. This should be taken into account when evaluating particle deposition.

As the 3D model is a full-scale anatomical model it enables both oral and nasal breathing. The pharynx, including the nasopharynx and the oropharynx that connect the oral cavity and the nasal cavity to the airways, can be seen in Figure 5.2.

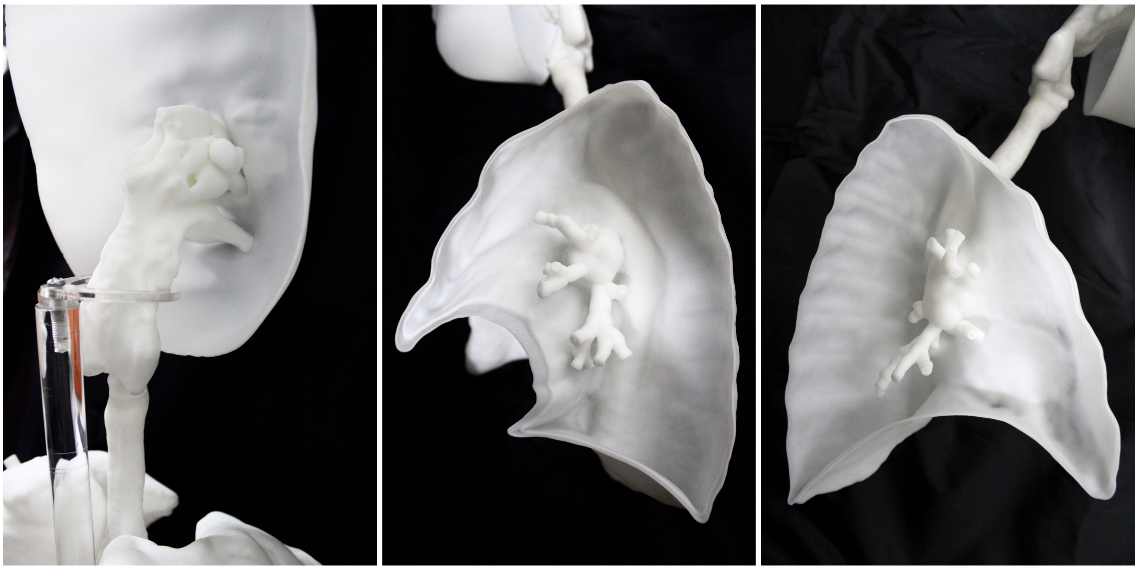

Figure 5.2. Details of the 3D printed model for the pharynx and the bronchioles for the left and right lung respectively.

Detailed images of the five individually printed parts of the 3D model can be found in Appendix F.

While there are limitations to the physiological properties of the model, the geometrical accuracy of the model still provides a much more representative model than previous studies when investigating particle deposition. Artificial breathing is implemented and particle concentration is sampled through plugs attached to the top and the bottom of each lung respectively.

5.2 Indoor Emission Sources

The indoor emission sources serve as the main parameter variation for this investigation. These are focused on cooking due to its high contribution to household particle concentration, as established in Chapter 1.

The size distribution and amount of particles generated by cooking may vary a lot based on different cooking factors such as food and oil type, temperatures and cooking style [Gao et al., 2013a]. This study mainly focuses on the generation of particles from heating of different types of cooking oil.

The following cooking oil types are used:

- Extra virgin olive oil from Olivoilà
- Refined corn oil from from Arawana Brand
- Refined peanut oil from Arawana Brand
- Refined sunflower oil from Arawana Brand

Throughout the study, the different oil types will simply be referred to as olive oil, corn oil, peanut oil and sunflower oil. The different oil types can be seen in Figure 5.3.

Figure 5.3. The oil types used for the measurements: corn oil, extra-virgin olive oil, peanut oil and sunflower oil respectively.

The chosen oil types are all commonly used for cooking on a global scale [Rosillo-Calle et al., 2009]. The oil types will be investigated to determine any differences in the particle concentration both by mass and number, the aerodynamic size distribution and the time-variant behaviour of the released particles.

The use of a real emission source means the particles monitored will be poly-dispersed, as is realistic in households. While mono-dispersed particles are easier to control, the use of the clean chamber enables easy monitoring of the released particles from the emission sources.

5.3 Laboratory Facilities

Ensuring little-to-no background concentration is an important part of the measurements. It allows for the particles released by the emission sources to be monitored more specifically with awareness of their origin. This requires the measurements be carried out where background concentration can be controlled, such as in a clean chamber. It is in these facilities, the full-scale laboratory measurements are conducted as they provide the opportunity of conducting experiments with no initial background concentration.

For these reasons the experiment is conducted at Xi'an University of Architecture and Technology (XAUAT) in Xi'an, China. XAUAT has a laboratory designated to particle studies, namely the Particle Transport Lab.

The Particle Transport Lab adheres to the requirements of IEA Annex 20. The International Energy Agency (IEA) specifies Annex 20 in Energy Conservation in Buildings and Community Systems as the standardized benchmark test case for room air distribution models [Nielsen, 1990]. The chamber is able to regulate fresh air supply, indoor temperature and humidity. The properties of the chamber can be seen in Table 5.1.

Table 5.1. Properties of the Particle Transport Lab located at XAUAT in Xi'an, China.

Properties	
Dimensions	5.0 m (L) × 3.5 m (W) × 2.5 m (H)
Ventilation types	Mixing ventilation
	Displacement ventilation
Filters	3-stage HEPA filters
Ventilation rate	$\leq 40\,\mathrm{h}^{-1}$
Inlet air temperature	15 - 35 °C ±0.1 °C
Indoor relative humidity	30% - 90% ±5%

The dimensions of the chamber vary slightly from the Annex 20 specifications. This is due to the physical limitations of the room in which the chamber is placed.

The air inlet and exhaust can be placed at multiple locations in the chamber on both the ceiling and side walls, enabling both mixing and displacement ventilation. The filters are able to filter out 99% of the particles above 1 μm from the ambient air.

The laboratory facilities enables the recognition of which parameters affect the indoor concentration, in relation to the mass balance approach described in Appendix A. The clean room acts as the spatial domain. The mechanical ventilation has a high single-pass removal efficiency, ensuring that a minimum of the outdoor concentration enters the control volume, and infiltration is minimal. This ensures the low background concentrations and therefore the ability to assess the exposure from within the control volume, which is the sole purpose of this study.

6 | Experimental Description

An experimental protocol is developed to ensure an understanding of how the measurements will be carried out. This involves the set-up of the measurements, their chosen variables and conditions, the desired results, the measurement procedure and the measurement accuracy based on the protocol.

6.1 Instruments

The measurements are both allowed and limited by the instruments available to the measurements. It has already been established in Chapter 5 that the 3D printed model, the chosen emission sources and the chamber form the basis of carrying out the measurements. However, the following pieces of equipment enable the full scale of the measurements to be carried out.

- Aerodynamic Particle Sizer 3321 (APS3321) from TSI
- Two SDS011 particle sensors from Nova Fitness
- Two PMS5003 particle sensors from Plantower
- Artificial pump and tubing
- Electric stove and pan
- Temperature and relative humidity (RH) sensors

The 3D printed airway model is connected to the artificial pump, which generates an airflow to simulate the breathing pattern. The electric stove and pan are used to heat the cooking oil, which generates the indoor airborne particles. The particle sensors are used to measure particle concentration for the duration of the measurement, including the initial background concentration check. The temperature and RH sensors are used to monitor the indoor climatic conditions within the chamber.

Particle Sensors

There are five particle sensors used for the measurements. The sensor types and their attributes can be seen in Table 6.1.

Table 6.1. Sensors used for the measurements.

Sensor	No. of Sensors	Features
TSI APS3321	1	Measures range from 0.5 - 20 μm Many possibilities for particle concentration type Sample time up to the user
SDS011	2	Measures $PM_{2.5}$ and PM_{10} Every 60 seconds
PMS5003	2	Measures $PM_{2.5}$ and PM_{10} Measurement in intervals from 2 s to 60 min

The particle sensors all allow for time-dependent measurements of mass concentration ($PM_{2.5}$ and PM_{10}). Furthermore the detailed size-resolved number concentration measured by the APS3321 will be analysed.

The detailed descriptions of how the particle sensors function can be seen in Appendix E.

6.2 Experimental Set-up

The set-up is based on the instruments that are available for the experiment as described above, as well as a human occupant. The human occupant is included to control the experiment from within the chamber, to create a thermal plume and for fire safety reasons as described in Appendix G.

Figures 6.1 - 6.3 show the measurement set-up within the clean room.

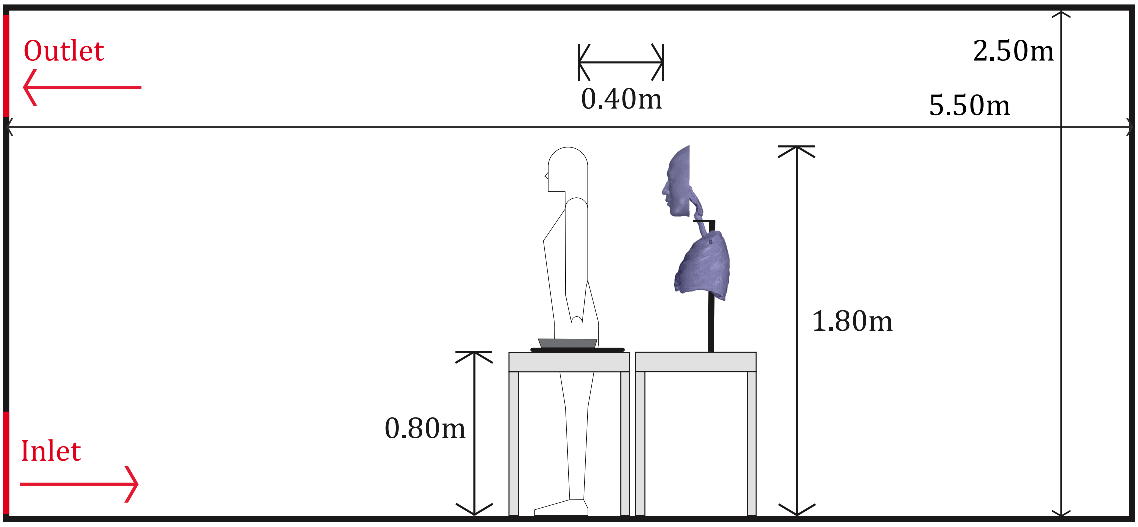

Figure 6.1. The principle of the measurement set-up seen from the side.

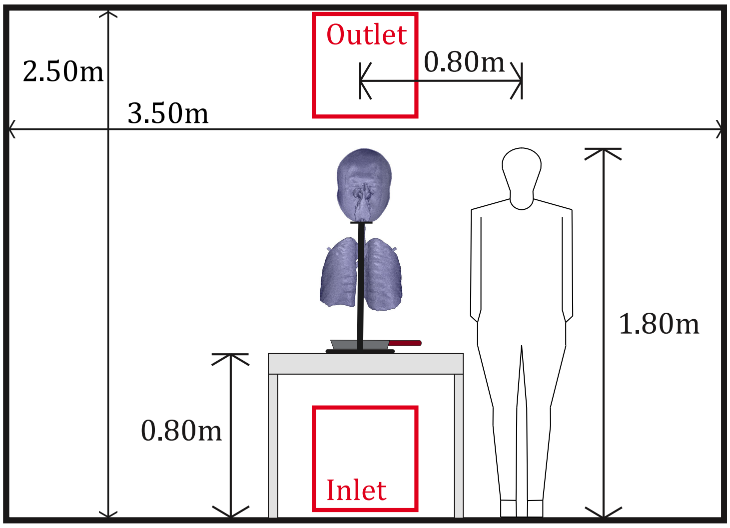

Figure 6.2. The principle of the measurement set-up seen from the side.

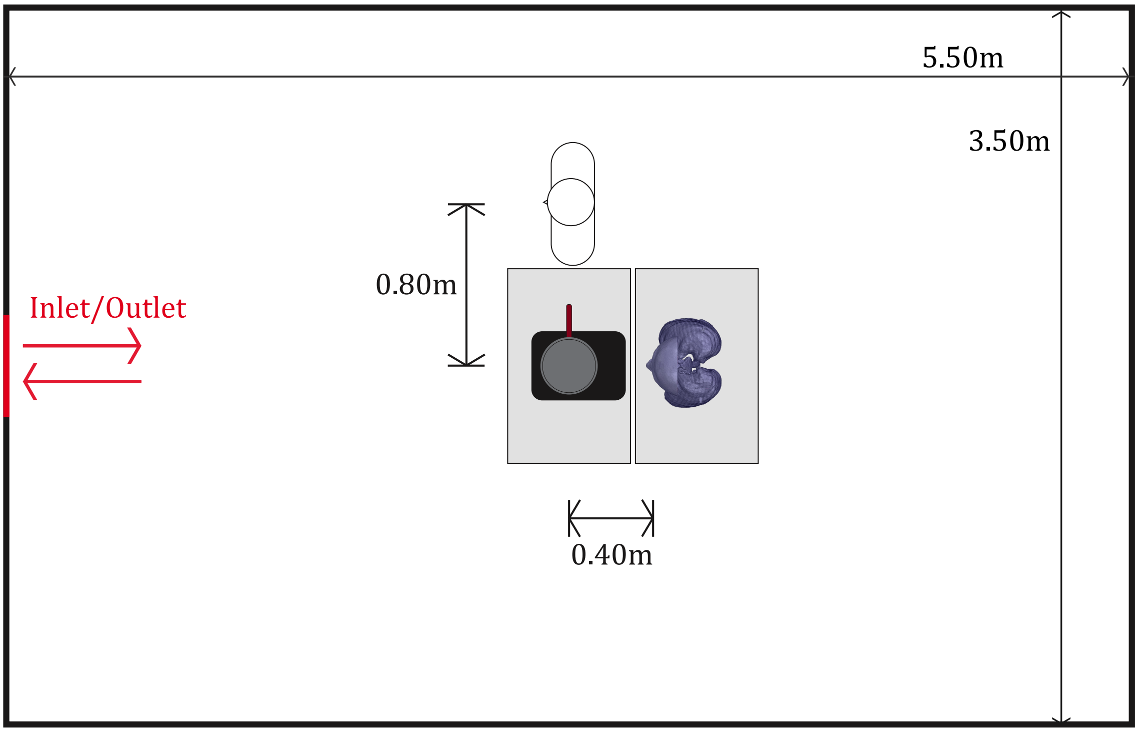

Figure 6.3. The principle of the measurement set-up seen from above.

Images of the measurement set-up can be seen in Figure 6.4. Additional images showing the measurement set-up can be seen in Appendix F.

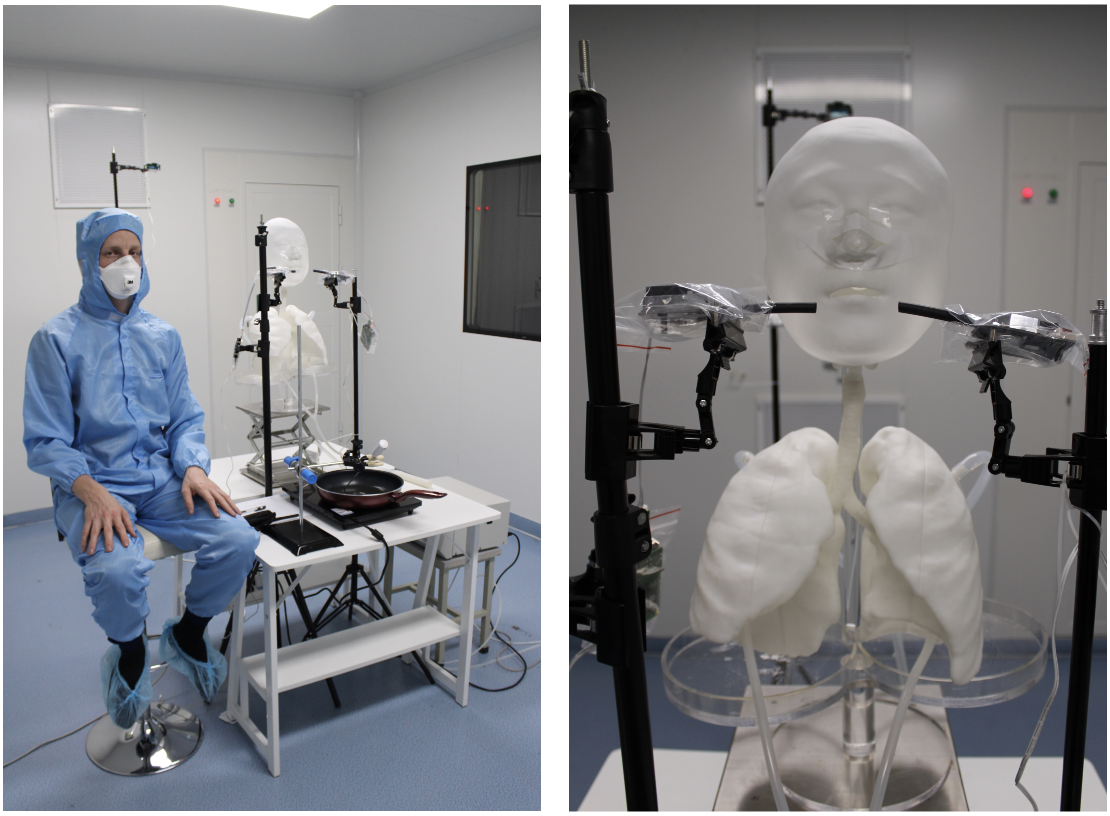

Figure 6.4. The measurement set-up for the investigation into the quantitative particle exposure of different cooking oil types.

A prediction of the flow pattern in the clean room is illustrated in Figure 6.5.

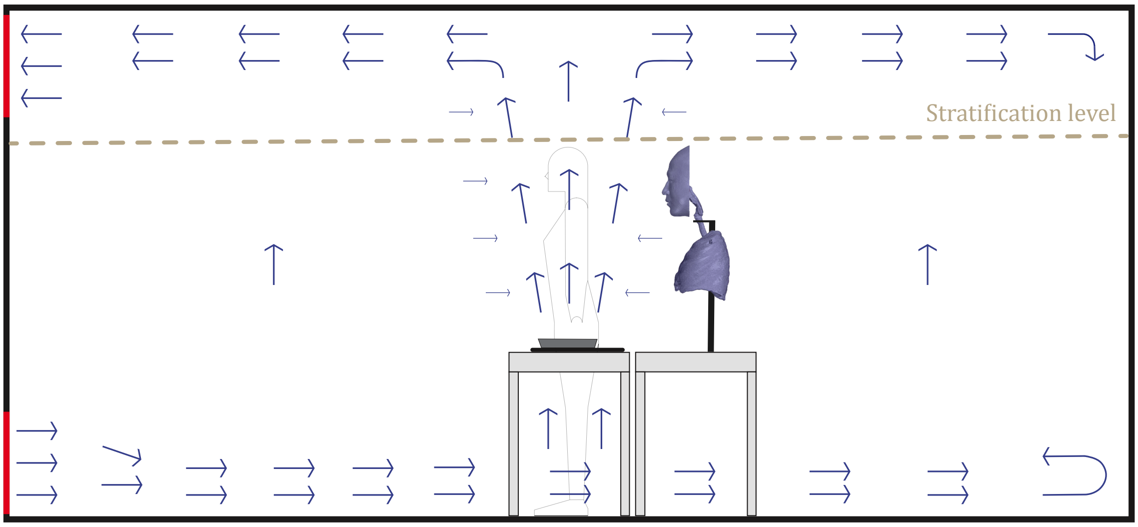

Figure 6.5. The predicted flow pattern in the clean room based on the displacement ventilation principle.

The room ventilation can be characterized as displacement ventilation, as the room ventilation is dominated by buoyancy forces. The initial average velocity at the inlet is 0.058 m/s and the Archimedes number is calculated to be 1.6×10^4. The calculation of the Archimedes number can be found in the Digital Appendix. A large Archimedes number implies that the buoyancy forces are dominant in the flow. Hence main driving forces behind the room ventilation derive from the electric stove and the occupant of the room as they are the main heat sources present. As the room ventilation is characterized as displacement ventilation it is expected that the distribution of the particle concentration is stratified, as can be seen in Figure 6.5. [Nielsen et al., 2007]

Locations of Particle Sensors

The particle concentration is measured at four different locations using the particle sensors, as can be seen in Table 6.2

Table 6.2. Locations and purpose of particle sensors in the clean room.

Location No.	Location	Particle Sensor	Sample Time	Purpose
1	In the 3D printed model at the plugs in the bottom of each lung	APS3321	4 s	Determining particle exposure in the airways
2/3	In the breathing zone of the 3D model (without influencing the breathing air flow)	Two SDS011	60 s	Comparing the mass concentration in the breathing zone Mapping the potential gradient of the particle concentration in the breathing zone
4	By the exhaust	PMS5003	2 s	Comparing the generation of particles between the different emission sources
5	In the room	PMS5003	10 s	Evaluating the gradient of particle concentration in the room

All four of the measurement locations are time-dependent, based on the sample times seen in Table 6.2. The measurement locations can be seen in Figures 6.6 - 6.8.

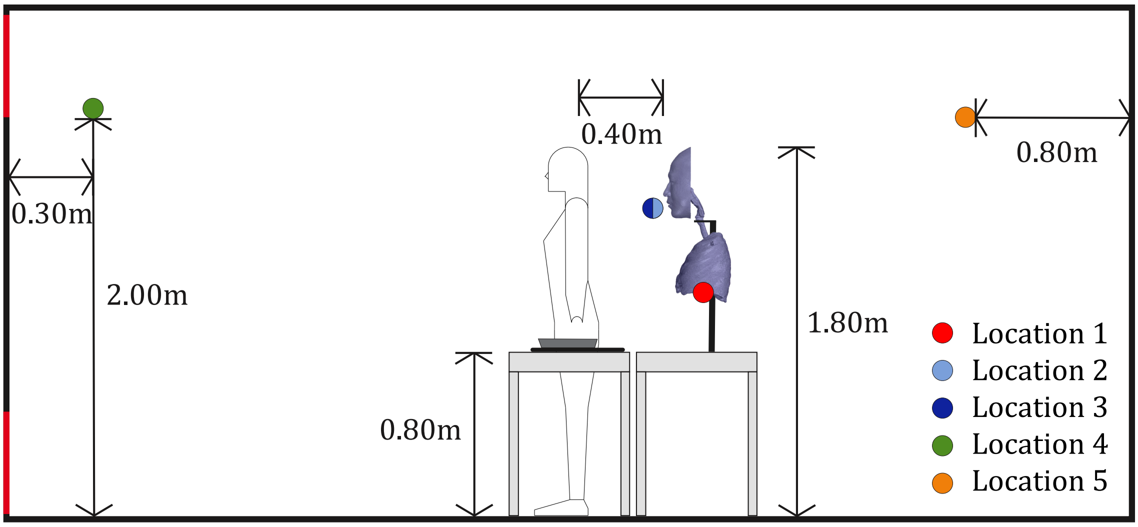

Figure 6.6. The sensor locations in the measurement set-up seen from the side.

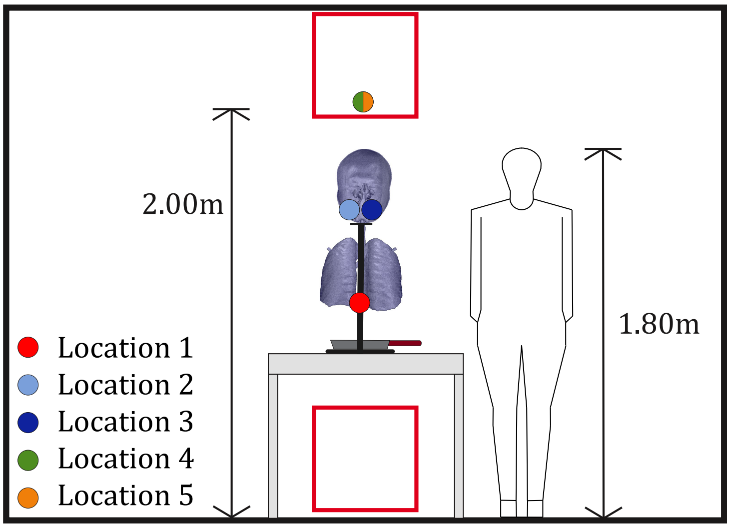

Figure 6.7. The sensor locations in the measurement set-up seen from the side.

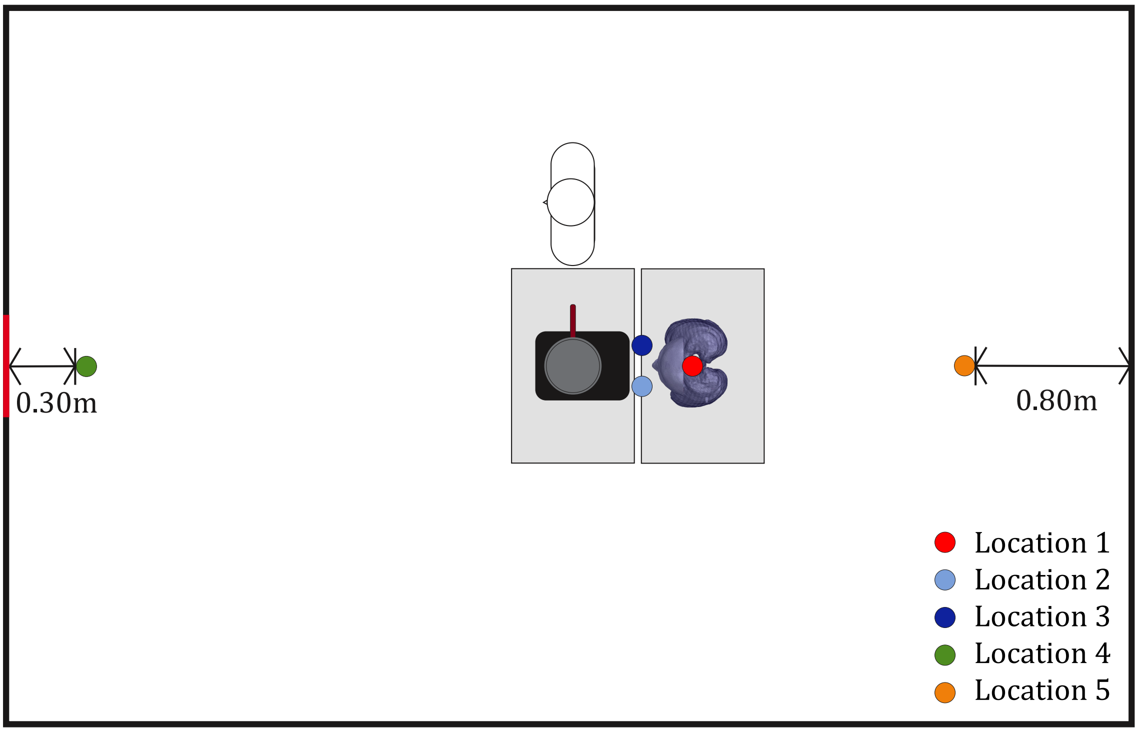

Figure 6.8. The sensor locations in the measurement set-up seen from above.

All four locations measure $PM_{2.5}$ and PM_{10} and thereby allow for an analysis of the spatiotemporal concentration distribution in the room. Furthermore, the placement of the APS3321 in the lower airways shows the size-distribution of the inhaled particle exposure.

6.3 Experimental Parameters

The emission sources serve as the varying parameter for this experiment. The other parameters are kept constant. These can be seen in Table 6.3.

Table 6.3. Fixed parameters of the experiment.

Clean room	T_i	22°C ±2°C
	Relative humidity H	-
	Ventilation type	Displacement
	Ventilation rate	$1.65\,\mathrm{h}^{-1}$
3D airway model	Activity/gender	Standing male (1.2 met)
	Height	1.80 m
	Breathing rate	10.65 l/s
	Breathing frequency	15 breathing cycles/minute
	Breathing type	Oral
Emission source	Type	Cooking oil
	Amount	1 dl
Additional Equipment	Heat source	Electric stove 1800 W (200°C)
	Container	Non-stick aluminum pan Diameter: 26 cm No lid used
Human occupant	Activity/gender	Standing male (1.2 met)
	Height	1.80 m
	Clothing	Antistatic clothing and shoes
	Exposure protection	Mask (N99 $PM_{2.5}$)
Ventilation Hood	Ventilation hood	Not used

Detailed descriptions of the fixed parameters and their derivation can be found in Appendix G.

6.4 Experimental Procedure

The measurements are each repeated five times to verify the achieved results, under the assumption that the experimental protocol is repeatable. For this reason each measurement must be carried out identically. The procedure has therefore been determined to ensure controlled performance of the experiments. This entails both the preparing and sampling of the measurement.

The measurements are carried out under the assumption that there is no background concentration when the measurements are initiated, which requires for the clean room to be prepared accordingly. The procedure prior to conducting the measurements can be seen in Table 6.4.

Table 6.4. Preparational tasks for the measurement.

Steps	Task	Estimated Time Taken
1	Surfaces in the chamber and equipment used are cleaned	30 minutes - 1 hour
2	Ventilation is run during the night at same ACH as the measurements	12 hours
3	Background concentration is tested by APS3321	10 minutes

By running the ventilation all the time, it both ensures that the clean room is cleaned in between measurements, as well as allowing the ventilation to reach steady state conditions when the measurements are initiated.

The actual measurement procedure can be seen in Table 6.5

Table 6.5. The procedure for carrying out the measurements.

Period	Event	Estimated Time Taken
Pre- source-active	1 dl of cooking oil is measured and prepared in a beaker.	1 minute
	Human occupant of the room is dressed in antistatic clothing, shoes and mask enters the clean room along with the cooking oil.	5 minutes
	All particle sensors are activated and checked to be working.	2 minutes
	1 dl of cooking oil is poured on the pan. The thermometer is used to measure initial temperature.	<1 minute
Source-active	The electric stove is turned on at 1800 Watts (200°C).	<1 minute
	The oil is heated for a constant duration of time.	2.5 minutes
	The electric stove is turned off by the human occupant.	-
Deactivated	Measurements are continued until the mass concentration by the exhaust reaches background concentration levels (±5%).	1.5 – 2 hours
	The human occupant remains stationary for the entire duration of the sampling period.	1.5 – 2 hours

Indoor climatic conditions are also monitored for the entire duration. The results of the monitored data can be seen in the Digital Appendix.

A fire safety plan has been developed to handle any fire-associated risks with the measurements. This can be seen in the Digital Appendix.

6.5 Experimental Accuracy

The experimental investigation is highly dependent on the many determined parameters for the measurements. While there will always be uncertainties and errors when conducting experimental work. Determining the accuracy of the measurement protocol as well as identifying any potential uncertainties and limitations to the set-up may help in reducing the amount of errors and improving the interpretation of measurement results.

6.5.1 Instrument Accuracy

The accuracy of the instruments may impact the results of the measurements. Prior to the measurements the accuracy of the instruments should be tested by calibration. For these measurements, two types of instruments were calibrated:

- The particle sensors
- The ventilation rate in the chamber

The particle sensors were calibrated using the APS3321, as this piece of equipment was recently calibrated by TSI, its manufacturer. Heated sunflower oil was used as the sample to calibrate over a sufficiently wide range of particle sizes.

The ventilation rate was calibrated by the TSI AccuBalance Air Capture Hood 8380 to ensure the desired flow rate in the clean room.

Results of the calibrations can be seen in Appendix H. These have been used on the measurement results.

6.5.2 Method Uncertainties

The measurements are subjected to a large number of uncertainties as several parts of the procedure are carried out manually. These include:

- Turning on the electric stove simultaneously with initiating the APS3321
- Measuring exactly 1 dl of oil for each measurement
- Ensuring minimal movement from the occupant of the room (in particular to due to the long duration of each measurement)
- Initiating the measurements under the desired indoor climatic conditions, such as indoor temperature and RH

The uncertainties are reduced to the extent possible by being meticulous in carrying out the measurement procedure.

6.5.3 Limitations

There limitations to the measurements should be taken into account when evaluating the results. These include the following:

- The 3D printed model is connected to the APS at the plugs in the bottom of each lung (connected using a three-way valve). Particles may be deposited along the boundaries of the lungs and there may be an uneven concentration distribution in the lung, so the measured sample may not be representative.
- There are no boundary conditions to the 3D printed model in the room. This means no physical boundaries in terms of the structural human envelope to the particle trajectories as well as no direct thermal plume, which influences particles trajectories.
- Realistic thermal conditions within the 3D model cannot be replicated.
- The measurements do not allow us to examine the actual particle trajectories and deposition within the model.
- The moisture conditions in real airways reach 99.5%. This may have an effect on the particle trajectories and deposition rate. However, these conditions could not be replicated within the 3D printed model.
- The nose hairs and mucous within the airways cannot be replicated within the 3D printed model. Furthermore the contraction and expansion of the human's organs are not simulated.
- The particle sensors have a limited working size range, meaning that particles outside the applicable range may not be measured.
- The particle density used to calculate the mass concentration by the APS3321 is manually chosen. However, the exact density is not known and instead assumed through literature.

7 Analysis of Experimental Results

A large number of results can be extracted from the conducted experiments. These contribute to a wider understanding of the exposure, both in terms of the investigated emission sources and inhaled particles in the lower airways. The health impact cooking oil particles have on the human occupant of a room depends on the toxicity, the intake fraction and the dose of the source [Nazaroff, 2008]. Both the intake fraction and dose, dependent on both the size and the number of inhaled particles, have been investigated in this study.

The raw data and the monitoring of the indoor climatic conditions during the experiments can be seen in the Digital Appendix.

7.1 Intake Fraction and Personal Exposure Fraction

The intake fraction iF is a ratio expressing the inhaled mass, $M_{inhaled}$, of an emission source to the released mass, $M_{released}$, from said emission source, as described in Chapter 2. Through the use of the 3D printed model, a more precise evaluation of the intake fraction is possible compared to previous studies.

Equation 7.1 shows the expression of the intake fraction.

$$iF = \frac{M_{inhaled}}{M_{released}} \tag{7.1}$$

Beyond the intake fraction it is also interesting to observe the relationship between the mass from the emission source in the breathing zone, M_{BZ}, with the mass released from the emission source. This is defined as the personal exposure fraction pF for this study and is expressed by Equation 7.2.

$$pF = \frac{M_{BZ}}{M_{released}} \tag{7.2}$$

The intake fraction and personal exposure fraction are calculated under the following assumptions and conditions:

- Only one person (the 3D printed model) is subjected to particle exposure. Thereby the population does not influence the intake fraction for the given measurements.
- The inhaled mass is the mass concentration measured in the lower airways for each measurement.

- The average mass concentration from the two particle sensors for each measurement at the breathing zone is used.
- The released mass concentration from the source is the average particle concentration measured by two particle sensors in close proximity to the emission source.
- The fractions are calculated by the integral of mass concentration for the entire duration of the measurements.

The locations of the particle sensors that measure the released mass concentration can be seen in Figure 7.1.

Figure 7.1. The sensor locations for measurements of the released mass from the emission sources.

The released mass was only measured for two oil types: olive oil and sunflower oil. The fractions will therefore only be investigated for these two oil types.

The intake fraction and personal exposure fraction of the two different oil types have been calculated for $PM_{2.5}$ and PM_{10} respectively and can be seen in Figures 7.2 and 7.3.

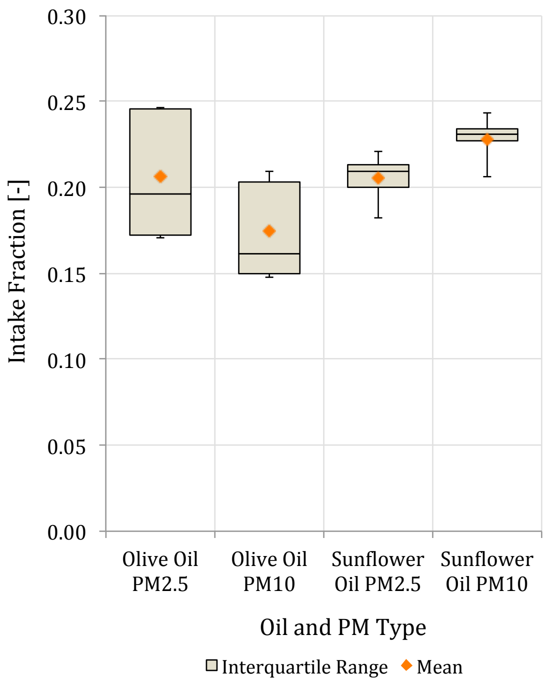

Figure 7.2. Intake fraction for olive oil and sunflower oil.

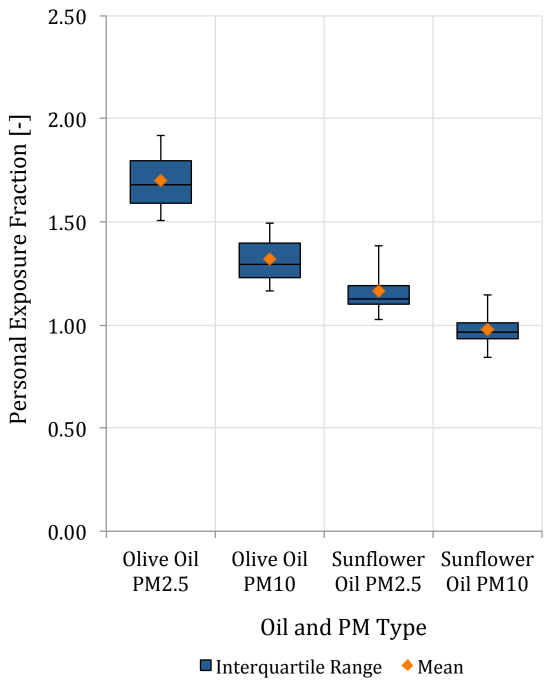

Figure 7.3. Personal exposure fraction for olive oil and sunflower oil.

The interquartiles range shows the 25th, 50th and 75th quartiles. The outliers shows the minimum and maximum values.

From Figure 7.2 it can be seen that there is very little variation in the intake fraction between the particulate matter and cooking oil types. This suggests similar size distributions in the number concentration, as the behaviour of the oil fumes are similar.

The intake fraction is very much dependent on the proximity to the source. For this reason high intake fractions were expected as the 3D printed model is relatively close to the emission source. However, the intake fraction is still significantly higher than other studies, including ones involving cooking oil [Gao et al., 2013a][Licina et al., 2017].

An analysis of the personal exposure index highlights the cause of this difference. The personal exposure index shows that the measured mass concentration in the breathing zone is actually higher than the measured mass concentration released by the emission source, as the pF exceeds 1.00. This suggests that the measurements of the mass released by the emissions source are unrepresentative of the actual mass released and should in fact be higher. The assumption of the measurements representing the released mass is therefore not true. A higher released mass concentration would in turn decrease the intake fraction and give more realistic results for both the intake fraction and particle exposure index.

To improve the investigation into the intake fraction, the correct mass released by the emission sources should be used. This could be done by changing the set-up of the measurements to get a better representation of the mass or by taking an empirical approach to the particles released by the sources. Real exposure of particles can be difficult to measure due to incomplete mixing conditions.

7.2 Size Distribution of the Inhaled Cooking Oil Particles

The number concentration measured by the APS3321 gives the number of the particles in a volume by aerodynamic diameter; it thereby gives the size distribution of the poly-dispersed particles. Knowing the size distribution of the particles for each oil may contribute to understanding the differences in the inhaled dose for the different oil types.

The number concentration, as previously mentioned, has only been investigated for the inhaled particles in the 3D printed model, as this is the location measured by the APS3321. The results in this section focus on the number concentration and thereby the size-resolved dynamics of the actual inhaled exposure by different oil types.

Figures 7.4 - 7.7 show the number concentration by the aerodynamic diameter. The number concentration has been calculated as the average over the following time ranges: 3 - 30 minutes, 35 - 65 minutes, 70 - 100 minutes and 105 - 125 minutes. The time range 105 - 125 minutes is not applicable to the corn and sunflower oil as the measurements were stopped after 100 minutes due to low background concentration levels.

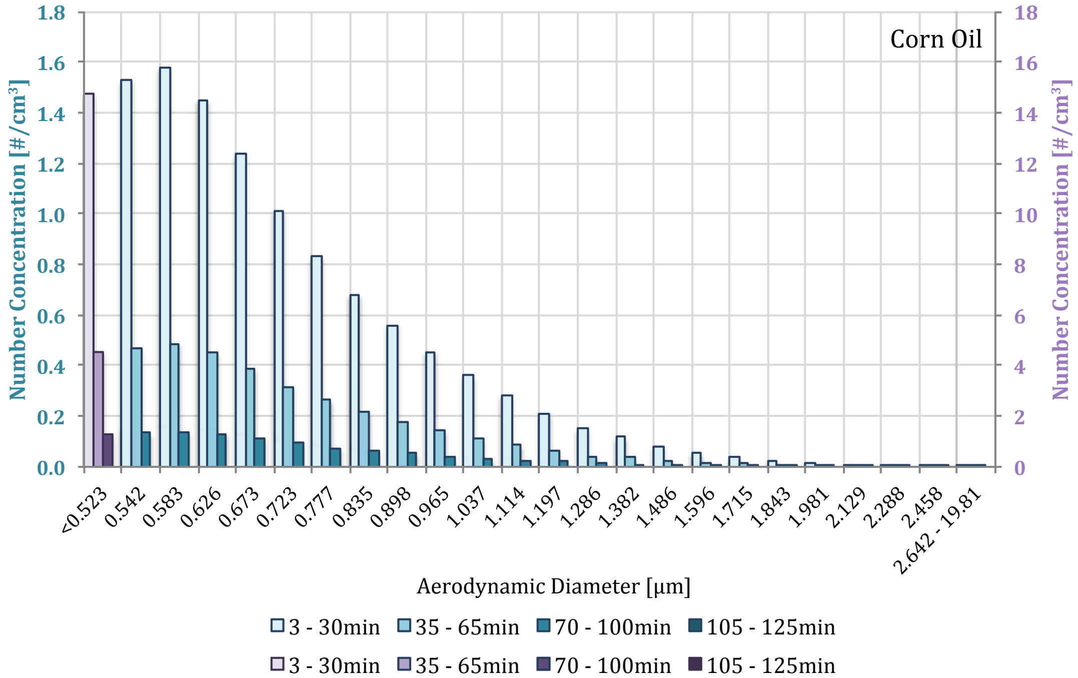

Figure 7.4. Number concentration [#/cm^3] of the inhaled particles from heated corn oil. The left axis is used for particles in the size range 0.542 - 19.81 μm and the right axis is used for particles below 0.532 μm.

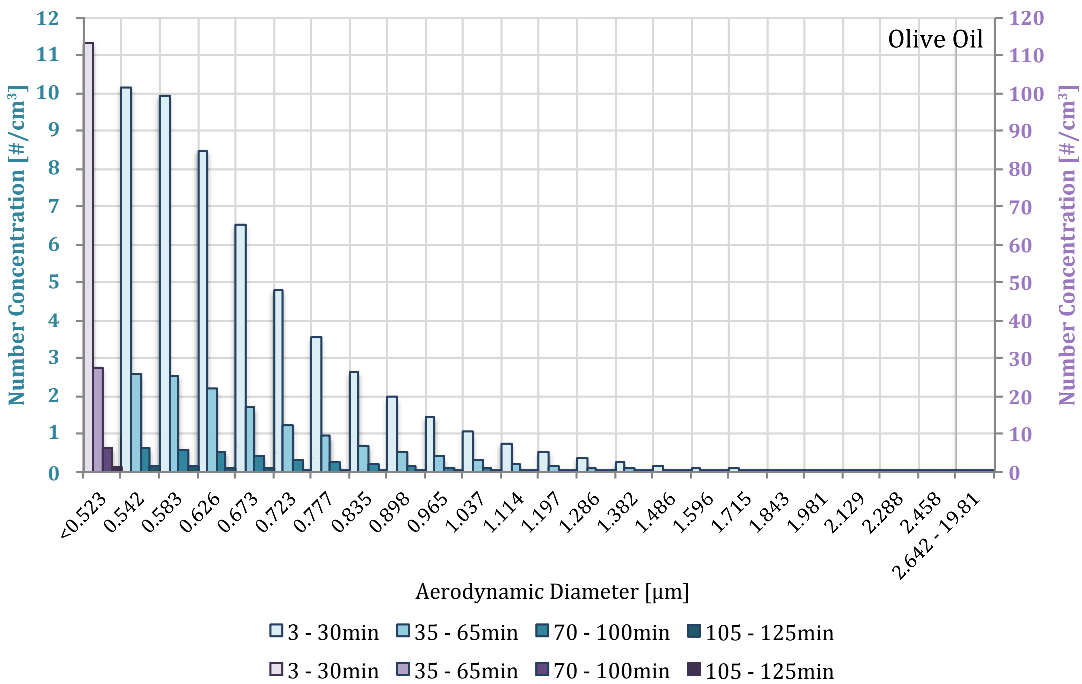

Figure 7.5. Number concentration [#/cm^3] of the inhaled particles from heated olive oil. The left axis is used for particles in the size range 0.542 - 19.81 μm and the right axis is used for particles below 0.532 μm.

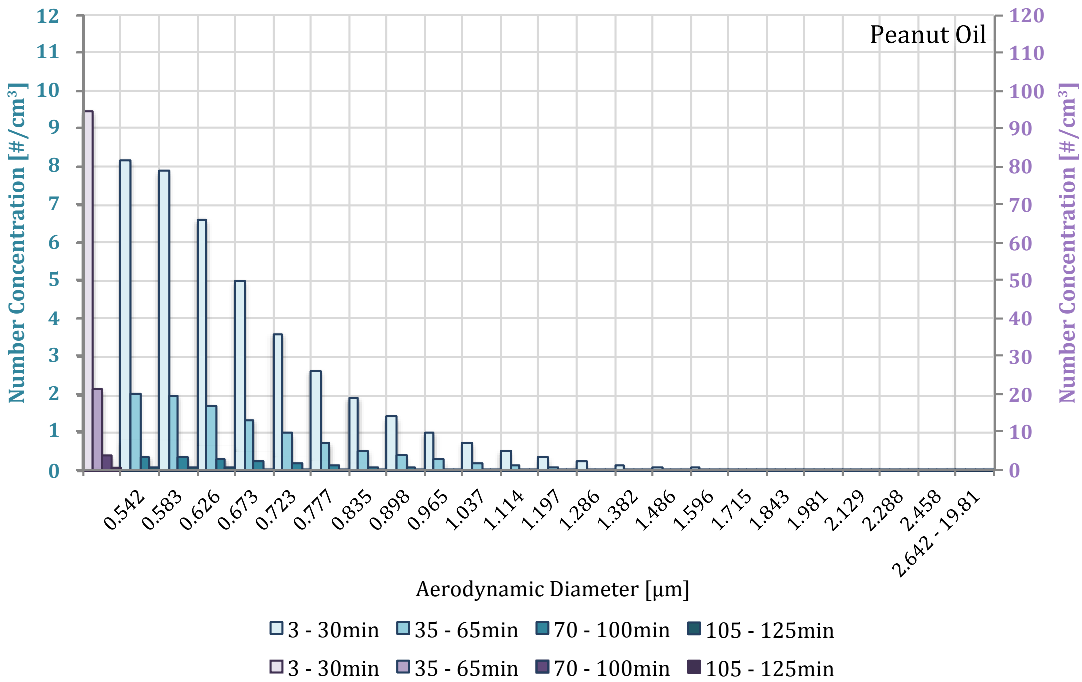

Figure 7.6. Number concentration [#/cm^3] of the inhaled particles from heated peanut oil. The left axis is used for particles in the size range 0.542 - 19.81 μm and the right axis is used for particles below 0.532 μm.

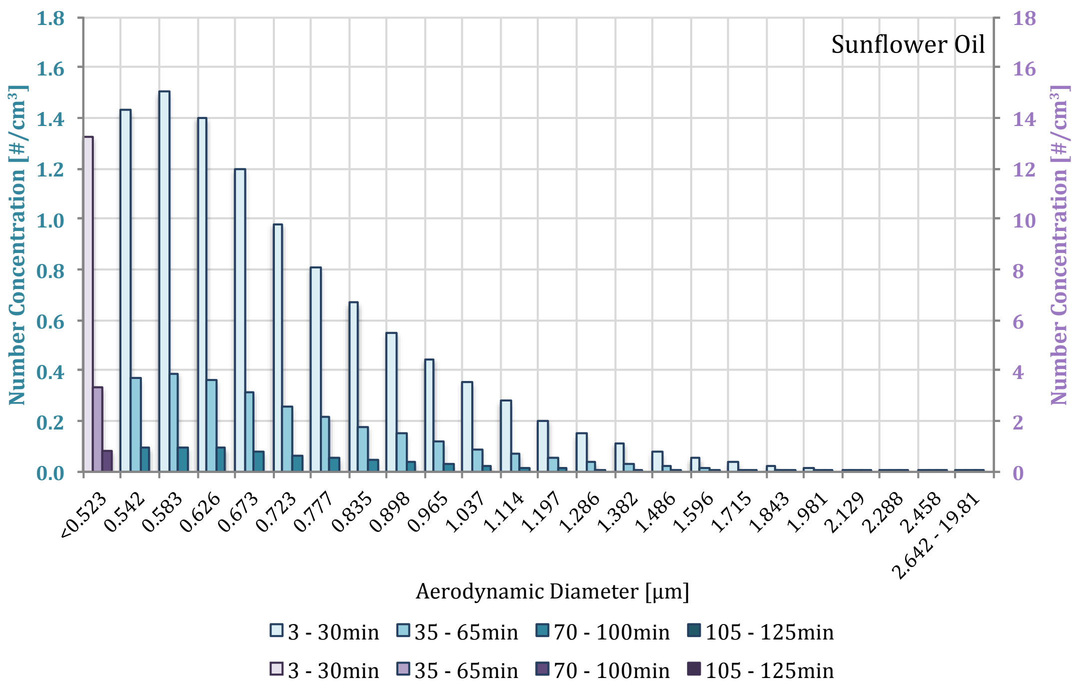

Figure 7.7. Number concentration [#/cm^3] of the inhaled particles from heated sunflower oil. The left axis is used for particles in the size range 0.542 - 19.81 μm and the right axis is used for particles below 0.532 μm.

As can be seen from the figures, the size distributions of the inhaled particles appear very similar between the different oil types. Additionally they show that the particles inhaled into the 3D printed model have a very low aerodynamic diameter; the majority are ultrafine and accumulation particles, being below 1.0 μm. In fact, the number concentration distributions indicate that coarse particles (>2.0 μm) very rarely enter the airways. In Chapter 2 it was established that deposition is expected in the lower airways, in particular for larger particles. The number concentration distribution within the airways will therefore be caused be a result of both the number concentration distribution of the emitted particles and the deposition that occurs within the airways.

In particular the number concentration for particles <0.523 μm is very high for all four oil types. The APS3321 includes Event 1, described in Appendix E, in the number concentration for particles below 0.523 μm [TSI, 2012]. This partly explains the high jump in the number concentration from <0.523 μm and to the number concentrations that occur in the range 0.542 - 19.81 μm.

The figures also show that the size distribution pattern of the aerodynamic diameters remains the same for the different time periods, despite the dilution of the particle concentration by the ventilation. This differs from the results of a cooking oil study described in Chapter 2, in which the volume-based size distribution of the particles from heated sunflower oil varies over time [Gao et al., 2013a]. However, the difference may be accounted for since Gao et al. [2013a] investigates the oil fume within the room, while this study investigates the size distribution within the airways, where the deposition of certain particle sizes occurs. Furthermore the size distribution of heated sunflower oil fume particles differ between this study and Gao et al. [2013a], confirming that the size distribution of particles may differ depending on the brand and treatment of the oil.

The actual number concentration for the four different oil types vary greatly, almost with a factor 10. As the size distributions appear so similar, the variation in the number concentration cannot be attributed to the differences in the aerodynamic diameters of the particles. However, the size-resolved metrics of the inhaled particles should still be compared more directly. The average percentage-wise size distribution for the whole time period of each of the oil type measurement can be seen in Figure 7.8.

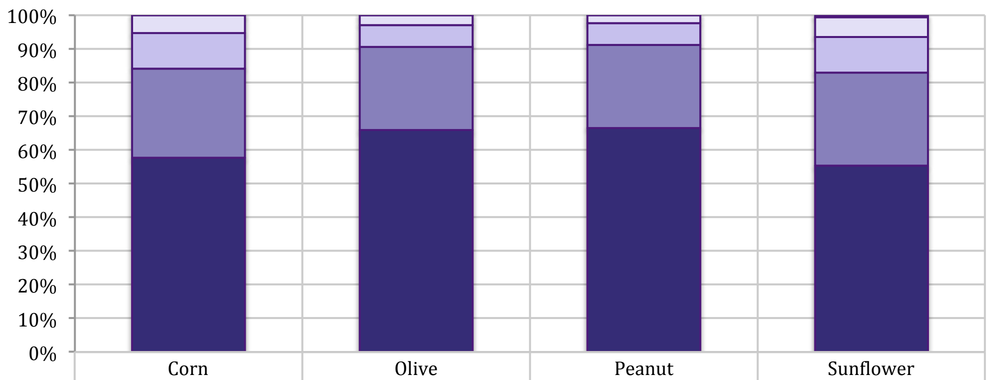

	Corn	Olive	Peanut	Sunflower
2.642 - 19.81 µm	0.17%	0.16%	0.15%	0.42%
1.037 - 2.458 µm	5.36%	2.62%	2.25%	5.87%
0.777 - 0.965 µm	10.14%	6.51%	6.22%	10.75%
0.542 - 0.723 µm	26.83%	24.99%	24.79%	27.85%
<0.523 µm	57.49%	65.72%	66.59%	55.12%

Oil Type

■<0.523 µm ■0.542 - 0.723 µm ■0.777 - 0.965 µm ■1.037 - 2.458 µm ■2.642 - 19.81 µm

Figure 7.8. The average size distribution of the number concentration for each oil type.

The figure contributes to the notion that the size distribution is similar for the four different oil types. Particles up to 1.0 μm take up more than 90% of the number concentration for all four of the oil types. There is very little variation within the different size ranges chosen for comparison. Olive oil and peanut oil have a slightly higher fraction of particles below 0.523 μm and a lower fraction of particles in the 0.542 - 0.965 μm size range compared to corn and sunflower oil.

These results should be taken into consideration when evaluating the mass concentration in the airways.

7.3 Spatiotemporal Behaviour of Cooking Oil Particles

The five different measurement locations for these measurements enable an evaluation of how the mass concentration varies in the room. This can be affected by several parameters including ventilation type, ventilation rate, thermal plume strength and the emission source. As all of the parameters remain constant excepting the emission source, the variation in the mass concentration in the different locations can be analysed in respect to the measurement setup. Furthermore the mass concentration has been measured to observe the entire period of particle exposure. Measurements at time zero start when the electric stove is turned on, thereby including the source-active and deactivated period.

Location 1 is within the lower airways, locations 2 and 3 are in the breathing zone, location 4 is by the exhaust and location 5 is in the back of the room at the same height as location 4 as can be seen in Figures 6.6 - 6.8.

Entire Duration of the Measurements

The measurements were carried out for at least 100 minutes for each of the measurements. The results of these can be seen in Figures 7.9 - 7.12.

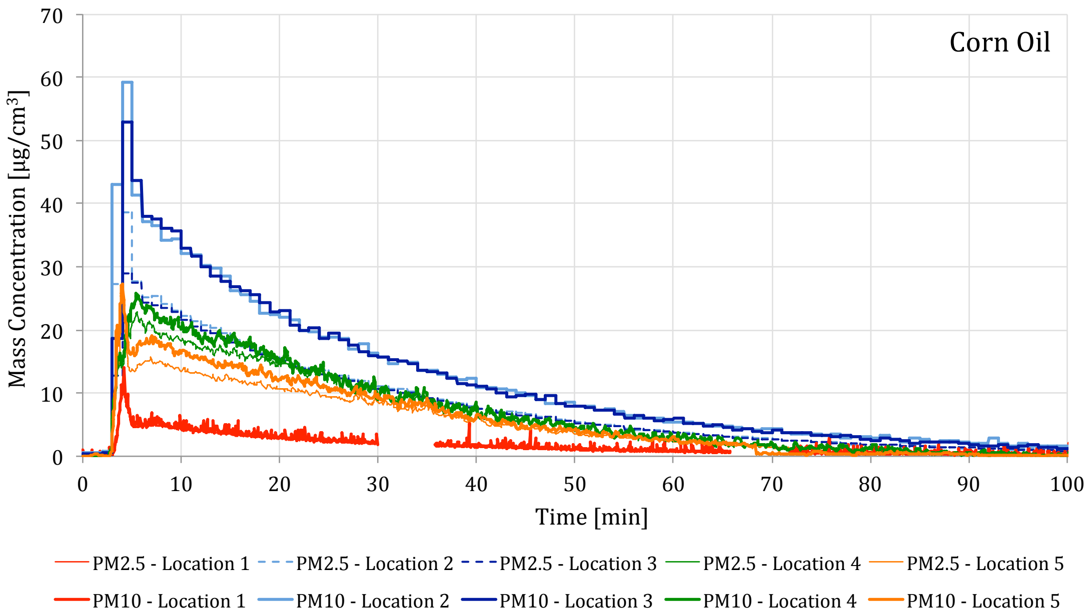

Figure 7.9. The mass concentration of the five measurement locations over time for both $PM_{2.5}$ and PM_{10} from heated corn oil.

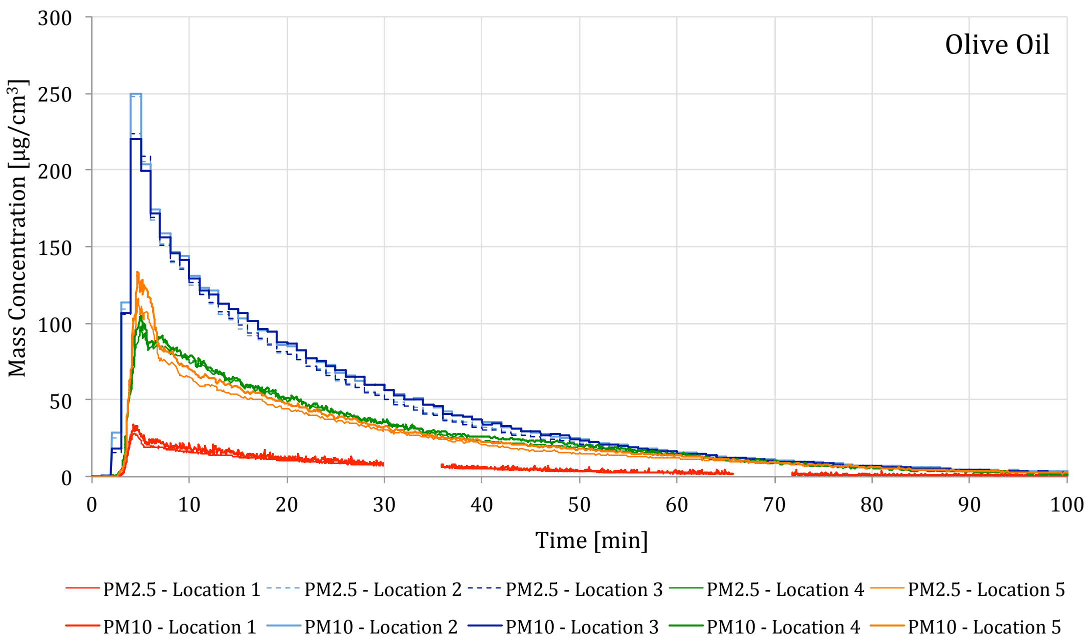

Figure 7.10. The mass concentration of the five measurement locations over time for both $PM_{2.5}$ and PM_{10} from heated olive oil.

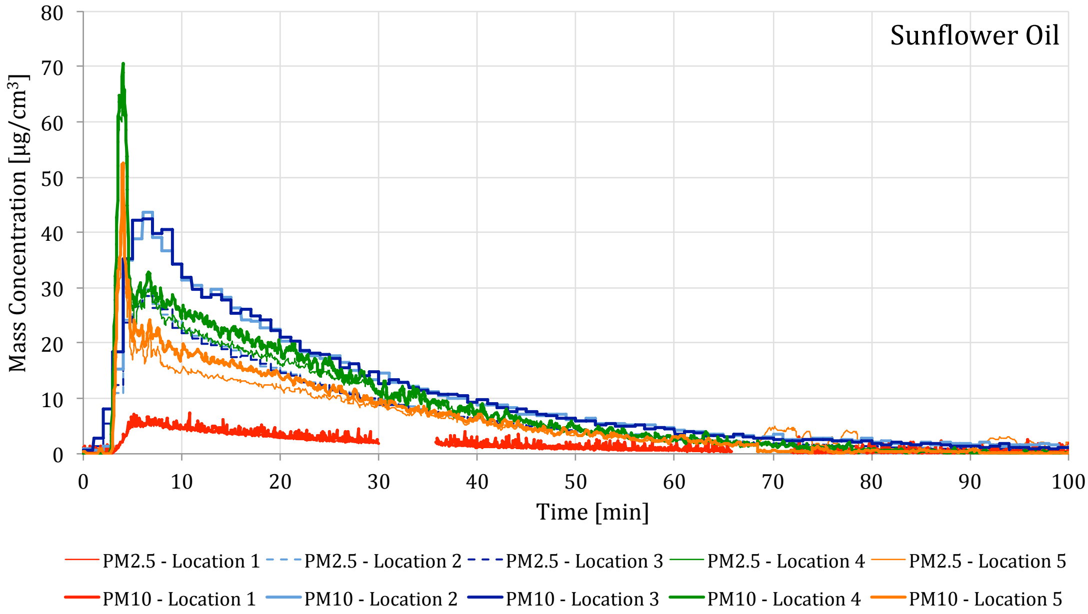

Figure 7.11. The mass concentration of the five measurement locations over time for both $PM_{2.5}$ and PM_{10} from heated peanut oil.

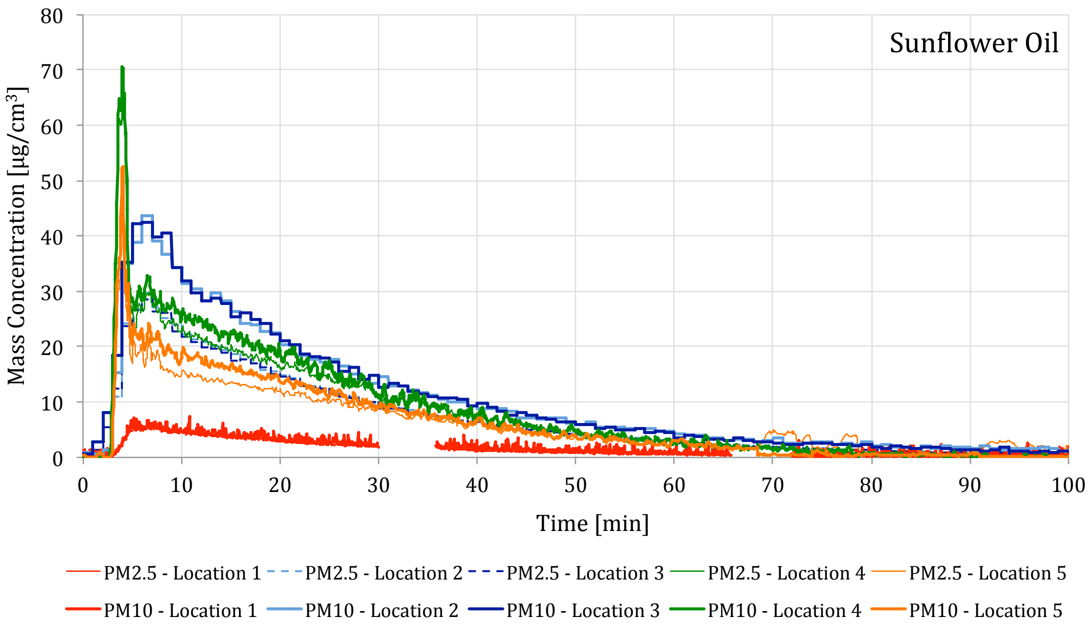

Figure 7.12. The mass concentration of the five measurement locations over time for both $PM_{2.5}$ and PM_{10} from heated sunflower oil.

All of the oil types show a clear peak in concentration levels where-after the concentration levels are slowly diluted by the ventilation.

Figures 7.9 - 7.12 show a large difference in the mass concentration levels from the four different cooking oil types. As previously mentioned, the differences the mass concentrations are not caused by a difference in size distributions but by the emission rates from the sources themselves. Olive oil generates the highest mass concentration, closely followed by peanut oil. Both sunflower and corn oil generate a substantially smaller mass concentration. This is supported by Figure 7.13 that shows a direct comparison of the mass concentrations in the airways between the four different oil types.

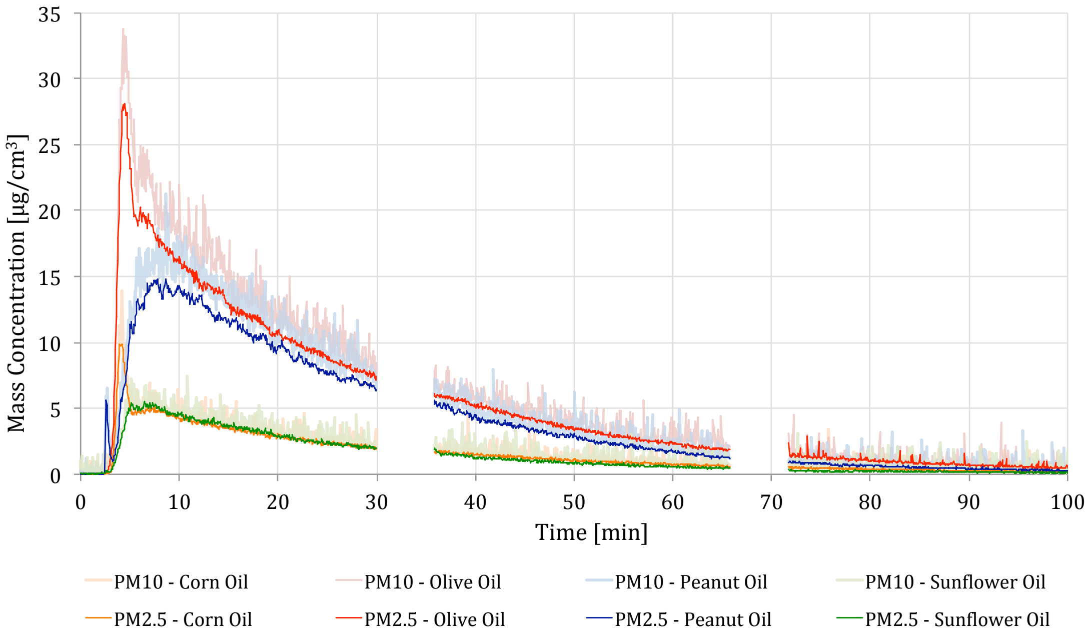

Figure 7.13. The mass concentration in the airways by the four different cooking oil types.

For the majority of the time, the mass concentration in the four locations is highest in the breathing zone. This corresponds with being in close proximity to the emission source, which is also effected by the strong thermal plume generated by the electric stove. The mass concentration is slightly higher by location 4 (exhaust) than location 5 (room), which corresponds to the air flow in the room. Only a fraction of the particles in the breathing zone are inhaled into the lower airways. This relationship is similar for all four of the oil types, indicating that due to similar size distributions, the particles in the airways are deposited in a similar manner to each other.

The figures also show that $PM_{2.5}$ and PM_{10} are very close to each other, which suggests that there are very few particles in the size range 2.5 - 10 μm. This supports the findings about the size distribution of the number concentration of the inhaled particles in the airways.

First Ten Minutes of the Measurements

The first ten minutes of the measurements have also been examined to analyse the peak concentrations in the different locations. Figures 7.14 - 7.17 show the first ten minutes of each measurement of the four different oil types.

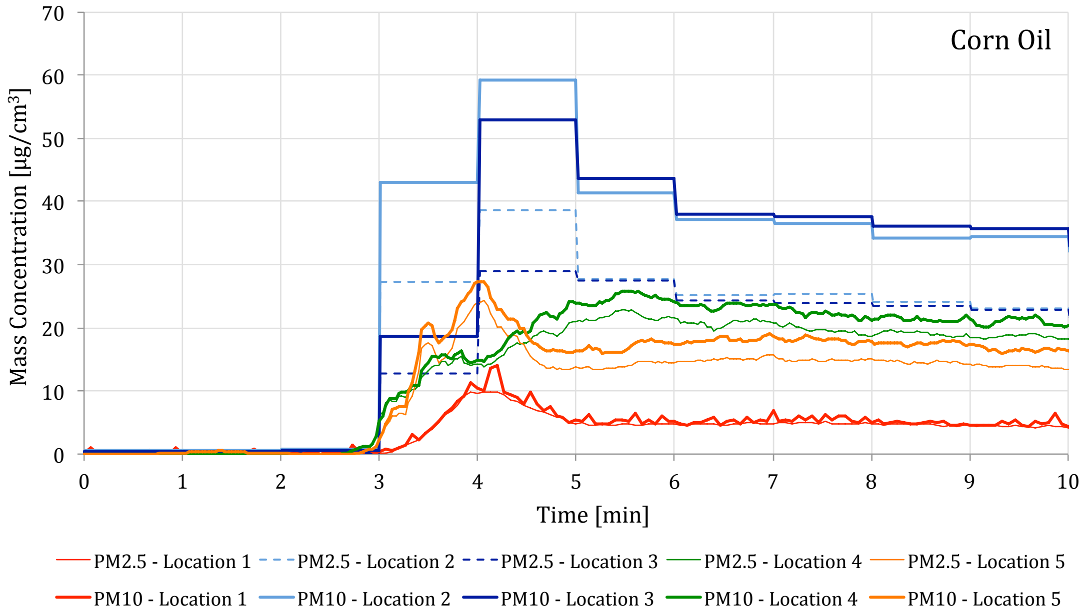

Figure 7.14. The mass concentration of the five measurement locations for the first ten minutes for both $PM_{2.5}$ and PM_{10} from heated corn oil.

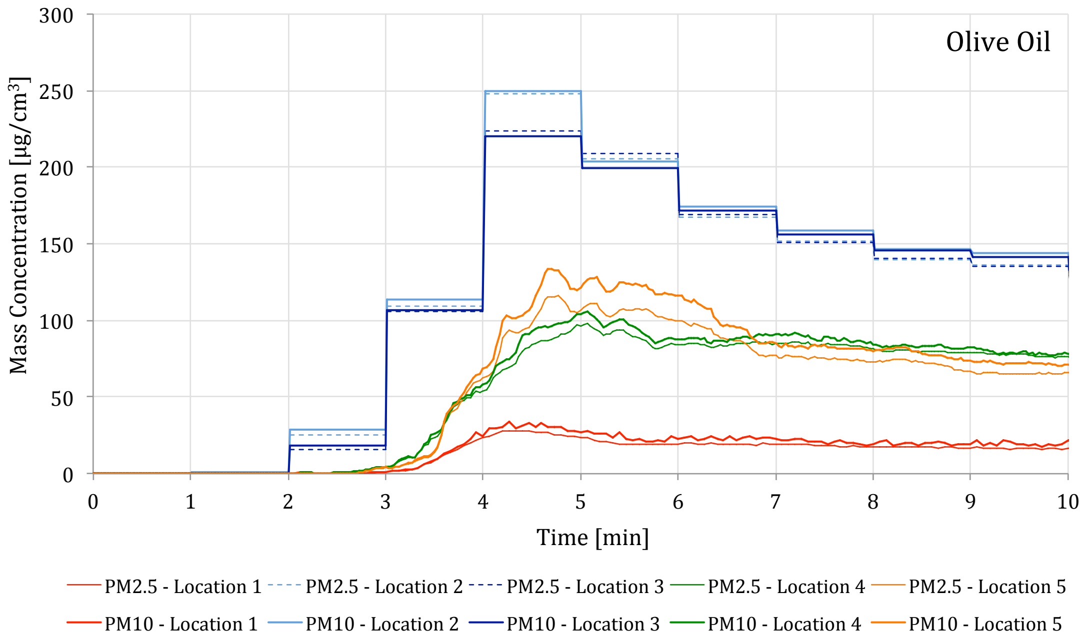

Figure 7.15. The mass concentration of the five measurement locations for the first ten minutes for both $PM_{2.5}$ and PM_{10} from heated olive oil.

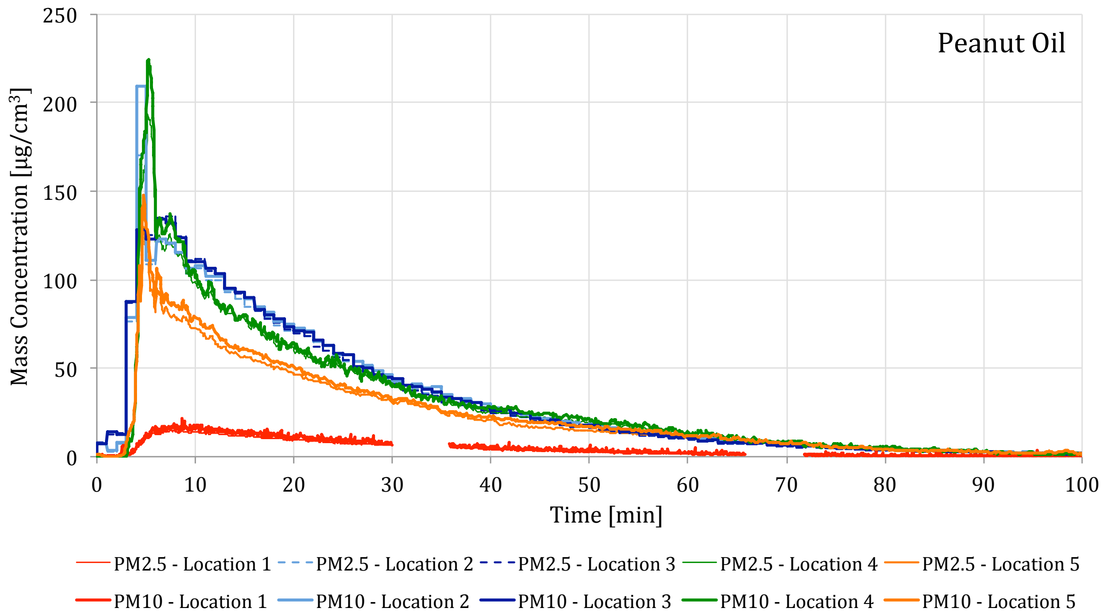

Figure 7.16. The mass concentration of the five measurement locations for the first ten minutes for both $PM_{2.5}$ and PM_{10} from heated peanut oil.

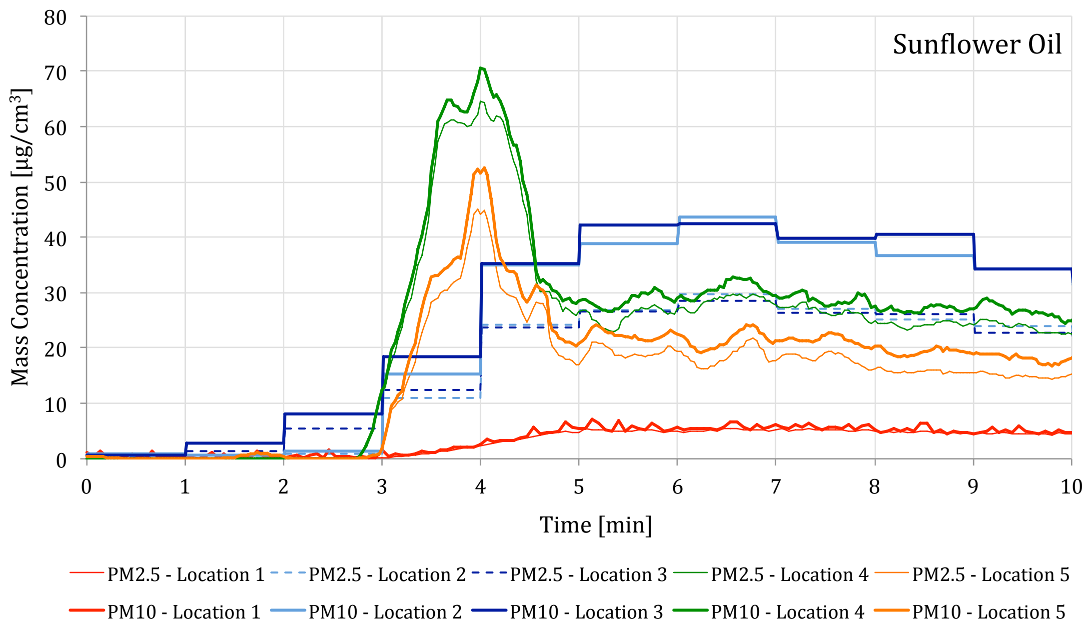

Figure 7.17. The mass concentration of the five measurement locations for the first ten minutes for both $PM_{2.5}$ and PM_{10} from heated sunflower oil.

Figures 7.14 - 7.17 show that the initial behaviour of the four different cooking oils vary from one another beyond the actual mass concentration levels.

For all four oil types each location experiences a peak in concentration levels. However, while corn and olive oil both experience the highest peaks in mass concentration in the breathing zone, both peanut oil and sunflower oil have initial higher peaks by the exhaust. This is due to the behaviour of the emissions from the heated cooking oil as the flow characteristics in the room should be the same. However, once more stable conditions are reached, after approximately ten minutes, the breathing zone mass concentration once again becomes dominant.

Furthermore, the time of the peaks varies between the different oil types. While inhaled mass concentration in the airways peaks simultaneously with the peak of the breathing zone mass concentration, there is a variation in the peak times of locations 4 and 5. These may once again have been caused by the behaviour of the particles influenced by the strong thermal plume.

For all four measurements locations and all four cooking oil types, there is a dead time of approximately 3 minutes; this is the time when the particle concentration starts increasing. However, it should be noted that the source is deactivated at 2 minutes 30 seconds. This means that the source particle concentration levels do not rise in the source-active period.

7.4 Evaluation of Cooking Emitted Particles by Oil Heating

Particle exposure by cooking emitted particles can be characterised by many different features, which enables a comparison of the four different oil types. Table 7.1 shows the resulting features, namely the peak mass concentration, the deposition fraction, the time constant, the intake fraction and the susceptible exposure index. The methods of calculation can be found in Appendix B.

Table 7.1. The peak mass concentration, deposition fraction, time constant and dead time for the four different oil types.

	Peak Mass Conc. [μg/cm^3]				**Deposition Fraction**	
Oil Type	Breathing Zone		Lower Airways			
	$PM_{2.5}$	PM_{10}	$PM_{2.5}$	PM_{10}	$PM_{2.5}$	PM_{10}
Corn oil	38.7	59.2	9.9	13.9	81.1%	82.6%
Olive oil	248.2	249.6	28.2	33.8	84.8%	83.4%
Peanut oil	170.1	209.4	14.8	21.3	84.6%	81.2%
Sunflower oil	29.8	43.6	5.5	7.4	80.9%	77.9%

	Time Constant τ_{rise}			**Dead Time**		
	Breathing Zone		Lower Airways	Breathing Zone		Lower Airways
	$PM_{2.5}$	PM_{10}	$PM_{2.5}/PM_{10}$	$PM_{2.5}$	PM_{10}	$PM_{2.5}/PM_{10}$
Corn oil	60.0 s	47.5 s	24.0 s	185 s	195 s	194 s
Olive oil	68.5 s	68.5 s	32.0 s	180 s	180 s	195 s
Peanut oil	62.0 s	60.0 s	80.0 s	185 s	190 s	205 s
Sunflower oil	96.0 s	87.5 s	65.0 s	175 s	185 s	194 s

The peak mass concentration in the lower airways and the breathing zone show that olive oil has the highest dose of mass concentration, followed by peanut oil. In comparison, both corn and sunflower oil contribute much less the concentration levels. This effect could be caused by the smoke points of the oils; all four cooking oils reached their smoke points before the source was deactivated. As can be seen in Appendix G, olive oil has a lower smoke point than the remainder of the oils. However, this would have to be investigated further to support the hypothesis.

The WHO guidelines values for $PM_{2.5}$ and PM_{10} are a 24-hour mean of 25 μg/cm^3 and 50 μg/cm^3 respectively as mentioned in Chapter 3 [World Health Organization, 2005]. All four oil types exceed the recommended 24-hour mean values for a time during the measurements. The cooking oil can therefore be assessed to be a major contributor to particle concentration to daily, as an occupant will also be subjected to other emission sources throughout the day. For this reason, control methods to limit the particle exposure should be considered.

The time constant gives information about the response to the activation of the emission sources. The dead time is the time taken from when the electric stove is heated before a reaction occurs upon the particle concentration. These have both been calculated for the mass concentration in both the breathing zone and in the lower airways in terms of the rise of particle mass concentration. The time constants in the lower airways have been assumed to be the same for $PM_{2.5}$ and PM_{10} as there is little difference in the mass concentrations between them. Corn oil is the fastest of the oils to respond to the heating process in terms of particle concentration. The large variation in the time constants in the lower airways can be explained by the inconsistencies in a peak concentration point. This applies to peanut oil, whose time constant is the only one that exceeds the time constants in the breathing zone. Identifying the time constant may be useful when evaluating future control strategies.

The deposition fraction is an index that represents the ratio between the deposited particles to the inhaled particles. The method of calculation for the experiment can be found in Appendix B. The deposition fraction for all four oil types is between 80.9% and 84.8% for $PM_{2.5}$ and 77.9% and 83.4% for PM_{10}. Normally the deposition rates would be expected to increase for larger particles due to the gravitational force, but due to the size distribution of the cooking oil particles, there are very few larger particles.

The susceptible exposure index (SEI) is used as a local ventilation index. As the supply concentration is assumed to be zero, it is a relationship between the mass concentration in the breathing zone compared to the mass concentration by the exhaust as described in Appendix B. Table 7.2 shows the SEI for the different oil types for $PM_{2.5}$ and PM_{10}. The calculated SEI is the steady state value reached when observing its dynamic behaviour.

Table 7.2. The susceptible exposure index for the different oil types for $PM_{2.5}$ and PM_{10}.

	SEI [-]	
	$PM_{2.5}$	PM_{10}
Corn oil	1.24	1.74
Olive oil	1.47	1.52
Peanut oil	1.02	1.03
Sunflower oil	0.96	1.34

As expected, the ratio is higher for PM_{10} than for $PM_{2.5}$. The SEI also shows a correlation with the previous number concentration results in the lower airway; there is a smaller difference in the SEI between $PM_{2.5}$ and PM_{10} for olive oil and peanut oil than there is for corn and sunflower oil. This supports the idea that olive oil and peanut oil generate fewer particles above 2.5 μm relative to the particles they generate below 2.5,μm.

SEI can be used as indicator as to the mixing in the room but it does not consider the actual dose of the emission source. Furthermore it should be taken into consideration that the larger particles have a larger settling velocity. Considering PM_{10} at the exhaust may therefore give an unreasonable representation due to the difference in the size distribution of the particle concentration at different locations.

The overall investigation shows little correlation between the different features of the cooking oil types. It can be concluded that olive oil and peanut oil contribute with the largest particle exposure. However, a further investigation into the chemical composition of the cooking oil fumes and potentially its toxicity may give further insight.

8 | Additional Investigations

The results for the investigation into particle exposure by different cooking oil types are conditioned by the parameters set for the measurements. It is therefore beneficial to carry out a deeper investigation into these parameters to identify any potential influences they may have on the exposure.

Two investigations have been carried out. These are the following:

- The impact of increasing the ventilation rate
- The effect of the thermal plume on particle concentration in the breathing zone

8.1 Investigation of Increased Flow Rate

The ventilation type for the measurements is displacement ventilation, which is mainly driven by the buoyancy effects, as mentioned in Chapter 6. The ventilation rate is set to 20 l/s, as described in Appendix G. Despite the buoyancy driven ventilation, an investigation is carried out in which the ventilation rate is doubled to 40 l/s to see its impact. This increases the air change rate from $1.65\,\mathrm{h}^{-1}$ to $3.30\,\mathrm{h}^{-1}$. This is the only parameter changed from the previous measurements. It has been assessed that the effect of the ventilation rate on the particle exposure is sufficiently examined through one oil type, namely sunflower oil.

Figures 8.1 and 8.2 shows the comparison between the measurements of the original ventilation rate and the increased ventilation rate. Only $PM_{2.5}$ has been compared, as there is little difference between $PM_{2.5}$ and PM_{10} .

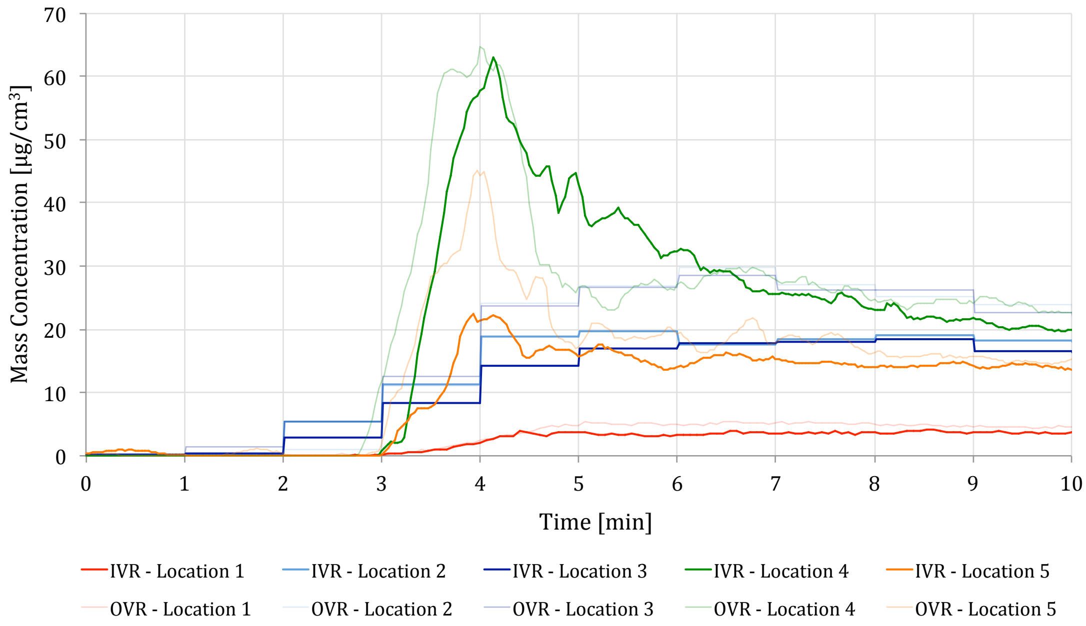

Figure 8.1. The first ten minutes of the $PM_{2.5}$ mass concentration of the five measurement locations for the original and increased ventilation rates. IVR is the increased ventilation rate and OVR is the original ventilation rate.

Figure 8.1 shows that the increased ventilation rate does have an impact on the particle concentration levels. The peak concentration levels in the breathing zone, the room concentration and most importantly, in the airways have been reduced. The exhaust concentration still has the same peak, which is to be expected, as the emission rate from the cooking oil is unchanged. This shows that increasing the flow rate strengthens the dilution in the different measurement locations. This can also be seen by Figure 8.2.

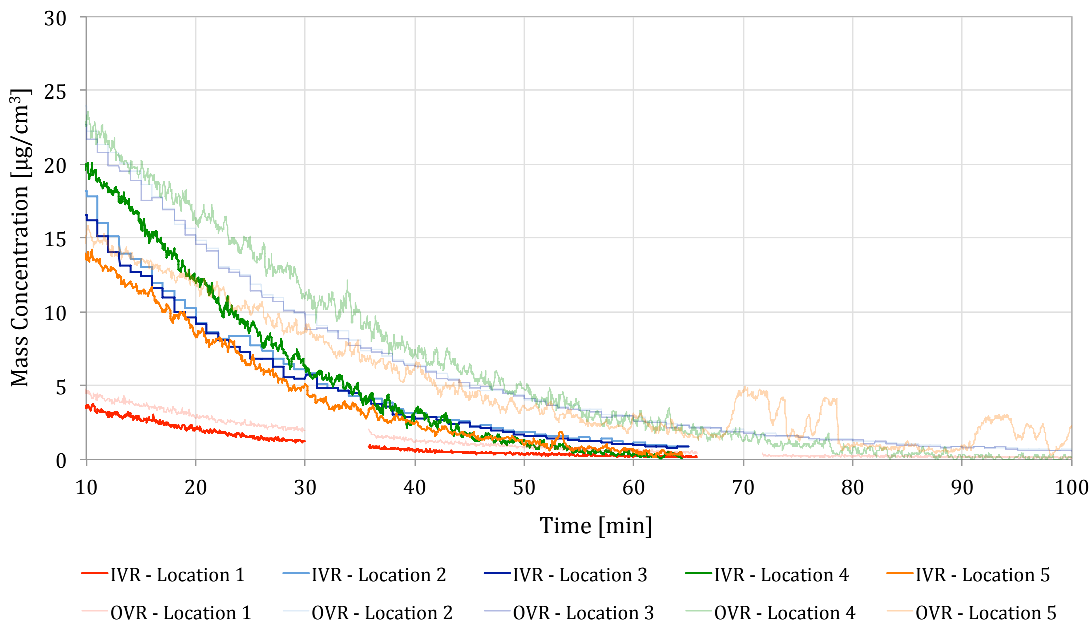

Figure 8.2. The $PM_{2.5}$ mass concentration of the five measurement locations for the original and increased ventilation rates from 10 minutes into the measurement. IVR is the increased ventilation rate and OVR is the original ventilation rate.

Figure 8.2 shows that, as expected, the mass concentration is diluted faster than in the measurements with the original flow rate. This adheres to the dilution equation, where the time constant is dependent on the air change rate. The difference in the time constants can clearly be seen from Figure 8.2.

However, due to the strength of the emitted particle concentration, increasing the flow rate had little effect on the inhaled dose. To fully comprehend the relationship between particle exposure and ventilation rate, further variations on the flow rate could be made and extended to include other ventilation types.

8.2 Investigation of the Thermal Plume Effect

In the measurements of particle exposure by different cooking oil types, the boundary conditions of the 3D printed airway model in terms of a realistic human occupant were not considered, as mentioned in Chapter 6. This includes both the physical boundaries and thermal boundary conditions. An investigation has thereby been carried out on using thermal manikins to investigate the influence of the thermal boundary condition on particle exposure in the breathing zone.

8.2.1 Experimental Description of the Thermal Plume Investigation

The thermal manikin is placed in the chamber in the previous location of the 3D printed model. The investigation entails using two different plume strength configurations in the thermal manikin to investigate the influence it has on the inhaled particles using two different cooking oils; sunflower seed oil and olive oil. These oils were chosen due to their difference in mass concentration.

The two plume strengths are based on the activity levels assumed for cooking; 1.2 met and 2.0 met. The heat effects can be seen in Table 8.1.

Table 8.1. Activity level and corresponding heat flux for the thermal manikin [Litewnicki and Zajas, 2010].

Activity Level [met]	Description [ISO 7730, 2006]	Total Heat Flux [W]
1.2	Sedentary activity (office, dwelling, school, laboratory)	78.4
2.0	Standing, medium activity (shop assistant, domestic work, machine work)	110.4

The APS3321 has been relocated to measure mass concentration in the breathing zone. The measurement set-up can be seen in Figure 8.3. Additional images can be seen in Appendix F.

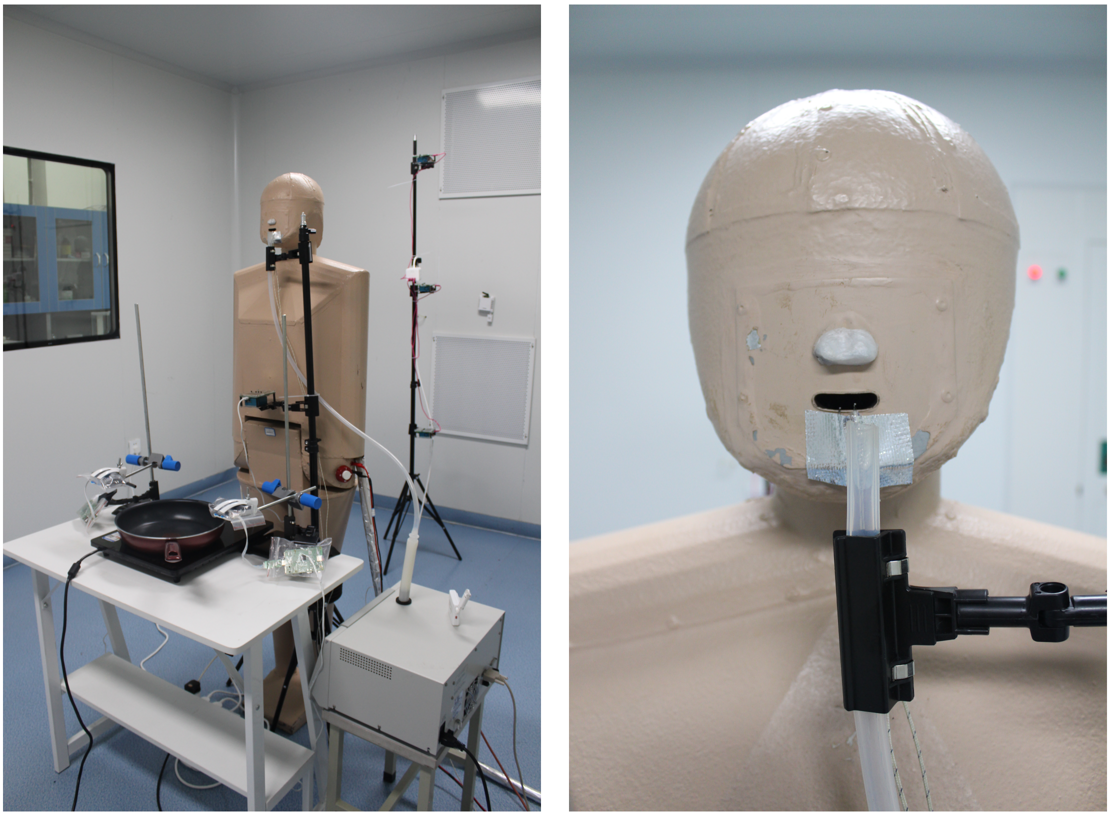

Figure 8.3. The measurement set-up for the thermal plume measurements.

The measurement protocol is otherwise the same as the previous measurements carrying out in this study.

8.2.2 Analysis of the Experimental Results

The results of the measurements for $PM_{2.5}$ can be seen below in Figures 8.4 - 8.7 for sunflower oil and olive oil respectively. Results for PM_{10} can be found in the Digital Appendix.

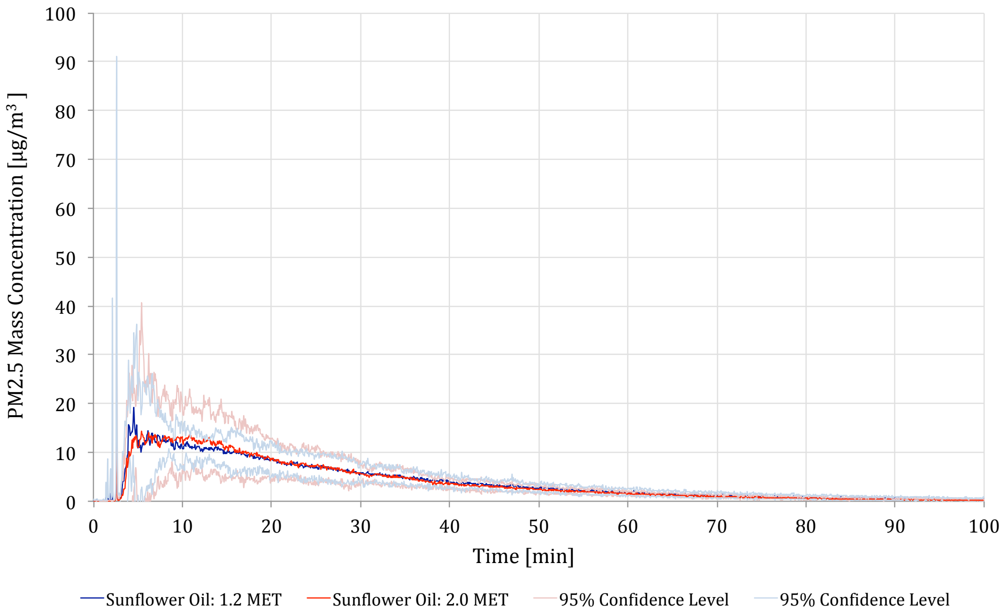

Figure 8.4. The mass concentration levels in the breathing zone of the thermal manikin for the whole duration of the measurement using sunflower oil and two different plume strengths.

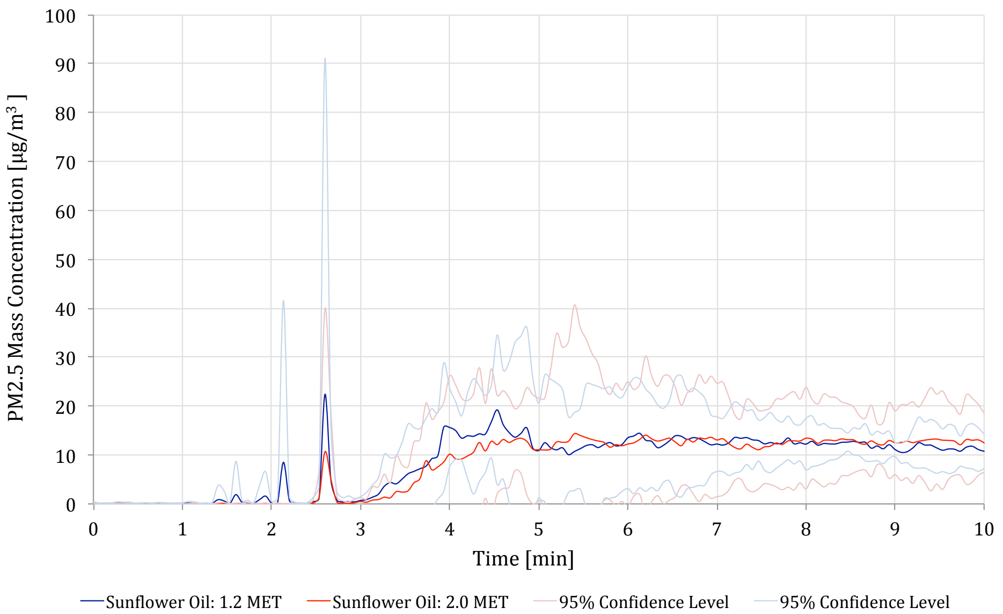

Figure 8.5. The mass concentration levels in the breathing zone of the thermal manikin for the first ten minutes of the measurement using sunflower oil and two different plume strengths.

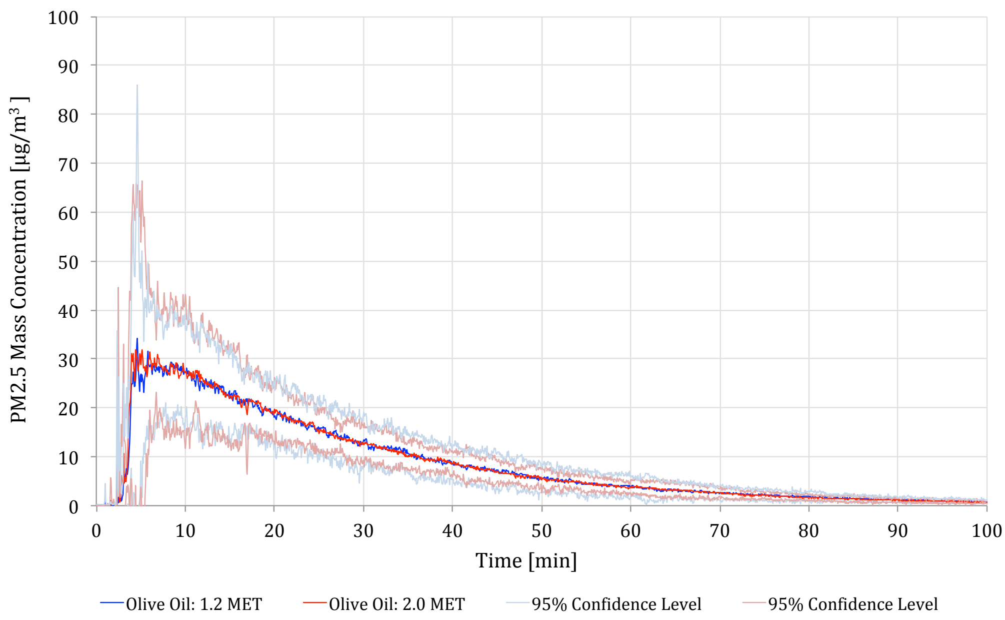

Figure 8.6. The mass concentration levels in the breathing zone of the thermal manikin for the whole duration of the measurement using olive oil and two different plume strengths.

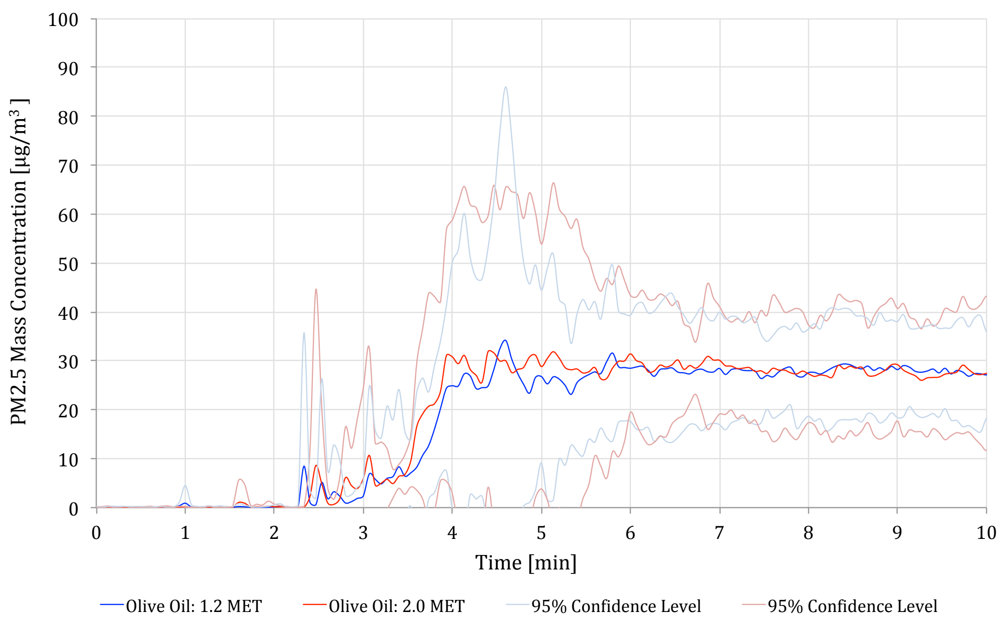

Figure 8.7. The mass concentration levels in the breathing zone of the thermal manikin for the first ten minutes of the measurement using olive oil and two different plume strengths.

Figures 8.4 - 8.6 show that for the investigated plume strengths, the thermal plume from the thermal manikin does not have a clear influence on the inhaled particle concentration. However, a study mentioned in Chapter 2 showed that the thermal plume had a strong influence on the intake fraction [Licina et al., 2017]. The main difference between this study and Licina et al. [2017] is the presence of the strong thermal plume generated by the electric stove. As mentioned in Chapter 6, the electric stove has a heat flux of 1800 W, much higher than the heat flux from the thermal manikin. This is evaluated to dominate the thermal plume to the extent where the different activity levels of the occupant have little-to-no impact on particle concentration in the breathing zone.

Further investigations could be made using no plume strength or increasing the plume strength further. However, it is evaluated that for cooking the investigated plume strengths represent realistic activity levels.

Part II

Numerical Investigation of Particle Exposure in the Lower Airways

The numerical investigation of particle exposure in the airways is conducted by using Computational Fluid Dynamics (CFD).

CFD simulations can be used to simulate fluid particle flow that is not reproducible or challenging to reproduce under experimental conditions. Furthermore CFD simulations are a cost effective alternative compared to simulating real fluid flow. However it should be seen as an alternative that accompanies experimental methods and acts in conjunction with experimental investigations. [Tu et al., 2013]

Additionally CFD simulations have the advantage of enabling visualisation of the airflow structures by vector and contour plots, which are useful when describing and analysing the physics that occur in the airways. [Tu et al., 2013]

9 Introduction to Computational Fluid Dynamics

In Computational Fluid Dynamics the governed equation of the fluid flow is expressed by the conversation laws of physics:

- Conservation of mass
- Balance of momentum (Newton's second law)
- Conservation of energy (First law of thermodynamics)

The governed equation is based on four term highlighted in Equation 9.1.

$$\text{Transient term} + \text{Convection term} = \text{Diffusion term} + \text{Source term} \tag{9.1}$$

The fluid flow are mathematically expressed by Equation 9.2, which is referred to as the Navier-Stokes equation or the transport equation. [Versteeg and Malalasekera, 2007]

$$\frac{\partial(\rho\Phi)}{\partial t} + div(\rho\overrightarrow{u}\Phi) = div(\Gamma_\Phi\overrightarrow{grad}\Phi) + S_\Phi \tag{9.2}$$

Where

ρ	Density of the fluid [kg/m^3]
Φ	Variable in the flow field
$\overrightarrow{u}$	Velocity [m/s]
Γ_Φ	The diffusion coefficient for the dependent variable Φ
S_Φ	Source term (creation of Φ per unit of volume and time)

Using the Navier-Stokes equation the conservation of mass can be expressed as the continuity equation, the Balance of momentum can be expressed as the momentum equation and the conservation of energy can be expressed as the energy equation.

To solve the air flow for a three-dimensional laminar isothermal case, there are four unknown parameters: pressure, velocity in x-direction, velocity in y-direction and velocity in z-direction. The variables can be calculated by applying three momentum equations and one continuity equation.

The Finite Volume Method is applied as the equations cannot be solved analytically. The transport equation is a coupled and non-linear partial differential equation. Hence numerical methods are applied to solve it. [Lund and Condra, 2016]

9.1 Spatial Discretization

The domain is discretized into control volume, where the transport equation can be integrated by using the Finite Volume Method. The transient, convection, diffusion and source term can be discretized by applying different spatial discretization scheme. The spatial discretization scheme is based on the Finite Difference Method, where the order of accuracy can be measured by Taylor series. A high order of accuracy, or large number cells, is important to obtain a small error in the solution, but a high order of accuracy, may also lead to instability. [Versteeg and Malalasekera, 2007]

In ANSYS Fluent the diffusion term and source term will be solved by the central difference scheme, which has a second-order of accuracy. [ANSYS Fluent, 2017] The convection term can be defined by different spatial discretization schemes such as the upwind scheme or the quick scheme.

When applying the first order upwind scheme it is assumed that the variable in the face is the same as the variable in the upstream cell centred value of the face. The advantage of the upwind scheme is that it results in stable calculations. The disadvantage is that the first order upwind scheme is very diffusive. The diffusive problem can be fixed by refining the mesh or using second order upwind scheme. [Versteeg and Malalasekera, 2007] In second-order upwind schemes the variable is determined by the two cells upstream of the face. [Wikipedia, 2017]

Quick scheme is accurate, but it can lead to instability problems. Applying a central differencing scheme can result in divergence or oscillations if the criterion for the Peclet number is not met. [Versteeg and Malalasekera, 2007]

9.1.1 Transient Simulations

A transient simulation is conducted, when the flow field changes over time. Transient simulations can be conducted using an explicit or implicit solver.

An explicit solver calculates the new value in the examined time step immediately by the already known cells from the previous time step. Explicit solver is quick but it has to meet some restrictions based on the ratio between the time step and the cell size, in order to achieve a stable and converged solution due to the numerical method. [Versteeg and Malalasekera, 2007]

An implicit solver calculates the new value based on the adjacent cells in time step and the known cell value from previous time step. Implicit solver is unconditionally stable, but small time steps are needed to ensure higher accuracy [Versteeg and Malalasekera, 2007]. The time step needs to be small enough to solve time-dependent features. [Yin, 2016]

The pressure-based solvers (uncoupled solver) use an implicit solver. If an explicit solution wants to be obtained then a density-based solver (coupled solver) needs to be applied. A pressure-based solver is chosen as it was developed for incompressible flows [ANSYS Fluent, 2017]. Gasses are incompressible as long the Mach number is below 0.3 according to high velocities [Munson et al., 2012].

9.2 Algorithms for Pressure and Velocity Coupling

SIMPLE (Semi-Implicit Method for Pressure-Linked Equations) algorithm is a coupling between pressure and velocity. It is used to avoid non-physical pressure field. Mathematically the pressure term appears in all the momentum equations. The pressure can be obtained from density and temperature, but if the flow is incompressible, the density is constant and the pressure is not linked to the density. Hence SIMPLE algorithm makes it possible to calculate the pressure in a new way by using a staggered grid combined with a guess and correction procedure. In the staggered grid the pressure, temperature etc. are calculated from the nodal points but the velocity components are calculated from the cell faces. [Versteeg and Malalasekera, 2007]

Other variations of SIMPLE such as SIMPLEC (SIMPLE Consistent) and PISO (Pressure Implicit with Splitting of Operators) can reduce the computational effort due to improved convergence. They result in a faster convergence which reportedly reduces the computer time by 30-50 %. The faster convergence is a result of the larger under relaxations factors that can be used. [Versteeg and Malalasekera, 2007]

The advantage of the different models depends on the flow conditions. The convergence will lead to the same solution, but the different algorithm may result in different stability and speed. PISO and SIMPLEC are useful for meshes with some degree of skewness, as the option of using a skewness correction is available. The skewness correction reduces convergence difficulties associated with mesh with high skewness. [ANSYS Fluent, 2017][CFD Online, 2017a]

SIMPLE, SIMPLEC and PISO all use the pressure-based segregated method, which is best suited for incompressible flow. In the segregated method an equation of a certain variable is solved for all cells in the domain, before the next variable is solved. Another possibility is coupled where all variables are solved for the given cell before the next cell is solved. [André Bakker, 2008]

To calculate the scalar at the cell faces and computing the gradients of the scalar ϕ Least Squared Cell Based Method is used. Another method, Gauss theorem, could be used for the same purpose. However the least squared cell based method has a higher accuracy for skewed unstructured meshes. [ANSYS Fluent, 2017]

9.3 Computational Grid

A computational grid, also called a mesh, must be developed in order to apply the Finite Volume Method. The function of a computation grid is to discretize an area or a volume into numerous cells on which numerical calculations can be conducted. [Versteeg and Malalasekera, 2007]

A good mesh is crucial in order to obtain high accuracy and reduce the computational time. The number of cells influences on the computational time. [Nielsen et al., 2007]

The cell quality can be defined by different characteristic terms describing the shape of the cell and scale ratio. The most used characteristics are:

- Orthogonal quality. The orthogonal quality describes the relationship between the cell centroid and the faces according to the adjacent cells. The best cells will approach an orthogonal quality of 1.0 and the worst will approach 0.0. [ANSYS Fluent, 2017]
- Aspect ratio. The aspect ratio describes the stretching of the cell, in terms of the ratio between the height and the width. The aspect ratio for a cell with identical sides is 1.0. Extreme aspect ratios may affect the accuracy. [ANSYS Fluent, 2017]
- Skewness. Skewness describes the difference between the shape of a equilateral cell and the shape of the cell. The maximum skewness should be below 0.95, and the average skewness significantly lower. [ANSYS Fluent, 2017]

A high resolution of cells is necessary in areas with relevant flow phenomena, such as inlet, heat sources, emission sources and boundary layers.

There are different types of grid systems. A quadrilateral mesh has the highest accuracy due to the alignment but a triangular mesh is preferable when constructing complex geometries [Versteeg and Malalasekera, 2007]. Different elements types are illustrated in Figure 9.1.

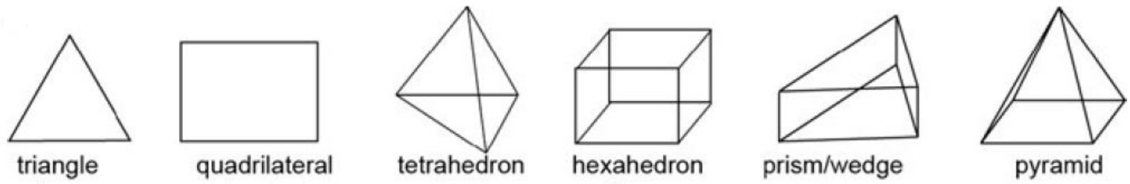

Figure 9.1. Different types of 2D and 3D elements [Tu et al., 2013].

A mesh independence test, also referred as grid convergence test, needs to be conducted in order to ensure that the mesh does not have an impact on the results. A mesh independence test determines the final amount of cells in the mesh whose results are independent of the mesh structure, while simultaneously containing as few cells as possible to reduce the computational power. [Nielsen et al., 2007]

9.4 Turbulence Models

Turbulent flow is a flow regime in fluid dynamics, which occurs with high Reynolds numbers. The Reynolds number is a dimensionless number which is defined as the ratio of the inertia forces to viscous forces. Turbulence is characterized by a chaotic flow with eddies. The turbulence creates a shear stress, as the randomly moving finite-sized fluid particles exchange momentum between each together. [Munson et al., 2012]

A turbulence model must be employed in order to be able to model the unknown shear stresses that act on the fluid. To model the turbulent flows characteristics, the Reynolds-

Averaged Navier Stokes (RANS) model can be applied. Other models such as Large Eddy Simulations (LES) and Direct Numerical Simulation (DNS) can also be used. LES and DES calculate movement of eddies and the influence of turbulence more accurately, but they have every strict demands for the mesh density and they are more expensive to simulate. The RANS models implement eddies into a mean flow by calculating the dominating effect from eddies. The RANS model is based on Equation 9.3. [Nielsen et al., 2007]

$$\Phi(t) = \overline{\Phi} + \Phi'(t) \tag{9.3}$$

Where

$\Phi(t)$	Instantaneous flow variable
$\overline{\Phi}$	Variable average
$\Phi'(t)$	Variable fluctuation

The expression of the instantaneous flow variable can be substituted into the transport equations and the continuity equation. From the substitution six new terms will occur for a three dimensional case: $\rho\overline{v'u'}$, $\rho\overline{v'w'}$ $\rho\overline{u'w'}$, $\rho\overline{u'u'}$, $\rho\overline{v'v'}$, $\rho\overline{w'w'}$.
The fluctuating variables, $\rho\overline{U_i'U_j'}$, are defined as the turbulence stresses. These stresses must be modelled for the system of equations to be solved. [Nielsen et al., 2007]

Turbulence stresses can be modelled from a turbulence viscosity. This analogy is referred as Boussinesq hypothesis. Boussinesq hypothesis for incompressible flow is shown in Equation 9.4. [CFD Online, 2017b]

$$\tau_{t.ij} = \rho\overline{U_i'U_j'} = \mu_t\left(\frac{\partial U_i}{\partial x_j} + \frac{\partial U_j}{\partial x_i}\right) \tag{9.4}$$

Where

$\tau_{t.ij}$	Molecular stresses [N/m^2]
$\rho\overline{U_i'U_j'}$	Turbulence stresses [N/m^2]
μ_t	Turbulence viscosity [N s/m^2]
$\frac{\partial U_i}{\partial x_j}, \frac{\partial U_j}{\partial x_i}$	The gradients of instantaneous velocity [1/s]

Boussinesq hypothesis makes it possible to calculate all the turbulence stresses from the instantaneous velocities which already are known from the momentum equations and the turbulence viscosity, thus reducing the numbers of equations to solve the problem. The turbulence viscosity can be calculated in different ways. For instance the Spalart-Allmaras model uses one transport equation to calculate the turbulence viscosity, where the k-ε model and the k-ω model uses two transport equations to solve the turbulence viscosity [Versteeg and Malalasekera, 2007]. The most commonly used turbulence models are the Standard k-ε model, RNG k-ϵ model, Realizable k-ϵ model and SST k-ω model. [Versteeg and Malalasekera, 2007] [Nielsen et al., 2007]

In general, the suitability of the different models are strongly dependent on their application [Nielsen et al., 2007].

Standard k-ε Model

The k-ε model uses the turbulent kinetic energy, k, and the dissipation rate, ε, to calculate turbulence viscosity. The kinetic energy [m^2/s^2] and the dissipation rate [$m^2/s^2/s$] is calculated from each transport equation. The dissipation rate is a physical variable. It describes the amount of kinetic energy which is transformed into internal energy per unit time. When applying the k-ε model the turbulent viscosity is calculated by Equation 9.5.

$$\mu_t = c_\mu \rho \frac{k^2}{\varepsilon} \tag{9.5}$$

Where c_μ is a constant. Larger velocity gradients result in larger k and ε values [Yin, 2016]. The standard k-ε model have a robust accuracy for a wide range of flow, but it is also overly diffusive for many situations and have a non-physical production of kinetic energy in regions of large strain rate, such as stagnations points. In addition it has an inaccurate prediction of the spreading rate from round jet. [Yin, 2016]

RNG k-ϵ Model

RNG k-ϵ model is an improved turbulence model of the standard k-ϵ model. It is adjusted by adding an extra term in the transport equation to calculate kinetic energy. The RNG k-ϵ model is better of handling high velocity gradients, regions with large strain rate and flows with streamline curvature. [Yin, 2016]

Realizable k-ϵ Model

The realizable k-ϵ model includes other modifications on the standard k-ϵ model, which improve the turbulent model. The transport equation for the kinetic energy is the same as the standard k-ϵ model, but a new formulation of μ_t and ϵ have been conducted. The realizable k-ϵ model is also better at handling high velocity gradients, regions with large strain rate and flows with streamline curvature. In addition the realizable k-ϵ model may be easier to converge and more accurate than RNG k-ϵ model. [Yin, 2016]

A common feature for the all the k-ε models is that they must be modified for near-wall regions. The wall treatment for k-ϵ models will be described in Section 9.5. [Yin, 2016]

SST k-ω Model

The SST k-ω model is a combination of k-ω model and the realizable k-ϵ model, where it calculates the dissipation rate from the kinetic energy and the turbulence frequency, ω. The k-ω model can be used in the near wall region without modification, but is overly sensitive to the initial input of the inlet [Yin, 2016]. Resolving the near wall region is important to estimate the pressure drop. [Tu et al., 2013]

9.4.1 Turbulence Modelling of Inlet

At the boundary inlet the turbulent kinetic energy and the dissipation rate are calculated from the turbulence intensity. The turbulence intensity, I, is an important parameter for turbulence modelling. The turbulence intensity should for internal flows be between 3% and 10%. Lower Reynolds Numbers result in a lower intensity value. The kinetic energy at the inlet is calculated from Equation 9.6. [Tu et al., 2013]

$$k_{inlet} = \frac{3}{2}(u_{inlet} I)^2 \tag{9.6}$$

Where

k_{inlet}	Turbulent kinetic energy at the inlet [m^2/s^2]
u_{inlet}	Inlet velocity [m/s]

The dissipation rate at the inlet is calculated from Equation 9.7 [Tu et al., 2013].

$$\varepsilon_{inlet} = c_\mu^{\frac{3}{4}} \frac{k_{inlet}^{\frac{3}{2}}}{c_\mu^{\frac{1}{4}} D} \tag{9.7}$$

Where

ε_{inlet}	Dissipation rate at the inlet [m^2/s^2/s]
D	Characteristic length scale or hydraulic diameter [m]

9.5 Wall Treatment

The no-slip condition at the wall boundary assumes that the velocity of a fluid is zero due to the wall friction. The wall affects the fluid with a shear force which reduces the velocity of the flow at the wall. Numerically this is implemented by calculating the properties in the first grid node from the wall boundary using additional formulae. [Yin, 2016]
Simulation of the fluid close to the wall can be conducted by different wall treatment. The type of formula required for calculation of the fluid flow depends on the Reynolds number and is represented by the dimensionless quantity y^+. y^+ can be calculated by Equation 9.8. [Versteeg and Malalasekera, 2007]

$$y^+ = \frac{y_p \cdot \rho}{\mu} \sqrt{\frac{\tau_w}{\rho}} \tag{9.8}$$

Where

μ	Dynamic viscosity of the fluid [N s/m^2]
y_p	Distance from the node to the wall [m]
τ_w	Shear stress at the node [N/m^2]

The fluid closest to the wall is dominated by viscous effects up to a distance of $y^+ <$ 5 where there are no eddying motions. Outside the vicious sublayer the vicious shear force will decrease and the turbulent shear force will increase [Versteeg and Malalasekera, 2007]. The kinetic energy is very low in the viscous sub-layer as there is a high destruction of kinetic energy [Yin, 2016]. There are different wall treatment models that can be applied in order to calculate effect from the wall shear force.

The standard wall function does not resolve the viscous affected region. The dissipation rate will in the first node not be calculated from the transport equation but from an equation based on the wall shear stress. The first grid point should be within $30 < y^+ <$ 500, also referred as the log-law region. [Yin, 2016]

The enhanced wall treatment resolves the viscous effect at the boundary as the k-ω model does. Thus the mesh requires a very dense mesh at the boundary layer. The y^+ need to be below 1 when applying the enhanced wall treatment. The aspect ratio of the mesh should not be too high as there should be at least ten grid point within 0-60 y^+. [Yin, 2016]

10 Introduction to Particle Dynamics

In Chapter 9 the method to determine fluid flow, also known as the continuous phase, was described. For this study particle trajectory motion is identified by the application of discrete phase modelling using the Euler-Lagrange approach. In addition to solving transport equations for the continuous phase, Fluent allows the simulation of a discrete second phase in a Lagrangian frame of reference. This second phase consists of spherical particles dispersed in the continuous phase. [ANSYS Fluent, 2017]

The two methods used when modelling air flow and particle transport in CFD simulations are the Eulerian and the Lagrangian approach. The Eulerian approach is based on the field concept in which parameters are known at specific locations in the flow. Air flow is commonly governed by Eulerian conservation equations, as it is regarded as one continuous fluid. The Lagrangian approach follows the individual particle as it moves through time and space.

Lagrangian approach is preferable for tracking the particles in the airways, as Lagrangian approach can determine the individual particles deposition sites more precisely [Tu et al., 2013]. Lagrangian approach splits the particle phase into a representative set of individual particles, which it then tracks separately through the flow domain by solving the equations of particle movement. [ANSYS Fluent, 2017]

The velocity and position of the particles can be found by stepwise time integration of the equation of particle motion as seen in Equation 10.2, where the acceleration is determined.

10.1 Equations of Particle Motion

The equations of particle motion for the individual particle come from Newton's second law, as seen in Equation 10.1. [Zhao et al., 2004]

$$\overrightarrow{F} = \frac{d\overrightarrow{u}_p}{dt} \tag{10.1}$$

Where

$\overrightarrow{F}$	External forces acting on the particle [m/s^2]
$\overrightarrow{u}_p$	Particle velocity [m/s]

The external forces working on the individual particles can be expressed by the following:

- Drag force
- Gravitational force
- Additional forces

The majority of the forces acting on the particle stem from the drag force and the gravitational force. Furthermore, not all additional forces are relevant, depending on the physical properties of the particle and the flow conditions. [Zhao et al., 2004]

The two main forces acting on the particle, the drag force and gravitational force, can be seen illustrated in Figure 10.1. [Zhao et al., 2004]

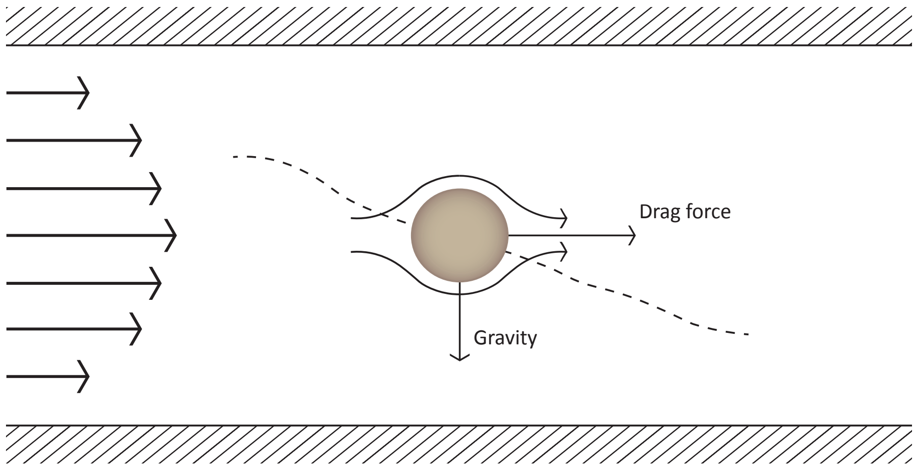

Figure 10.1. The two main external forces that affect particle motion in air flow [Tu et al., 2013][Ed.].

The external forces that act on the particle can be expressed by Equation 10.2. [Zhao et al., 2004]

$$\vec{F} = \frac{\vec{u} - \vec{u}_p}{\tau_r} + \vec{g}\left(1 - \frac{\rho}{\rho_p}\right) + \vec{F}_a \tag{10.2}$$

Where

$\vec{u}$	Fluid velocity [m/s]
τ_r	Relaxation time of the particle [s]
$\vec{g}$	Gravitational acceleration [m/s^2]
ρ	Fluid density [kg/m^3]
ρ_p	Particle density [kg/m^3]
$\vec{F}_a$	Additional forces [m/s^2]

The drag force per unit is expressed by the first term in the equation. The relaxation time is calculated by Equation 10.3. [Zhao et al., 2004]

$$\tau_r = \frac{\rho_p d_p^2}{18\mu} \frac{24}{C_D Re_p} \tag{10.3}$$

Where

d_p	Particle diameter [m]
μ	Dynamic viscosity of the fluid[kg/ms]
C_D	Drag coefficient [-]
Re_p	Particle Reynolds number [-]

The relaxation time is the time required for a particle to adjust its velocity to a new condition of forces.

The Particle Reynolds Number, used to find the relaxation time, is calculated by Equation 10.4. [Zhao et al., 2004]

$$Re_p = \rho d_p \frac{\vec{u} - \vec{u}_p}{\mu} \tag{10.4}$$

Through Equation 10.2 and Equation 10.4, the drag force can be calculated. As is evident by the equation for relaxation time, the drag force is particularly sensitive towards the diameter of the particle.

10.1.1 Additional Forces

There is a large number of additional forces that potentially act on the particle, represented by $\vec{F}_a$. These are highly dependent upon the characteristics of both the particle and the fluid in which it is immersed. They include Saffman's lift force, Brownian force, virtual mass force, thermophoretic force, pressure gradient force and Magnus lift force. Not all of the forces are influential, as they depend on the case at hand. [Zhao et al., 2004]

In the following sections, the equations for the additional forces are explained and analysed to determine which given situations they are applicable to.

Brownian Motion Force

The Brownian motion force represents the random motion of the particle. The motion is caused by collision between the suspended particles and the molecules of the surrounding medium. Its components are modelled as a Gaussian white noise process with spectral intensity as calculated by Equation 10.5. [Zhao et al., 2004] [ANSYS Fluent, 2017]

$$S_o = \frac{216\nu k_B T}{\pi^2 \rho d_p^5 (\frac{\rho_p}{\rho})^2 C_c} \tag{10.5}$$

Where

S_o	Spectral intensity [W]
ν	Kinematic viscosity of the fluid [m^2/s]
k_B	Boltzmann constant [J/K]
T	Fluid temperature [K]
C_c	Cunningham correction factor [-]

The spectral intensity is used to find the Brownian motion force by Equation 10.6. [Zhao et al., 2004]

$$\overrightarrow{F}_B = \zeta\sqrt{\frac{\pi S_o}{\Delta t}} \tag{10.6}$$

Where

ζ	Zero-mean, unit-variance-independent Gaussian random numbers [-]
Δt	Time step size [s]

The Brownian force largely depends on the size of the particles. This can be seen in Equation 10.5, where the spectral intensity increases as particle size decreases. Thereby it can be concluded that Brownian force largely occurs for smaller particles.

Furthermore, the Brownian force is influenced by the densities of both the particle and fluid. A low-density particle in a high-density fluid experiences an increase in the force compared to a high-density particle in a low-density fluid.

Saffman's Lift Force

Saffman's lift force can also be expressed as lift due to shear. It is recommended for particles smaller than 1.0 μm [ANSYS Fluent, 2017]. Saffman's lift force is calculated by Equation 10.7. [Zhao et al., 2004]

$$\overrightarrow{F}_{Saff} = \frac{2K\nu^{1/2}\rho d_{ij}}{\rho_p d_p (d_{lk} d_{kl})^{1/4}}(\overrightarrow{u} - \overrightarrow{u}_p) \tag{10.7}$$

Where

K	Constant value of 2.594 [-]
d_{ij}	Deformation tensor [1/s]
ρ_p	Particle density [kg/m^3]

The lift force occurs for low density particles. It increases for a low-velocity particles immersed in a high-velocity fluid. Saffman's lift force potentially becomes the dominant force near the walls, where the velocity gradient is high. [Zhao et al., 2004]

Virtual Mass Force

The virtual mass force pulls the adjacent fluid, as with a ball in water, adding to the effective mass of the particle. [Zhao et al., 2004]

It is calculated by Equation 10.8.

$$\overrightarrow{F}_{vm} = C_{vm}\frac{\rho}{\rho_p}\left(\overrightarrow{u}_p \nabla \overrightarrow{u} - \frac{d\overrightarrow{u}_p}{dt}\right) \tag{10.8}$$

Where

C_{vm}	Virtual mass factor [-]

The virtual mass force is largely dependent on the relationship between the fluid density and the particle density, as it can been seen from Equation 10.8. For this reason it is often neglected in indoor air simulations. [Zhao et al., 2004]

Thermophoretic Force

For particles whose diameters are smaller than the gas mean free path (0.066 μm), the thermophoretic force depends on the temperature gradient in the surrounding gas molecules. [ANSYS Fluent, 2017]

The force is calculated by Equation 10.9. [ANSYS Fluent, 2017]

$$\overrightarrow{F}_{th} = -D_{T,p}\frac{1}{m_p T}\nabla T \tag{10.9}$$

Where

$D_{T,p}$	Thermophoretic coefficient [$\frac{\mathrm{kgm^2}}{\mathrm{s^2}}$]
m_p	Particle mass [kg]

The temperature gradient expresses the direction and rate in which the temperature surrounding the particle changes. The thermophoretic force thereby occurs when there are temperature differences in the surroundings. A higher temperature differences gives a larger force.

Pressure Gradient Force

The pressure gradient force occurs when there is a pressure difference. This causes the particles to distribute until more equal pressure distribution has been reached.

$$\overrightarrow{F}_{PG} = \frac{\rho}{\rho_p}(\overrightarrow{u}_p \nabla \overrightarrow{u}) \tag{10.10}$$

The pressure gradient force is dependent upon the densities and velocities of both the particle and the fluid. As with the virtual mass force, the pressure gradient force can often be neglected for indoor air simulations as the density of the particle is often much higher than the density of the fluid. [Zhao et al., 2004]

Magnus Lift Force

The Magnus lift force occurs when a particle rotates in a fluid. The lift occurs due to a pressure difference across the particle's surface. When the fluid is dragged at a higher rate on one side of the particle, the resultant pressure difference causes the particle to move towards the side with lesser pressure. [Zhao et al., 2004]

Magnus lift force can be calculated by Equation 10.11

$$F_M = \frac{1}{2}\rho A_p C_L \frac{|\overrightarrow{V}|}{|\overrightarrow{\Omega}|}(\overrightarrow{V} \times \overrightarrow{\Omega}) \tag{10.11}$$

Where

A_p	Cross-sectional area of the particle [m^2]
C_L	Coefficient of lift [-]
$\overrightarrow{V}$	Relative fluid - particle velocity [m/s]
$\overrightarrow{\Omega}$	Relative fluid - particle angular velocity [m/s]

The Magnus lift force is dependent on the rotation of the particles. Large velocities from the particle front and from the particle rear increase the force. The force is also increased as the size of the particle increases.

10.2 Turbulent Dispersion of Particles

The turbulent dispersion due to turbulent flow can be modelled using stochastic tracking. The turbulent dispersion can be added to gain a more realistic physical result. [André Bakker, 2008]
The turbulent dispersion is determined by applying the instantaneous fluid velocity in the equation of particle motion seen in Equation 10.1; thus the turbulent fluctuation, u', needs to be calculated. The turbulent fluctuation can be calculated by a discrete random walk model, where the turbulent velocity components are calculated by Equation 10.12. [ANSYS Fluent, 2017]

$$u' = \zeta\sqrt{\frac{2k}{3}} \tag{10.12}$$

Where

ζ	Normally distributed random number [-]
k	Turbulence kinetic energy [m^2/s^2]

In discrete random walk tracking each injection's trajectories are tracked a multiple of times in order to get a statistical sampling. The trajectories are referred as numbers of tries. The stochastic tracking requires a large number of stochastic tries to get a statistically significant sampling. [ANSYS Fluent, 2017]

10.3 Discrete Phase Modelling

The discrete phase can interact with the fluid flow in the exchange of mass, energy and momentum. An exchange between the discrete phase and the fluid flow could for instance occur when the fluid flow creates a drag force on a particle, in turn affecting the fluid flow. [ANSYS Fluent, 2017]

The interaction between particles and fluid is called coupled Discrete Phase Modelling (DPM). The particles interaction on the fluid flow will be given as a DPM source in each cell. This DPM source will be updated after each iteration. In coupled DPM the flow solution and DPM solution should reach convergence. A flow diagram illustrating the calculation process in Fluent is shown in Figure 10.2. [ANSYS Fluent, 2017]

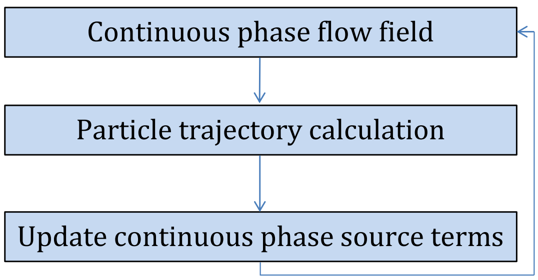

Figure 10.2. Flow diagram of coupled discrete phase calculations [ANSYS Fluent, 2017][Ed.].

In uncoupled DPM the fluid flow will act on the particles but the particles will not act on the fluid flow. This one-way coupling can be used if the discrete phase volume fraction is 10^{-3} or less. [Tu et al., 2013]

Interactions between particles can be neglected when the phase has a low volume fraction, usually less than 10-12%. This make the Euler-Lagrange approach much simpler. The particle-particle interaction can be included using Discrete Element Model (DEM collision model) if necessary. [ANSYS Fluent, 2017]

10.3.1 Boundary Conditions for Discrete Phase Modelling

Once a particle reaches a physical boundary, the resulting trajectory must be determined. This varies depending on the particle and the actual boundary. The types of boundary conditions for the discrete phase model are as follows. [ANSYS Fluent, 2017]

- *Reflection*: The particle rebounds off the boundary with a change in its momentum. It reflects by elastic or inelastic collision.
- *Trap*: The particle is trapped at the surface and its trajectory path is halted.

- *Escape*: The particle 'exits' the control volume at the boundary. Often used at the outlet.

11 Numerical Framework of the Airway Model

In order to determine the size-resolved regional particle deposition within the airways, a CFD simulation is conducted which includes both the continuous phase and the discrete phase. To prepare the simulation the physics regarding the continuous phase and the discrete phase need to be modelled in terms of assumptions for the boundary conditions and the flow properties.

The airway model used for this investigation is based on the 3D printed model as described in Chapter 4. However the geometry of the 3D printed model must be modified in order to enable mesh generation. A description of the modification of the airway model can be found in Appendix J.

A simplified simulation of the trachea has been conducted to get better acquainted with the software Fluent and the physics applied in the software. Further description of purpose of the test case and the conclusions of the investigations can be found in Appendix I.

The lower airway exposure from cooking oil is examined for this study. To simulate a cooking activity it is assessed that the occupant has an activity level of 1.2 METS, equivalent to still-standing activity [CR 1752, 1998]. The activity level of the occupant is an important variable as an increase in the activity level will result in an increase of the breathing rate, which in turn impacts flow conditions in the airways.

The CFD simulations will be conducted as an isothermal case as the inhaled air reaches the human body temperature quickly after it enters the airways. The airflow is assumed to be incompressible, which is acceptable as the Mach number is below 0.3. [Munson et al., 2012]

To calculate the individual particle trajectory the Euler-Lagrange approach is applied. One-way coupling between the discrete phase and the continuous phase is chosen, as the volume fraction is assumed to below 10-12%. The one-way coupling between the discrete phase and the continuous phase is also deemed to be sufficient in Tu et al. [2013] when examining particle exposure in the airways .

The examination of particle exposure will be focused on particles with an aerodynamic diameter between 0.1 μm and 10.0 μm, which covers the three categories of particles size in Section 3.1: ultrafine, accumulation and coarse particles. The mass of one particle with an aerodynamic diameter of 10.0 μm is 1,000,000 times bigger than one particle with an aerodynamic diameter of 0.1 μm.

The occupant is limited to oral breathing as in the measurements, since this is the most critical breathing path in regards to particle exposure. Nasal breathing helps filter particles by both nose hair and mucous and the airway pathway for nasal breathing is longer and more complicated compared to oral breathing as mentioned in Appendix C.

For steady state simulations the inlet at the mouth is defined as velocity inlet and the outlets at the plugs located in the top of the lungs are defined as pressure outlets. The location of the inlet and outlets are illustrated in Figures 11.1 and 11.2.

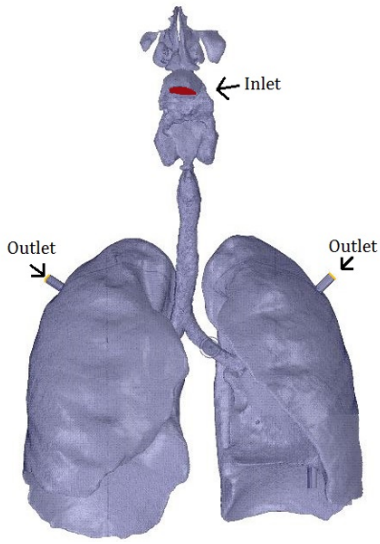

Figure 11.1. Front view of the locations of inlet and outlet in the airway model.

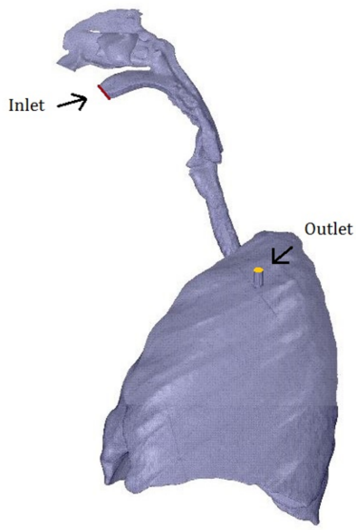

Figure 11.2. Side view of the locations of inlet and outlet in the airway model.

Pressure outlet is applied as the boundary condition at the outlet. Pressure outlet generates the same pressure at the outlets, which is the same condition as during the experimental investigation. In order to compare the CFD simulations with the experimental investigation the boundary conditions need to be similar. The velocity inlet is based on the mean breathing rate of a still-standing human male of 10.65 L/min. A description of modelling of the breathing function can be found in Appendix C.7.

The walls are defined as stationary walls with no-slip condition. In accordance with the discrete phase boundary conditions, the reflection of particles is not considered, as Naseri et al. [2017] states that the probability for reflection is negligible small. Hence the particles will be trapped when they touch the wall. Moisture conditions in the airways may alter the size distribution of the particles in the respiratory tract by hygroscopy, as mentioned in Section 3.3.1, and thereby the deposition of the particles. However the influence of moisture on particle sizes will not included in this study as the chemical composition of the smoke particles and the specific reaction in terms of hygroscopy is unknown.

Further description of the set-up can be found in the Digital Appendix.

11.1 Steady State vs Transient Simulations

The influence of using steady state simulations compared to transient simulations can be determined by calculating the dimensionless Womersley number and the Strouhal number.

The Womersley number expresses the pulsatile flow frequency in relation to viscous effects, while the Strouhal number expresses oscillating flow mechanisms. However the criteria for the Womersley number and the Strouhal number vary for different cases, and in general the criteria are dependent on which part of the respiratory system is investigated [Naseri et al., 2017]. It has not been possible to find research on this topic for a geometry or case similar to the one used in this study.

By comparison with Bahmanzadeh et al. [2016] it is estimated that a transient simulation of the airways will require 160 time steps to conduct a transient simulation of the airways with a breathing cycle of 4 seconds. In Bahmanzadeh et al. [2016] they conducted a transient simulation of the nasal cavity over two breathing cycles. They found it necessary to use a time step of 0.05 s for the sinusoidal breathing function by comparing different solutions with a time step of 0.1 s, 0.05 s and 0.02 s. If a transient simulation is conducted on the airway model a new time step independence test needs to be conducted to determine the number of time steps as the geometry in this study is unique.

The simulations will be conducted as either steady state or transient depending on the computational time of the final mesh because of time constraints. The final mesh is determined by the mesh independence test.

The steady state simulation will result in a numerical error as particle deposition is noticeably affected by the acceleration and deceleration in transient simulations. Steady state simulations tend to give a lower deposition rate compared to transient simulations [Naseri et al., 2017].

Depending on whether the investigation will be based on a steady state simulation or a transient simulation. The SIMPLEC Algorithm will be used to solve the pressure linked equations, if the simulation is conducted as steady state. The PISO Algorithm will be used in case a transient simulation is conducted as PISO is highly recommended for transient flow calculations. [ANSYS Fluent, 2017]

11.2 Modelling of Turbulent Behaviour

The airflow in the airways may be characterised as laminar, transitional or turbulent due to the variations of the geometry in the airway. A calculation of the Reynolds number in the trachea shows that the Reynolds number is approximately 900, which indicates that the flow is laminar. The calculation is based on an airflow of 10.65 L/min. The calculation can be found in the Digital Appendix.

However the highly irregular geometry in the airways may disturb the fluid streamlines of laminar flow and eventually lead to a chaotic motion, which is characteristic of turbulent flows. [Tu et al., 2013]

A turbulent model will thereby still be used to model the turbulent behaviour. A turbulent flow compared to a laminar flow is more chaotic with a higher level of mixing, which leads to a higher momentum and heat transfer in turbulent flow. The velocity profiles also tend to be more flat than parabolic, as they are for laminar flow. [Tu et al., 2013]

In Tu et al. [2013], it is recommended to use Low Reynolds Number Models such as Low-

Reynolds k-ε and Low-Reynolds k-ω. These turbulence models can model the physics of transitional flow and they have "shown to provide improvements over the standard RANS models". [Tu et al., 2013]

They are also widely used in other papers to simulate the airflow in the airways [Rahimi-Gorji et al., 2016][Choi et al., 2009][Qi et al., 2017]. However, they need to be used with caution as they only estimate the impact of transitional flows. LES and DES will resolve the transitional behaviour but are too computationally expensive. [Tu et al., 2013]

The Low-Reynolds k-ω model is not recommended to use in ANSYS Fluent [2017] as they are not "widely calibrated", and it is not possible to use the Low-Reynolds k-ε model in the applied CFD software Fluent.

Therefore a standard RANS model will be used for this study, even though it is intended for fully developed turbulent flow [Tu et al., 2013]. The Realisable k-ϵ model will be used to calculate the influence of turbulence, as it could help ease convergence and provide more accurate results compared to other k-ϵ models. The k-ω model is not used as it overly sensitive to the initial input of the inlet, as described in Section 9.4.

11.3 Near-Wall Treatment

The near-wall region has a big impact on the airflow in the airways, especially at the narrow air passages in the bronchioles. The enhanced wall treatment will be used to resolve the viscous-affected area near the wall in order to increase the accuracy along the boundaries. This will thereby increase the computational demands as the use of enhanced wall treatment will result in an increased number of cells. To apply enhanced wall treatment it is necessary to have a fine mesh near the boundaries, where the first cell should uphold $y^+ < 1$, as described in Section 9.4.

11.4 Convergence Criteria

The convergence criteria are the same as mentioned in Appendix I, where the following scenarios should be satisfied. [Versteeg and Malalasekera, 2007]

- The continuity, momentum and k-epsilon residuals needs to be below 10^{-3}.
- The residuals should not fluctuate.
- The overall mass balance is obtained with an error of maximum 0.1%.

In addition to the residuals, the velocity magnitude of a cross section of the lung volume and the bronchi and a cross section of the trachea and the larynx will be integrated and calculated for every tenth iteration. The locations of the cross sections are shown in Figure 11.3.

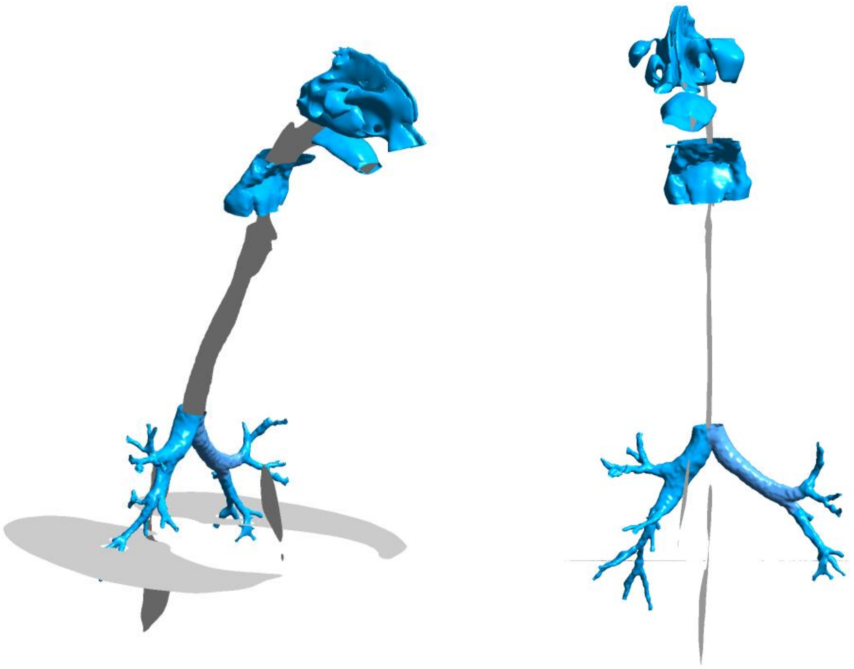

Figure 11.3. Location of the two cross sections used as a tool to determine if the simulation is converged.

12 Meshing of the Airway Model

The mesh of the airway model is conducted by using a hybrid mesh based on prism and tetrahedral cells. The prism elements are located at the boundary as prism cells are useful for resolving near-wall gradients. The tetrahedral elements are used to fill the remaining volume as they are useful for complex geometries. [ANSYS Fluent, 2017]

A hybrid mesh should in general lead to better convergence and a more accurate solution. [Tu et al., 2013]

Tetrahedrals do not stretch or bend during local refinement, leading to very small cells, hence making the refinement ineffective in resolving wall boundary gradients. Additionally the alignment of the tetrahedral elements leads to errors. [ANSYS Fluent, 2017]

The mesh is constructed in the software ICEM, where the process used to generate the mesh is shown in Figure 12.1.

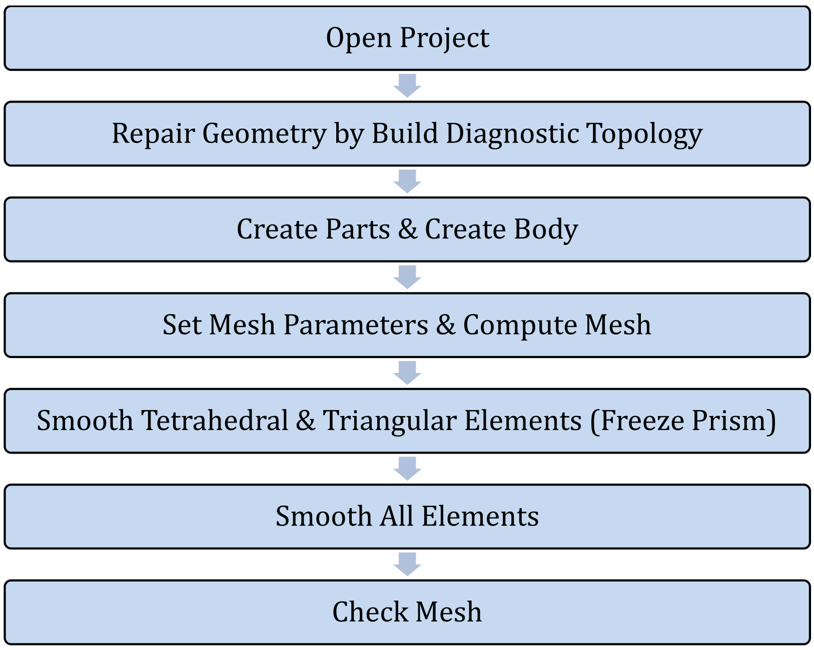

Figure 12.1. The applied process for meshing the airways with prism and tetrahedral elements.

The Octree approach is applied to generate the tetrahedral elements as it is a powerful smoothing algorithm, which provides good element quality. [ANSYS Fluent, 2017]

The prism layers are computed at the same time as the tetrahedral elements. Other methods to generate the prism such as the pre-inflation method and post-inflation method, where the prism layer is generated based on a valid surface mesh or volume mesh could have been used. These different methods have been tested; however, they show no major advantages in regards to generation of the prism layers.

According to the mesh quality, the maximum skewness should be below 0.95 and it is aimed to keep a high average orthogonal quality, a low average aspect ratio and a low average skewness as mentioned in Section 9.3.

In Appendix K, a description of the structural concept of the mesh used in this study can be found. This entails local refinement in terms of the complex geometry of the airways.

To highlight the structure of the mesh, Figures 12.2 and 12.3 shows the mesh at the bottom part of the trachea and Figures 12.4 and 12.5 shows the mesh of the right lung. It can be seen on the figures that the grid increases smoothly from the boundaries.

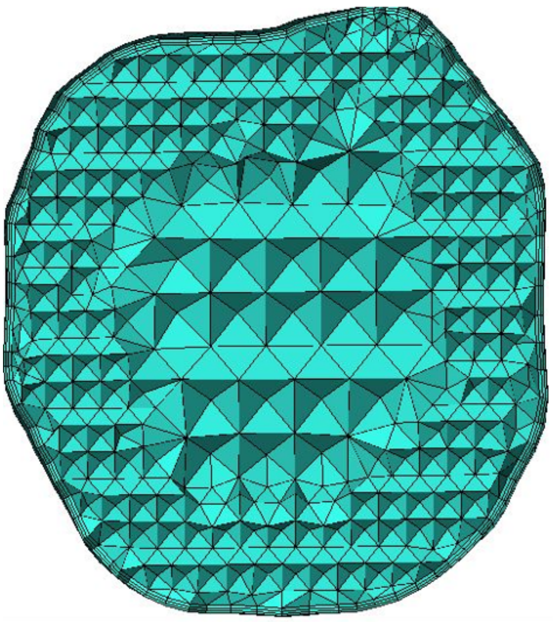

Figure 12.2. The structure of the mesh in the trachea.

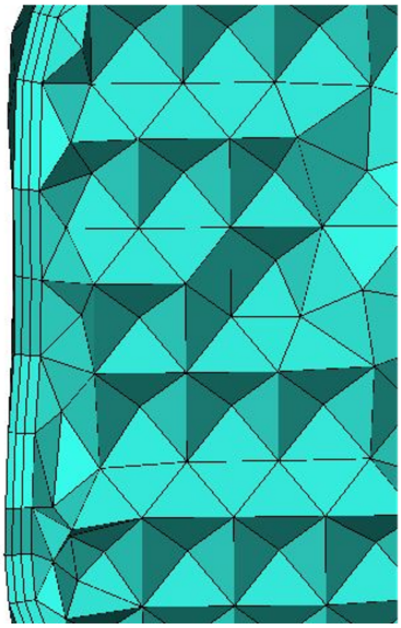

Figure 12.3. The structure of the mesh of the trachea at the boundary.

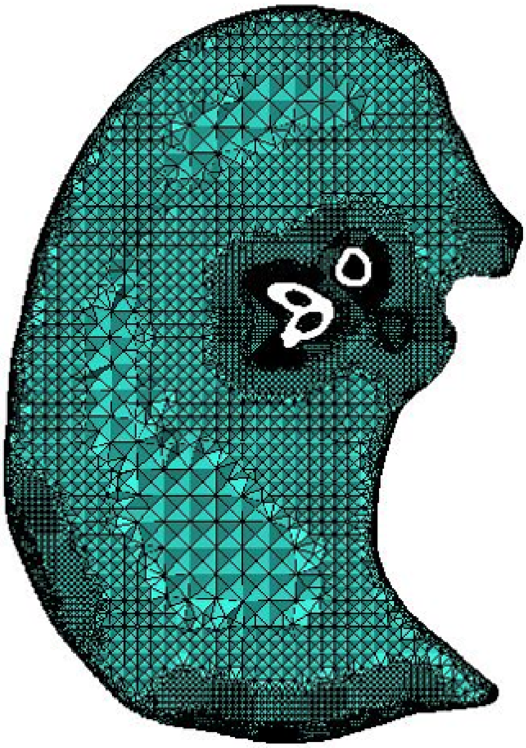

Figure 12.4. The structure of the mesh in the right lung.

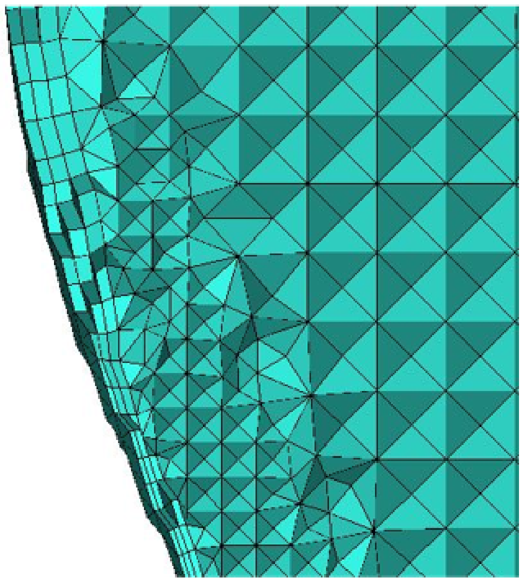

Figure 12.5. The structure of the mesh of the right lung at the boundary.

In Section K.2 the mesh parameters for each part are listed in Table K.2. The mesh parameters are choose wisely to construct a mesh which meet the requirements for the mesh quality and the y^+ value at the boundaries. The table contains information about the initial height of the prism, the maximum size at the surface and the choice of modelling the surface with a prism layer or tetrahedral elements.

It has been investigated if a floating prism layer could improve the mesh quality instead of applying tetrahedral elements in the critical regions of the mesh. Floating prism layers should give a smooth transition between the elements [ANSYS Fluent, 2017]. However it did not improve mesh quality for this case. Mesh reports can be found in the Digital Appendix.

Elements with a mesh quality lower than 0.20 occur at the regions of the airway where there is a big curvature; for instance at some part of the lung shell and at the end of the bronchioles. Figure 12.6 shows the geometry of airway model and the location of the elements with a mesh quality lower than 0.20.

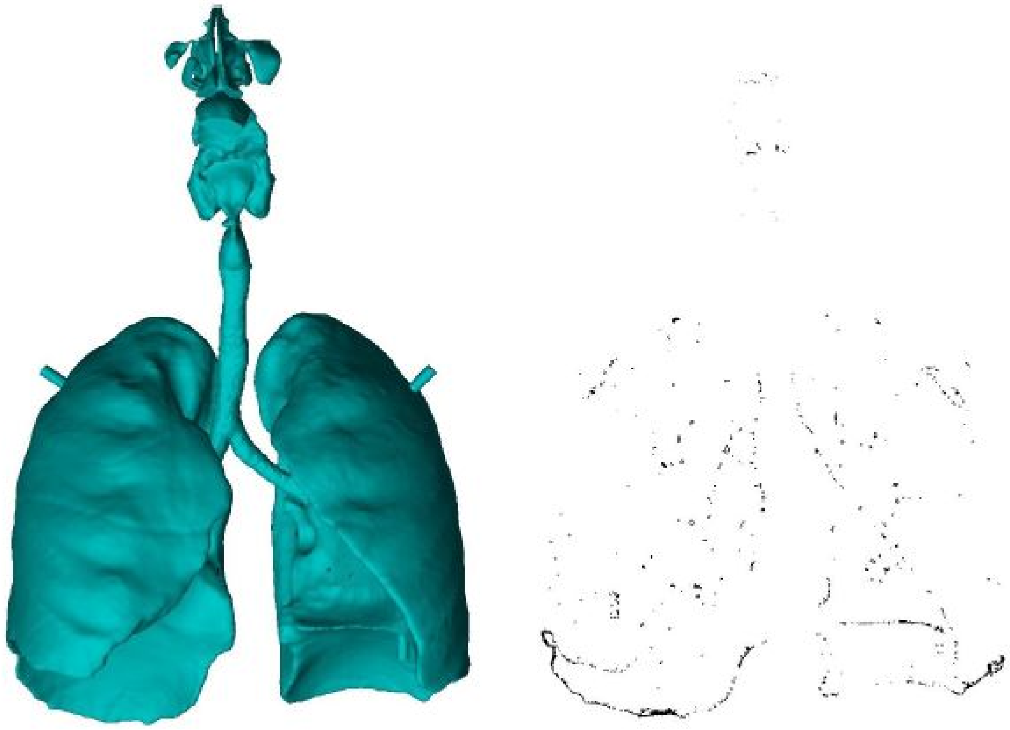

Figure 12.6. Geometry of the airway model and the location of elements with a mesh quality below 0.20.

The mesh seems to be sufficiently ready to initiate a mesh independence test, as it is only 0.0068% of the total numbers of element, which has a quality below 0.2.

A contour plot of the y^+ can be seen in Figure 12.7. Additional contour plots of the y^+ can be seen in the Digital Appendix.

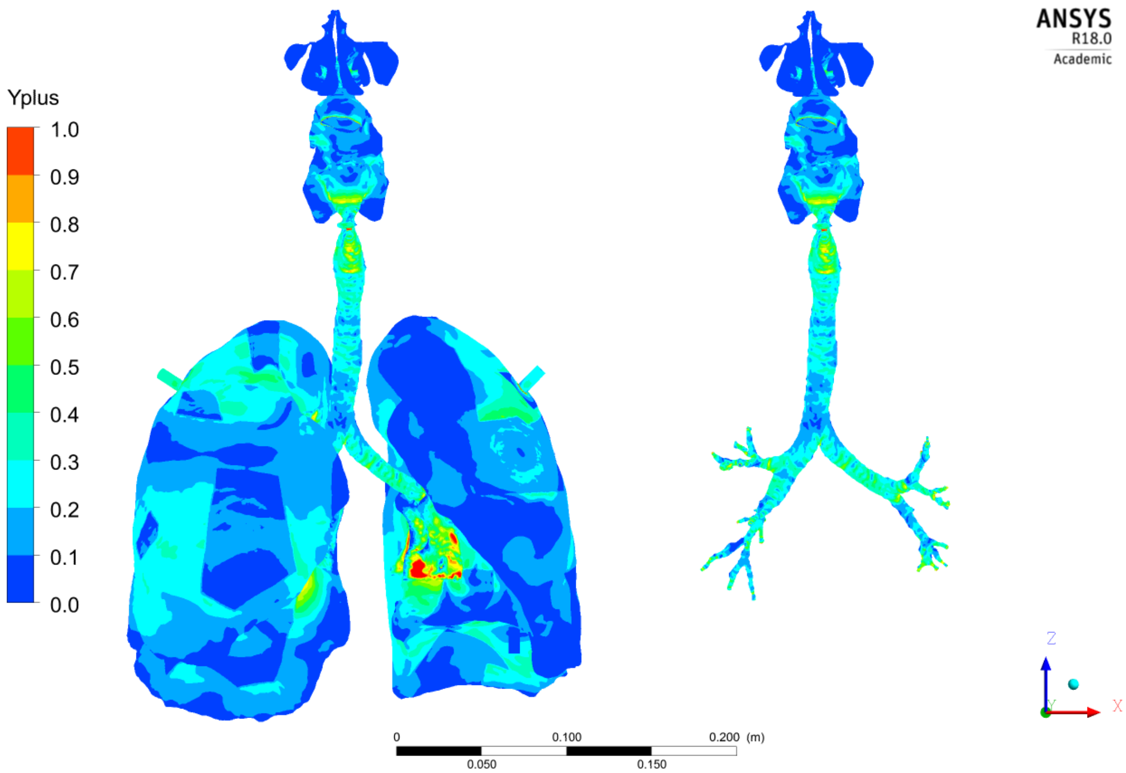

Figure 12.7. Contour map of the y^+ values at the wall boundary of the airway model.

12.1 Mesh Independence Test

The total numbers of cell used in the final mesh is determined by performing a mesh independence test. The mesh is refined progressively until the tolerance of the surface integral is below 1.0%. A similar procedure has been used in Qi et al. [2017].

The different meshes are compared by examining the maximum velocity in different planes in the airway. The planes cover the whole airway as illustrated in Figure 12.8. Further visualizations of the locations can be found in the Digital Appendix.

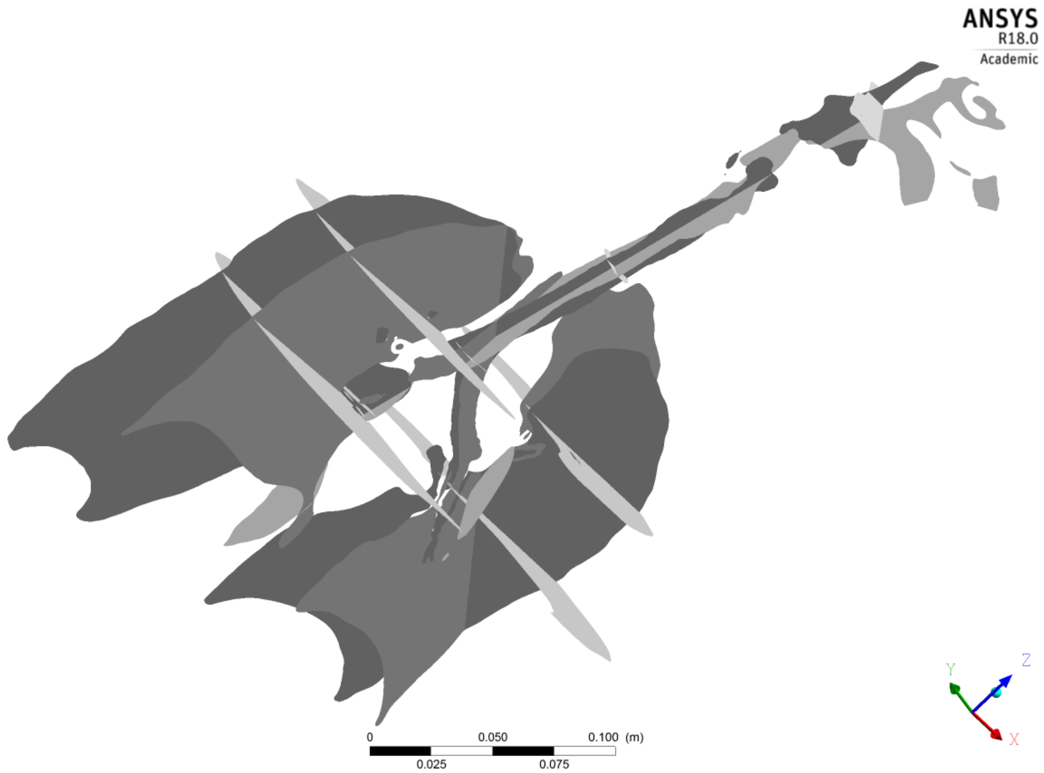

Figure 12.8. Locations of the different planes used to determine the total number of cells in the mesh.

The meshes are generated by scaling the baseline mesh, where the maximum size of all the parts is increased by a factor of 1.30 or decreased by a factor of 1/1.30. An overview of the number of elements and the scale factor can be found in Table 12.1. Mesh settings for each mesh and documentation of convergence can be found in the Digital Appendix.

Table 12.1. Scale factor and numbers of cells for the conducted mesh independence test. * In order to reduce the number of elements a local refinement has been made in certain parts of the mesh, as the mesh extended 40 million elements if the global refinement was conducted.

Scale factor	Numbers of cells
0.592*	31,822,039
0.769	20,132,793
1.000	18,920,484
1.300	16,210,451
1.690	9,815,654

Based on the conducted analysis of the comparison of velocity magnitudes in the planes, the mesh with 20,132,793 elements is determined to be mesh independent. The percentage difference between the surfaces integrals of the different mesh sizes can be found in Table 12.2.

Table 12.2. Percentage difference between the surfaces integrals of the different mesh sizes.

Plane coverage	**31822039-20132793**	**20132793-18920484**	**18920484-16210451**	**16210451-9815654**
Lung, Bronchi	-0.1%	0.2%	**1.4%**	-0.1%
Oropharynx	-0.2%	0.2%	0.0%	0.6%
Trachea, Larynx, Lung	-0.2%	0.6%	-0.4%	0.4%
Trachea	0.0%	-0.1%	0.1%	0.0%
Trachea, Bronchi, Lung	-0.4%	0.6%	0.6%	0.0%
Lower Part of Lung	0.6%	0.0%	0.8%	**1.2%**
Upper Part of Lung	-0.1%	**1.3%**	0.5%	**1.3%**

Conducting a mesh independence test based on a comparison of the different velocity profiles, which was done for the test case in Appendix I, is not deemed to satisfying for this case due to the complexity of the geometry and the flow. However the velocity profiles are used to visualize the different solution and to gain a better understanding of the influence of the refinement. A velocity profile of one of the bronchioles is shown in Figure 12.9.

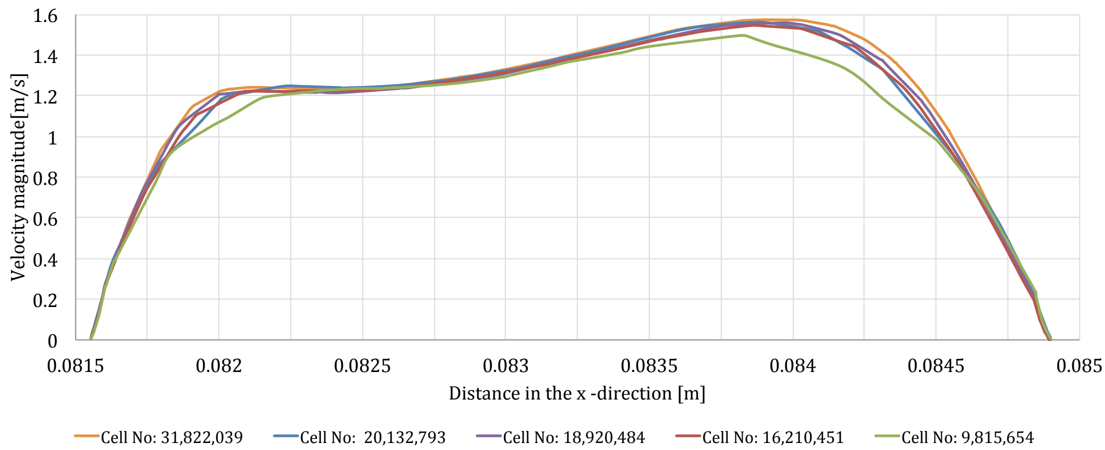

Figure 12.9. Velocity profiles of the different meshes at one of the bronchioles.

The velocity profiles show little variation in the maximum velocity between the mesh with 16,210,451 cells and the mesh with 31,822,039 cells. Hence the mesh with 20,132,793 elements is deemed to be acceptable. Velocity profiles of various locations in the airway can be found in the Digital Appendix.

The computational time to reach convergence is compared for the two different solutions with 20,132,793 cells and 31,822,039 cells. This is approximately 58 hours and 94 hours respectively on a PC workstation with 64 GB of ram, 6 Cores and 3.50 GHz CPU's. The solutions reached convergence after approximately 15,000 iterations.

It has been attempted to decrease the computational time by applying different methods. The computational time is related to the complexity of the model, number of elements and the quality of the mesh.

The number of elements has been attempted to be decreased by using the scalable wall treatment where refinement at the boundaries could be avoided. Increasing the initial height of the prism layer resulted in a decreased mesh quality, where low under-relaxations factors must be applied to obtain convergence.

Few papers describe the procedure for generation of the mesh of the airways, but they do not describe how they generated a high quality mesh with a low number of elements. In addition to this their geometry differs from this study as they do not include the enclosed lung volume.

The mesh quality is attempted to be improved by adjusting the Curvature Based Refinement, which is an automatic local refinement at the curves in ICEM, but it did not have a positive effect.

Later adjustments with local refinements of the mesh parameters could be applied to reduce the numbers of cells further. However it seems to be limited how much the numbers of elements can be reduced as the number of elements are mainly dependent on the refinement in the lung volume, where most of the elements are located.

Hence a steady state simulation will be conducted due to time restraints on the computational time for this study.

13 Post-Processing of Simulation Results

A steady state simulation is conducted for this study due to restraints set on the computational time. A mesh quality report, documentation for convergence and a detailed set-up description can be found in the Digital Appendix.

13.1 Continuous Phase of the Airway Model

The particle trajectories are dependent on the continuous flow within the airways. Figure 13.1 shows the velocity magnitude at the cross section of the mouth, nasal cavity, pharynx and larynx. Additional contour plots of the cross sections can be found in the Digital Appendix.

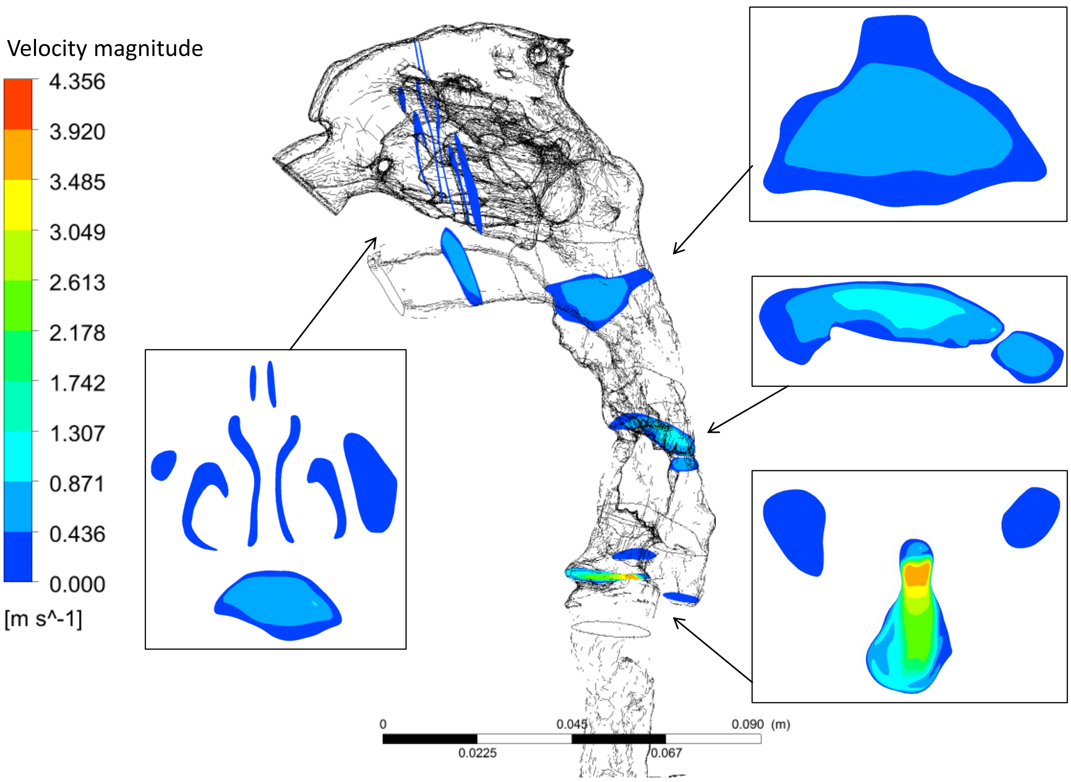

Figure 13.1. The velocity magnitude at the cross sections of the mouth, pharynx, nasal cavity, larynx and the bottom part of the larynx.

Figure 13.1 shows that the velocity magnitude varies in relation to the diameter of the airway. The velocity magnitude in the nasal cavity is almost 0.0 m/s as there is no nasal inhalation or exhalation. The velocity magnitude is highest in the larynx, which generates a jet due to its narrow air passage. The laryngeal jet is also visualized in Figure 13.2 where a big acceleration and deceleration occur.

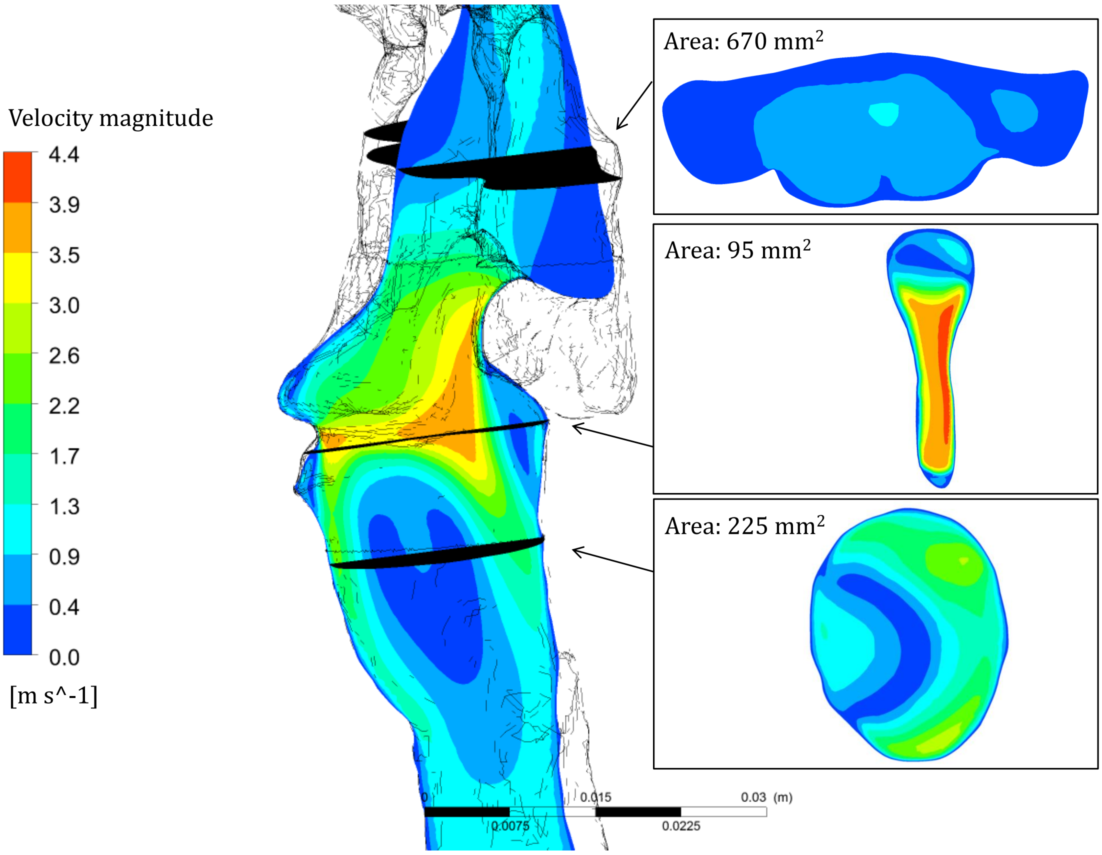

Figure 13.2. The velocity magnitudes in the larynx.

The laryngeal jet is known to be highly sensitive to the upper airway geometry and has a dominant feature in the airway flow, as mentioned in Section K.1. [Choi et al., 2009]

The flow within the lung shells are dominated by the bronchioles' outlets, which launch air into the lung volume as visualized in Figure 13.3.

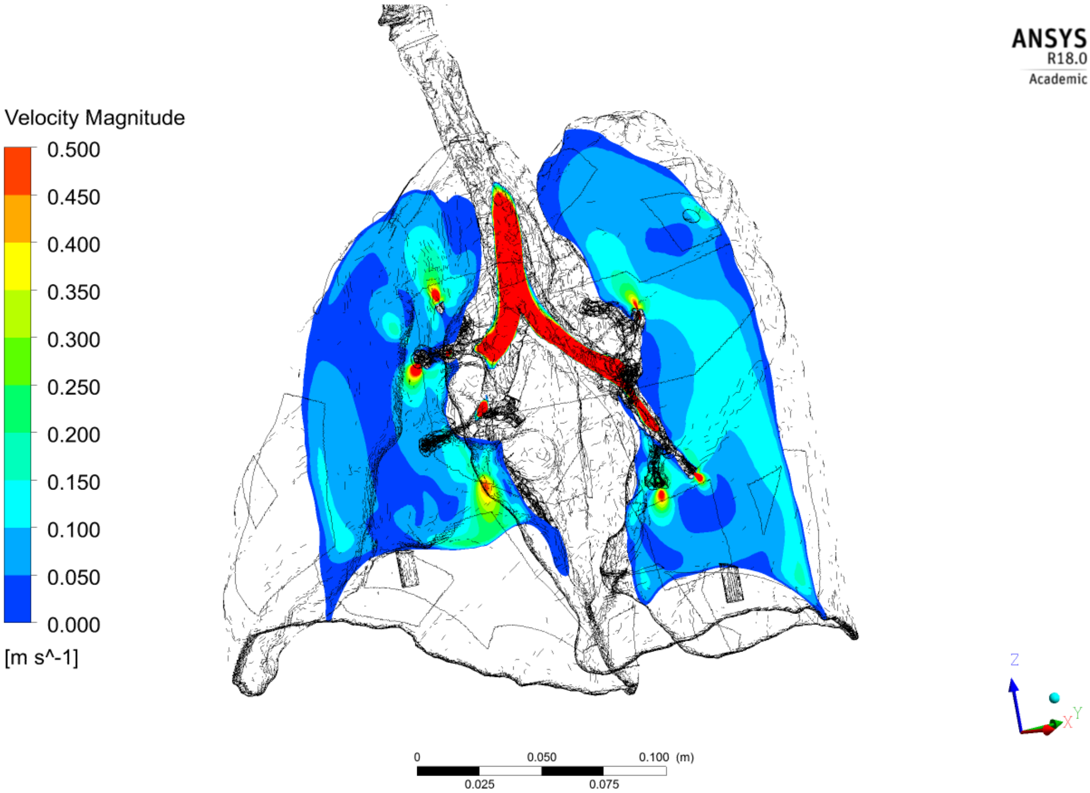

Figure 13.3. The velocity magnitudes in the lung volume.

Due to the pressure distribution, 44% of the total mass flow is exhausted at the right lung and 56% of the total mass flow is exhausted in the left lung. The distribution of the mass flow for each bronchiole is shown in Figure 13.4.

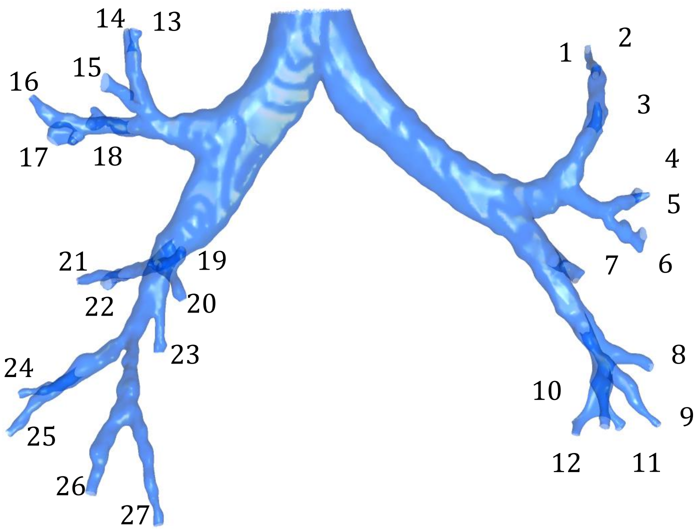

Mass flow rate distribution			
B1:	3.37%	**B15:**	6.64%
B2:	3.20%	**B16:**	2.57%
B3:	2.28%	**B17:**	6.24%
B4:	3.77%	**B18:**	3.38%
B5:	1.65%	**B19:**	1.73%
B6:	6.76%	**B20:**	2.71%
B7:	4.35%	**B21:**	2.70%
B8:	3.24%	**B22:**	7.60%
B9:	2.13%	**B23:**	4.96%
B10:	7.16%	**B24:**	2.39%
B11:	1.85%	**B25:**	2.98%
B12:	3.55%	**B26:**	5.13%
B13:	3.13%	**B27:**	2.46%
B14:	2.09%		

Figure 13.4. The distribution of the mass flow for each bronchiole in the airway model.

13.2 Discrete Phase of the Airway Model

To examine the particle trajectories in the airways, 193,080 particles are tracked by the Lagrangian approach. The fraction between the trapped, escaped and uncompleted particles can be seen in Figure 13.5.

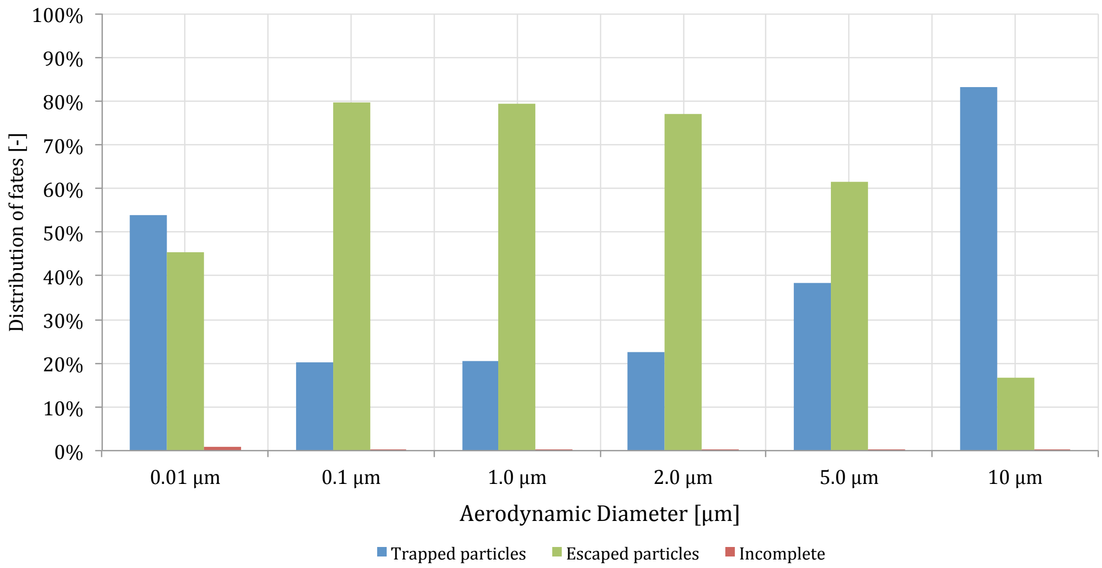

Figure 13.5. Distribution of trapped, escaped and uncompleted particles for a Discrete Phase simulation with injected mono-dispersed particles with an aerodynamic diameter of 0.01 μm, 0.1 μm, 1.0 μm, 2.0 μm, 5.0 μm and 10.0 μm respectively.

Figure 13.5 shows that the accumulation range (0.1 - 2.0 μm) has the lowest fraction of trapped particles. The same tendency was also found in the test case in Appendix I, as larger particles have a higher deposition due to higher impaction and a higher gravitational force.

The difference between the fates of particles with aerodynamic diameters of 0.1 - 1.0 μm is very small. Diffusion should be the primary mechanism for deposition of particles below 0.5 μm according to the theory described in Section 3.3. However, the influence of the Brownian motion on the fates of the particles is only influential for particles below 0.05 μm for this case. The results can be seen in the Digital Appendix.

The same tendency was found in Wang et al. [2009], where the deposition efficiency of particles with an aerodynamic diameters between 0.001 - 300 μm, moving through the nasal cavity with a flow rate of 10 L/min was examined. They concluded that the lowest deposition efficiency occurs in the range between 0.015-10.0 μm due to the low influence from diffusion, impaction and gravitational settling.

The amounts of escaped particles are quite critical as most of the particles below 1.0 μm escape through the lower airway model. However this does not necessitate that all the escaped particles will be absorbed directly into the bloodstream, as the bronchioles in a real human airway consist of further generations of branches than the airway model used in this study. Furthermore, mucous and nasal hair, which is not incorporated in the model, will filter particles as described in Appendix C. Particles greater than 5-10 μm are usually removed in the upper respiratory system, which indicates that the mucous and nasal hair has a large impact on filtration. [Tu et al., 2013]

The purpose of this numerical investigation is to supplement the experimental investigation and to use the numerical model to gain a better understanding of the experimental results. Hence the numerical model needs to replicate the experimental model.

Virtual Mass Force, Saffman's Lift Force and Pressure Gradient Force are concluded to have an insignificant influence on the particle trajectories in Appendix I. However an investigation into the forces is still included as the computational time for the discrete phase simulations is very small due to the particles being simulated with one way coupling. An investigation of the influence of the additional forces can be found in the Digital Appendix.

The particle trajectories for particles with aerodynamic diameters of 1.0 μm and 10.0 μm are visualized in Figure 13.6 and Figure 13.7 respectively.

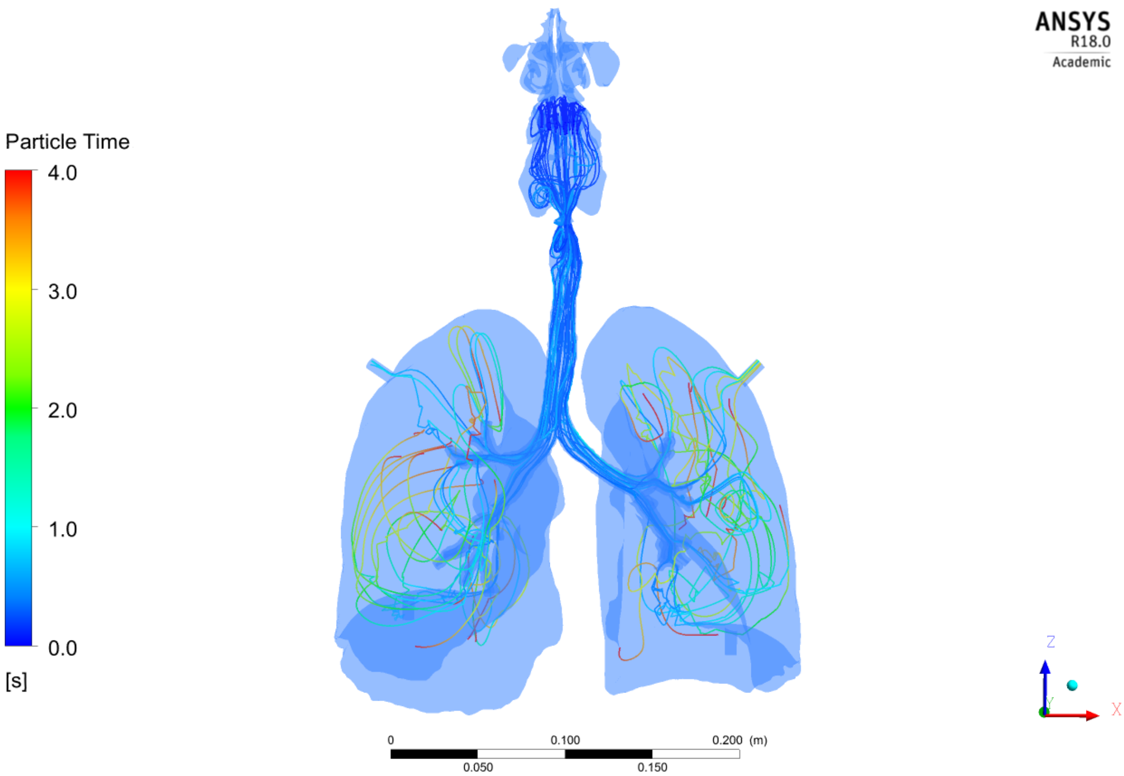

Figure 13.6. Particle trajectories of particles with an aerodynamic diameter of 1.0 μm.

Figure 13.6 shows that the gravitational force on the particles with an aerodymanic diameter of 1.0 μm is smaller as the particles keep floating in the lung shell.

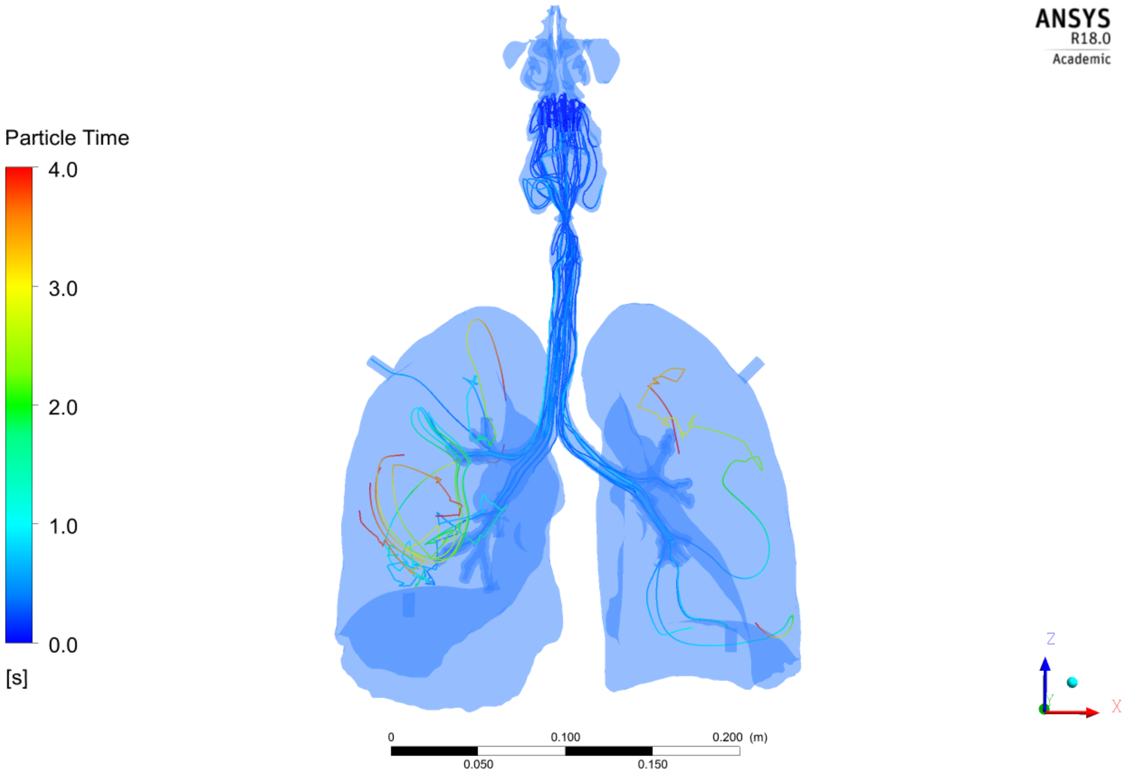

Figure 13.7. Particle trajectories of particles with an aerodynamic diameter of 10.0 μm.

The particle trajectories for particles with an aerodynamic diameter of 1.0 μm is also illustrated in Figure 13.8. In the figure, the particle locations are visualised during the first 4 s after the particles are injected into the domain.

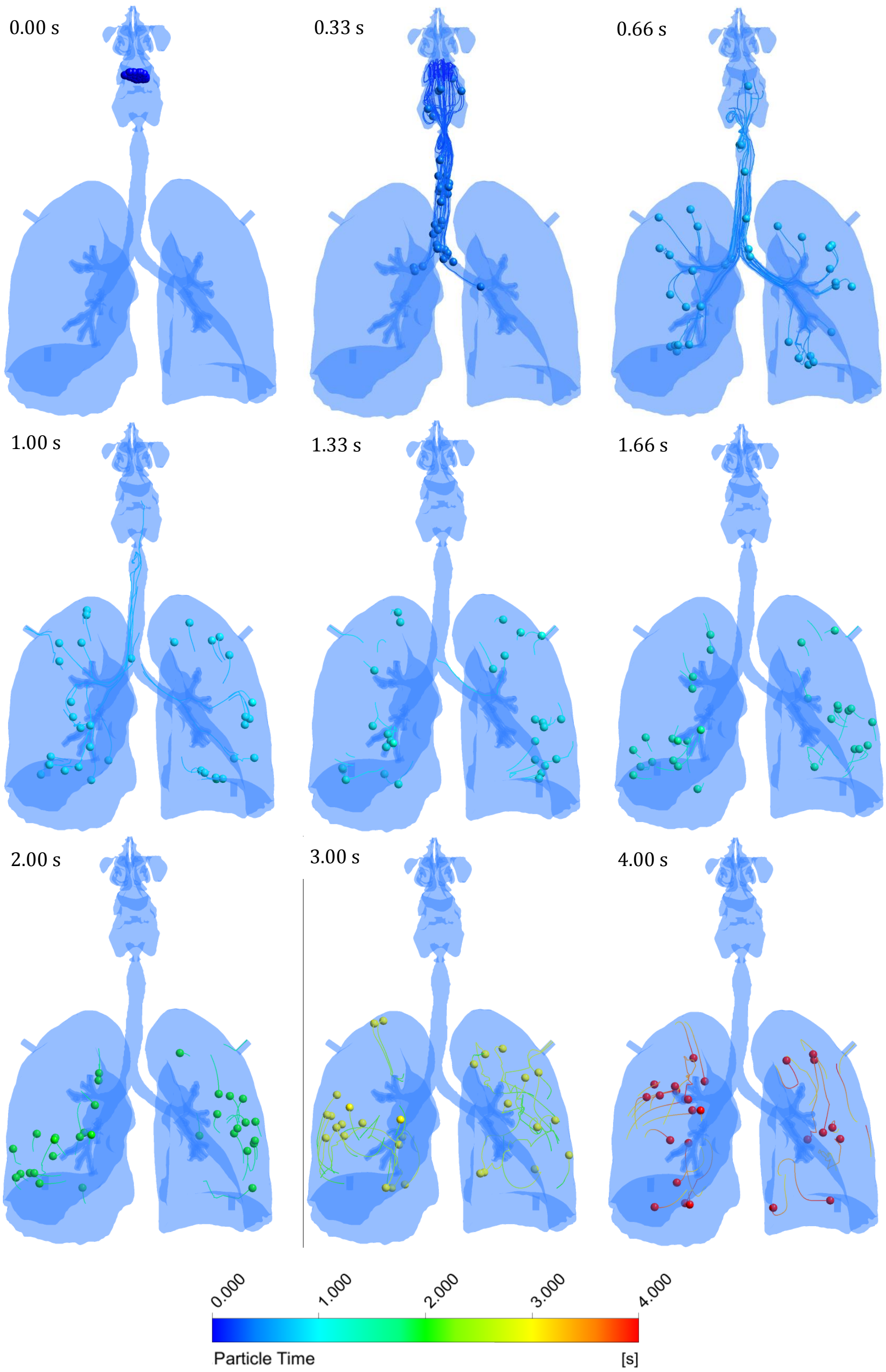

Figure 13.8. Particle locations for particles with an aerodynamic diameter of 1.0 μm during the first 4 s after particles are injected into the domain.

13.2.1 Location of the Deposited Particles

The ratio between the number of deposited particles and the total number of released particles is defined as the deposition fraction and is widely used in research papers [Naseri et al., 2017] [Rahimi-Gorji et al., 2016]. The particle deposition can be used to characterise the risk of exposure by the aerodynamic size of the particles. It can also be used to develop and assess drug treatment methods for airway diseases, which has previously been the main reason behind conducting investigations into particle deposition in the airways. [Naseri et al., 2017]

The deposited particles in the different anatomical regions by the different particle sizes are given in Table 13.1. The anatomical regions are illustrated in Figure 13.9.

Table 13.1. The deposition fraction of particles with an aerodynamic diameter of 0.1 μm, 1.0 μm, 2.0 μm, 5.0 μm and 10.0 μm.

Region	**0.1 μm**	**1.0 μm**	**2.0 μm**	**5.0 μm**	**10.0 μm**
Nasal Cavity	0.4%	0.5%	0.4%	0.6%	0.8%
Mouth	0.3%	0.3%	0.5%	0.9%	3.2%
Pharynx	0.5%	0.5%	0.6%	0.9%	2.3%
Larynx	2.1%	2.3%	2.4%	4.9%	18.9%
Trachea	1.5%	1.5%	1.5%	2.7%	7.7%
Bronchi Left	2.1%	2.3%	2.6%	3.9%	14.8%
Bronchi Right	3.5%	3.7%	4.2%	6.6%	20.3%
Total Lower Airway	10.5%	10.9%	12.2%	20.5%	68.0%
Lung Left	4.1%	4.0%	4.3%	7.5%	6.6%
Lung Right	5.5%	5.5%	6.0%	10.3%	8.6%
Total	20.1%	20.4%	22.5%	38.3%	83.2%

Table 13.1 shows that the deposition fraction for particles with an aerodynamic diameter of 0.1 μm and 1.0 μm are similar. Most of these particles are deposited in the lower airways, more specifically the bronchus. This is due to a more narrow air passage in the lower part of the airways.

While the toxicity of the particles is unknown and depend on the emission source, the dose of the particles also influences the health impact. It is noticeable that the differences between the deposition fraction for particles with an aerodynamic diameter of 0.1 μm and 1.0 μm are similar, but the difference in dose is by a factor of 1000. This is an important factor to consider when characterising particle exposure.

The high deposition fraction in the lungs stem from the air movement in the lung volume, which is a mainly categorized as being low velocity with high local velocities from the bronchioles' outlets, as illustrated in Figure 13.3. Most of the airborne particles will in reality be deposited in the next generations of bronchioles or escape though the mouth during exhalation. To predict the distribution of the particles fates during exhalation an unsteady simulation must to be conducted. This has not been possible in this study due to time constraints.

Overall a higher particle deposition occurs in the right bronchi, which corresponds with the theory on the anatomy of the respiratory system as described in Appendix C.

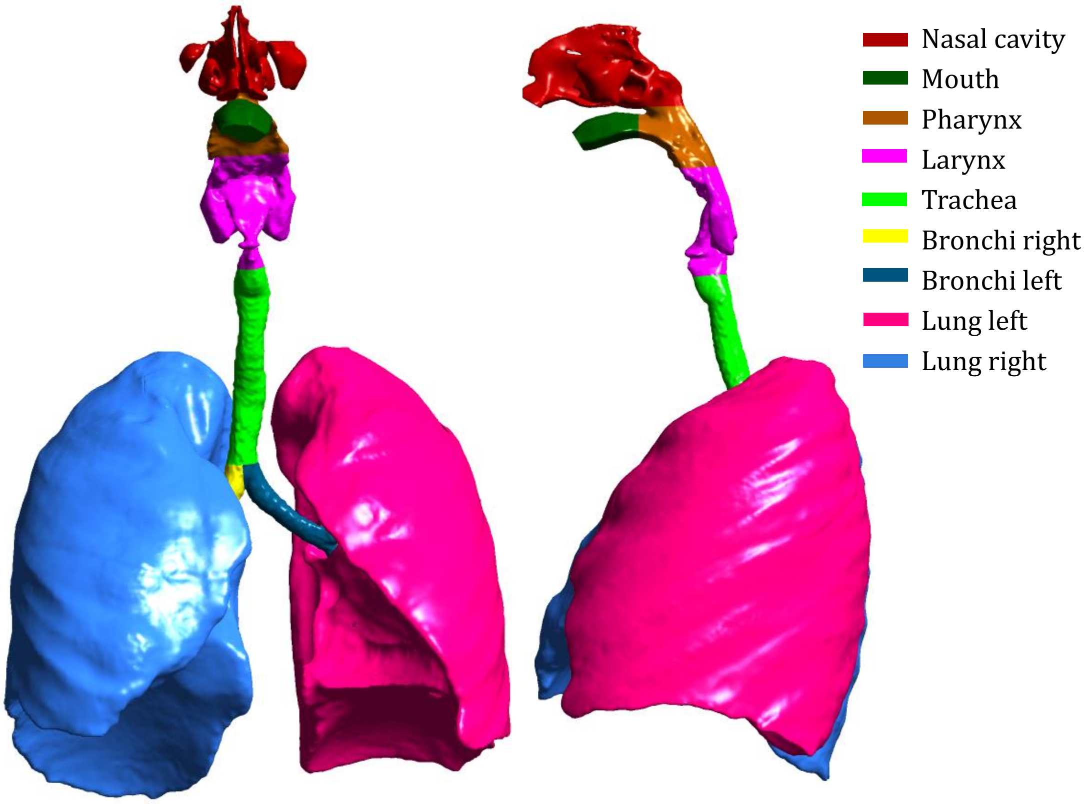

Figure 13.9. The division of the anatomical regions for the airway model.

Table 13.2 shows the deposition fraction in the bronchi to highlight the high deposition in the narrow air passages. The bronchial tree is divided into six parts as illustrated in Figure 13.10.

Table 13.2. The deposition fraction for particles with an aerodynamic diameter of 0.1 μm, 1.0 μm, 2.0 μm, 5.0 μm and 10.0 μm in the bronchial tree.

Right side	**0.1 μm**	**1.0 μm**	**2.0 μm**	**5.0 μm**	**10.0 μm**
B.R	0.2%	0.2%	0.3%	0.4%	0.8%
B.R.1	2.2%	2.3%	2.6%	4.2%	11.9%
B.R.2	1.1%	1.2%	1.4%	2.0%	7.5%
Left side	**0.1 μm**	**1.0 μm**	**2.0 μm**	**5.0 μm**	**10.0 μm**
B.L	0.4%	0.4%	0.4%	0.5%	1.2%
B.L.1	1.0%	1.1%	1.3%	1.9%	4.8%
B.L.2	0.7%	0.8%	0.9%	1.6%	8.8%

Table 13.2 shows that most particles are deposited in the narrow passages of the bronchioles. Most of the particles are deposited in B.R.1 and B.L.1, which could be due to impaction caused by the large angles between the branches. An airway model including more branches will increase the fraction of deposited particles.

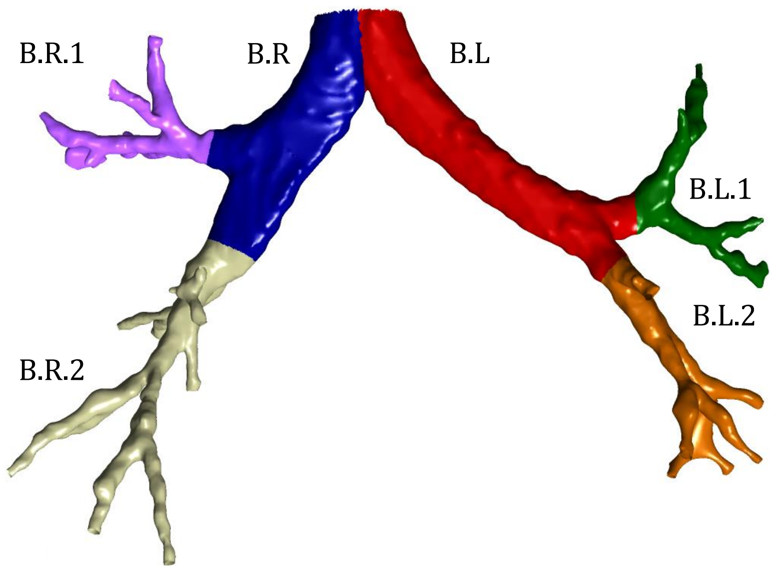

Figure 13.10. The division of the bronchioles to investigate particle deposition.

Pie charts of the distribution of the deposited particle can be found in the Digital Appendix.

13.2.2 Influence of the Surface Roughness

A study showed that small difference in the surfaces' smoothness had a noticeable impact on the micro-particles deposition rate [Shi et al., 2007]. Hence the influence of the surface roughness of the 3D printed model will be investigated.

The roughness of the 3D printed model is around 0.1 mm, based on the details given from the 3D printing. However it is not possible to specify the roughness of the wall as enhanced wall treatment is used together with a k-ϵ turbulence model.

The roughness of the surfaces can be implemented by using the SST k-ω turbulence model. Hence a simulation with SST k-ω is conducted to examine the influence of the roughness. The roughness height is chosen to be 0.1 mm and the roughness constant is 0.5, as the roughness over the surfaces is assumed to be uniform.

A higher surface roughness results in a higher shear stresses at the wall. According to the continuous flow, implementing the roughness will result in modified version of the standard law-of-the-wall model, which is used to calculate the physics at the wall depending on the y^+ value. A rough surface creates a more turbulent flow at the boundaries. The influence of implementing the surface roughness is shown in Figure 13.11, where the deposition fraction of particles with an aerodynamic diameter of 1.0 μm is shown for a simulation including the surface roughness and a simulation with a smooth surface. Both simulations are based on the SST k-ω turbulence model. Documentation for convergence can be found in the Digital Appendix.

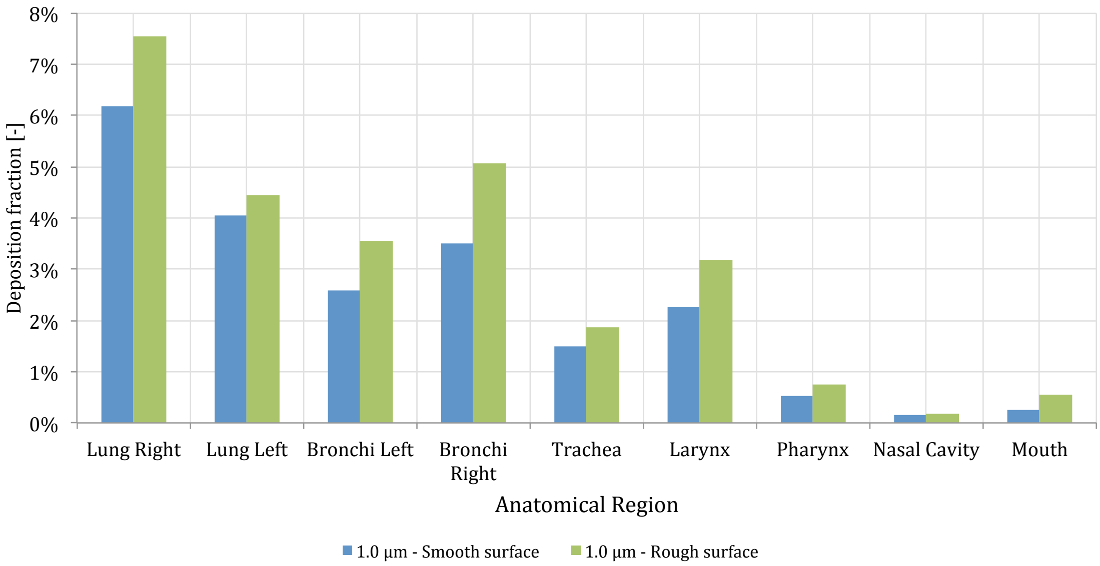

Figure 13.11. The deposition fraction for airway model with a smooth surface and a rough surface for particles with an aerodynamic diameter of 1.0 μm.

Figure 13.11 shows that the deposition fraction is higher for the simulation with a rough surface, which could be due to the more turbulent flow at the boundary. Table 13.3 shows the fates of the particles for the two SST k-ω model simulations and the Realizable k-ϵ model simulation.

Table 13.3. Fates of the particles with an aerodynamic diameter of 1.0 μm and 10.0 μm for the two SST k-ω model simulations and the Realizable k-ϵ model.

Particle size	**Simulation model**		**Particle fate**		
	Turbulence model	Surface	Trapped	Escaped	Incomplete
1.0 μm	Realizable k-ϵ model	Smooth	20%	79%	0%
	SST k-ω model	Smooth	21%	78%	1%
	SST k-ω model	Rough	27%	73%	0%
10 μm	Realizable k-ϵ model	Smooth	83%	17%	0%
	SST k-ω model	Smooth	86%	14%	0%
	SST k-ω model	Rough	89%	11%	0%

Table 13.3 shows that the simulations with the SST k-ω model predicted a higher deposition fraction compared to the Realizable k-ϵ model. This variation is due to the different method of calculating the turbulent viscosity. It cannot be determined whether the SST k-ω model or the Realizable k-ϵ model is advantageous. However, according to the theory description in Section 9.4 the SST k-ω should be overly sensitive to the initial input of the inlet [Yin, 2016].

Including the surface roughness of the 3D model results in an increased deposition. The fraction of trapped particles is 6.1% higher for particles with an aerodynamic diameter of 1.0 μm and 2.4% higher for particles with an aerodynamic diameter of 10.0 μm.

13.3 Comparison of Numerical Investigations

The numerical results of this study are compared to other studies in order to identify the impact of the different approaches to examining particle exposure in the lower airways. The lower airways have been investigated by Naseri et al. [2017] and Rahimi-Gorji et al. [2016], which have also used a CT-scanning of the upper and lower airways as well as similar flow rate conditions. A summary of Naseri et al. [2017] and Rahimi-Gorji et al. [2016] can be found in Table 13.4.

Table 13.4. Summary of Naseri et al. [2017] and Rahimi-Gorji et al. [2016] used to compare with the present study.

Title	Details of regional particle deposition and airflow structures in a realistic model of human tracheobronchial airways: two-phase flow simulation	Numerical investigation of transient transport and deposition of microparticles under unsteady inspiratory flow in human upper airways.
Reference:	[Naseri et al., 2017]	[Rahimi-Gorji et al., 2016]
Year published	2016	2017
Method	CFD simulation on a CT-scanned airway model	CFD simulation on a CT-scanned airway model
Breathing type	Oral breathing – 10.0 L/min	Nasal breathing – 12.8 L/min
Anatomy construction	From mouth to 6th generation of tracheobronchial airway	From nose to bottom of trachea
Validated by	Zhao and Lieber model	SLA nasal replica

As mentioned in Appendix C the human respiratory system varies greatly between people. Therefore a variation in the CT-scanning is also expected. The geometries and division of the anatomical regions of Naseri et al. [2017], Rahimi-Gorji et al. [2016] and the present study are illustrated in Figure 13.12.

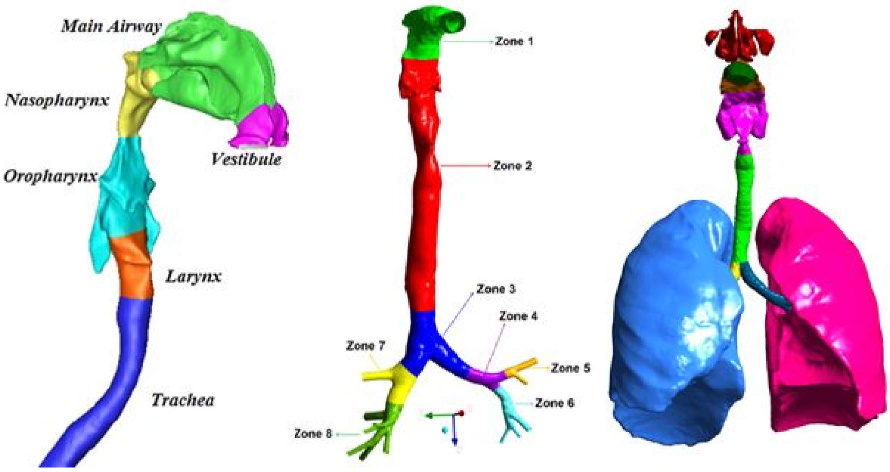

Figure 13.12. Airway models used in [Naseri et al., 2017], [Rahimi-Gorji et al., 2016] and the present study.

Figure 13.12 shows a clear difference between the geometries and the division of the anatomical regions. To compare the different results the airway model is divided into three parts:

- Upper airway (UA)
- Pharynx, larynx, trachea (PLT)
- Bronchi (BC)

The data has been obtained visually from the papers, and the collection of data can be found in the Digital Appendix. A comparison of the particle deposition from Naseri et al. [2017], Rahimi-Gorji et al. [2016] and the present study can be seen in Figure 13.13.

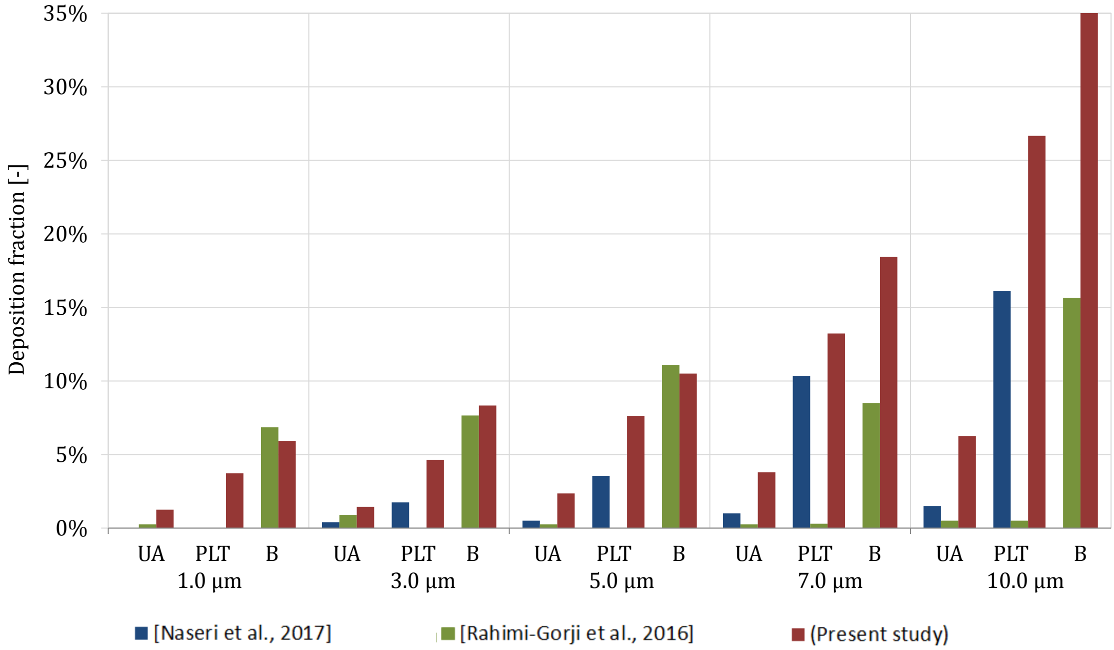

Figure 13.13. Particle deposition of [Naseri et al., 2017], [Rahimi-Gorji et al., 2016] and the present study for particles with an aerodynamic diameter of $1.0\,\mu$m, $3.0\,\mu$m, $5.0\,\mu$m, $7.0\,\mu$m and $10.0\,\mu$m. Rahimi-Gorji et al. [2016] does not include data for particles with an aerodynamic diameter of $1.0\,\mu$m and does not simulate the particle exposure in the bronchi.

Figure 13.13 shows that Rahimi-Gorji et al. [2016] has a low estimation of the particle deposition in the pharynx, larynx, trachea. However, the conditions of the deposition in the bronchi are similar to the present study. Naseri et al. [2017] has similar results with the present study, but they have a lower estimation of particle deposition.

In general there is a big variation in the different results. The variation is based on the different geometries with different definitions of the anatomical division. These make it difficult to compare the studies with one-another. The papers also use different turbulence models and boundary conditions, but a lack of information in the papers makes it impossible to reproduce the applied settings and to conduct a more detailed analysis of variation between the different cases. The results should be similar as the purpose for the investigation is the same.

Naseri et al. [2017] and Rahimi-Gorji et al. [2016] are both validated according to experimental data. However the validation is only based on one anatomical part, which is idealized. The Zhao and Lieber model and the SLA nasal replica used for validation is shown on figure 13.14 and 13.15.

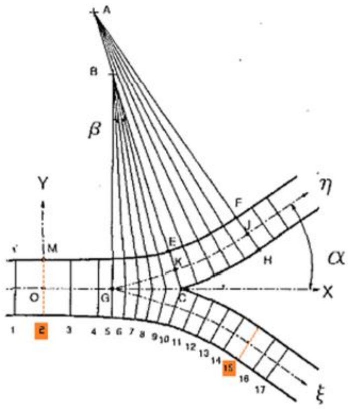

Figure 13.14. The Zhao and Lieber model used for validation of the airflow in tracheobronchial airways [Zhao and Lieber, 1994].

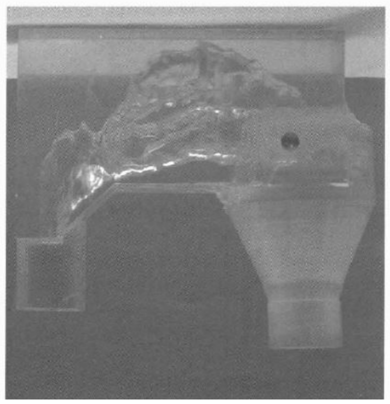

Figure 13.15. The SLA nasal replica model used for validation of particle deposition in the nasal cavity [Kelly et al., 2004].

A CFD simulation is a great numerical approach to predicting fluid flow, but it is based on assumptions to model the flow, which influences the output. These assumptions create an uncertainty for predicting the actual flow conditions. Hence the CFD simulations should be compared with a benchmark to ensure their validity.

A benchmark model which consists of the whole airway model is missing to validate the models more accurately.

Part III

Final Assessment of the Investigations

A final assessment of the experimental and numerical investigations is conducted to summarise, discuss and conclude on the findings of this study.

14 Comparison of Airway Deposition

The experimental and numerical investigations have both been carried out on the same 3D airway model. This allows for a comparison between the findings. While the investigations have their individual advantages, they collectively allow for better assessment of particle exposure.

The one parameter that is evaluated for both the experimental and numerical investigation is the deposition fraction, which is described in Appendix B.

The experimental investigation concluded that the number concentration within the airways mainly lie in ultrafine and accumulation regions (<2.0 μm). The mass concentrations for $PM_{2.5}$ and PM_{10} are very similar, further confirming the size distributions of the cooking emitted particles by oil heating.

In the numerical investigation the deposition fractions were investigated for particles in the range of 0.1 μm - 10.0 μm. The deposition fraction for particles in the range of 0.1 μm - 2.0 μm can easily be compared with the $PM_{2.5}$ results from the experiments.

Table 14.1 shows the deposition fractions from the experimental and numerical investigations respectively.

Table 14.1. Deposition fractions from the experimental and numerical investigations for $PM_{2.5}$ and 0.1,μm - 2.0,μm respectively.

	Experimental		**Numerical**	
Deposition fraction	Corn oil	81.1%	0.1 μm	20.1%
	Olive oil	84.8%	1.0 μm	20.4%
	Peanut oil	84.6%	2.0 μm	22.5%
	Sunflower oil	80.9%		

There is a large difference in the deposition fractions, even though the size distribution of the particles has been considered. This difference was expected as the conditions and metrics are defined differently for the two investigations.

Deposition fraction is calculated for the experimental and numerical investigation using two different metrics: airborne mass concentration and particle fates respectively. While the ratio should theoretically be the same, the methods for obtaining the different metrics contribute to the different values of deposition fraction.

In the experiment the airborne mass concentration within the lung volume is measured while subjected to artificial breathing. The CFD simulations are on the other hand calculated from a steady state simulation. If the numerical investigation was transient, the deposition fraction would be higher, as it is expected that many of the particles which enter the lung volume will be subjected to the change in flow direction and deposit or escape during exhalation.

Additionally the mouth opening and the lips are included in the experimental investigation, while the particles are injected directly in the oral cavity for the numerical investigation. This also accounts for some of the differences between the investigations.

It is important to note that though there is a big difference in the deposition fractions, both investigations are still equally correct under the assumptions made to the model and parameters set. Both the CFD simulations and the measurements will vary from a real human occupant; however, the strength in this investigation lies in analysing the results under the conditions they were performed in. Future technological developments will help in acquiring more knowledge on the subject. At the time of this study, the use of the CT-scanned airway model is state-of-the-art and thereby already an improvement from previous studies.

15 | Discussion

The experimental and numerical investigations have been carried out using parameters, assumptions and conditions to achieve well founded results. While these have been chosen with great care, complications with the procedure and parameters have shown up through the different stages of the investigation. These are identified as they should be considered when assessing the results.

In the experimental investigation, mass concentration is used as a metric to examine the particle exposure. While four of the sensors measure this directly, the APS3321 calculates it through the particle density. The particle density is assumed to be 1 g/cm^3, as used in a similar study. However, the density of cooking oil is usually around 0.93 g/cm^3 and the density of oil fume particles is unknown. This could lead to an uncertainty in the mass concentration levels within the airways. The density of the oil fume particles should be measured.

Calibrations of the PMS5003 and SDS011 particle sensors have been carried out by the APS3321. Through this, the density of 1 g/cm^3 has been taken into account, which achieves the real ratio between the mass concentration of the different sensors. However, the calibrations were carried out using sunflower oil, which has a low size distribution. Hence the majority of the cooking emitted particles were below 2.5 μm. The calibrations of PM_{10} for the different sensors may then cause too high of a reduction in the PM_{10} levels. The calibrations should potentially have been carried out using a different sample.

Furthermore the particle sensors are limited by their measuring ranges. This affects the calibrations carried out using the APS3321 as some of the released particles from the heated cooking oil lie outside the measured ranges of all the particles sensors. It is therefore debatable whether the calibrated mass concentrations are realistic.

It is uncertain whether the locations of the sensors in the breathing zone and by the emission source were placed ideally. This is one of the reasons why two sensors were placed at each location. The sensors in the breathing zone were located approximately 5 cm from the mouth. The sensors could have been located closer, but this could eventually affect the flow conditions. The mass concentration in the breathing zone was shown to be higher than the mass concentration by the emission source. This is a clear indicator that the sensors by the emission source could be relocated.

To further investigate emissions from the heated cooking oil, several sensors could have been placed above the pan at different heights to measure the mass concentration as the particles rise with the thermal plume. However this may also interfere with the flow.

Additionally the APS3321 could have been used to replace the SDS011 or the PMS5003 sensors to determine the size-resolved number concentration along with the mass concentration in the breathing zone and by the emission source. This would increase knowledge on particle concentration and increase the comparability with the CFD simulations. However, as only one APS3321 was available, all of the sensor locations would not have been measurable at the same time. This would involve an increased amounts of measurements, as well as the uncertainty that there may be variations between each repetition.

For the investigation into particle exposure of the different cooking oil types, the occupant is put in the clean room for the entire duration of the measurement. The occupant remained fairly still standing for the majority of the measurements, but he will have caused some disruption to the steady flow in the room. The difference in the mass concentrations between the four different cooking oil types has been attributed to potentially being caused by the smoke points of the oil. However, observation of the smoke points was only carried out once. A deeper investigation into the smoke points of the oil, including the time after smoke point occurs, as a parameter variation would help determine its impact.

The experiments were conducted under a fixed set of parameters. Each measurement was repeated five times to ensure a representative result. It can be discussed whether this is sufficient to gain accurate results, or whether it would have been beneficial to carry out more repetitions.

In terms of the numerical investigation, the main limitation is that a steady state simulation has been carried out on a case with a cyclic flow. A RANS model is also used for the modelling of turbulence, which neglects the vortex structures and assumes fully turbulent flow. Both assumptions generate a systematic error but have been necessary to apply due to limitations on the computational power.

It can be questioned whether the comparison of the different meshes in the mesh independence test is conducted to a sufficient degree. A mesh with a lower number of elements will decrease the computational time and potentially make transient simulations possible for further investigations. The mesh independence test could be focused on particle deposition, as this is the main research topic for the numerical investigation of the airways. However, the different solutions cannot be compared directly as the initial locations and the amount of released particles differ for the meshes. This is due to the varying number of nodes and their locations at the surface for each mesh.

A better prediction for the fluid flow in the airways could also been obtained by applying the actual inlet and outlet conditions. The inlet and outlet conditions could have been measured experimentally and used directly as boundaries conditions in the CFD simulations. However, these inlet and outlet conditions are time dependent and the impact of using an average measured value compared to the chosen boundary conditions will be negligibly small compared to the uncertainty of conduction a steady state simulation.

In the airway model used for the numerical investigation, the modification in the mouth limits a section of the oral cavity. This should be included in future investigations as it may have had an effect on particle deposition.

16 | Conclusion

This study on lower airway exposure to cooking generated particles by a CT-imaging based 3D printed human airway model was conducted through experimental and numerical investigations.

The experimental investigation determined the quantitative particle exposure by heating cooking oil. It showed a clear difference in the mass concentrations between the different cooking oil types where olive oil and peanut oil contributions were significantly higher than contributions from corn oil and sunflower oil. However, the size distributions of the number concentration in the airways were very similar. This suggests that the high mass concentration is caused by the cooking oil type, and more specifically its smoke point.

The size distributions showed a majority of ultrafine and accumulation particles ($<2.0\,\mu$m), which correlates with the mass concentration levels of $PM_{2.5}$ and PM_{10}.

The particle concentration rose after the source-active period. Incomplete mixing could be seen by the four sensor locations, as the flow was characterised by the thermal plume and stratification. The breathing zone had the highest concentration levels, followed by the exhaust and then the room concentration. The mass concentration in the breathing zone exceeded the WHO guideline values for 24-hour mean of $PM_{2.5}$ and PM_{10}.

In the airways, the deposition fractions were determined to be 77.9 - 84.8% for the different cooking oil types. These similarities coincide with the similar size distributions. The calculated intake fraction showed inaccurate measurements of the mass released from the emission source and could therefore not be concluded upon.

The numerical investigation determined the size-resolved regional particle deposition within the airways. It showed that the majority of particles in the examined range are deposited in the narrow regions of the airway model such as the bronchi and the larynx. Accumulation particles have the smallest deposition fraction in the lower airways of approximately 11%. The deposition fractions were similar in the size range 0.1 - 1.0 μm, but the dose differs significantly between the individual particles sizes.

Applying a surface roughness increased the deposition fraction, which is mainly due to a more turbulent flow.

The particles are kept airborne for a long time in the lung volume. A transient simulation, which implements the breathing cycle, will increase the deposition fraction as most of the airborne particles will be deposited or escape during exhalation. However, transient simulations of the airway model require a lot of computational power, as a dense mesh is necessary due to the complexity of the geometry.

The geometry has a big influence on particle deposition based on a comparison with other studies. Simulation results vary from case to case. Therefore a proper benchmark model is needed to obtain more valid results.

Finally it can be concluded that there is a difference in the deposition fractions between the experimental and numerical investigations. This is due to the different parameters set and assumptions applied. While the deposition fractions may differ, the results from both investigations are still valid in terms of their circumstances.

16.1 Recommendations for Future Investigations

Based on this study, a number of topics have been identified for further investigation.

- An investigation should be carried out into the smoke points of the cooking oil and their chemical composition to determine its influence on emission rate and thereby the inhaled dose of the different cooking oil types.
- Further parameter variations should be examined in an experimental investigation to determine potential influences on particle exposure from indoor emission sources. This could include variations on the proximity to the source, indoor climatic conditions and the measurement procedure.
- A transient simulation including the LES turbulence model should be conducted to predict particle deposition during the actual breathing cycle and to improve predictions on the turbulent behaviour in the airways. This will enable a more thorough comparison with the experimental investigation, which could eventually be used as a benchmark model.
- A new mesh should be simulated, which includes the whole oral cavity and eventually the breathing zone. This could improve knowledge on the interaction between the breathing zone and deposition in the airways.
- An investigation should be launched into control methods to limit particle exposure to the human occupant. This will help in identifying efficient strategies to minimise the health impact. Suggested control methods include implementing a ventilation hood, wearing a mask and altering the room ventilation.

Bibliography

Adams, **1993**. William C Adams. *Measurement of breathing rate and volume in routinely performed daily activities*. California Air Resources Board, 1993.

André Bakker, **2008**. André Bakker. *Computational Fluid Dynamics - Course Material and Lectures:*. `http://www.bakker.org/dartmouth06/engs150/`, 2008.

ANSYS Fluent, **2017**. ANSYS Fluent. *Fluent Documentation*. `https://www.sharcnet.ca/Software/Ansys/17.2/en-us/help/ai_sinfo/flu_intro.html`, 2017.

Bahmanzadeh et al., **2016**. Hojat Bahmanzadeh, Omid Abouali and Goodarz Ahmadi. *Unsteady particle tracking of micro-particle deposition in the human nasal cavity under cyclic inspiratory flow*. Journal of Aerosol Science, Volume: 101, Pages: 86 – 103, 2016. ISSN 0021-8502.

Barrett et al., **2010**. Kim Barrett, Heddwen Brooks, Scott Boitano and Susan Barman. *Ganong's Review of Medical Physiology*. ISBN 978-0-07-160568-7". McGraw-Hill, 23rd edition, 2010.

Buonanno et al., **2009**. G. Buonanno, L. Morawska and L. Stabile. *Particle emission factors during cooking activities*. Atmospheric Environment, Volume: 43(20), Pages: 3235 – 3242, 2009. ISSN 1352-2310.

CFD Online, **2017a**. CFD Online. *Meaning of PISO Corrections*. `https://www.cfd-online.com/Forums/fluent/184255-meaning-piso-corrections.html#post672500`, 2017.

CFD Online, **2017b**. CFD Online. *Boussinesq eddy viscosity assumption*. `https://www.cfd-online.com/Wiki/Boussinesq_eddy_viscosity_assumption`, 2017.

Chakravorty, **2017**. Dibya Chakravorty. *STL File Format for 3D Printing – Simply Explained*. `https://all3dp.com/what-is-stl-file-format-extension-3d-printing/#pointone`, 2017.

Choi et al., **2009**. Jiwoong Choi, Merryn Tawhai, Eric Hoffman and Ching-Long Lin. *On intra- and intersubject variabilities of airflow in the human lungs*. Physics of fluids (Woodbury, N.Y. : 1994), Volume: 21, 2009.

Collins English Dictionary, **2018**. Collins English Dictionary. *Terminal velocity*. `https://www.collinsdictionary.com/dictionary/english/terminal-velocity`, 2018.

CR 1752, **1998**. CR 1752. *Ventilation For Buildings - Design Criteria For The Indoor Environment*, 1998.

Deng et al., 2018. Qihong Deng, Cuiyun Ou, Jiao Chen and Yuguang Xiang. *Particle deposition in tracheobronchial airways of an infant, child and adult*. Science of The Total Environment, Volume: 612(Supplement C), Pages: 339 – 346, 2018. ISSN 0048-9697.

DS/EN 15251, 2007. DS/EN 15251. *Input-parametre til Indeklimaet ved Design og Bestemmelse af Bygningers Energimæssige Ydeevne Vedrørende Indendørs Luftkvalitet, Termisk Miljø, Belysning og Akustik*, 2007.

Gao et al., 2013a. Jun Gao, Changsheng Cao, Qianfen Xiao, Bin Xu, Xiang Zhou and Xu Zhang. *Determination of dynamic intake fraction of cooking-generated particles in the kitchen*. Building and Environment, Volume: 65(Supplement C), Pages: 146 – 153, 2013. ISSN 0360-1323.

Gao et al., 2013b. Jun Gao, Changsheng Cao, Xu Zhang and Zhiwen Luo. *Volume-based size distribution of accumulation and coarse particles (PM0.1–10) from cooking fume during oil heating*. Building and Environment, Volume: 59, Pages: 575–580, 2013. doi: 10.1016/j.buildenv.2012.10.009.

Guha, 2008. Abhijit Guha. *Transport and Deposition of Particles in Turbulent and Laminar Flow*. Annu. Rev. Fluid Mech, Volume: 40, 2008.

He et al., 2004. Congrong He, Lidia Morawska, Jane Hitchins and Dale Gilbert. *Contribution from indoor sources to particle number and mass concentrations in residential houses*. Atmospheric Environment, Volume: 38(21), Pages: 3405 – 3415, 2004. ISSN 1352-2310.

Heyder et al., 1986. J. Heyder, J. Gebhart, G. Rudolf, C.F. Schiller and W. Stahlhofen. *Deposition of particles in the human respiratory tract in the size range 0.005–15 μ m*. Journal of Aerosol Science, Volume: 17(5), Pages: 811 – 825, 1986. ISSN 0021-8502.

Hussein et al., 2006. Tareq Hussein, Thodoros Glytsos, Jakub Ondráček, Pavla Dohányosová, Vladimír Ždímal, Kaarle Hämeri, Mihalis Lazaridis, Jiří Smolík and Markku Kulmala. *Particle size characterization and emission rates during indoor activities in a house*. Atmospheric Environment, Volume: 40(23), Pages: 4285 – 4307, 2006. ISSN 1352-2310.

Institut for Miljøvidenskab, 2016. Institut for Miljøvidenskab. *Niveauer og tendenser: Partikler (PM10, PM2.5 og TSP)*. `http://www2.dmu.dk/1_viden/2_miljoe-tilstand/3_luft/4_maalinger/5_niveauer/6_partikler/partikler_generelt.asp`, 2016.

ISO 7730, 2006. ISO 7730. *Ergonomics of the Thermal Environment - Analytical Determination and Interpretation of Thermal Comfort using Calculation of the PMV and PPD Indices and Local Thermal Comfort Criteria*, 2006.

Kamens et al., 1991. Richard Kamens, Chung te Lee, Russell Wiener and David Leith. *A study of characterize indoor particles in three non-smoking homes*. Atmospheric Environment. Part A. General Topics, Volume: 25(5), Pages: 939 – 948, 1991. ISSN 0960-1686.

Kelly et al., 2004. James T. Kelly, Bahman Asgharian, Julia S. Kimbell and Brian A. Wong. *Particle Deposition in Human Nasal Airway Replicas Manufactured by Different Methods. Part II: Ultrafine Particles*. Aerosol Science and Technology, Volume: 38(11), Pages: 1072–1079, 2004.

Kolanjiyil and Kleinstreuer, 2017. Arun V. Kolanjiyil and Clement Kleinstreuer. *Computational analysis of aerosol-dynamics in a human whole-lung airway model*. Journal of Aerosol Science, Volume: 114(Supplement C), Pages: 301 – 316, 2017. ISSN 0021-8502.

Licina et al., 2017. Dusan Licina, Yilin Tian and William W. Nazaroff. *Inhalation intake fraction of particulate matter from localized indoor emissions*. Building and Environment, Volume: 123(Supplement C), Pages: 14 – 22, 2017. ISSN 0360-1323.

Lim et al., 2012. Soogil Lim, Jeonghoon Kim, Taehyun Kim, Kiyoung Lee, Wonho Yang, Sangil Jun and Seungdo Yu. *Personal exposures to PM2.5 and their relationships with microenvironmental concentrations*. Volume: 47, Pages: 407–412, 2012. ISSN 1352-2310.

Litewnicki and Zajas, 2010. Michal Litewnicki and Jan Zajas. *Microenvironment around people*, 2010.

Liu et al., 2016. Li Liu, Yuguo Li, Peter Nielsen, Jianjian Wei and Rasmus Jensen. *Short-range airborne transmission of expiratory droplets between two people*. Indoor Air, Volume: 27, 2016.

Lund and Condra, 2016. Erik Lund and Thomas J. Condra. *Notes and Exercises for Numerical Methods*. 7. semester in course: Numerical methods, 2016.

Marshall and Nazaroff, 2009. Julian D. Marshall and William W. Nazaroff. *Intake Fraction*. `https://depts.washington.edu/airqual/reports/Intake%20Fraction%20--%20proofs.pdf`, 2009.

Martin and Finlay, 2007. Andrew R. Martin and Warren H. Finlay. *A general, algebraic equation for predicting total respiratory tract deposition of micrometer-sized aerosol particles in humans*. Journal of Aerosol Science, Volume: 38(2), Pages: 246 – 253, 2007. ISSN 0021-8502.

Matson, 2005. Uve Matson. *Indoor and outdoor concentrations of ultrafine particles in some Scandinavian rural and urban areas*. Science of The Total Environment, Volume: 343(1), Pages: 169 – 176, 2005. ISSN 0048-9697.

Melina, 2019. Vesanto Melina. *Smoke Points of Oils*. `https://www.veghealth.com/nutrition-tables/Smoke-Points-of-Oils-table.pdf`, 2019.

Munson et al., 2012. B.R. Munson, A.P. Rothmayer and T.H. Okiishi. *Fundamentals of Fluid Mechanics, 7th Edition*. Wiley, `https://books.google.dk/books?id=GQMcAAAAQBAJ`, 2012. ISBN 9781118214596.

Naseri et al., 2017. Arash Naseri, Sana Shaghaghian, Omid Abouali and Goodarz Ahmadi. *Numerical investigation of transient transport and deposition of microparticles* *under unsteady inspiratory flow in human upper airways*. Respiratory Physiology & Neurobiology, Volume: 244, Pages: 56 – 72, 2017. ISSN 1569-9048.

Nazaroff, **2004**. William W. Nazaroff. *Indoor particle dynamics*. Indoor Air, Volume: 14, Pages: 175–183, 2004. ISSN 1600-0668.

Nazaroff, **2008**. William W. Nazaroff. *Inhalation intake fraction of pollutants from episodic indoor emissions*. Building and Environment, Volume: 43(3), Pages: 269 – 277, 2008. ISSN 0360-1323. Indoor Air 2005: Modeling, Assessment, and Control of Indoor Air Quality.

Nielsen et al., **2007**. Peter V. Nielsen, Francis Allard, Hazim B. Awbi, Lars Davidson and Alois Schälin. *Computational fluid dynamics in ventilation design*. ISBN 2-9600468-9-7. Rehva, 2007.

Nielsen, **1990**. Peter Vilhelm Nielsen. *Specification of a Two-Dimensional Test Case: (IEA)*. Institut for Bygningsteknik, Aalborg Universitet, 1990. International Energy Agency, Energy Conservation in Buildings and Community Systems, Annex 20: Air Flow Pattern within Buildings PDF for print: 22 pp.

Nova Fitness Co., **2015**. Ltd Nova Fitness Co. *Laser PM2.5 Sensor Specification*. Nova Fitness Co., Ltd, version 1.3 edition, 2015.

Palmgren, **2009**. Finn Palmgren. *Luftforurening med partikler: et sundhedsproblem*. ISBN 9788770701266, Miljøbiblioteket. Hovedland, Roskilde, 2009.

Park and Allaby, **2016**. Chris Park and Michael Allaby. *A Dictionary of Environment and Conservation*. ISBN 9780199641666. 2016.

Qi et al., **2017**. Shouliang Qi, Baihua Zhang, Yueyang Teng, Jianhua Li, Yong Yue, Yan Kang and Wei Qian. *Transient Dynamics Simulation of Airflow in a CT-Scanned Human Airway Tree: More or Fewer Terminal Bronchi?* Computational and Mathematical Methods in Medicine, 2017.

Rahimi-Gorji et al., **2016**. Mohammad Rahimi-Gorji, Tahereh Gorji and Mofid Gorji-Bandpy. *Details of regional particle deposition and airflow structures in a realistic model of human tracheobronchial airways: Two-phase flow simulation*. Computers in Biology and Medicine, Volume: 74, 2016.

Rosillo-Calle et al., **2009**. Frank Rosillo-Calle, Luc Pelkmans and Arnaldo Walter. *A Global Overview of Vegetable Oils, with Reference to Biodiesel*, 2009.

Russo and Khalifa, **2010**. Jackie S. Russo and H. Ezzat Khalifa. *CFD assessment of intake fraction in the indoor environment*. Building and Environment, Volume: 45(9), Pages: 1968 – 1975, 2010. ISSN 0360-1323.

Schlesinger et al., **1977**. Richard B. Schlesinger, Daryl E. Bohning, Tai L. Chan and Morton Lippmann. *Particle deposition in a hollow cast of the human tracheobronchial tree*. Journal of Aerosol Science, Volume: 8(6), Pages: 429 – 445, 1977. ISSN 0021-8502.

Shi et al., 2007. Huawei Shi, Clement Kleinstreuer and Zhe Zhang. *Modeling of inertial particle transport and deposition in human nasal cavities with wall roughness*. Journal of Aerosol Science, Volume: 38(4), Pages: 398 – 419, 2007. ISSN 0021-8502.

Stabile et al., 2012. L. Stabile, F.C. Fuoco and G. Buonanno. *Characteristics of particles and black carbon emitted by combustion of incenses, candles and anti-mosquito products*. Building and Environment, Volume: 56(Supplement C), Pages: 184 – 191, 2012. ISSN 0360-1323.

Stabile et al., 2014. L. Stabile, E.R. Jayaratne, G. Buonanno and L. Morawska. *Charged particles and cluster ions produced during cooking activities*. Science of The Total Environment, Volume: 497-498(Supplement C), Pages: 516 – 526, 2014. ISSN 0048-9697.

Sutherland, 2002. John W. Sutherland. *Air quality primer*. `http://www.mfg.mtu.edu/cyberman/environment/air/index.html`, 2002.

The Free Dictionary by Farlex, 2017. The Free Dictionary by Farlex. *Alveoli*. `https://medical-dictionary.thefreedictionary.com/Alveoli`, 2017.

Trafik & Byggestyrelsen, 2016. Trafik & Byggestyrelsen. *Danish Building Regulation 2015*, 2016. Downloadet: 15-02-2017.

TSI, 2012. TSI. *Model 3321 Aerodynamic Particle Sizer - Operation and Service Manual*. TSI, revision g edition, 2012.

Tu et al., 2013. Jiyuan Tu, Kiao Inthavong and Goodarz Ahmadi. *Computational fluid and particle dynamics in the human respiratory system*. ISBN 9789400744875. Springer, 2013.

Versteeg and Malalasekera, 2007. H. K. Versteeg and W. Malalasekera. *An introduction to computational fluid dynamics - the finite volume method*. ISBN: 978-0-13-127498-3, Second Edition. Pearson Education Limited, 2007.

Wang et al., 2009. S.M. Wang, K. Inthavong, J. Wen, J.Y. Tu and C.L. Xue. *Comparison of micron- and nanoparticle deposition patterns in a realistic human nasal cavity*. Respiratory Physiology & Neurobiology, Volume: 166(3), Pages: 142 – 151, 2009. ISSN 1569-9048.

Wei See and Balasubramanian, 2006. Siao Wei See and Rajasekhar Balasubramanian. *Physical Characteristics of Ultrafine Particles Emitted from Different Gas Cooking Methods*. Aerosol and Air Quality Research, Volume: 6, Pages: 82–92, 2006.

Wikipedia, 2017. Wikipedia. *Upwind scheme*. `https://en.wikipedia.org/wiki/Upwind_scheme`, 2017.

World Health Organization, 2005. World Health Organization. *WHO Air quality guidelines for particulate matter, ozone, nitrogen dioxide and sulfur dioxide - Summary of risk assessment*, 2005.

World Health Organization, 2012. World Health Organization. *Indoor air pollution*. `http://www.who.int/indoorair/guidelines/hhfc/en/`, 2012.

Xu et al., 2017. X.Y. Xu, S.J. Ni, M. Fu, X. Zheng, N. Luo and W.G. Weng. *Numerical investigation of airflow, heat transfer and particle deposition for oral breathing in a realistic human upper airway model*. Journal of Thermal Biology, Volume: 70(Part A), Pages: 53 – 63, 2017. ISSN 0306-4565. Assessing and modeling of the thermal impact of human-clothing environment.

Yin, 2016. Chungen Yin. *Computational Fluid Dynamics – Turbulence modelling*. Fall semester in course: CFD, 2016.

Yong, 2016. Zhou Yong. *PMS5003 Series Data Manual*. Plantower, version 3 edition, 2016.

Youn et al., 2016. Jong-sang Youn, Janae Csavina, Kyle P. Rine, Taylor Shingler, Mark Patrick Taylor, A. Eduardo Sáez, Eric A. Betterton and Armin Sorooshian. *Hygroscopic Properties and Respiratory System Deposition Behavior of Particulate Matter Emitted By Mining and Smelting Operations*. Environmental Science & Technology, Volume: 50(21), Pages: 11706–11713, 2016.

Zhang et al., 2005. Z. Zhang, C. Kleinstreuer, J.F. Donohue and C.S. Kim. *Comparison of micro- and nano-size particle depositions in a human upper airway model*. Journal of Aerosol Science, Volume: 36(2), Pages: 211 – 233, 2005. ISSN 0021-8502.

Zhao et al., 2004. Bin Zhao, Ying Zhang, Xianting Li, Xudong Yang and Dongtao Huang. *Comparison of indoor aerosol particle concentration and deposition in different ventilated rooms by numerical method*. Building and Environment, Volume: 39(1), Pages: 1 – 8, 2004. ISSN 0360-1323.

Zhao and Lieber, 1994. Yao Zhao and Baruch B. Lieber. *Steady Inspiratory Flow in a Model Symmetric Bifurcation*. Journal of Biomechanical Engineering, pages Pages: 488–496, 1994.

A | Mass Balance Approach

The mass balance approach applies the principle of *conservation of mass* and can be used to analysis the particle concentration within a room. The mass balance approach is described below and is illustrated in Figure A.1.

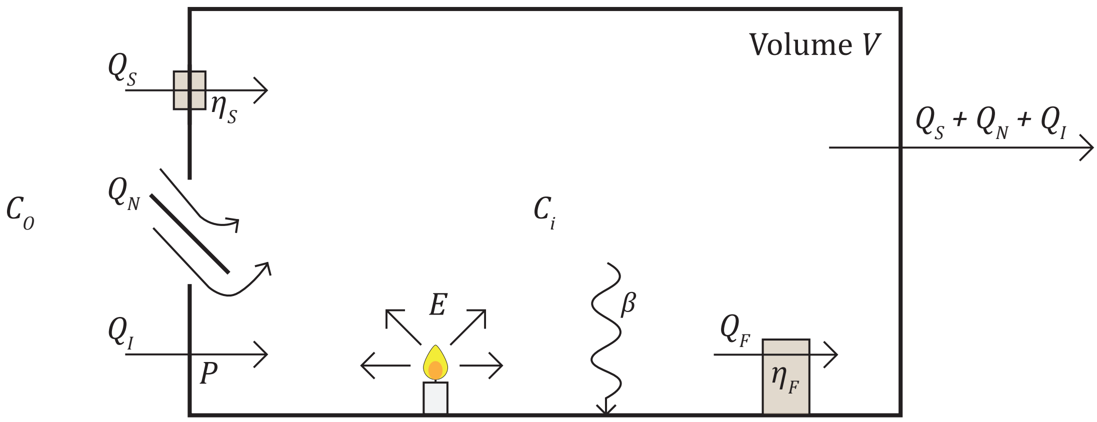

Figure A.1. Illustration of the processes that affect indoor particle concentration based on the mass balance equation [Nazaroff, 2004].

In the mass balance approach the indoor particle concentration, c_i (μg/cm^3), is assumed to be uniformly distributed within the spatial domain with interior volume, V (m^3). Air supply is delivered from outside the control volume with outdoor concentration C_o (μg/cm^3).
There are three different methods of supply; mechanical ventilation, Q_S (m^3/h), natural ventilation, Q_N (m^3/h) and infiltration, Q_I (m^3/h). Mechanical ventilation has a filter with a single-pass removal efficiency, η_S (-). Natural ventilation allows for free flow of particles through the openings, such as windows, as there are no filters placed in these. For infiltration it is assumed that a fraction, P (-), of the particles outside penetrate into the room.[Nazaroff, 2004].

Based on the conservation of mass, the airflow that enters the control volume must balance out with the airflow exiting the control volume. [Nazaroff, 2004].

Beyond the air supplied to the room, additional processes within the control volume may affect particle concentration. Air purifiers with a particle control filter with flow rate Q_F (-) may be inserted to minimise the particle concentration. The filters in the air purifiers also have a single-pass removal efficiency η_F (-). Particles may be supplied by emission sources within the control volume; the source rate E (μg/h) depends on the emission source. Finally some of the particles within the room will most likely be deposited onto room surfaces, such as tables, the floor, etc. This is expressed through the first-order loss-rate coefficient β (h^{-1}). [Nazaroff, 2004].

Indoor emission sources often occur periodically, instead of one steady source rate. Furthermore, the outdoor concentration varies greatly depending on its location, and may also occur periodically. The dominant source of the particles may therefore vary between the outdoor concentration and the indoor emission sources.

All of the above can be translated into a governing equation as seen in Equation A.1.

$$\begin{aligned}\frac{d(C_iV)}{dt} =& E + C_o[Q_S(1-\eta_S) + Q_N + Q_I P] \\ & - C_i[Q_F\eta_F + \beta V + (Q_S + Q_N + Q_I)]\end{aligned} \tag{A.1}$$

The left-hand side of the equation expresses the net rate of accumulation of the particle mass affecting the indoor concentration. The right-hand side expresses the indoor emission of particles from sources, the supply of particle matter from outdoor air and the removal from the indoor air. It is also possible to express the equation as time-invariant; however, a steady-state case is often unrealistic in terms of particle concentration, due to varying indoor emission, ventilation rates and outdoor concentration levels.[Nazaroff, 2004].

It is important to note that many of the variables included in the mass-balance equation are dependent on particle size. Ideally the equation should therefore be applied to each individual particle size in order to examine the indoor particle concentration of the room.

B | Particle Exposure Indexes

B.1 Susceptible Exposure Index

The susceptible exposure index, which is close related to local ventilation index, can be calculated from equation B.1. [Liu et al., 2016]

$$\varepsilon_i = \frac{(C_i - C_s)}{(C_r - C_s)} \tag{B.1}$$

Where

C_i	Concentration at the inhaled air of the susceptible individual
C_s	Concentration at the supply
C_r	Concentration at the return (exhaust)

An average values over a specified period can be used if the susceptible individual is breathing. A fully mixed room have a susceptible exposure index on 1.0. [Liu et al., 2016]

B.2 Deposition Fraction

The deposition fraction, DF, of the measurement results is calculated by Equation B.2.

$$DF = 1 - \frac{\text{Mass concentration in the lower airways}}{\text{Mass concentration in the breathing zone}} \tag{B.2}$$

The deposition fraction is calculated based on the mass concentration as this is what the SDS011 sensors in the breathing zone measure. The deposition fraction may vary over time, in particular within the first five minutes of the measurements when peak concentration is reached.

C Anatomy of the Human Respiratory System

The human respiratory system secures the transport of air to and from the lungs. This entails the supply of oxygen to the blood stream through inhalation simultaneously with the removal of carbon dioxide from the blood stream and the body through exhalation.

With each breath, oxygen enters the mouth or nose during inhalation. This is passed through the larynx and the trachea and divided into the two lungs though the bronchi. Each bronchi branch into several bronchial tubes, which are connected the alveolar ducts and lead to the alveoli where the gas exchange occurs. Carbon dioxide is then transported by the same route during exhalation, as illustrated on Figure C.1. [Palmgren, 2009].

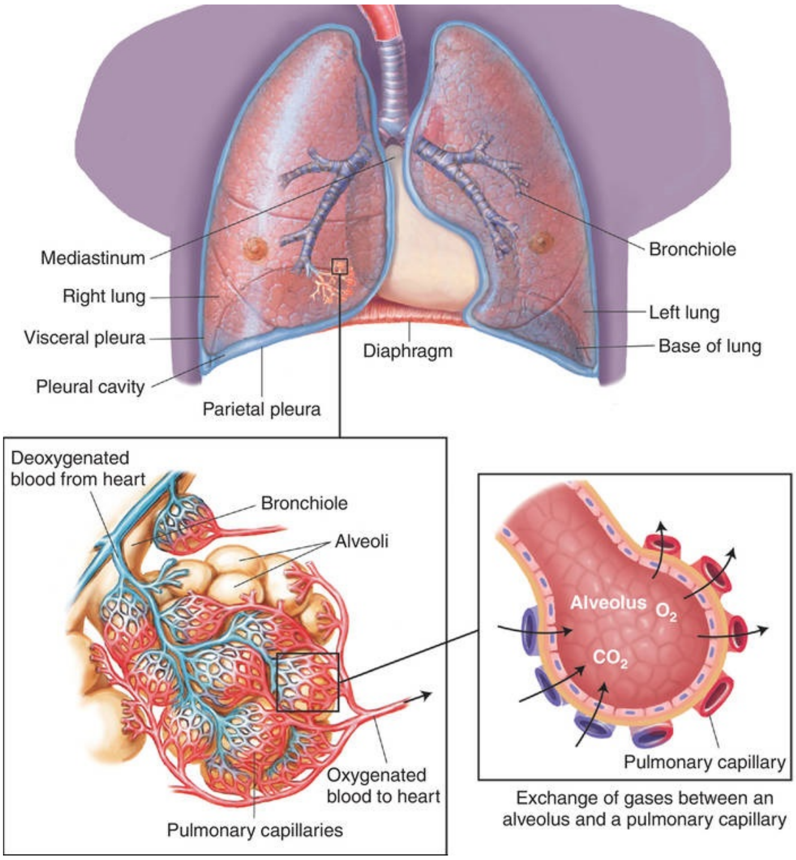

Figure C.1. Illustration of the human lungs with bronchioles and alveoli [The Free Dictionary by Farlex, 2017].

The exchange is indirect as blood acts as the passing medium of the gases.

The inhalation and exhalation of air is enabled by the contraction of the diaphragm, a muscle placed under the lungs. The contraction of the diaphragm causes an increase in volume of the thorax and lungs and thereby a decrease in pressure relative to the atmospheric air pressure. Air is inhaled as it travels from an area of high pressure to an area of lower pressure. The diaphragm then relaxes, returning to its initial equilibrium position and conducting an opposite pressure pattern, causing exhalation. [Tu et al., 2013]

In addition to transportation of the gases, the respiratory system functions include warming, humidifying and filtering the inhaled air.

An understanding of the functions of different anatomical parts of the respiratory system aids in understanding particle trajectories in the airways due to the surrounding boundary conditions. These can be split up in the following: nose and nasal cavity, pharynx, larynx, trachea, bronchi and bronchial tubes, and alveoli and alveolar ducts.[Tu et al., 2013]

C.1 Nose and Nasal Cavity

The nose and nasal cavity serve as the path for air to reach the lungs and is a part of the upper respiratory tract. Its size and shape may vary greatly between individuals, for example due to race and ethnicity, or diseases. [Tu et al., 2013]

The inhaled air is heated by a natural heat transfer process from the blood vessels located in the nasal cavity. The filtering of inhaled particles occurs through the nose hairs. The mucous traps particles such as dust and bacteria, while antibacterial enzymes destroy the particles in the nasal cavity. The mucous that builds up in the nose is transported to the throat, where it is in turn swallowed into the digestive system. The mucous layer changes in response to the climatic condition, affecting the narrowing or expanding the airway passages. The mucous wall is connected to a nerve which triggers a sneeze reflex if it comes into contact with particles.[Tu et al., 2013]

C.2 Pharynx

The pharynx, also referred to as the throat, provides a passageway for both the digestive and respiratory system. It is part of the upper respiratory tract.

The pharynx can be divided into three anatomical parts: the nasopharynx, the oropharynx, and the laryngopharynx. The nasopharynx and the oropharynx respectively connect the nasal chambers and the mouth to the laryngopharynx, or the posterior of the pharynx.

The pharynx is used to control passage of the body's intake. Food and drink is carried on through to the oesophagus, whereas air enters into the trachea. This is controlled by the epiglottis, part of the larynx, which is an elastic cartilage tissue that acts as a lid over the trachea. The epiglottis ensures that when food or drink is consumed, it cannot enter the trachea, thereby stopping breathing during consumption. If this happens, a cough reflex is triggered. [Tu et al., 2013]

C.3 Larynx

The larynx in the upper respiratory tract is also known as the voice box. It is used to produce the sounds at the vocal folds used for speaking, and to transport air from the pharynx to the trachea. The larynx is located in the anterior of the neck.

The larynx has ciliated mucous lining used to remove foreign particles. The mucous moves in an upward direction, out of the larynx and into the pharynx, to prevent it from entering the lungs. The ciliated mucous lining of the larynx has the same physiological features as the nasal cavity, where it can humidify and warm the inhaled air and remove particles. [Tu et al., 2013]

C.4 Trachea, Bronchi and Bronchioles

The tracheobronchial tree forms the upper part of the lower respiratory tract. These may vary in both diameter, length and number of divisions between each individual person.

The trachea is a hollow cartilaginous tube that extends from the larynx to the two main bronchi. It is 11-14 cm long, with a diameter of 1.0-2.7 cm. The diameter is commonly slightly larger for males than females.

The trachea divides into an asymmetrical left and right bronchus. There is an increased chance of particles depositing in the right bronchus, as it has a shorter, wider structure and is more vertical than the left bronchus. Figure C.2 shows the structure of the tracheobronchial tree dependent on the zone and generations. [Tu et al., 2013]

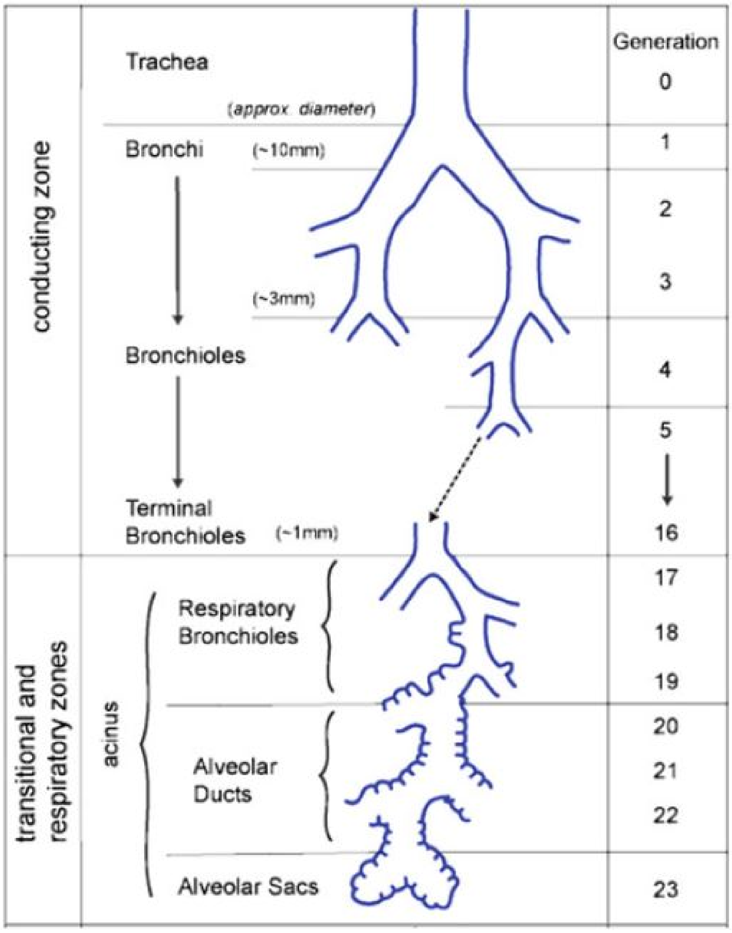

Figure C.2. Anatomical division of the tracheobronchial tree by generations [Tu et al., 2013].

The bronchi continue to divide for about 23 generations from the main bronchi. Initially the bronchi are supported by cartilaginous rings, which become more irregular plate of cartilage, until they eventually disappear at a diameter of approximately 1 mm. Once there is no cartilaginous support, they are referred to as bronchioles; these occur around generations 5-16. While the diameter of the individual bronchi decreases for each generation, the overall cross-sectional area of the bronchi increases as the number of bronchi increases, allowing for easy passage of the air. [Tu et al., 2013]

The bronchi also have the possibility to heat, humidity and remove particles. The mucous layer will be moved upward towards the pharynx and lead towards the oesophagus, such as in the larynx. The bronchioles do not contain mucous producing cells. Instead, foreign particles are removed by macrophages (white blood cells).

In the bronchi and the bronchioles the decreased diameter will reduce the inertial effect and essentially become a laminar flow.

C.5 Alveolar Ducts and Alveoli

Alveolar ducts are lined with alveoli, making a small cluster of cells that resemble a berry. These often appear at around the 20th generation and onwards. They are lined with elastic and collagen fibres. At the end of the alveolar ducts are the alveolar sacs, which are the end of the airway passages in the human respiratory system. The alveoli are connected to a network of blood capillaries, in which oxygen and carbon dioxide are exchanged through diffusion in less than a second.

Some of the bronchioles may also contain alveoli at the walls and are therefore referred to as being transitional.

C.6 Variations of the Human Respiratory System

The human respiratory system may vary greatly between people from different races, ethnicities and genders; hence it is impossible to model a human respiratory system which is representative of the whole human race.

Variations of the nose may come from climate adaptation to different eco-geographical locations. Small constricted nostrils can facilitate heat and moisture exchange and are advantageous in cold or dry climate environments. A bigger cross-sectional area for the nostrils prevents a lower heat transfer during exhalation. Another variation occurs at the laryngeal prominence (Adam's apple) in the larynx, where the difference between gender and age is prominent. Furthermore there is a general difference in the diameter of the airways between gender and age.

Beyond these genetic dispositions, there are a larger number of diseases that may cause other variations for every part of the respiratory system.

C.7 Modelling of the Breathing Function

A human male in a still-standing position has a mean breathing rate of 10.65 L/min and at rest a human breathes between 12-18 times a minute [Adams, 1993] [Barrett et al., 2010]. The breathing rate is defined as pulmonary breathing, which includes both inhalation and exhalation. The breathing rate can be reasonably assumed to be cyclic, where the breathing conditions are controlled by a sinusoidal function. The time-dependent flow rate is defined by Equation C.1. [Bahmanzadeh et al., 2016]

$$Q(t) = Q_{peak} \cdot sin(2\pi f t) \tag{C.1}$$

Where

$Q(t)$	Time-dependent flow rate [L/min]
Q_{peak}	Peak airflow rate which represents the maximum breathing intensity [L/min]
f	Frequency of breathing [1/s]

The frequency of breathing is chosen to be 15 times per minute, which is also used in Bahmanzadeh et al. [2016] and Liu et al. [2016]. The peak airflow rate can be calculated from the mean breathing rate by integration. Equation C.2 shows a modified version of Equation C.1 used to calculate the peak airflow rate.

$$\int_{t_1}^{t_2} Q_{mean} \mathrm{d}t = \int_{t_1}^{t_2} Q_{peak} sin(2\pi f t) \mathrm{d}t \tag{C.2}$$

By solving Equation C.2, the peak airflow is 16.73 L/min. Figure C.3 shows the time-dependent breathing function.

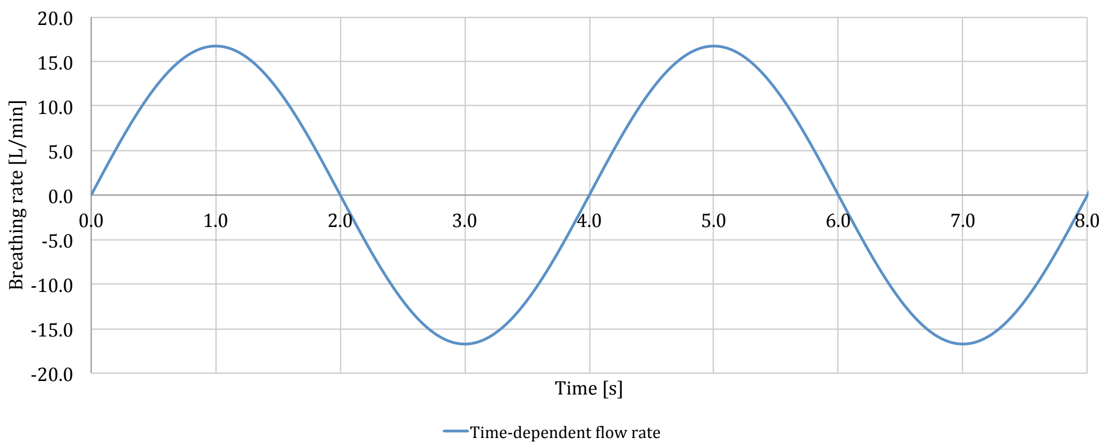

Figure C.3. The time-dependent breathing rate over one breathing cycle.

For conducting transient simulations the time dependent breathing rate needs to be applied. For steady state simulations the mean breathing rate of 10.65 L/min can be used.

D Morphometry of the Tracheobronchial Tree Cast

The morphometry of the tracheobronchial tree can be used to compare with previous studies on the lower airways. The airways vary from each person, so it is necessary to have a tool to compare the different examined airways. A table of the tracheobronchial tree can be found in Table D.1. The tracheobronchial tree is visualised on Figure D.1. The anatomy of the human respiratory system can be found in Appendix C.

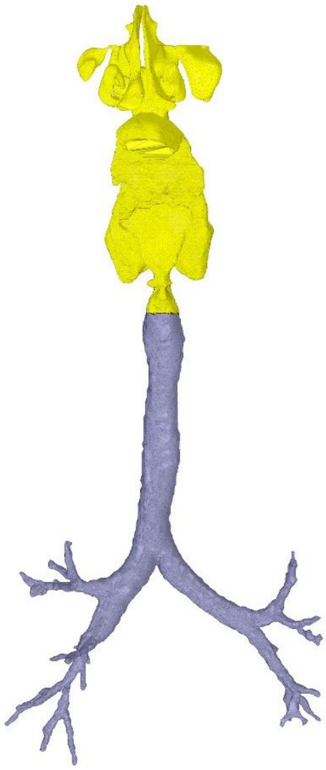

Figure D.1. The lower airway model used in this study. The blue part highlights the tracheobronchial tree of the airway.

The diameter in Table D.1 is the initial equivalent diameter after the bifurcation. The angle is the angle between the normal of the father branch and the normal of the sub branch. The methodology to find the diameter, angle and length can be found in the Digital Appendix. The table is based on work in Schlesinger et al. [1977].

Table D.1. Morphometry of the tracheobronchial tree cast.

Generation	**No. of**	**Diameter [mm]**			**Angle of branching [°]**			**Length [mm]**		
no.	**branches**	Mean	S.d	Range	Mean	S.d	Range	Mean	S.d	Range
0	1	16.22	-	-	0	-	-	119.89	-	-
1	2	12.85	1.38	(11.87-13.82)	31.45	4.45	(28.30-34.60)	44.06	16.68	(32.26-55.86)
2	4	8.06	1.29	(6.95-9.73)	29.08	18.75	(9.20-52.60)	15.74	3.33	(12.44-20.31)
3	8	5.11	0.96	(4.08-7.13)	33.69	14.29	(8.90-51.50)	8.89	5.54	(3.28-18.36)
4	14	3.57	1.31	(1.92-6.66)	24.47	8.95	(8.60-37.70)	11.60	3.11	(6.47-17.93)
5	14	2.71	0.82	(1.77-4.26)	26.44	14.25	(9.70-61.20)	7.60	3.48	(2.04-12.68)
6	6	3.41	0.54	(2.73-4.28)	27.02	8.83	(16.60-38.00)	13.51	3.43	(9.35-18.75)
7	6	2.72	0.77	(1.57-3.45)	26.60	9.42	(15.70-39.30)	15.35	6.77	(7.40-22.96)

E | Equipment

The following appendix contains descriptions of the particle sensors and the working principle used the full-scale laboratory experiments.

E.1 Aerodynamic Particle Sizer S3321

The Aerodynamic Particle Sizer (APS) Model 3321 spectrometer measures count size distributions of the aerodynamic diameter. The aerodynamic diameter can be measured for the particle range 0.5 - 20.0 μm. [TSI, 2012]

The APS3321 can be applied to many investigations, such as the monitoring of indoor air quality and inhalation toxicology. A picture of the APS3321 can be seen in Figure E.1.

Figure E.1. The APS3321 spectrometer.

E.1.1 Method

The APS3321 works by measuring the time-of-flight of particle transported through the nozzle under accelerated flow conditions. Time-of-flight is measured by two laser beams placed at the entry and exit point. For each particle that crosses the laser beams, a double-crested profile is created. [TSI, 2012]

The set-up of the APS3321 and the corresponding aerosol flow can be seen in Figure E.1.1.

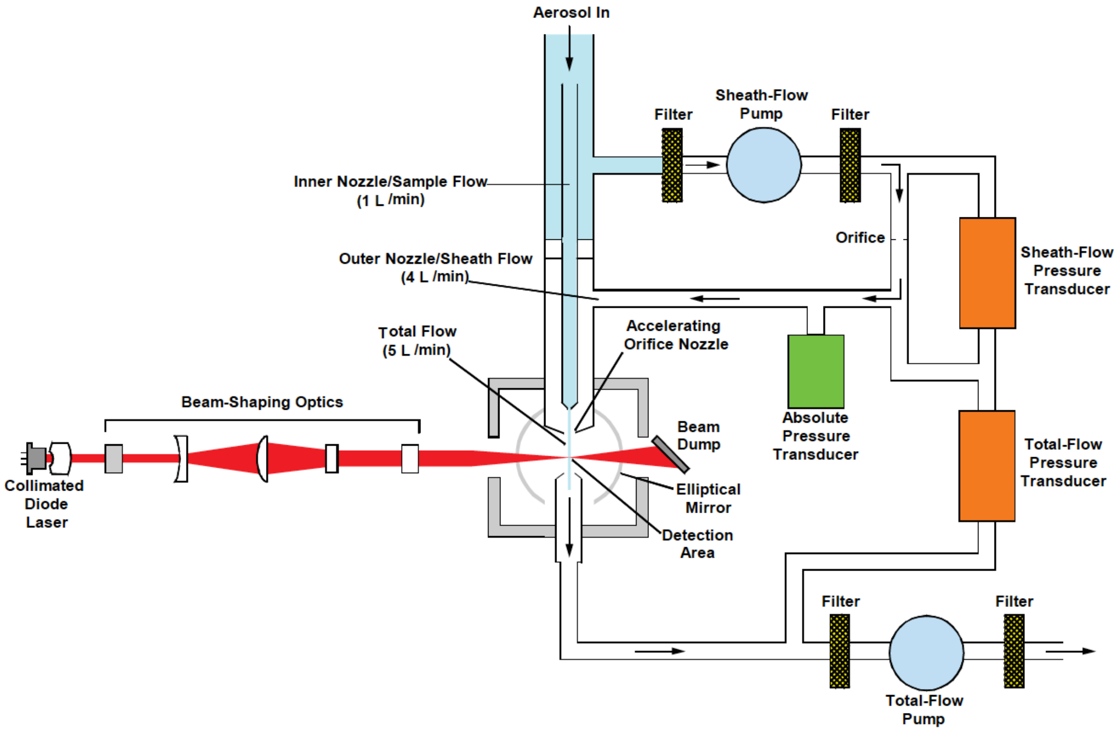

Figure E.2. The aerosol flow within the APS3321 spectrometer.

The air sample is absorbed into the inner nozzle at a sample flow of 1 L/min. Some of the aerosol is carried through to the sheath-flow pump, where it has been filtered both before and after. The sheath-flow pump accelerates the flow to the sheath flow to 4 L/min. The sheath flow allows the air flow to be centred as it travels through the accelerating orifice nozzle. The sample flow of 1 L/min is thereby accelerated by the sheath flow to 5 L/min. Under these accelerated conditions, time-of-flight of the particles may be measured due to inertial properties, and then the aerodynamic size of the particle can be determined. [TSI, 2012]

The filters prior and posterior to the pumps ensure pure samples and prevent damage to the APS3321.

E.1.2 Events

The APS3321 measures double-crested profiles to determine the aerodynamic diameter of the particles. The profile of the particles may be classified into four different events.

The double-crested profile is registered by the differential circuit.

The APS3321 can detect coincidence, the appearance of more than one particle in the sensor's measuring volume. This decreases the risk of false counts, while providing more accurate size-resolved number concentrations, and more efficient small-particle size counts. [TSI, 2012]

Event 1

The first event occurs when only one of the crests exceeds the threshold. This event often occurs because of small particles. This event is illustrated on Figure E.1.2.

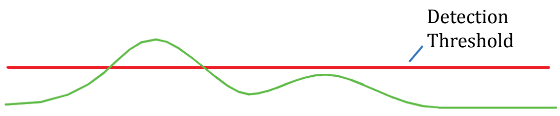

Figure E.3. The profile of Event 1 [TSI, 2012].

Event 2

Event 2 is a valid double-crested profile. Both of the crests exceed the detection threshold and the time-of-flight is measured. This event is illustrated on Figure E.1.2.

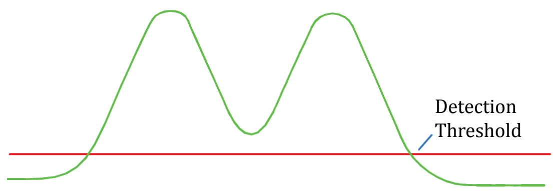

Figure E.4. The profile of Event 2 [TSI, 2012].

Event 3

Event 3 occurs when there are two particles in the gate window at the same time. The second particle enters the gate window before the first particle has left. This event is illustrated on Figure E.1.2.

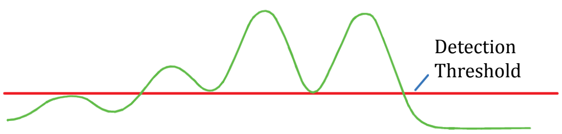

Figure E.5. The profile of Event 3 [TSI, 2012].

Event 4

Event 4 occurs when the time-of-flight of the particle exceeds the maximum timer range of 4.096 μs. This could occur for either a very large or a recirculating particle. This event is illustrated on Figure E.1.2.

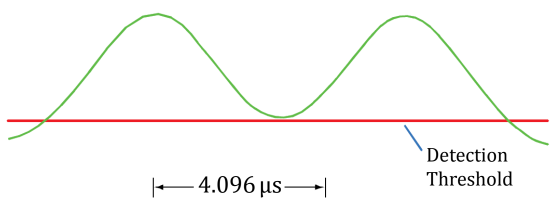

Figure E.6. The profile of Event 4 [TSI, 2012].

E.2 Particulate Matter Sensor 5003

The PMS5003 particle sensors, developed by Plantower, measure mass concentration (μg/cm^3) down to 0.3 μm. An image of the PMS5003 sensor can be seen in Figure E.2.

Figure E.7. The PMS 5003 particle concentration sensor [Yong, 2016].

The PMS5003 particle sensor uses light-scattering intensity to determine the mass concentration. Particles are absorbed into the light-scattering cavity with a laser inside it. The laser radiates the particles suspended in the air. The angle is recorded in which the laser is reflected off the particles. [Yong, 2016]

E.3 Super Dust Sensor 011

The SDS011 particle sensors from Nova Fitness Co. measure the mass concentration of $PM_{2.5}$ and PM_{10}. The particle sensors are able to measure particles in the size range 0.3 - 10 μm from 000.0 - 999.9 μg/cm^3. An image of the SDS011 sensor can be seen in Figure E.3. [Nova Fitness Co., 2015]

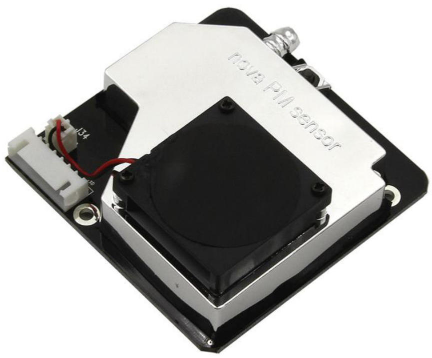

Figure E.8. The SDS011 particle concentration sensor [Nova Fitness Co., 2015].

As with the PMS5003, the SDS011 measures by the laser-scattering principle. It has a built-in fan and a response time of less than 10 s. The particle sensor has a working temperature range of -10 °C to 50 °C and a working Relativ humidity below 70%. The accuracy of the SDS011 is 70% for 0.3 μm and 98% for 0.5 μm. [Nova Fitness Co., 2015]

F Images from the Experimental Investigations

This appendix contains images of the equipment and the measurement set-up used for the experimental investigation in lower airway exposure.

F.1 3D Printed Model

Figures F.1 - F.3 show the individual parts of the 3D printed model.

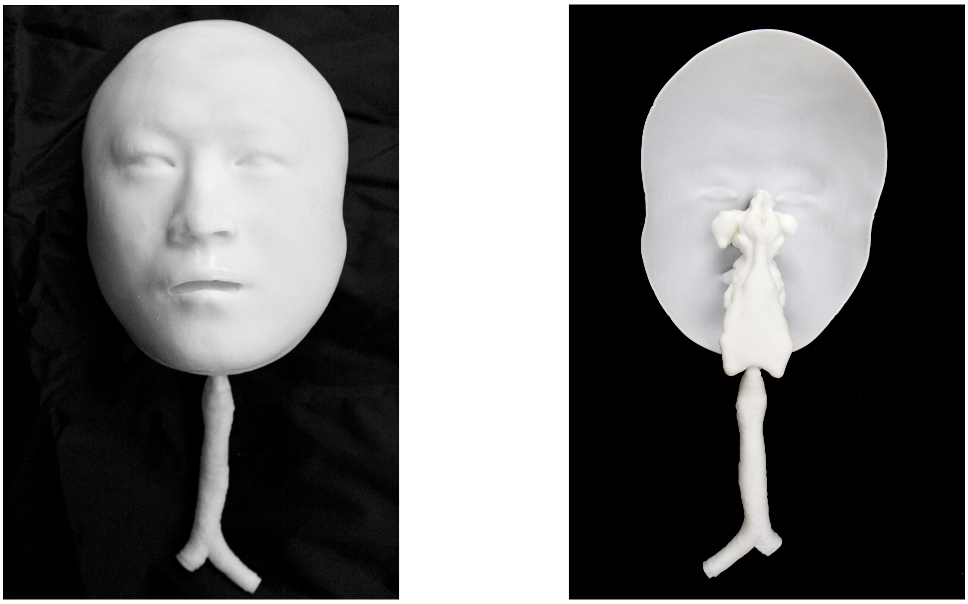

Figure F.1. The nasal cavity, mouth, pharynx, larynx, trachea and upper part of the bronchi in the 3D printed model.

Figure F.2. The outer parts of the left and right lung shell of the 3D printed model.

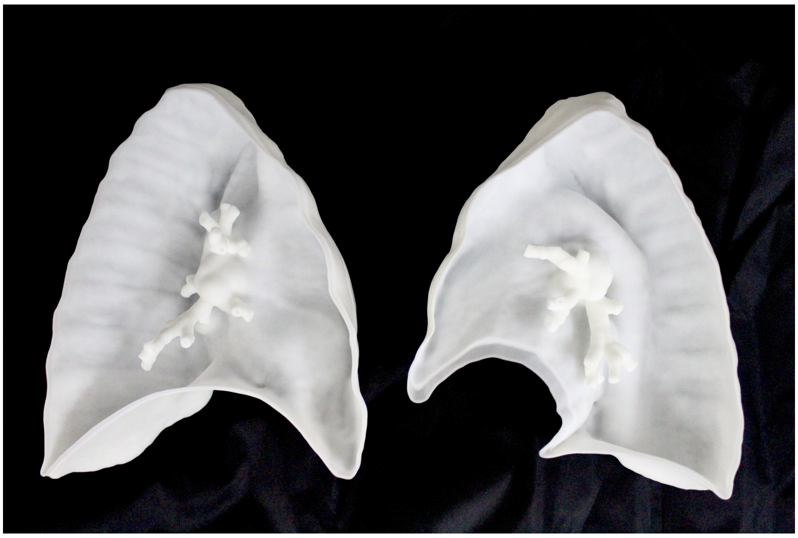

Figure F.3. The attached bronchi/bronchioles on the inner left and right lung shell in the 3D printed model.

F.2 Measurement Set-up of the Investigation of Particle Exposure by Different Cooking Oil Types

Figures F.4 - F.8 show images of the set-up used in the measurements investigating particle exposure by different cooking oil types.

Figure F.4. The measurement set-up for investigation of particle exposure by different cooking oil types from a front view.

Figure F.5. The measurement set-up for investigation of the particle exposure by different cooking oil types from a side and back view.

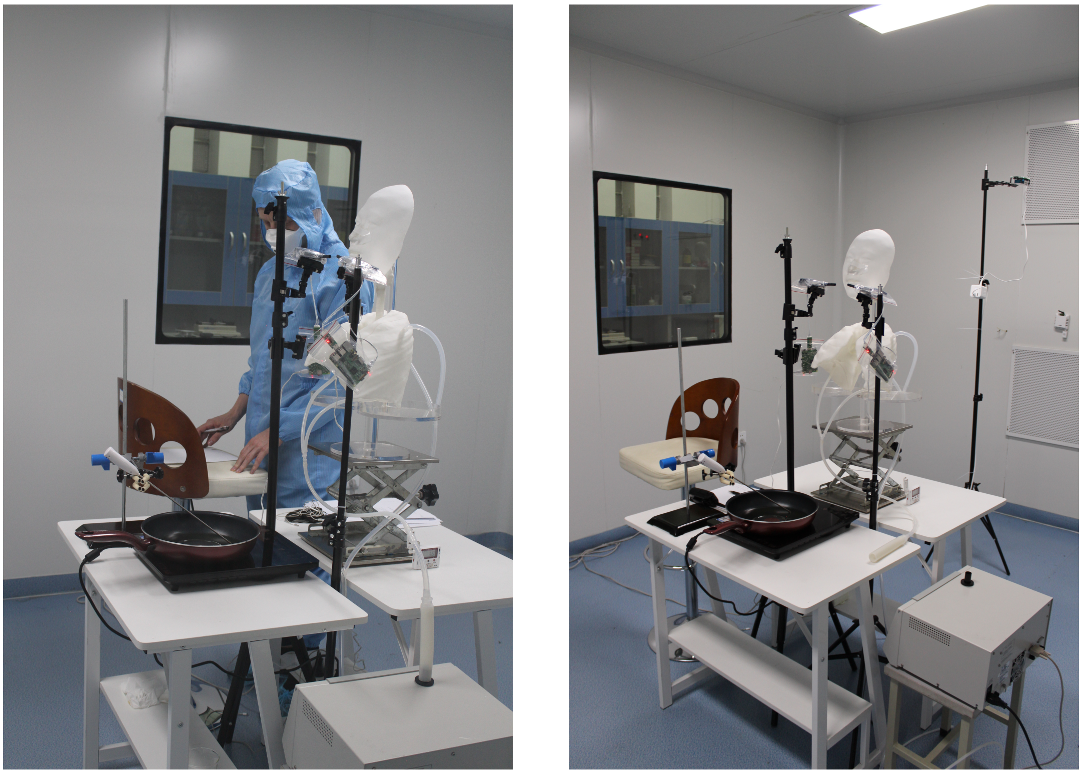

Figure F.6. The measurement set-up for investigation of the particle exposure by different cooking oil types. The left image shows the human occupant in a standing position taking notes and the right image shows the set-up without the human occupant.

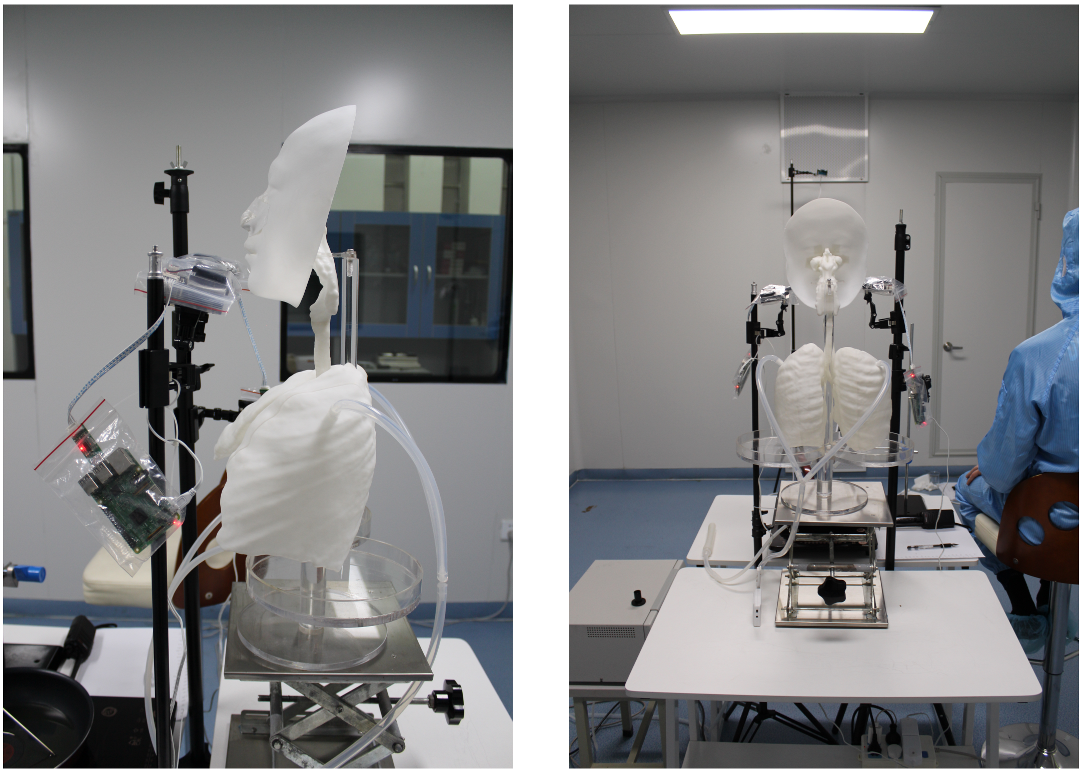

Figure F.7. The measurement set-up for investigation of particle exposure by different cooking oil types. The left image shows the location of the 3D printed model from the side and the right image shows it from behind.

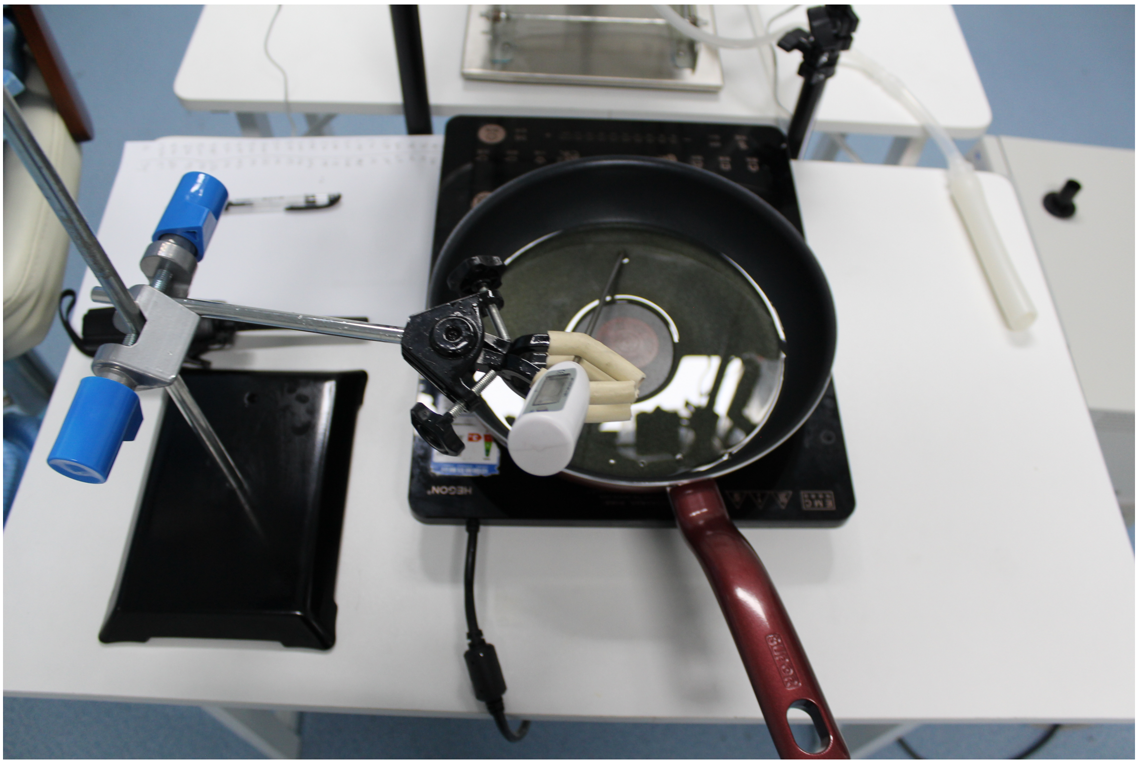

Figure F.8. The measurement set-up for investigation of the particle exposure by different cooking oil types. The image shows the electric stove and pan with cooking oil.

F.3 Measurement Set-up of the Investigation of Thermal Plume

Figures F.9 - F.10 show images of the set-up used in the measurements investigating the impact of the thermal plume on particle concentration in the breathing zone.

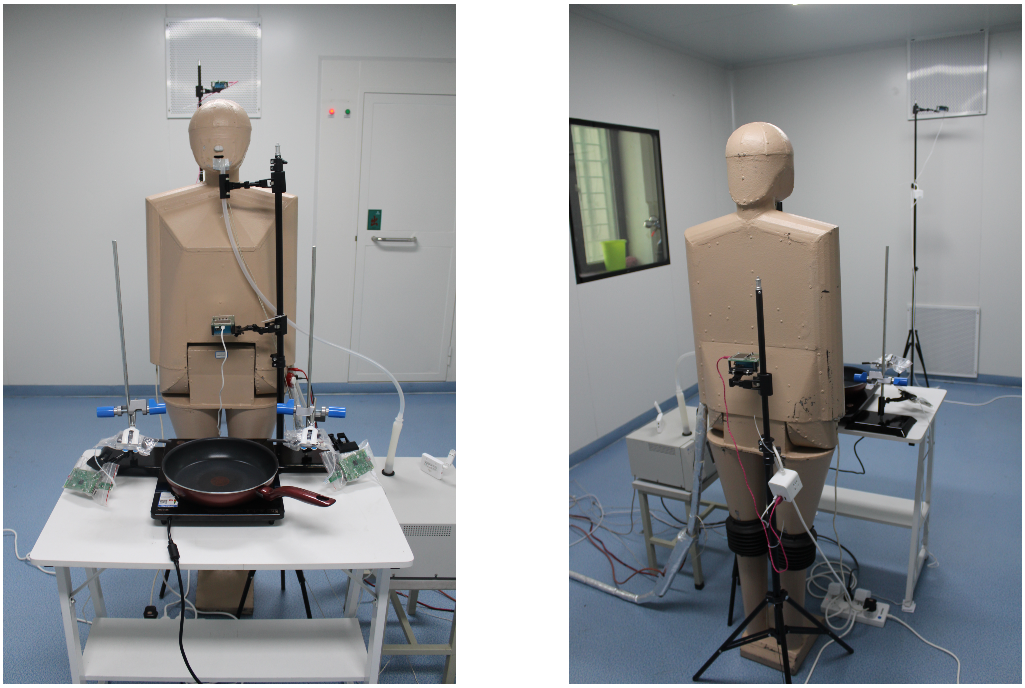

Figure F.9. The measurement set-up for thermal plume measurements from a front and back view.

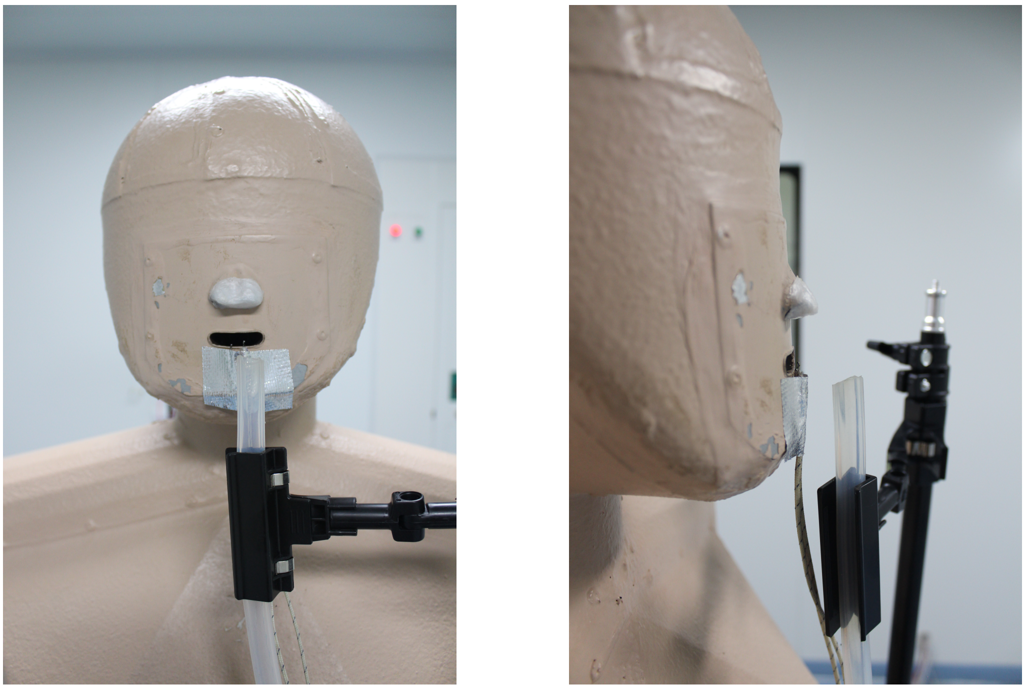

Figure F.10. The measurement set-up for thermal plume measurements, showing the location of the APS3321 sensor in the breathing zone of the manikin.

G | Measurement Parameters

The parameters of the measurements have been chosen based on regulations and typical real-life situations. The parameters can be seen listed in Chapter 6. The reasons behind each chosen parameter are described in this Appendix.

G.1 Clean Room

The fixed parameters for the clean room can be seen in the Table G.1.

Table G.1. Fixed parameters of the clean room.

T_i	**RH**	**Ventilation type**	**Ventilation rate**
22°C ±2°C	-	Displacement ventilation	$1.65\,\mathrm{h}^{-1}$

The indoor temperature of 22°C ±2°C is determined by indoor climate category II from DS/EN 15251 [2007].

The humidifier in the air handling unit does not work properly, so relative humidity cannot be controlled in the clean room. The relative humidity may have an influence on the particle trajectories as the relative humidity affects the evaporation of droplets, as established in Chapter 2. The relative humidity should still be monitored for each measurement.

Displacement ventilation is applied in the room. Inlet and outlet are placed on the same wall, with the inlet near the floor and the outlet near the ceiling. This can be seen in Figures 6.1, 6.2 and 6.3 on page 22. The ventilation rate is set based on the Danish Building Regulations 2018. These state the following:

"*Kitchens must be provided with extractor hoods with exhaust ventilation above the hotplates. The extractor hood must have adjustable, mechanical extraction and vents to the external air and be sufficiently efficient to trap damp and gaseous pollutants from food preparation. It must be possible to increase the extraction to at least 20 l/s.*"

[Trafik & Byggestyrelsen, 2016]

Using the flow rate of 20 l/s as a guideline, this would be the equivalent of an air change rate of $1.65\,\mathrm{h}^{-1}$ for the clean room.

The cooking oils will be ‘activated’ on a pan placed on an electric stove.

G.2 3D Airway Model

The 3D printed airway model is placed at standing height, as this is the most realistic position regarding cooking activities. This is determined to be 1.80 m, as can be seen in Chapter 6. As the airways were modelled from a human male, the breathing rate is based on a standing male with an activity level of 1.2 METS as established in Appendix C.7 with a mean breathing rate on 10.65 L/min and with 15 breathing cycles per minute. Based on the breathing rate a sampling length on the APS3321 is determined to be 4 s.

Breathing will only be carried out through the oral opening for the various oil experiments.

It should be ensured that the flow rate within the lungs of the 3D printed model is sufficient to ensure well-mixed conditions, so that the measured particle concentration is representative of the whole lung space. As the breathing rate in the airways 10.65 L/min and the lung volume is approximately 3.42 L, the air change rate is 185 h^{-1}. Thereby well-mixed conditions are assumed. The calculation of the volume of the lungs can be found in the Digital Appendix.

G.3 Human Occupant

A human occupant is placed adjacent to the pan/electric stove and the 3D printed model to simulate that of a chef standing next to the source. Reasons for this are listed below:

- The human occupant generates a natural thermal plume. This is not the case for the 3D printed model. By having the 3D printed model in close proximity to the human, similar thermal conditions are approached, as if the 3D model had its own thermal plume.
- The human occupant is able to control the electric stove, the thermometer and any other potential equipment in the room. By having a stationary occupant, interruptions to the particle trajectories and airflow are minimal.
- Fire safety reasons. The human occupant is able to extinguish the fire quickly by being in close proximity.

It is important that the occupant of the room is stationary and remains still to avoid any disturbances to the airflow and particle trajectories of the room. His movement should thereby be limited.

The main tasks of the human occupant are:

- Turning on/off the electric stove
- Pouring the oil onto the pan
- Monitoring the temperature of the oil
- Observing when the smoke point is reached
- Being prepared in case of fire

The human occupant is a sitting male at 1.80 m.

G.4 Emission Sources

The cooking oil amount has been determined to be 1 dl based on Gao et al. [2013a] and Gao et al. [2013b]. The density of the cooking oil is assumed to be 1 g/cm^3 in the APS3321.

G.4.1 Smoke Points

The smoke points of the oil occur when heated oil starts generating smoke. The difference in smoke points may have an effect on the generated particles by each oil type and should thereby be taken into consideration. The smoke points of the oils have been investigated prior to the measurements by heating the oil under the same conditions as for the experiment. The smoke point is reached when smoke becomes clearly visible from the oil.

The smoke points of the different oil types based on literature can be seen in Table G.2. However, the smoke points may still vary based on the exact brand of oil and its method of processing. The smoke points of the cooking oils used in these measurements have therefore been tested and can also be seen in Table G.2.

Table G.2. Smoke points of the four oil types [Melina, 2019].

		Corn oil	**Olive oil**	**Peanut oil**	**Sunflower oil**
Smoke Points	Tested	~165°C	~145°C	~180°C	~190°C
	Literature	232°C	191°C	232°C	232°C

H | Calibration of Instruments

This appendix contains the calibration graphs carried out for the instruments used in the measurements.

H.1 Calibration of Particle Sensors

All eight of the particle sensors have all been calibrated using sunflower oil against the APS3321.

The resulting coefficients from the calibrations can all be seen in Table H.1.

Table H.1. Coefficients for calibration of the particle sensor data.

Particle Sensor	$\mathbf{PM_{2.5}}$	$\mathbf{PM_{10}}$
PMS5003 Sensor 1	0.4540	0.3852
PMS5003 Sensor 2	0.3166	0.2895
PMS5003 Sensor 3	0.2280	0.2314
PMS5003 Sensor 4	0.2689	0.2657
PMS5003 Sensor 5	0.2493	0.2516
PMS5003 Sensor 6	0.2552	0.2553
SDS011 Sensor 6	0.5668	0.4962
SDS011 Sensor 7	0.5489	0.4572

It should be noted that PMS5003 Sensors 3 - 6 were only used for the thermal plume measurements.

The calibrations may have been limited by the use of sunflower oil, as this has very limited particle matter above the size of 2.5 μm, possibly compromising the calibration for PM_{10}. Calibrations could therefore potentially be carried out using monodispersed particles or different emission sources for comparison.

The calibration graphs for each sensor and particulate matter type can be seen below. The calibration graphs can also be found with higher resolution in the Digital Appendix.

H.1.1 Calibration for $PM_{2.5}$

Figures H.1 to H.8 show the $PM_{2.5}$ calibration graphs for the eight sensors. Data for the PMS5003 sensor calibrations were collected every and data for the SDS011 sensor calibrations were collected every minute.

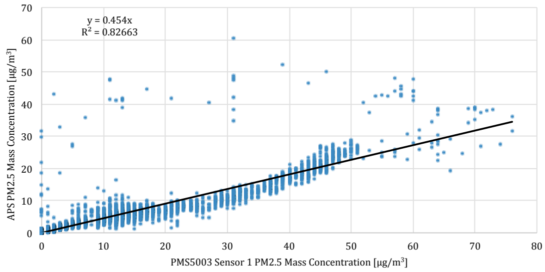

Figure H.1. $PM_{2.5}$ calibration graph for PMS5003 Sensor 1.

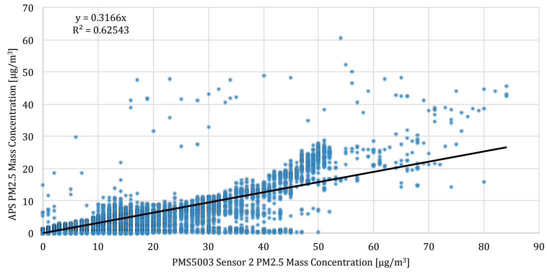

Figure H.2. $PM_{2.5}$ calibration graph for PMS5003 Sensor 2.

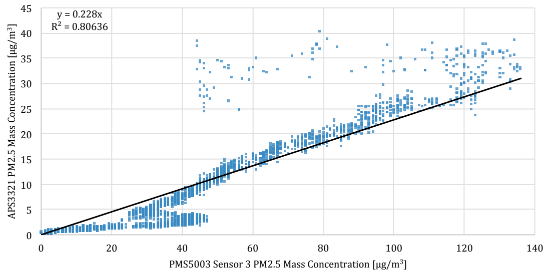

Figure H.3. $PM_{2.5}$ calibration graph for PMS5003 Sensor 3.

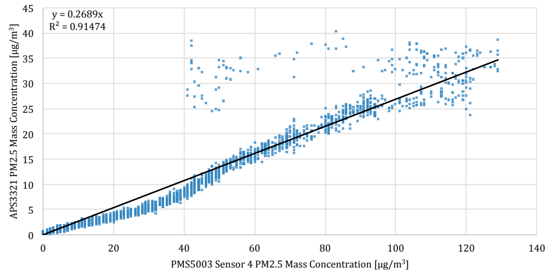

Figure H.4. $PM_{2.5}$ calibration graph for PMS5003 Sensor 4.

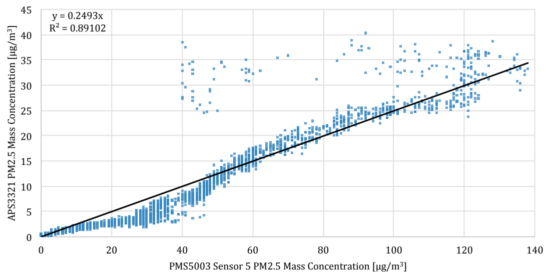

Figure H.5. $PM_{2.5}$ calibration graph for PMS5003 Sensor 5.

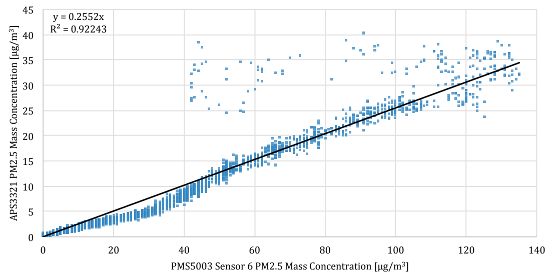

Figure H.6. $PM_{2.5}$ calibration graph for PMS5003 Sensor 6.

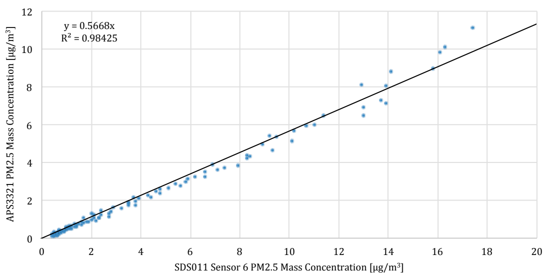

Figure H.7. $PM_{2.5}$ calibration graph for SDS011 Sensor 6.

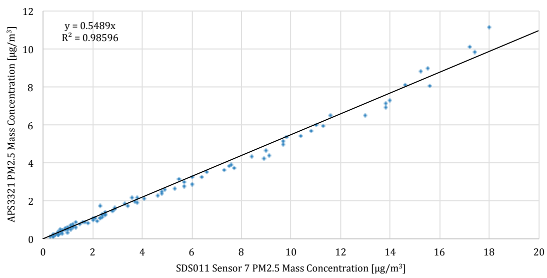

Figure H.8. $PM_{2.5}$ calibration graph for SDS011 Sensor 7.

H.1.2 Calibration for PM_{10}

Figures H.9 to H.16 show the PM_{10} calibration graphs for the eight sensors. Data for the PMS5003 sensor calibrations were collected every and data for the SDS011 sensor calibrations were collected every minute.

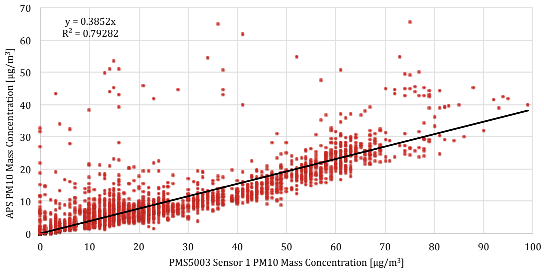

Figure H.9. PM_{10} calibration graph for PMS5003 Sensor 1.

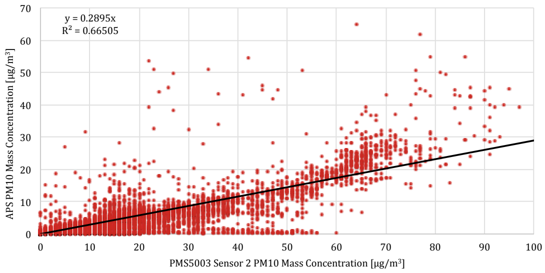

Figure H.10. PM_{10} calibration graph for PMS5003 Sensor 2.

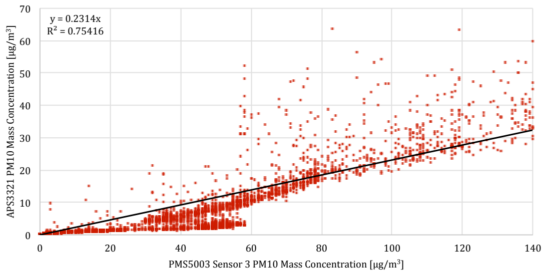

Figure H.11. PM_{10} calibration graph for PMS5003 Sensor 3.

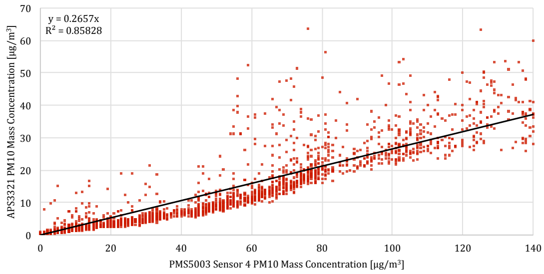

Figure H.12. PM_{10} calibration graph for PMS5003 Sensor 4.

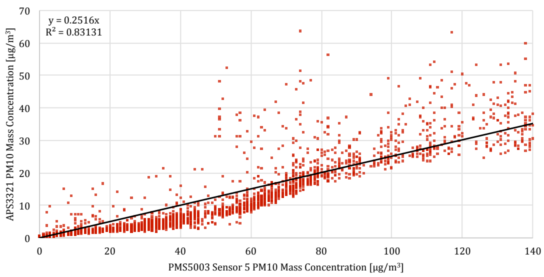

Figure H.13. PM_{10} calibration graph for PMS5003 Sensor 5.

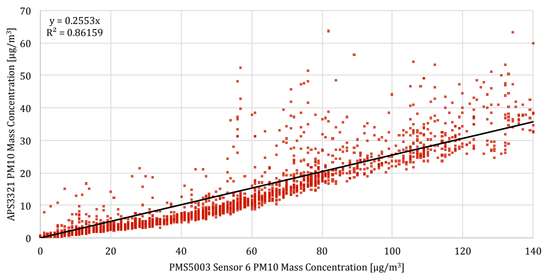

Figure H.14. PM_{10} calibration graph for PMS5003 Sensor 6.

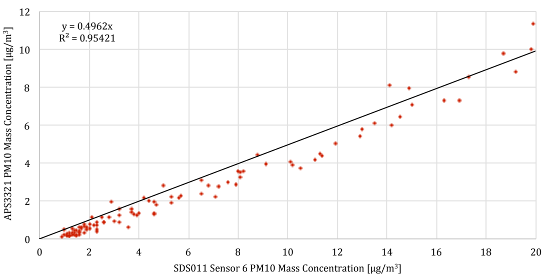

Figure H.15. PM_{10} calibration graph for SDS011 Sensor 6.

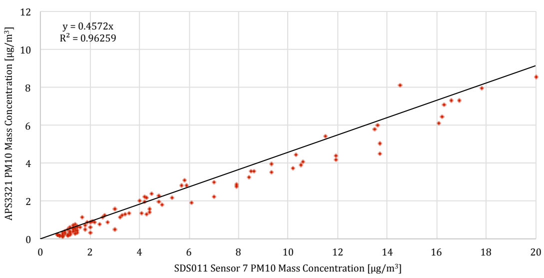

Figure H.16. PM_{10} calibration graph for SDS011 Sensor 7.

H.2 Calibration of Ventilation System

The ventilation flow rate in the clean chamber is controlled by the frequency. The fan in the air handling unit has been calibrated by using TSI equipment. The calibration results can be seen in Figure H.17.

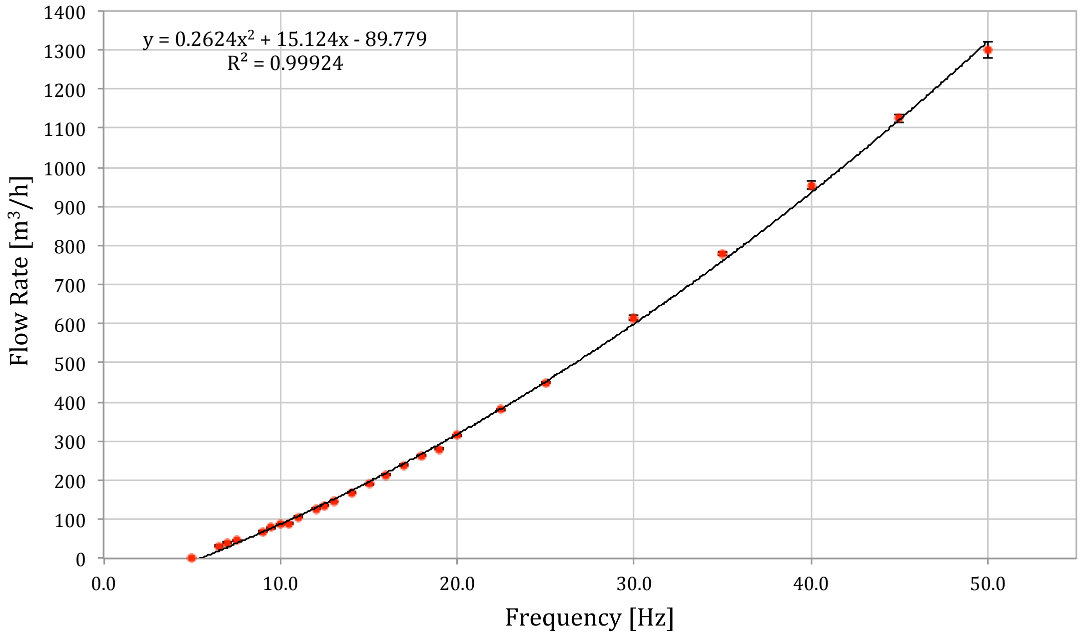

Figure H.17. Flow rate versus frequency in the clean room.

Based on the above graph, the frequency was set for the desired ventilation flow rates during the measurements.

I Preliminary Investigation of a Cylindrical Test Case

This appendix investigates a basic cylindrical geometry developed in a tube shape, roughly approaching the structure of a trachea. This is carried out to get better acquainted with the software Fluent and the physics applied in the software.

I.1 Methodology

By varying the settings and physical models of the simulations, it is possible to investigate the effect that the different settings may have on particle motion and behaviour, while simultaneously becoming more familiar with the theory.

I.1.1 Case Description

The geometry used is the of a long cylinder tube, measuring 1 m in diameter and 3 m in length. The initial velocity of air flow is 2 m/s. The case is considered isothermal. The geometry of the cylinder can be seen in Figure I.1 and the mesh can be seen in Figure I.2.

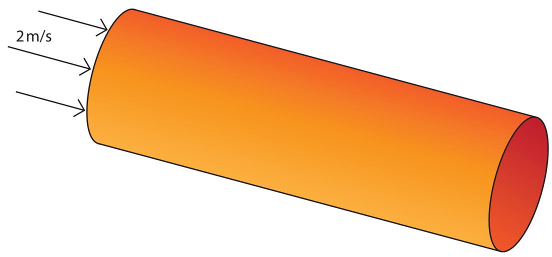

Figure I.1. The geometry of the cylinder tube used in the case.

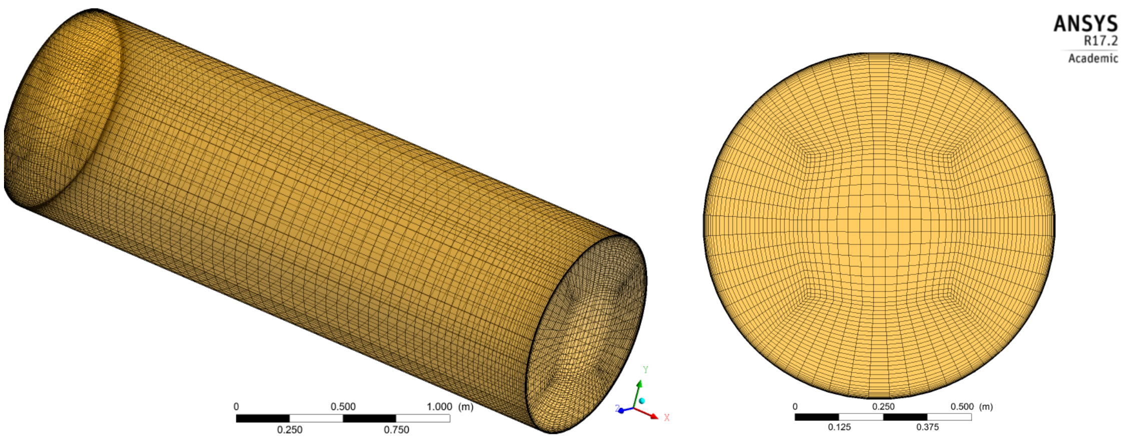

Figure I.2. The mesh of the cylinder tube used in the case.

Variations in the setting are applied as seen in Table I.1.

Table I.1. Variation in the settings for the cylinder tube simulations. * The influence of turbulent dispersion on the discrete phase is examined in test nr. 8.

Test no.	**Phase**	**Time step size**	**Boundary conditions**	**Particle size**	**Particle initial velocity**
1	Steady	-	Trap/Escape	$10\,\mu$m	2 m/s
2	Transient	0.05 s	Trap/Escape	$10\,\mu$m	2 m/s
3	Transient	0.01 s	Trap/Escape	$10\,\mu$m	2 m/s
4	Steady	-	Reflection/Escape	$10\,\mu$m	2 m/s
5	Steady	-	Trap/Escape	$1\,\mu$m	2 m/s
6	Steady	-	Trap/Escape	$100\,\mu$m	2 m/s
7	Steady	-	Trap/Escape	$10\,\mu$m	0 m/s
8*	Steady	-	Trap/Escape	$10\,\mu$m	2 m/s

Test nr. 1 serves as the benchmark with one parameter being changed for the remainder of the tests.

The phase is changed between steady and transient phase. As mentioned in Chapter 2, steady state is usually unrealistic as particle injections are often episodic. Two transient simulations are carried out, each with different time steps of 0.01 s and 0.05 s respectively. This also enables an evaluation of how different time steps may affect the particle trajectories.

The boundary conditions of the walls of the cylinder and the outlet must also be defined. The outlet is always defined as escape, as the particles are carried through the lower airways into the lungs in the realistic model. The walls are defined as either trap or reflection, as previously mentioned in Chapter 10.

The particle size has an influence of the forces affecting the particle's trajectory. The relaxation time is larger for particles with a bigger diameter, affecting the drag force. The three particle sizes investigated in this case are $1\,\mu$m, $10\,\mu$m and $100\,\mu$m.

Finally the influence of the initial velocity of the particle is investigated by varying between a particle in motion at 2 m/s and a particle in stand-still.

I.1.2 Set-up of the CFD simulations

Realisable k-ϵ model has been used to simulate the continuous phase, as the Reynolds Number is in the order of 10^5. The calculation can be found in the Digital Appendix. The enhanced wall treatment has been used to solve the viscous affected area near the wall. The inlet is defined as velocity inlet with a turbulent intensity of 5% and the outlet is defined as a pressure outlet. The turbulent intensity of 5% is recommended by André Bakker [2008]. A more detailed description of the set-up in Fluent can be found on the Digital Appendix.

Meshing of the Cylinder

The mesh of the cylinder is conducted with hexahedral cells. A mesh independence test has been conducted to determine the numbers of cells in the mesh. As illustrated in Figure I.3 the velocity profile doesn't change significantly when the numbers of cells exceed 379905 cells.

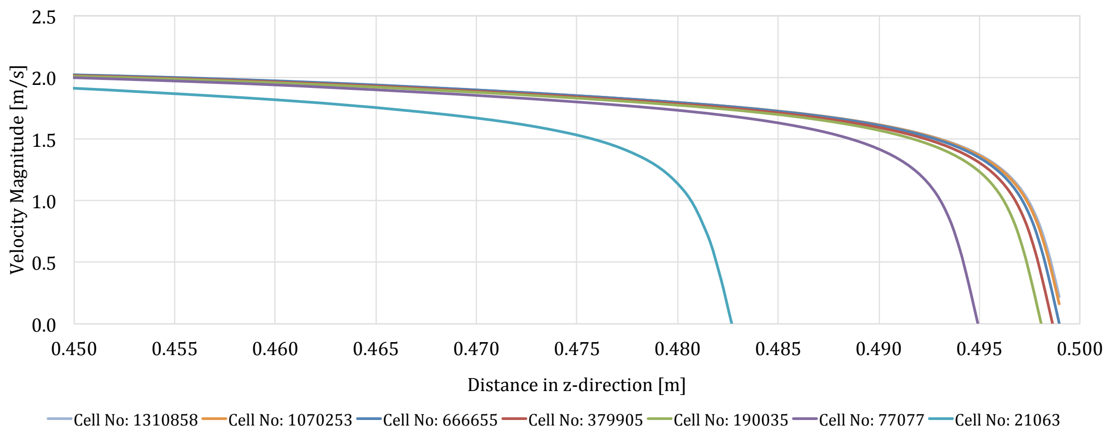

Figure I.3. Velocity profile in the cylinder from the difference meshes.

The y^+ value can be estimated from hand calculations in order to avoid a long iterative process, as the y^+ value is dependent on the shear force and the distance from the node to the wall. The y^+ should be below 1.0, when using the enhanced wall treatment with the k-ε model. The hand calculations can be found in the Digital Appendix. Figure I.4 shows that the y^+ value meets the requirements for using the enhanced wall treatment, where the y^+ value should be below 1.0.

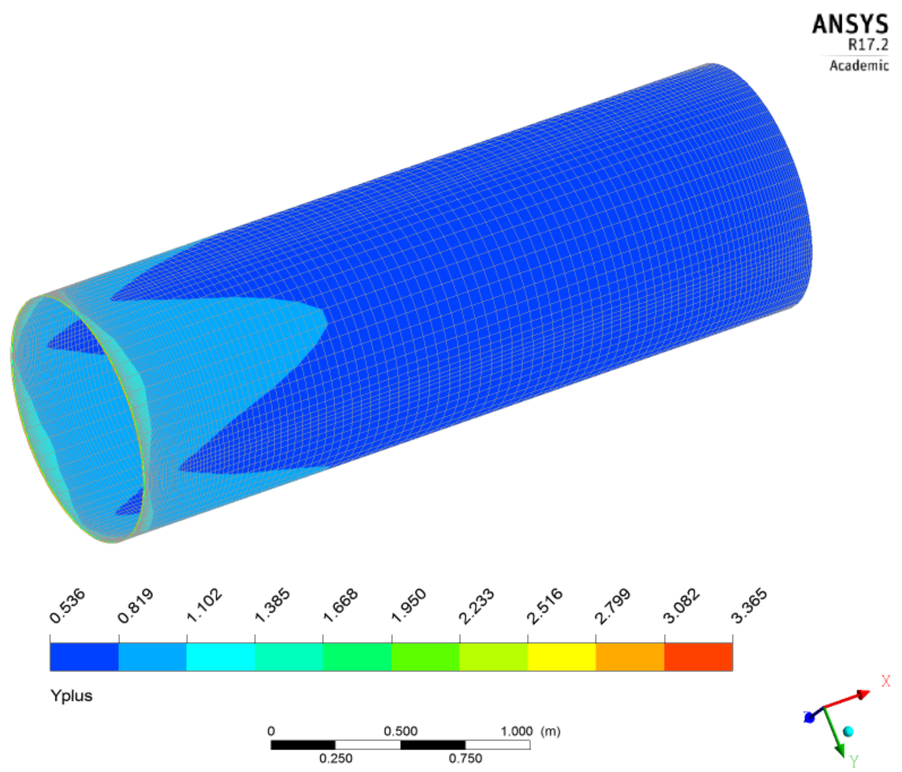

Figure I.4. Contour map of the y^+ values at the wall boundary.

It is only at the inlet, where y^+ is above 1.0, which is assessed to be acceptable.
The dense mesh at the wall boundary results in extreme aspect ratio, due to the small height of the cells. This is necessary to maintain a low y^+ value with a non-uniform mesh.

Convergence

To determine whether or not a solution is converged the following scenarios should be satisfied. [Versteeg and Malalasekera, 2007]

- The continuity, momentum and k-epsilon residuals need to be below 10^{-3}.
- The residuals should not fluctuate.
- The overall mass balance is obtained with an error of maximum 0.001%

Discrete Phase Modelling

The discrete phase is modelled by coupled discrete phase modelling, where the discrete phase is updated for each iteration. The interactions between particles are neglected as the mass rate of the injection is $1.0 \cdot 10^{-20}$. The released particles are monodispersed with a density of $1.0\,\mathrm{kg/m^3}$. A detailed description of the set-up can be found in the Digital Appendix along with a guide for the discrete phase modelling in ANSYS Fluent.

The additional forces mentioned in Section 10.1.1 have been investigated. These include the Brownian force, Saffman's lift force, virtual mass force, pressure gradient force and Magnus lift force. The thermophoretic force is neglected as the cylinder test case is isothermal. The wall reflection in test nr. 4 is modelled with a constant reflection coefficient 0.8.

I.2 Post-Processing of Simulations Results

The simulation results are observed in two parts: the continuous phase and the discrete phase. The results of the cylinder simulations are visualized by cross sectional planes. This is illustrated in Figure I.5.

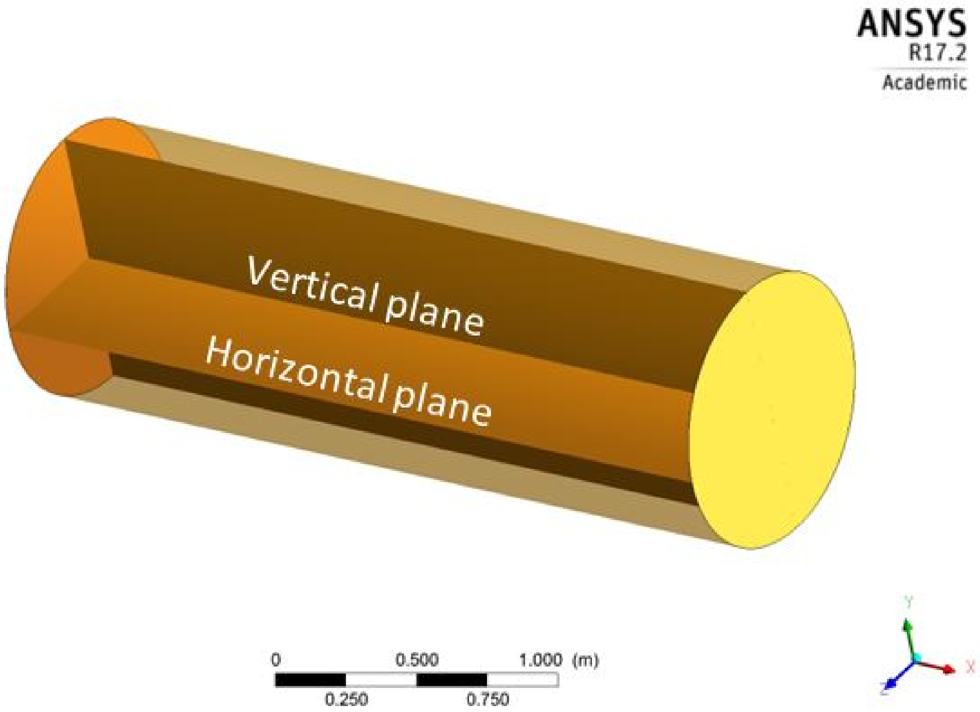

Figure I.5. Visualization of the planes used for illustrating the air flow.

I.2.1 Continuous Phase of the Cylinder Simulations

The velocity magnitudes in the near wall region is lower than 2.0 m/s as illustrated in Figures I.8 - I.11.

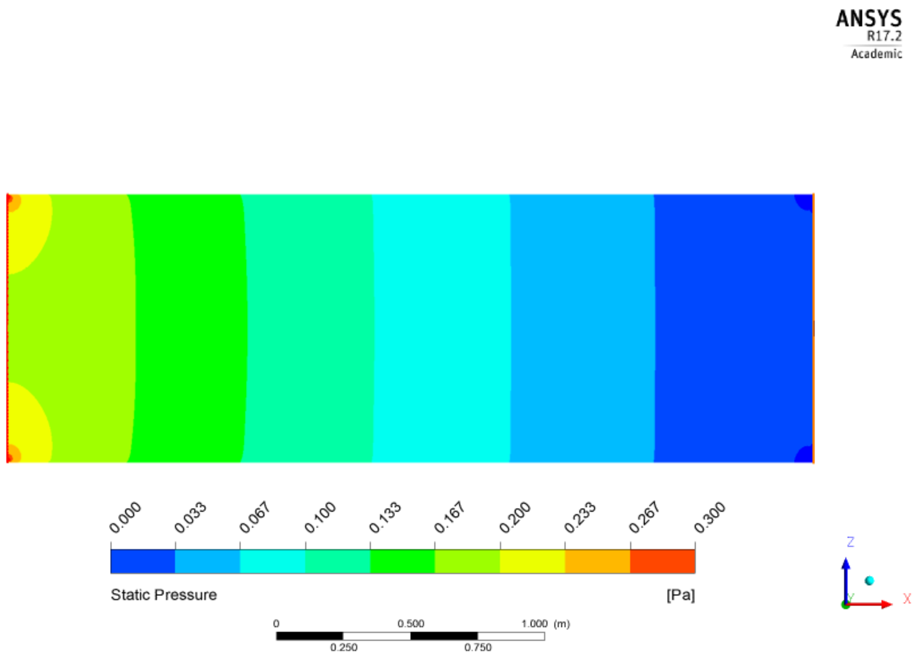

Figure I.6. Contour plot of the static pressure of the vertical plan.

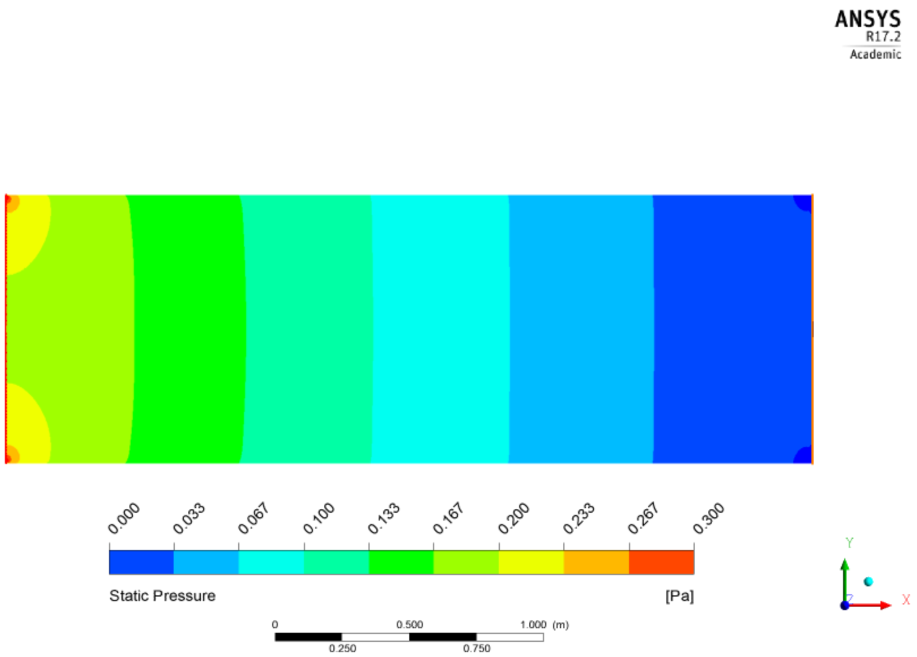

Figure I.7. Contour plot of the static pressure of the horizontal plan.

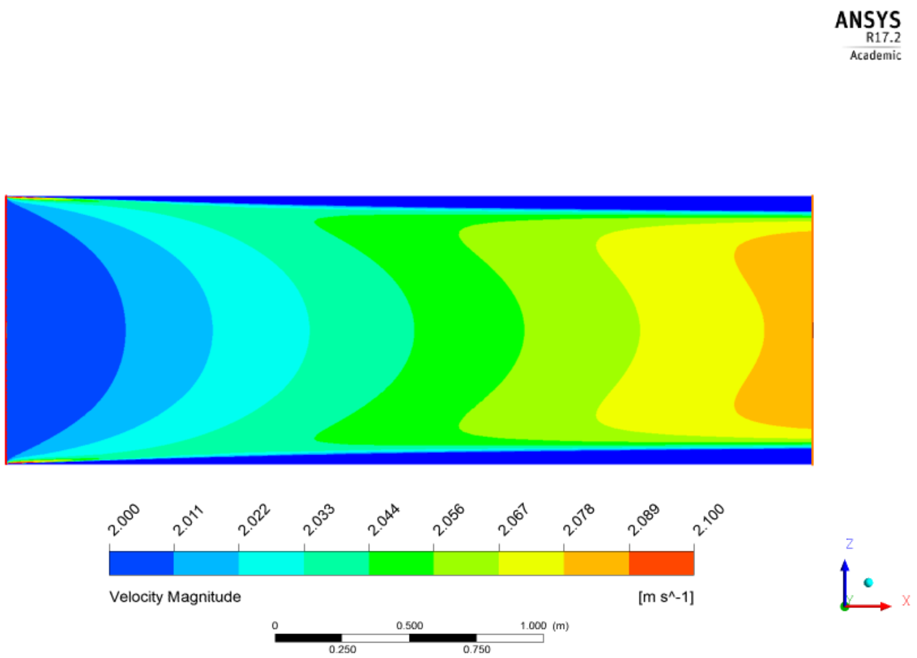

Figure I.8. Contour plot of the velocity magnitude of the vertical plan.

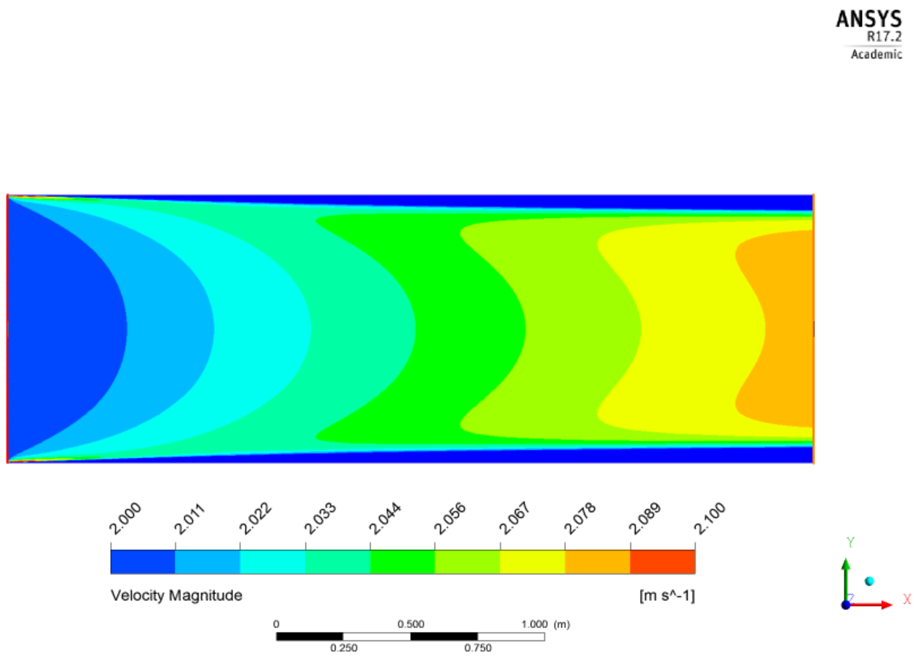

Figure I.9. Contour plot of the velocity magnitude of the horizontal plan.

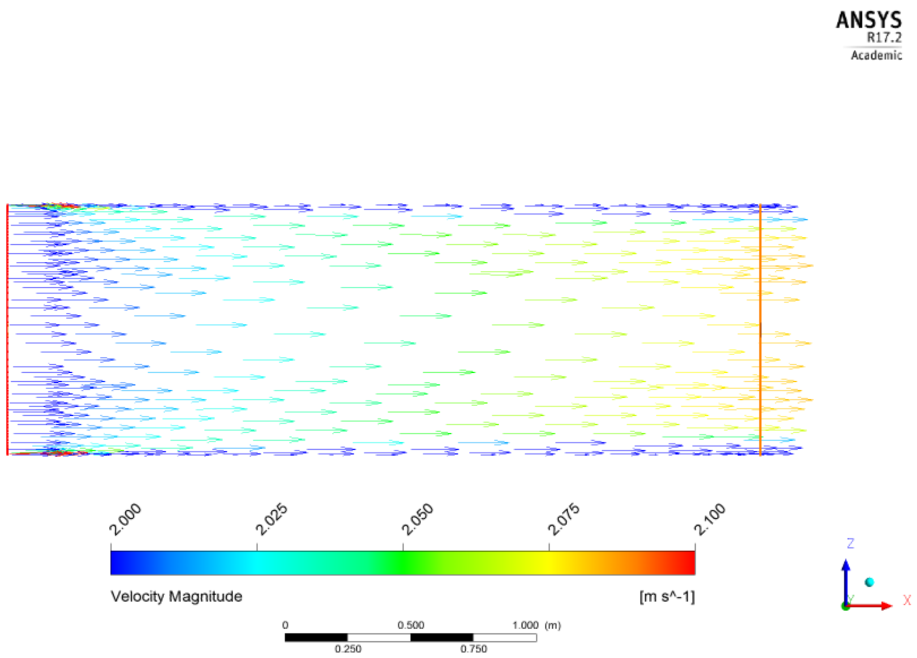

Figure I.10. Vector plot of the velocity magnitude of the vertical plan.

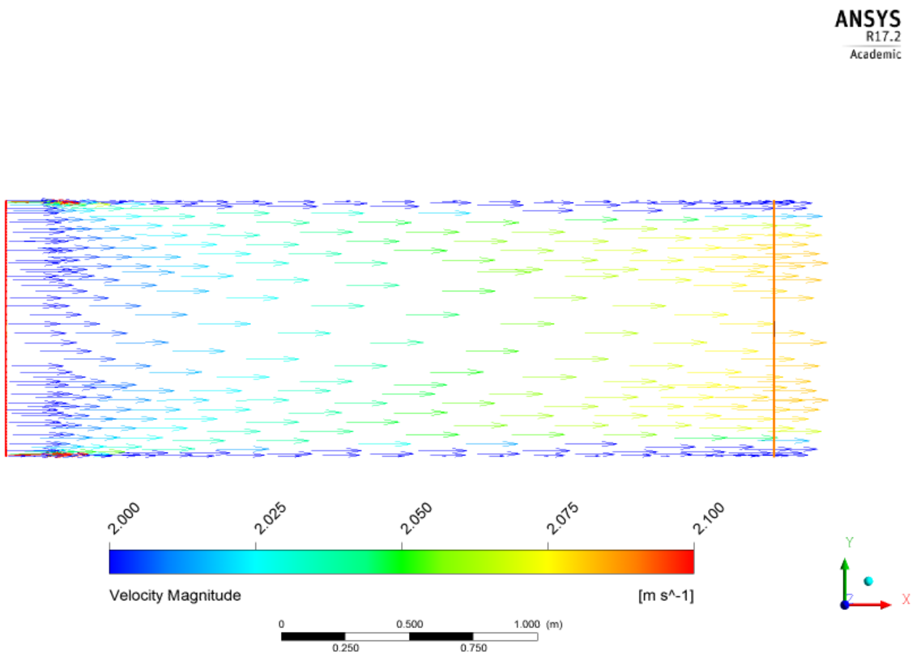

Figure I.11. Vector plot of the velocity magnitude of the horizontal plan.

Figure I.8 and I.9 shows that the velocity magnitude changes in the x direction. The flow develops and the distance at which the flow becomes fully developed is defined as the entrance length. The entrance length can be estimated by Equation I.1.

$$L_e = 4.4(Re)^{1/6} \cdot D \tag{I.1}$$

Where

L_e	Entrance length [m]
D	Diameter of the pipe [m]
Re	Reynolds number [-]

The estimated entrance length is 31.2 m with a Reynolds number of $1.27 \cdot 10^5$ and a diameter of 1.0 meter. Thus the flow does not become fully developed in the cylinder. This is visualized in Figure I.12.

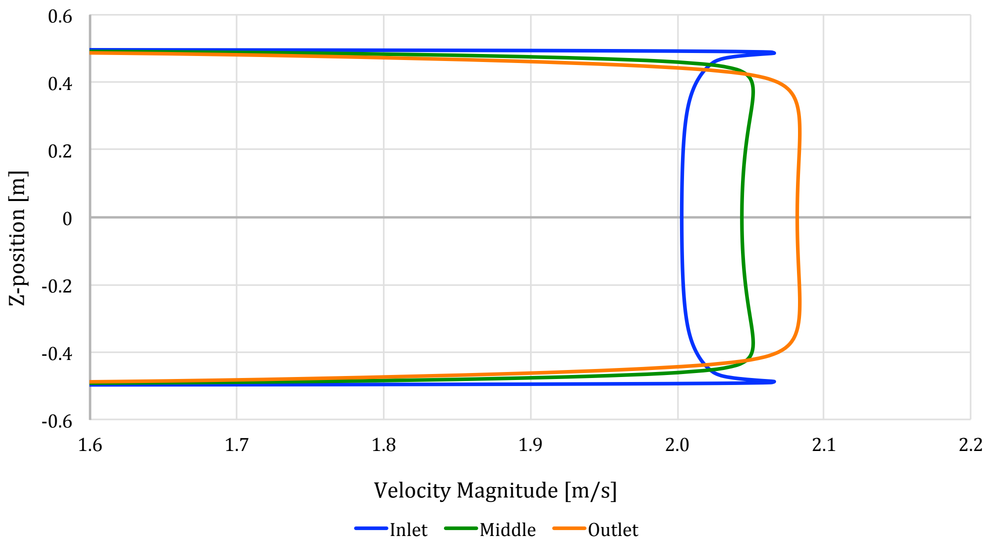

Figure I.12. Velocity profile for cell centred values at the inlet (x=0), the middle (x=1.5), and outlet (x=3.0).

Acceleration at the Inlet

Figures I.7 and I.6 show that there is a high static pressure zone at the inlet near the wall. The pressure zone is a result of the chosen boundary conditions, where the static pressure needs to be high in order to meet the requirements for the chosen boundary conditions. The boundary conditions account that the inlet velocity should be 2.0 m/s, and there should be a no slip condition at the wall. To meet these requirements, the flow needs to have an initial pressure to move the fluid forward. The high local pressure zone results in an acceleration, which is the reason for the peak in profile velocity for the inlet at the wall. The high local pressure zone is highlighted in Figure I.13.

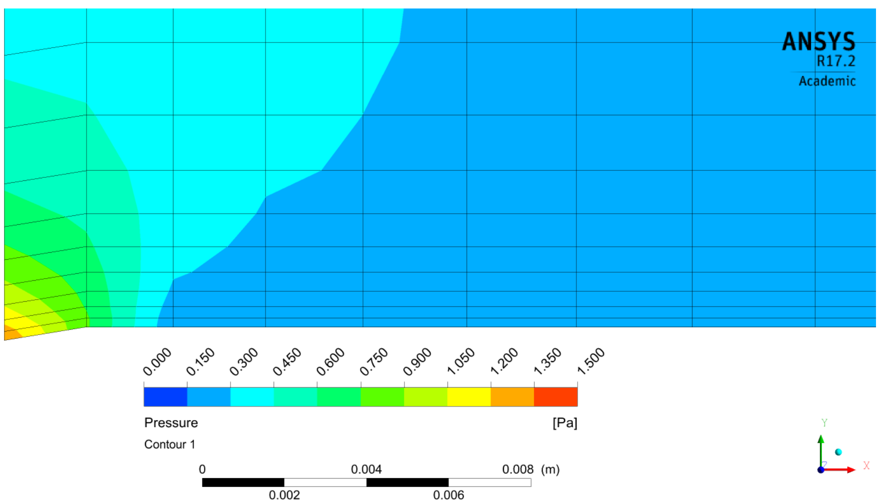

Figure I.13. Contour plot of the static at the inlet of the horizontal plan.

The velocity at the boundary layer drops fast at the inlet due the wall shear stress.

Development of Turbulent Kinetic Energy and Dissipation Rate Near the Wall

Figure I.2.1 illustrates the impact of the wall shear stress on the kinetic energy and the dissipation rate, where the kinetic energy is zero at the wall and the dissipation rate reaches it maximum at the wall. Close to the wall in the buffer layer, the production of turbulent kinetic energy increases due to a high velocity gradient, where it after the peak stabilizes towards the centre line.

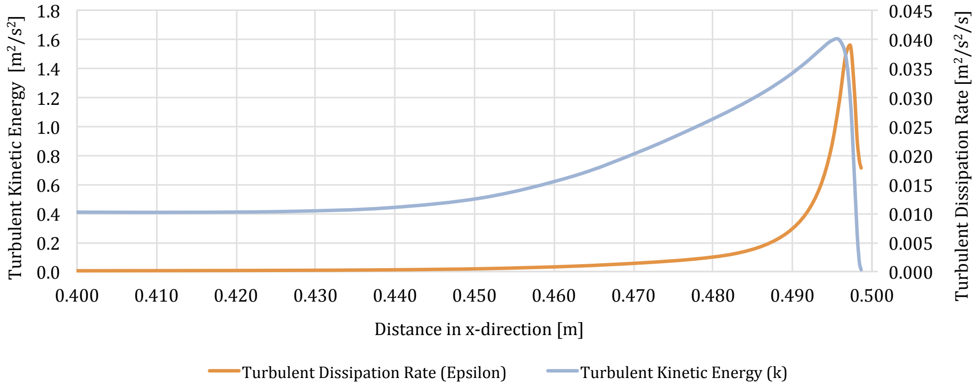

Figure I.14. The turbulent kinetic energy and dissipation rate at the near wall region at the outlet.

I.2.2 Discrete Phase of the Cylinder

Table I.2 shows the fates of the particles for each test. The particle trajectories from steady state simulations (1, 4-8) are illustrated in Figures I.15 - I.19. The particle trajectories from the transient simulations (test no. 2 and test no. 3) can be found in the Digital Appendix. The particle residence time is the time the particle has spent in the flow domain.

Table I.2. Fates of the particles in the cylinder simulations.

Test no.	Escaped		Trapped		Incomplete		Total
	[No]	[%]	[No.]	[%]	[No.]	[%]	[No.]
1	2,690	91.3%	255	8.7%	-	-	2,945
2	26,799	91.0%	2,651	9.0%	-	-	29,450
3	134,193	91.1%	13,057	8.9%	-	-	147,250
4	2,715	92.2%	-	-	230	7.8%	2,945
5	2,897	98.4%	48	1.6%	-	-	2,945
6	1,257	42.7%	1,688	57.3%	-	-	2,945
7	2,697	91.6%	248	8.4%	-	-	2,945
8	2,612	88.7%	333	11.3%	-	-	2,945

For the transient simulations, the whole particle release needs to be considered each time the particles are injected, which causes the increase in number of released particles for test no. 2 and test no. 3. Thus each iteration is more expensive in computational power for unsteady simulations. The particles trajectories for the test no. 2 and test no. 3 can be found in the Digital Appendix.

The fates of test no. 1, 2 and 3 are almost as expected as there is no difference in the set-up. The small difference between the results may be due to a numerical error. An animation of test no. 2 can be found in the Digital Appendix.

Test no. 4 shows that there are incomplete particles when reflection is chosen as boundary condition. Incomplete particles occur when the trajectories are terminated once the maximum allowable number of time steps is exceeded [André Bakker, 2008]. The problem with incomplete particles can be solved by increasing the number of steps in the tracking parameter in Fluent. This has been tested from 25,000 steps to 250,000 steps but for this case the number of incomplete particle trajectories stays the same. Figures I.20 and I.21 show that the particles are stuck along the wall boundary due to the no-slip condition.

It can be concluded from test no. 1, 5 and 6 in Table I.2 that larger particles deposit at a quicker rate due to higher gravitational force. This is visualized in Figures I.15 and I.17. Almost all particles with a size of 1 μm have escaped.

Reducing the initial velocity to 0 m/s in test no. 7 does has considerably little impact on the particle trajectories based on results in Table I.2 and on the visualized figures. However it has a higher amount of escaped particles, which may be due to impaction.

The turbulent dispersion has a big influence on the particle trajectories, as can be seen in Table I.2; the number of trapped particles has increased. The turbulent dispersion of particles is also visualized in Figure I.18 and Figure I.19. The number of tries for test no. 8 is 1.0 in order to compare the trajectories by visualization. The number of tries increases the numbers of tracked trajectories proportionally. A higher number of tries increases the calculation time. Thus the number of tries is a balance between accuracy and calculation time. Test results with a simulation of 10 tries and 100 tries can be found in the Digital Appendix.

The interaction between the discrete phase and the continuous phase are negligible for these tests, as the mass flow of the particle is $1.0{\cdot}10^{-20}$ kg/s and the mass flow for the carrying medium is 1.9 kg/s. It has been examined and fits with the theory about Discrete Phase Modelling from Section 10.3. The test results can be found in the Digital Appendix.

The effect of Brownian motion force on particle deposition in the cylinder has been investigated for the following size of particles: 0.1 μm, 1.0 μm and 10.0 μm. The Brownian force was only found to have a minor influence on 0.1 μm particles and no influence at all on 1.0 μm and 10.0 μm particles. Brownian motion usually influences particles smaller than 2.0 μm [Tu et al., 2013]. The small reaction may be due to the small ratio between the length and diameter of the cylinder. The influence of the Brownian motion on particles could therefore be investigated in an extended cylinder.

The influences of the remaining additional forces on the test case have also been examined. The forces have an insignificant influence on the results. They are negligible due to the following:

- Saffman's lift force: Minor velocity differences between the particles and the fluid
- Virtual mass force and pressure gradient force: High-density particles in low-density fluid
- Magnus lift force: Simple flow with small particles, little rotation of the particles

The results can be found in the Digital Appendix.

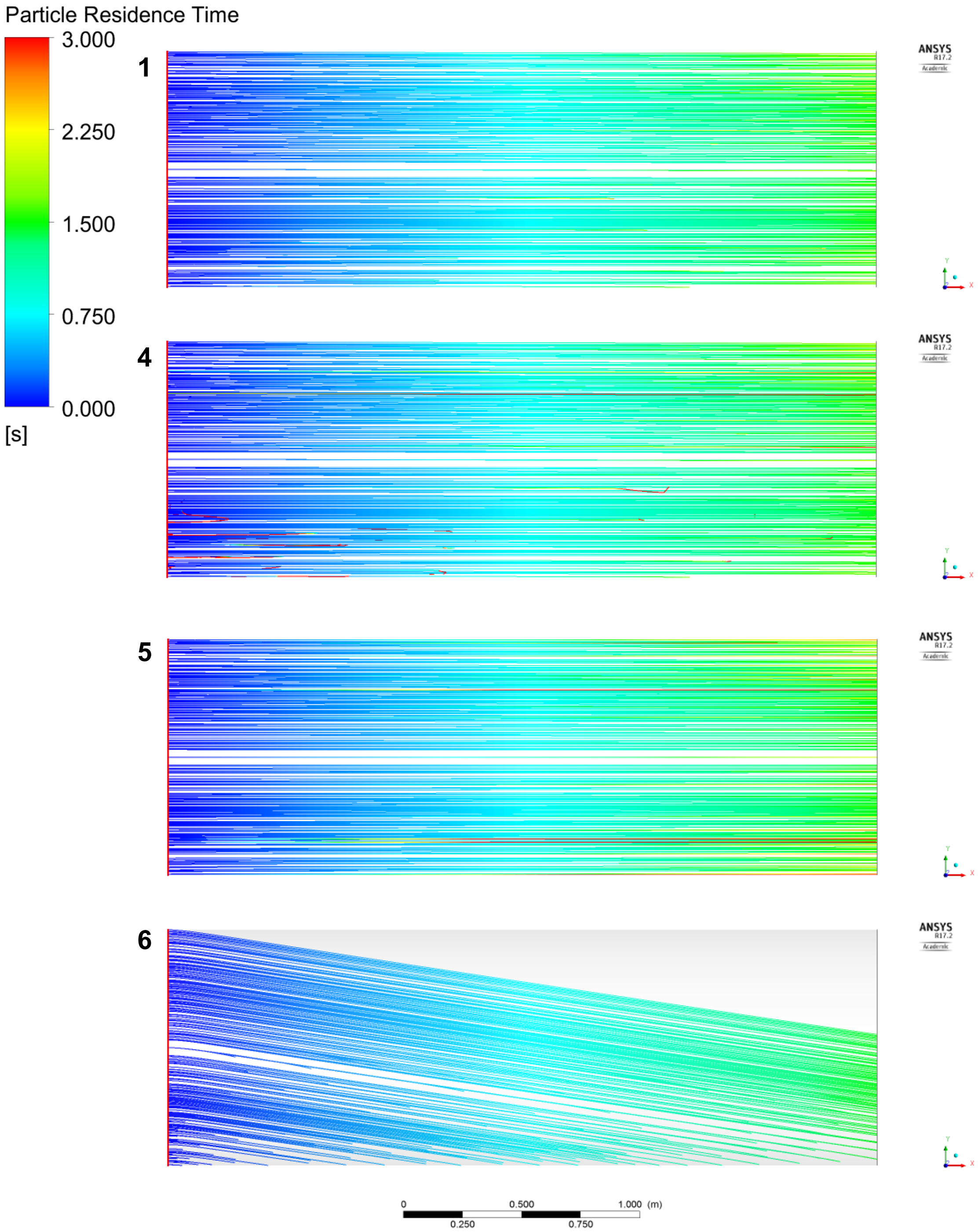

Figure I.15. Particle residence time for test no. 1, 4-6 from a side view.

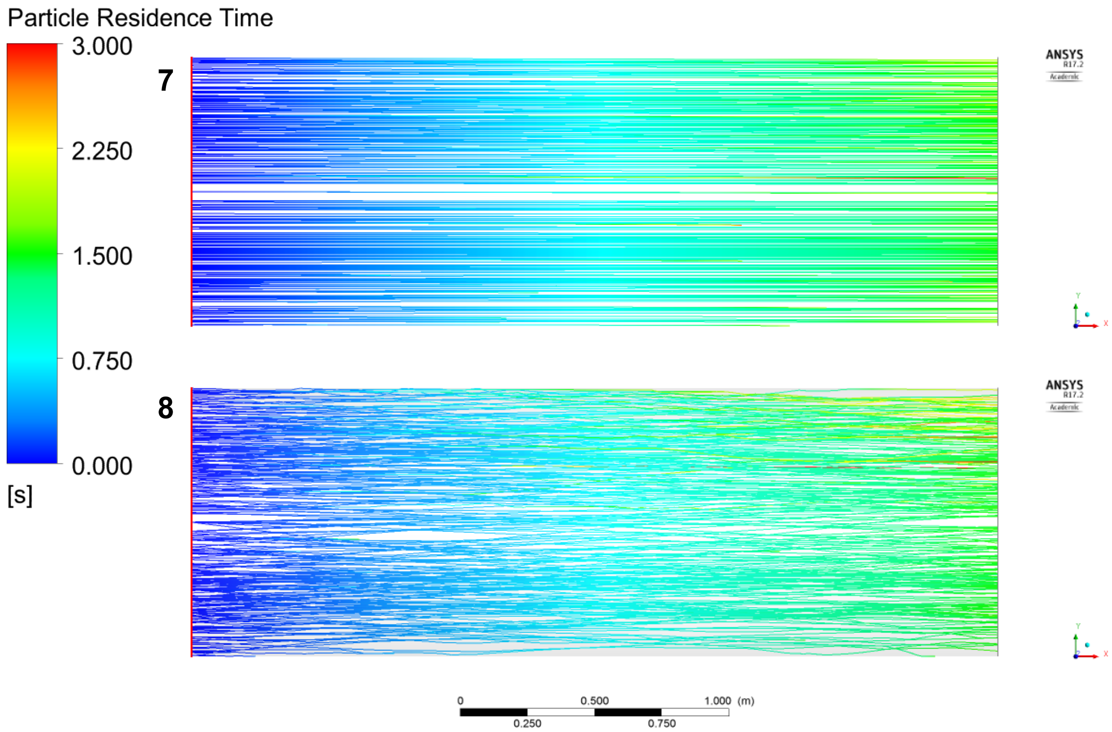

Figure I.16. Particle residence time for test no. 7-8 from a side view.

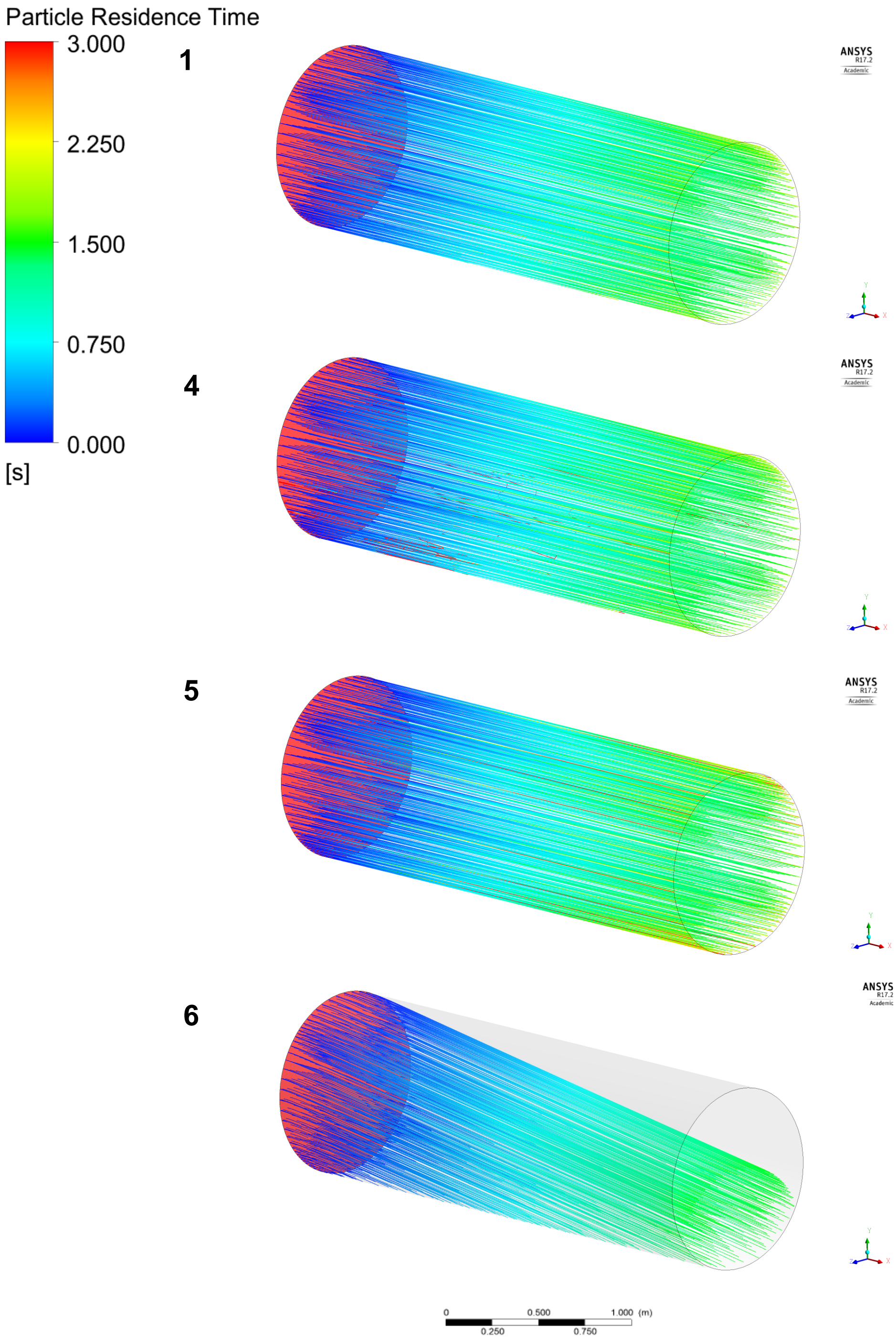

Figure I.17. Particle residence time for test no. 1, 4-6 from a trimetric view.

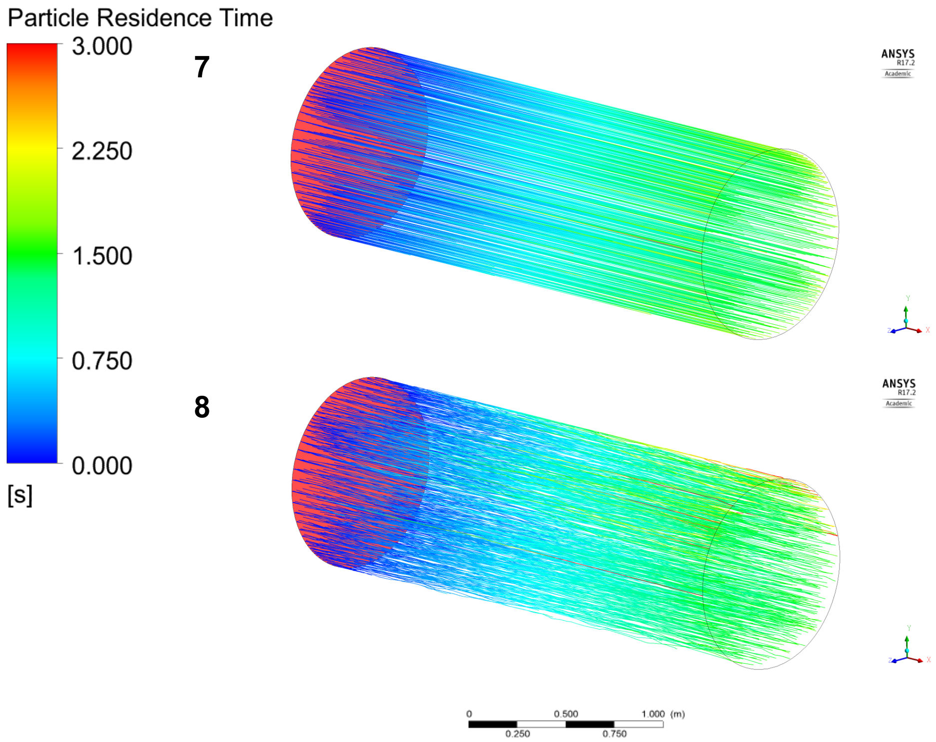

Figure I.18. Particle residence time for test no. 7-8 from a trimetric view.

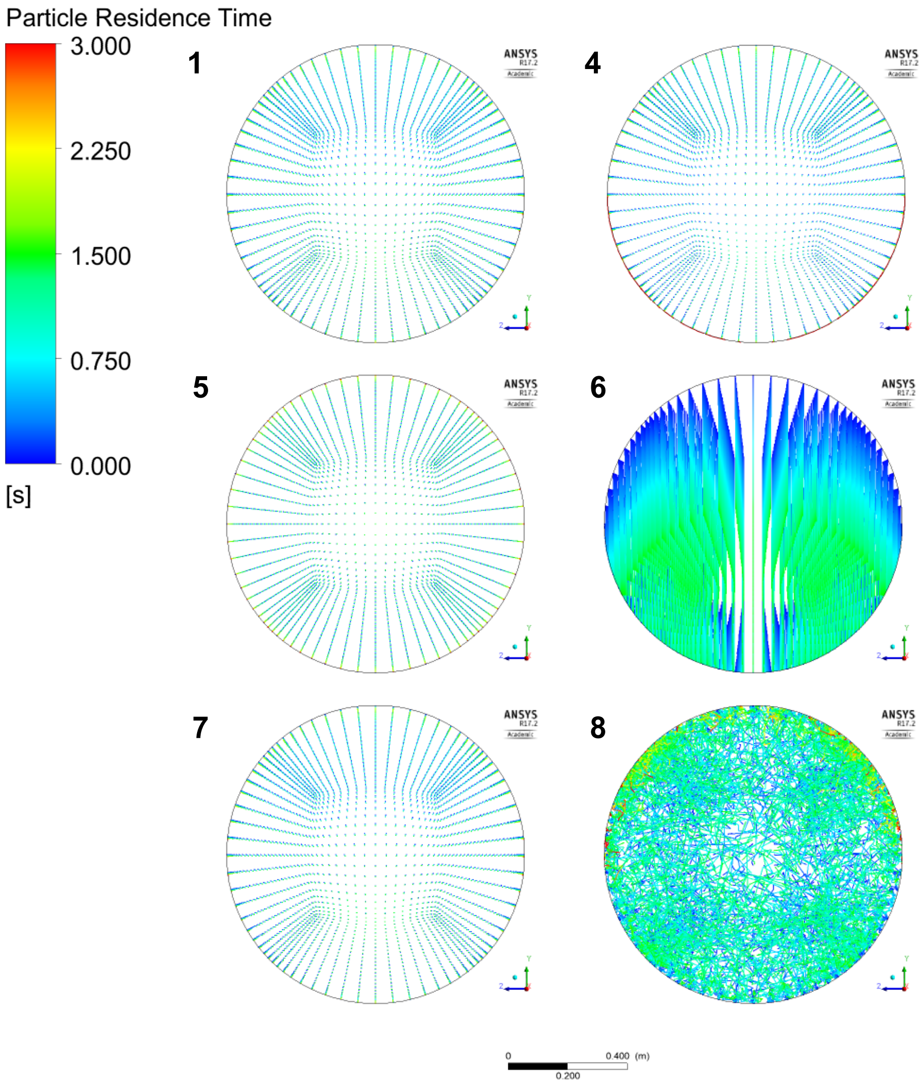

Figure I.19. Particle residence time for test no. 1, 4-8 from the back view.

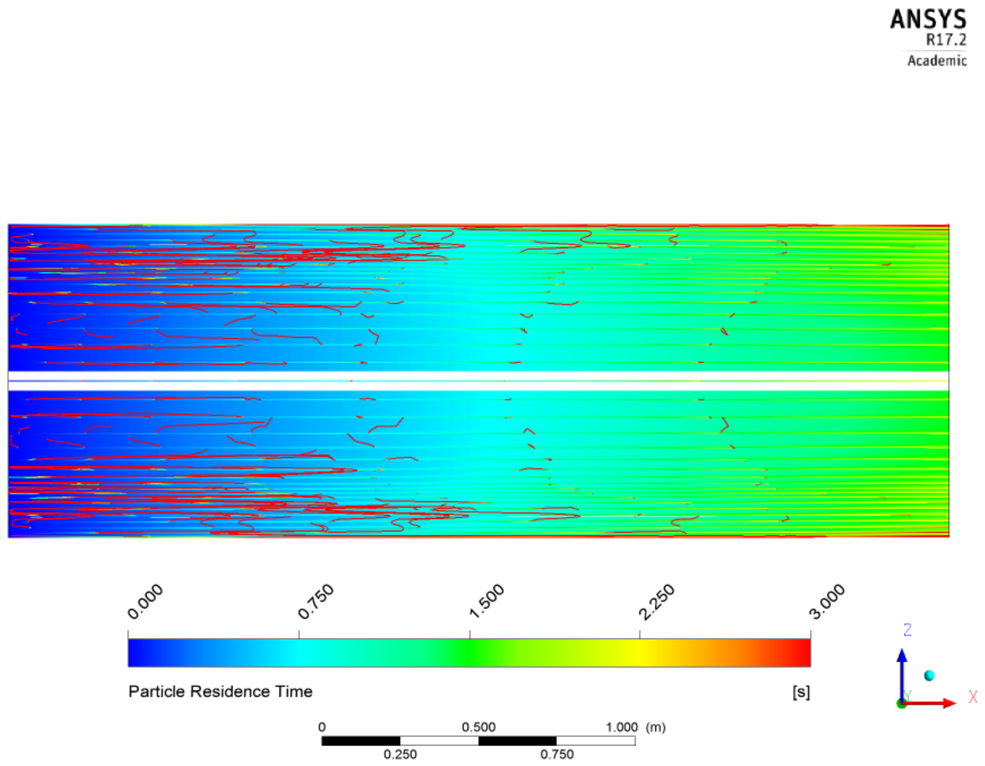

Figure I.20. Particle residence time for test no. 4 from a side view with a higher numbers of steps.

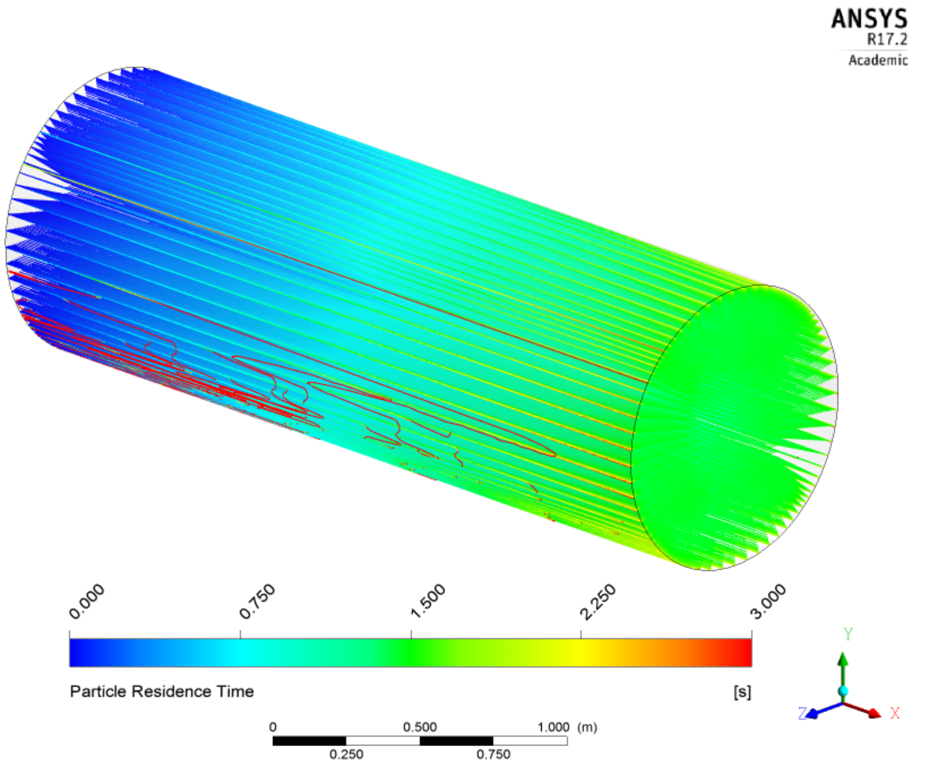

Figure I.21. Particle residence time for test no. 4 from a trimetric view a higher numbers of steps.

J Geometry Modification for Meshing

The geometries must be modified in order to enable mesh generation. The 3D printed airway model consists of five individual bodies and inlet and outlets are not defined as one plane surface. Different software exists that enables the modification of STL files. For this study the software SpaceClaim, a part of the ANSYS package, is used to modify the geometry.

Stereolithography (STL) files describe the surface geometry of three-dimensional objects, as illustrated in Figure J.1. STL files are widely used for 3D printing. [Chakravorty, 2017]

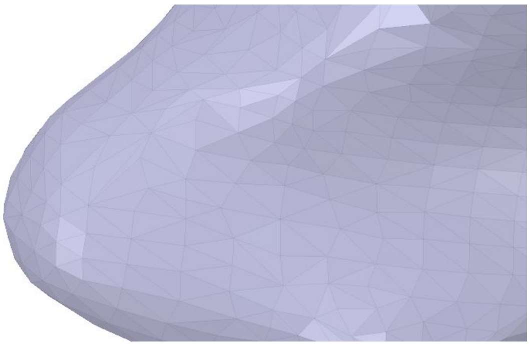

Figure J.1. The triangular construction of the surface from the STL file.

Two different methods in SpaceClaim have been examined in order to modify the geometry:

- Modifying the STL file directly using the facets tool bar
- Applying reverse engineering on the STL file

The facets tool bar is not available through the student license of ANSYS. A workstation at Aalborg University has therefore been used.

Direct Facets Modification

The STL files can be modified directly and saved as a new STL file. The advantage of modifying the facets directly is that it does not reproduce the actual scanning as with reverse engineering. Furthermore, a tool in SpaceClaim can be applied that auto-fixes any problems there might be with the solid facet geometry.

However, it was not found possible to divide the facets into different parts when modifying them directly in the STL file in SpaceClaim. This therefore needs to be carried out in the software ICEM.

Reverse Engineering Modification

Reverse engineering can be used on the STL file to reproduce the geometry, thus enabling the faceted airway model to be divided into multiple surfaces. The surface creates an approximation of the geometry, where the accuracy of the reproductions is dependent on the numbers of samples, which are used to generate the surface. A higher number of samples results in higher accuracy; however, it also increases the size of the model. An example of the generation of a surface from the airway model by applying reverse engineering is shown in Figure J.2.

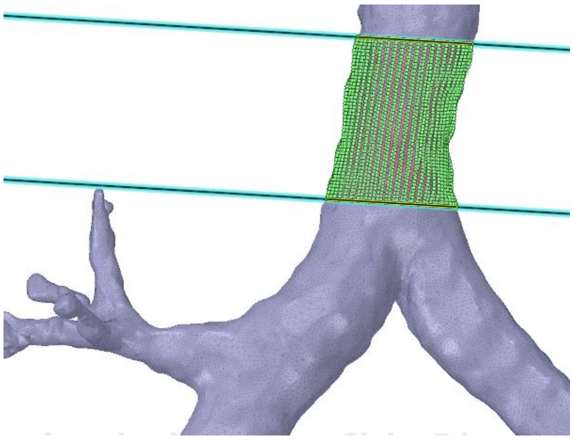

Figure J.2. Reverse engineering applied on the airway model.

The main advantage is the division of the airway model into smaller surfaces in SpaceClaim, and thereby easier to control. The disadvantages of reverse engineering are the manual, time-consuming work and the limitation in the approximation of the geometry.

Final Modified Airway Model

Direct facets modification is applied to modify the geometry of the 3D printed airway model instead of reverse engineering due to the complexity of model, where the bronchioles are located in the enclosed cavity of the lungs. Hence the airway path of the 3D printed airway model and the airway model used for CFD simulation is the same. The only exceptions are a modification created at the mouth and the surface roughness of 0.1 mm in the 3D printed model, which is not implemented in the CFD airway model. Despite these small differences, the CT-scanning of the airways, the 3D printed airway model and the CFD airway model have the same geometry.

A description of the procedure for modifying the facets directly and a descriptions of the modification of the models can be found in Section J.1. A description of how to modify the airway model by reverse engineering can be found in the Digital Appendix as both methods were tested.

The modified geometry of the airway model, which is used for meshing, is shown on Figures J.3 and J.4.

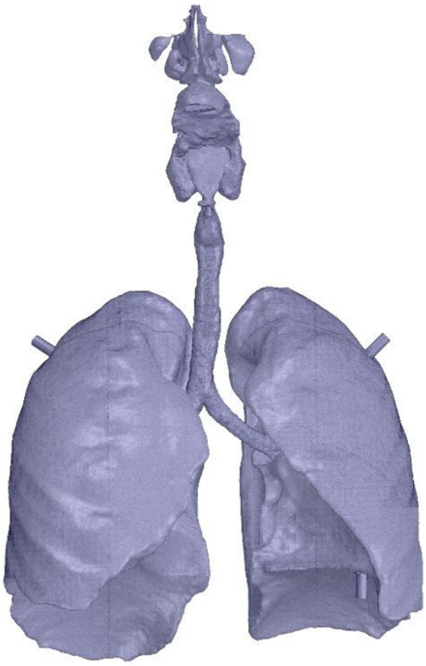

Figure J.3. Front view of the final modified air model.

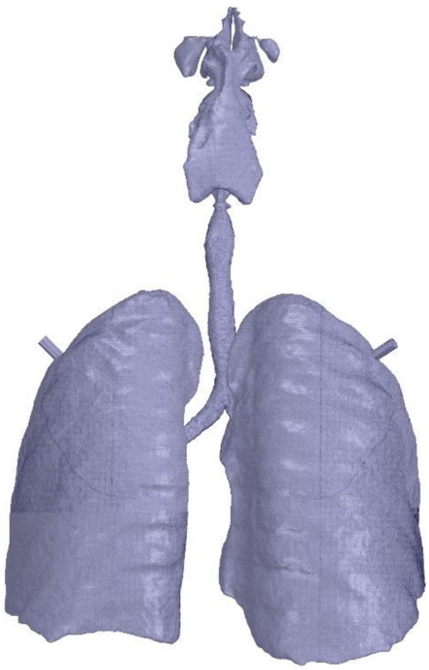

Figure J.4. Back view of the final modified air model.

J.1 Generation of the Airway Model

The 3D printed airway model consist of five parts, which can be assembled; face and upper airway, airway to left lung, airway to right lung, left lung, right lung. Each part is illustrated from the digital drawings in Figures J.5- J.14.

Figure J.5. Front view of face and upper airway.

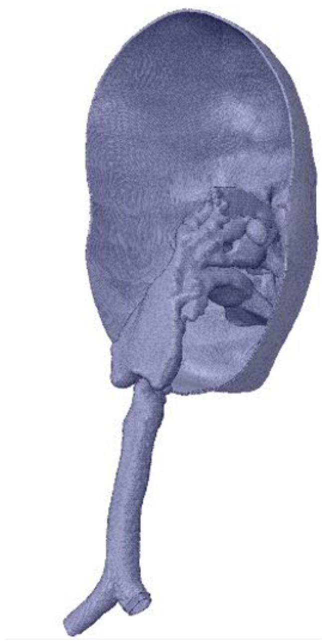

Figure J.6. Back view of face and upper airway.

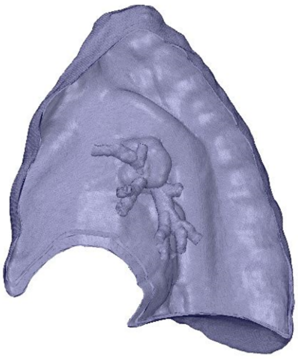

Figure J.7. Front view of airways to left lung.

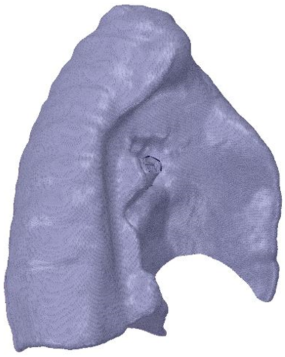

Figure J.8. Back view of airways to left lung.

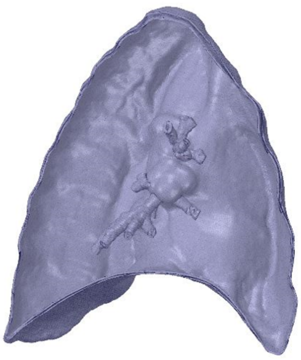

Figure J.9. Front view of airways to right lung.

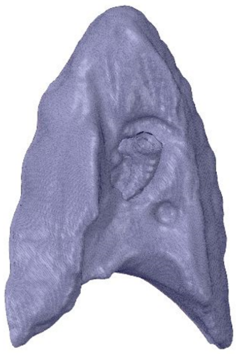

Figure J.10. Back view of airways to right lung.

Figure J.11. Front view of left lung.

Figure J.12. Back view of left lung.

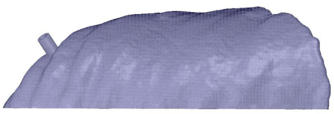

Figure J.13. Front view of right lung.

Figure J.14. Back view of right lung.

The 3D printed model of the airway is constructed by merging each of the 3D printed parts together. The external layer of the model is deleted, leaving the internal part of the model on which the simulations will be carried out. New surfaces have been created at the mouth, nostrils and the outlet plugs in the lungs so the internals part of the airways become a watertight solid. The new surfaces need to be drawn finely in order to avoid conflicts with the overlapping facets. The model is cleaned for overlapping facets and the merged parts are checked to ensure a smooth transition between each part.

The surfaces at the nostrils and the mouth are modified from the original openings as the surfaces need to be a straight plane without any curvature. The locations of the surfaces are highlighted in Figure J.15. The location of the surface at the mouth opening ensures a low discharge factor as a high discharge factor will give an inaccurate pressure distribution.

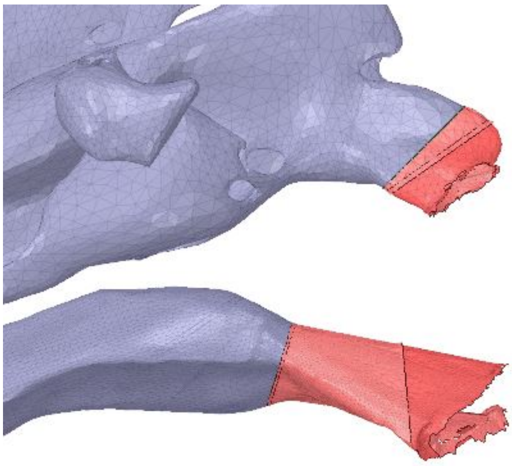

Figure J.15. Location of the surfaces at the mouth and the nostrils.

The modified facets geometry, which is ready for meshing, is then exported to an STL file, which can be opened in the meshing software ICEM.

K Structural Concept of the Mesh

The structure of the mesh is determined in order to meet the requirements for the mesh quality and the y^+ value at the boundaries.

K.1 Local Refinement

The y^+ value is adjusted by coarsening and refining the mesh. An estimation of the y^+ value by hand calculations cannot be carried out as the hand calculation procedure requires turbulent flow. Due to big variations in the geometry and the flow conditions, local refinement needs to be conducted for the final adjustment. The mesh is divided into different parts dependent on the respiratory anatomy and to obtain the possibility of doing local refinement. The local refinement is conducted on the bronchus, the larynx and the lung volume:

- The bronchus are divided into three parts in each lungs to obtain more detailed information about the location of the deposited particles and to refine the mesh at the narrowest part.
- Each lung is divided into four parts to increase the mesh quality and to carry out local refinement. Tetrahedral elements are used at the boundary layer in the lung volume at the bronchus to improve the mesh quality and reduce the number of bad elements. This is highlighted after a comparison between the mesh with prism layer in the lung volume and a mesh with tetrahedral elements along the boundary in the lung volume. The mesh reports can be found in the Digital Appendix. The rest of the lung volume is divided into three parts due to local refinement:
  - *Plug*: At the plug located at the top of the lung, which acts as the outlet
  - *Refined*: In the areas of the lung volume, which are affected by the bronchi's jets.
  - *Coarse*: In the remainder of the lung volume
- The larynx is divided into two parts as the bottom part of the larynx needs to be modelled with a dense mesh in order to capture the critical flow region. The narrow passage of the larynx generates a laryngeal jet, which is the most prominent inhalation phenomenon that determines the flow behaviour in the trachea and the bronchus [Choi et al., 2009]. Thus the mesh needs to be very fine is this region. The narrowest part of the larynx is approximately 3.7 mm.

An illustration of the subdivisions of the mesh is shown in Figure K.1. The bronchioles inside the lung shells are illustrated in Figure K.2.

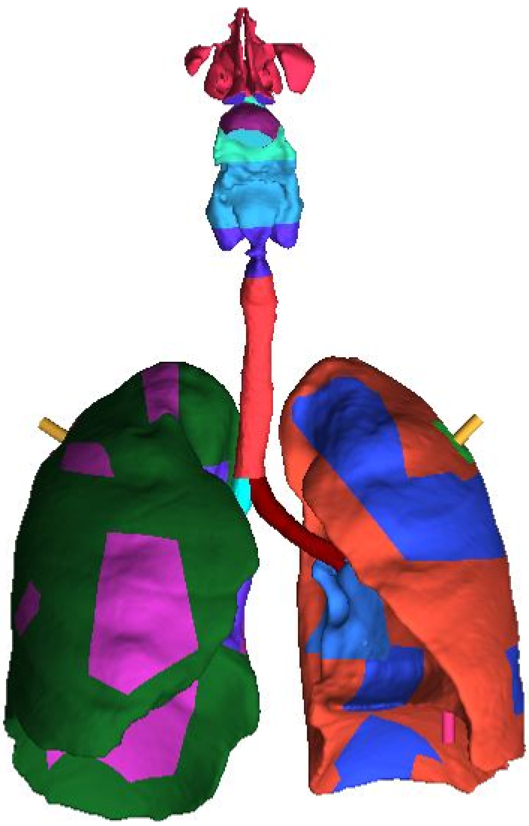

Figure K.1. The airway model divided in different parts to conduct local refinement.

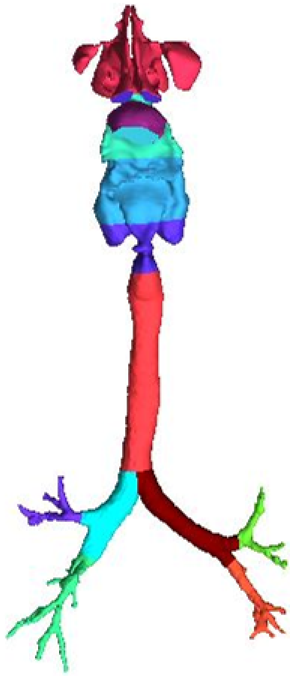

Figure K.2. The airway model divided in different parts to conduct local refinement without the lung shell.

The nasal cavity and surface at the nostrils is coarsened to reduce the number of elements, as breathing is only conducted from the mouth for this study.

K.2 Mesh Parameters for the Baseline Model

Table K.2 shows the mesh parameters applied on the baseline model used to conduct the mesh independence test.

Table K.1. Mesh parameters for the baseline model used to generate meshes in the software ICEM.

Part name [-]	**Prism Layer** [Yes/No]	**Maximum size** [mm^3]	**Initial height** [mm]	**Ratio** [-]
Inlet_nose	No	5	0	2
Inlet_mouth	No	0.5	0	1.2
Plug_top_left	No	0.5	0	1.2
Plug_bottom_left	Yes	2	0	1.2
Fluid	No	5	0	0
Lung_right_bronchi	No	5	0	1.2
Lung_left_bronchi	No	5	0	1.2
Plug_top_wall	Yes	0.6	0.03	1.2
Plug_bottom_wall	Yes	2	0.3	1.2
Bronchi_right_t	Yes	1	0.06	1.2
Mouth	Yes	0.8	0.05	1.2
Nasal_cavity	No	10	0	2
Pharynx	Yes	0.8	0.09	1.2
Larynx	Yes	0.8	0.06	1.2
Trachea	Yes	1	0.06	1.2
Bronchi_left_t	Yes	1	0.06	1.2
Bronchi_right_t1	Yes	0.5	0.03	1.2
Bronchi_right_t2	Yes	0.5	0.03	1.2
Bronchi_left_t1	Yes	0.5	0.03	1.2
Bronchi_left_t2	Yes	0.5	0.03	1.2
Larynx_bottom	Yes	0.4	0.04	1.2
Plug_top_right	No	0.5	0	1.2
Plug_bottom_right	Yes	2	0	1.2
Lung_right_coarse	Yes	3	0	0
Lung_left_coarse	Yes	3	0	0
Lung_right_plug	Yes	1	0.05	1.2
Lung_right_refined	Yes	1	0.11	1.2
Lung_left_plug	Yes	1	0.05	1.2
Lung_left_refined	Yes	1	0.11	1.2

L Documents in the Digital Appendix

In the Digital Appendix, procedures, documentation for convergence, relevant calculations etc. are attached. The contents in the Digital Appendix is ordered according to each chapter.

6. Experimental Description

- **Folder:** Examination of ventilation type

  Excel: Archimedes number XIan chamber

  Word: Calculation sheet of Archimedes number and velocity inlet

7. Analysis of Experimental Results

- **Folder:** Indoor climatic conditions - monitoring
- **Folder:** Particle Sensor Raw Data

8. Additional Investigations

- **Folder:** Investigation of the Thermal Plume Effect PM10

11. Numerical Framework of the Airway Model

- Word: Calculation of cunningham correction factor
- Word: Calculation of hydraulic diameter of the inlet at the mouth
- Word: Calculation of the Reynolds number of the trachea
- Word: CFD airwaysetup DMP
- Word: Fluent– DPM Procedure Screenshots

12. Meshing of the Airway Model

- **Folder:** Mesh independence - Plans and lines
- **Folder:** Mesh independence - residual, summary, line export
- **Folder:** Mesh Quality Investigations

  Folder: Floating or tetrehedrals

  Folder: Lung volume prism or tretrahedrals
- **Folder:** Yplus - Baseline
- Excel: Mesh independence generation
- Word: Procedure for CFD simulations

13. Post-Processing of Simulation Results

- **Folder:** Comparison with papers
- **Folder:** Convergence documentation
- **Folder:** Postprocessing - Contours plots
- **Folder:** Postprocessing DPM

  Excel: Particle datatreatment

  Folder: Summary files
- HTML: Mesh Quality report - EAMEM0769

D. Morphometry of the Tracheobronchial Tree Cast

- **Folder:** Procedure
- **Folder:** Screenshoots angles
- **Folder:** SpaceClaim models
- Excel: Morphoemtry EAM

G. Measurement Parameters

- Word: Calculations of the volume of the two lungs

H. Calibration of Instruments

- **Folder:** Particle Sensor PM2.5
- **Folder:** Particle Sensor PM10

I. Preliminary Investigation of a Cylindrical Test Case

- **Folder:** Fluent set-up investigations
- **Folder:** Results - Continuous phase
- **Folder:** Results - Discrete phase
- Excel: Cylinder - Mesh independence test
- Word: Estimate wall distance y+
- Word: Reynoldsnumbercalculator
- Word: Set-up of Testnr1 (Fluent)

J. Geometry Modification for Meshing

- Adobe: Modifying the airway model by Reverse Engineering